Dottorato di Ricerca in Architettura, Ingegneria delle costruzioni e Ambiente costruito

Ph.D. Degree in Architecture, Built environment and Construction engineering

Emanuele Gandelli

Advanced tools for the design of sliding isolation systems for seismic-retrofitting of hospitals

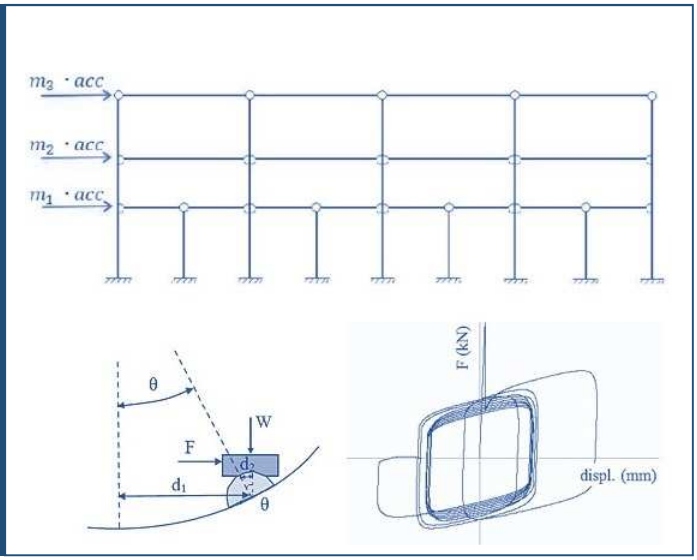

POLITECNICO DI MILANO
DOCTORAL PROGRAMME IN ARCHITECTURE, BUILT ENVIRONMENT AND CONSTRUCTION ENGINEERING

ADVANCED TOOLS FOR THE DESIGN OF SLIDING ISOLATION SYSTEMS FOR SEISMIC-RETROFITTING OF HOSPITALS

Doctoral Dissertation of:
Emanuele Gandelli

Supervisors:
Prof. V. Quaglini
Prof. M.G. Limongelli

Tutor:
Prof. S. Capolongo

Chair of the Doctoral Program:
Prof. E. De Angelis

March 2017 – Cycle XXIX

To the memory of victims of recent Central Italy earthquake

Acknowledgements

First, I express my sincere gratitude to Prof. Virginio Quaglini for having uninterruptedly supported and supervisioned my research activities during all this long adventure. I am very grateful also to Prof. Maria Pina Limongelli who helped me to solve some of the most challenging issues addressed in the thesis. Thank you to Prof. Stefano Capolongo for the valuable information about the layout of systems in hospital buildings, and to Prof. Enrico De Angelis, Head of the PhD program, for the complex coordination of all the doctoral activities.

I want to acknowledge also the great assistance provided by Eng. Mattia Penati and Prof. Edie Miglio in implementing a new "isolator element" in OpenSees® FEM code and the availability of the Arch. Carlo Nisticò in sharing the information concerning the structural elements of the Lamezia Terme hospital.

A special mention goes to Dr. Gianmario Benzoni, and to Prof. Giuseppe Lomiento for the great opportunity to cooperate with their research group during my stay at the UCSD of San Diego, California.

A big thank to my friends of the BJA team (Dub, Dan, Vaz, Rib, and Dani), and to the ones of the ABC Dept. (Giulia, Elisa, Gaia, Antonella and Ana) for the pleasant leisure moments spent together.

Last but not least, to the long-life friends of the TCD team (Ceco, Ste, Fede, Dami, Serg, Filip, Cisky, Torti, John, and Laura), and to my family that allowed me to overcome with serenity the hardest moments… simply thank you!

Contents

CHAPTER 3 – SEISMIC PERFORMANCE OF HOSPITAL BUILDINGS

CHAPTER 4 – DEVELOPMENT OF DESIGN TOOLS

Abstract

Hospitals' full operation after a major seismic event is of primary importance for the management of post-earthquake emergency. However, the traditional approach for earthquake-resistant structures based on strengthening the building structure may turn out not to be the optimal design strategy, because hospitals are characterized by a massive presence of non-structural components and valuable technological content (e.g. medical equipment) that are largely sensitive to displacements and accelerations induced by earthquakes. Since its introduction, base isolation strategy proved to be an effective solution for the protection of hospitals and hospital content from earthquake-induced damages, enhancing their resilience and entailing substantial decrease in time and cost of repair compared to a conventional fixed-base structure. Sliding isolators, over other devices, present some valuable advantages especially for the seismic retrofitting of existing buildings: high load-carrying and displacements capacity combined with compact dimensions, independence of the oscillation period on the mass of the superstructure, and minimization of torsional effects in case of asymmetric buildings. Nevertheless, in spite of the large diffusion worldwide occurred in the last decade, a full understanding of the performances, and limits, of sliding isolators has not been yet completely achieved. Shaded areas are the properties of the sliding materials, the behaviour of the isolator under real earthquakes rather than laboratory tests, and the unavailability of finite element formulations for structural analysis capable to represent the actual behaviour of the isolators in particular conditions (e.g. at breakaway and during long duration excitation). Within this framework, the scope of this research project is the development of new tools for the design of seismic retrofitting interventions of buildings with high technological content (with a focus on hospitals) by means of sliding isolation systems. The cornerstones of the study are: (1) the establishment of a FEM approach for the assessment of the frictional heating in sliding isolators; (2) the numerical investigation of the re-centring capability; (3) the improvement of an existing finite element formulation of the "isolator" element in order to reproduce both the resistance to sliding at breakaway and the decrease in damping due to the frictional heating; (4) proposal of a "step by step" procedure for the design of the isolation layout suitable for retrofitting interventions of strategic buildings by means of sliding isolators; (5) application of the proposed tools to a real case-study hospital.

Introduction

The present thesis is focused on the characterization of the sliding behavior of curved surface sliders for base isolation and the development of advanced numerical tools for the design of sliding isolation systems for seismic-retrofitting of hospitals.

Hospitals' full operation after a major seismic event is of primary importance for the management of post-earthquake emergency. However, recent earthquakes have shown that the traditional approach for design of earthquake-resistant structures based on the strengthening, though preventing the collapse of the building, may result in severe damages to non-structural elements and electro-medical equipment, eventually compromising the operability of the hospital. On the contrary, seismic mitigation design by means of base isolation and/or energy dissipation has shown to be an effective solution for the protection of hospitals and hospital content from earthquake-induced damages, enhancing their resilience and entailing substantial decrease in time and cost of repair compared to a conventional fixed-base structure.

Among the current isolation hardware, curved surface sliders (known in North America as the Friction Pendulum System) feature favourable characteristics like high load-carrying and displacements capacity combined with compact dimensions, oscillation period virtually independent on the mass of the superstructure, and minimization of torsional effects in case of asymmetric buildings, which make them the most suitable device for seismic retrofitting of existing buildings, like e.g. hospitals. Nevertheless, in spite of the large diffusion worldwide occurred in the last decade, a full characterization and modelling of the behaviour of sliding isolators has not been yet completely achieved, and this is also reflected in the codes and in the design tools available to structural engineers.

The present thesis is therefore focused on the characterization of the sliding behavior of curved surface sliders for base isolation and the development of advanced numerical tools for the design of sliding isolation systems for seismic-retrofitting of hospitals.

The thesis is divided into six chapters.

The first three chapters aim at providing the reference state of the art for the whole research project. In particular, *Chapter 1* describes the basic operational principles, and the dynamics of base-isolated structures. Two well acknowledged categories of anti-seismic hardware (elastomeric and sliding isolators) are introduced. Seismic limit states and relevant performance requirements for base-isolated buildings according to the Italian Building code are summarized.

Chapter 2 describes more in details the Curved Surface Slider (CSS) isolator starting from its main components and its kinematics. The main advantages deriving from the use of CSS devices for seismic retrofitting interventions, as well as the main drawbacks related to their actual behavior during the earthquake are discussed. Indeed, it is well known that the effective stiffness and damping of these devices strongly depend on the friction coefficient of the sliding material used at the sliding surfaces. Mathematical models available in literature that describe the dependence of the friction coefficient on the instantaneous sliding velocity, temperature, and vertical load acting on the devices are critically presented. Among the main limits of these formulations, some open fields of research are investigated in the present study.

Chapter 3 describes the specific issues related to the implementation of the base-isolation technique for the seismic protection of hospital buildings, and introduces a performance approach to quantify their resilience during the earthquake attack. Among hospital's physical components, in addition to the common structural elements (e.g. beams and columns), there is a huge number of non-structural components (NSCs) like distribution lines, medical electrical equipment, etc. that are largely vulnerable to the effects of the earthquake. NSCs indeed can be divided into "*acceleration-sensitive*" and "*drift-sensitive*" elements. Breakdown thresholds for each NSC, suitable for use in a fault-tree analysis when assessing the overall seismic response of the hospital complex, are identified from a literature survey.

Within *Chapter 4*, some of the open issues related to the dynamic response of CSS isolators during the seismic shaking are investigated, and advanced tools for a more reliable design are proposed.

The first issue is the frictional heating of the sliding surface and its effect on the coefficient of friction and consequently on the equivalent damping and stiffness of the device. A 3D thermo-mechanical model of a CSS isolator is developed in Abaqus® FEM software to reproduce the heat flow at the sliding surfaces and the associated temperature increase as a function of friction, pressure and velocity; the model is then validated by comparing the results of numerical analyses to the results of experimental tests carried out at the Eucentre Lab. in Pavia (Italy).

A second practical issue is represented by the re-centring capability of CSS isolators. In order to assess the re-centering criterion provided in the European seismic design code even in presence of an offset displacement produced by either previous seismic or non-seismic loads, several analyses have been carried out by means of a simple nonlinear SDOF model. The effect of the initial offset on the peak and residual seismic displacements, more evident for high-friction devices, is quantified.

A third issue is the high coefficient of friction developed at the breakaway, which increases the resistance to initiate sliding. Though this phenomenon is well known and observed in practice, a suitable numerical formulation is still missing in commercial software. In the present thesis the effect of the breakaway is modeled in numerical analyses by introducing

elasto-fragile trusses at the isolation level of a base-isolated building and calibrating the strength of the trusses on the expected resistance of the isolators at the breakaway. The suitability of the approach is demonstrated in a case study relevant to a model of a three-storey building implementing CSS isolators developed in OpenSees® FEM software. The results show that the breakaway has a significant influence mainly on peak floor accelerations and inter-storey drifts in case of CSSs equipped with medium or high friction sliding material.

Again in *Chapter 4*, a new friction model (named "*BVNC"*), capable to simultaneously describe the breakaway and the frictional heating effects, as well as more acknowledged phenomena like the dependence of the friction coefficient on the instantaneous sliding velocity and normal load, already implemented in OpenSees®, is presented. The proposed formulation is eventually validated against the hysteretic force-displacement curved obtained in experimental tests on full scale CSS isolators carried out at the SRMD Lab. of University of California, San Diego.

Finally, in order to account for the *"BNVC"* model in dynamic analyses, the plastic behavior regulating the response of the isolator element available in the OpenSees® library is modified and an "*ad hoc*" code is compiled.

In *Chapter 5*, a "*conceptual design*" of isolation systems for seismic retrofitting interventions of strategic buildings with high technological contents is suggested. The procedure is developed step-by-step and, gradually increasing the complexity of the required calculations, aims at identifying optimized solutions capable to ensure the seismic protection of both structural and non-structural components.

In last part of the work (*Chapter 6*), the hospital of Lamezia Terme, located in a high seismic prone area in southern Italy, is chosen as case study to assess the proposed conceptual design. More reliable numerical results are obtained implementing the modified isolator element in seismic dynamic analyses. For each seismic design level provided by Italian Building code, the proposed solution for the sliding isolation system is shown to widely fulfil the performance requirements for both structural and non-structural elements.

Last, in the *Conclusions* section, the main outcomes of the study are summarized, the innovative steps are enlightened, and some general indications are drawn.

CHAPTER 1

Seismic isolation technique

1.1 Operational principles

Seismic isolation is an effective technique used worldwide to protect buildings and structures, as well as non-structural components, from the damaging effects of earthquakes. Some recent researches have shown that this strategy was used, although rather rudimentary, by ancient Greek and Persian [1-2]. Other studies describes recent developments and diffusion of seismic isolation starting from the first isolators prototypes of the second half of the nineteenth century up to modern ones developed in the last three decades [3-5]. In Italy, in the last years, this technique is spreading especially for the protection of public buildings and large infrastructures [6].

Seismic isolation is based on the simple idea of decreasing the acceleration response of the structure by shifting its fundamental period to higher values (Fig. 1.1-left); in addition, peak displacements can be reduced by means of a damping increase (Fig. 1.1-rigth).

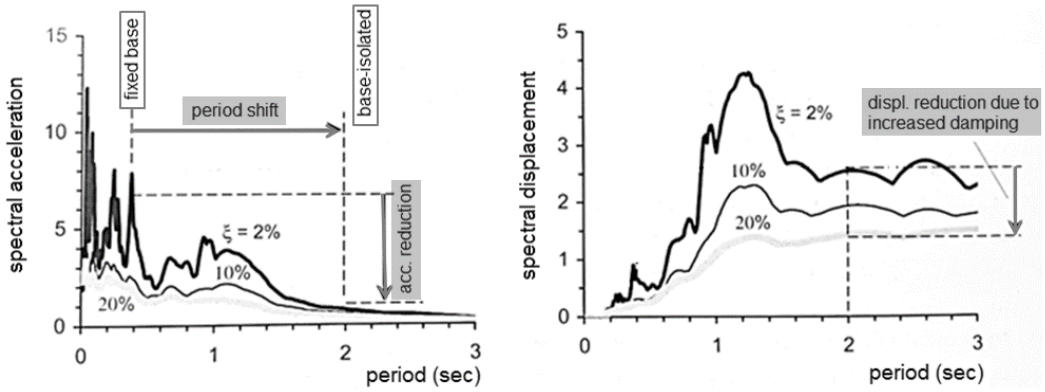

Figure 1.1. Theoretical basis of seismic isolation: shift of the fundamental period of the structure (left) and increase of its damping (right)

For this purpose, horizontally flexible isolation devices are introduced between the foundations and the superstructure in order to separate the mass of the building from the ground motions and limit the transmission of accelerations and shear forces. In this regard,

Fig. 1.2 provides a qualitative comparison between the response of seismic-isolated and traditional fixed-base structures.

According to the EN 1998-1 (Eurocode 8, part1) [7] the fundamental functions required to the isolation system are: (1) sustain and transmit the vertical loads of the superstructure in both service and seismic conditions (*load bearing capacity*); (2) decouple the mass of the superstructure from the ground motion (*lateral flexibility*); (3) prevent cumulative displacements during seismic sequences, as well as reduce the residual displacement (*recentring capability*); (4) reduce or limit the base displacements due to the lengthening of the fundamental period of the structure (*damping increase*); (5) provide a lateral restraint under service horizontal loads (*sufficient elastic stiffness*).

The main drawbacks of this design approach are the need to accommodate the large movements of the isolated structure during seismic events which may be harmful for supply lines of electricity, water, gas, etc., and cause "hammering" with adjacent buildings, as well as the presence of residual displacements at the end of the earthquake.

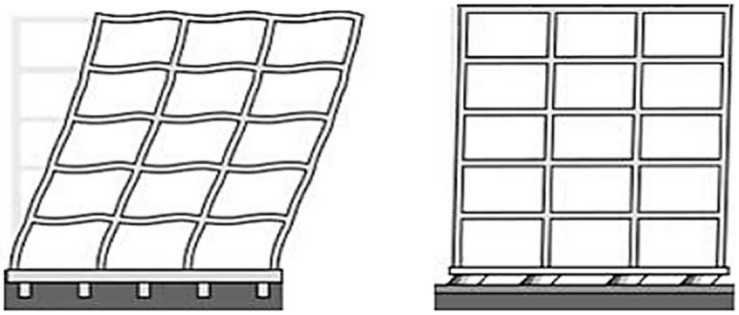

Figure 1.2. Qualitative comparison between the seismic response of "*fixed-base*" (left) and "*base-isolated*" buildings (right)

1.2 Dynamics of base-isolated structures

The linear theory of MDOF base-isolated structures was firstly given by Kelly in 1990 [8] and then deepened in cooperation with Naeim in 1999 [4], while a more refined nonlinear theory, based on the Bouc-Wen model [9], was developed by Nagarajaiah *et al.* in 1991 [10]. However, an insight into the behaviour of base-isolated buildings can be obtained by considering a simple 2-DOF "*shear-type*" frame (Fig. 1.3).

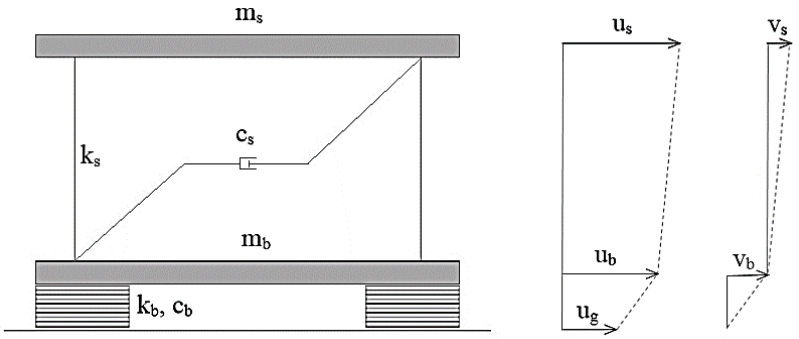

Figure 1.3. Parameters of the 2-DOF isolated system

The mass m_s represents the superstructure of the building and m_b the mass of the base slab above the isolation system. The superstructure stiffness and damping are k_s and c_s, while the stiffness and damping of the isolation system are k_b and c_b. The absolute displacements of the two masses are denoted by u_b and u_s, and, since useful for the analysis, also the relative displacement of the isolation system v_b, and the inter-storey drift v_s are introduced:

$$v_b = v_b(t) = u_b(t) - u_g(t) \tag{1.1}$$

$$v_s = v_s(t) = u_s(t) - u_b(t) \tag{1.2}$$

The equations of motion of the 2-DOF model can be obtained by writing simple equilibrium equations between the dynamic internal forces (D'Alembert principle) at the superstructure and isolation levels (Fig. 1.4):

$$m_s\ddot{u}_s + c_s\dot{v}_s + k_s v_s = 0 \tag{1.3}$$

$$m_b\ddot{u}_b + c_b\dot{v}_b - c_s\dot{v}_s + k_b v_b - k_s v_s = 0 \tag{1.4}$$

Noting that $\ddot{u}_s = (\ddot{u}_g + \ddot{v}_b + \ddot{v}_s)$ and substituting in Eq. 1.3:

$$m_s\ddot{v}_b + m_s\ddot{v}_s + c_s\dot{v}_s + k_s v_s = -m_s\ddot{u}_g \tag{1.5}$$

Furthermore, replacing $\ddot{u}_b = (\ddot{u}_g + \ddot{v}_b)$ in Eq. 1.4:

$$m_b\ddot{u}_g + m_b\ddot{v}_b + c_b\dot{v}_b - c_s\dot{v}_s + k_b v_b - k_s v_s = 0 \tag{1.6}$$

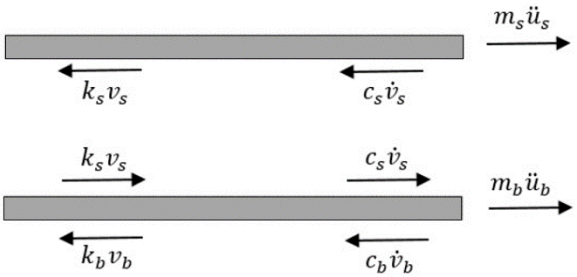

Figure 1.4. Dynamic equilibrium of the 2-DOF isolated system

Combining the Eq. 1.5 and 1.6, the two equation governing the dynamics of the system are obtained:

$$\begin{cases} (m_s + m_b)\ddot{v}_b + m_s\ddot{v}_s + c_b\dot{v}_b + k_b v_b = -(m_s + m_b)\ddot{u}_g \\ m_s\ddot{v}_b + m_s\ddot{v}_s + c_s\dot{v}_s + k_s v_s = -m_s\ddot{u}_g \end{cases} \tag{1.7}$$

which can be written in matrix form as:

$$\begin{bmatrix} m_s + m_b & m_s \\ m_s & m_s \end{bmatrix} \begin{bmatrix} \ddot{v}_b \\ \ddot{v}_s \end{bmatrix} + \begin{bmatrix} c_b & 0 \\ 0 & c_s \end{bmatrix} \begin{bmatrix} \dot{v}_b \\ \dot{v}_s \end{bmatrix} + \begin{bmatrix} k_b & 0 \\ 0 & k_s \end{bmatrix} \begin{bmatrix} v_b \\ v_s \end{bmatrix} = -1 \begin{bmatrix} m_s + m_b & m_s \\ m_s & m_s \end{bmatrix} \begin{bmatrix} 1 \\ 0 \end{bmatrix} \ddot{u}_g \tag{1.8}$$

and in compact form ($r = [1\ 0]^T$):

$$[M]\{\ddot{v}\} + [C]\{\dot{v}\} + [K]\{v\} = -[M]\{r\}\ddot{u}_g \tag{1.9}$$

Let:

$$\gamma = \frac{m_s}{m_s + m_b} \tag{1.10}$$

$$\varepsilon = \left(\frac{\omega_b}{\omega_s}\right)^2 = \frac{k_b/(m_s + m_b)}{k_s/m_s} = \frac{k_b m_s}{k_s(m_s + m_b)} = \left(\frac{T_s}{T_b}\right)^2 \tag{1.11}$$

A typical range of values for the first parameter is $0.5 < \gamma < 1.0$, while a typical assumption for the second one is $\varepsilon = O(10^{-2})$.

The mode shapes (ϕ_1 and ϕ_2) of the combined system (Eq. 1.8) and the related natural frequencies (ω_1 and ω_2) are calculated by means of the classical eigenvalue problem:

$$\left([K] - \omega_i^2[M]\right)\{\phi_i\} = 0 \tag{1.12}$$

the characteristic equation is obtained solving the determinant of the matrix $\left(K - \omega_i^2 M\right)$:

$$[(m_s + m_b)m_s - m_s^2]\omega^4 - [(m_s + m_b)k_s + k_b m_s]\omega^2 + k_s k_b = 0 \tag{1.13}$$

dividing by $[(m_s + m_b)m_s]$ and substituting $\gamma = m_s/(m_s + m_b)$:

$$(1 - \gamma)\omega^4 - \left(\omega_s^2 + \omega_b^2\right)\omega^2 + \omega_s^2\omega_b^2 = 0 \tag{1.14}$$

whose solutions (eigenvalues) to the first order of ε are:

$$\omega_1 = \omega_b\sqrt{1 - \gamma\varepsilon} \cong \omega_b \tag{1.15}$$

$$\omega_2 = \frac{\omega_s}{\sqrt{1-\gamma}}\sqrt{1+\gamma\varepsilon} \cong \frac{\omega_s}{\sqrt{1-\gamma}} \tag{1.16}$$

and the related mode shapes (eigenvectors) are (Fig. 1.5):

$$\phi_1 = \begin{bmatrix}1\\ \varepsilon\end{bmatrix} \cong \begin{bmatrix}1\\ 0\end{bmatrix} \tag{1.17}$$

$$\phi_2 = \begin{bmatrix}1\\ -\frac{1}{\gamma}[1-(1-\gamma)\varepsilon]\end{bmatrix} \cong \begin{bmatrix}1\\ -1\end{bmatrix} \tag{1.18}$$

In the modal space ($v = \phi\, q$):

$$v(t) = \begin{bmatrix}v_b(t)\\ v_s(t)\end{bmatrix} = \phi_1 q_1(t) + \phi_2 q_2(t) = \begin{bmatrix}\phi_{11}\\ \phi_{21}\end{bmatrix} q_1(t) + \begin{bmatrix}\phi_{12}\\ \phi_{22}\end{bmatrix} q_2(t) \tag{1.19}$$

the response of the isolated structure becomes:

$$[M]\{\phi\}\ddot{q} + [C]\{\phi\}\dot{q} + [K]\{\phi\}q = -[M]\{r\}\ddot{u}_g \tag{1.20}$$

and, premultipling by Φ^T, two decoupled equations of motion are obtained:

$$\{\Phi\}^T[M]\{\phi\}\ddot{q} + \{\Phi\}^T[C]\{\phi\}\dot{q} + \{\Phi\}^T[K]\{\phi\}q = -\{\Phi\}^T[M]\{r\}\ddot{u}_g \tag{1.21}$$

or similarly:

$$\begin{bmatrix}m_1 & 0\\ 0 & m_2\end{bmatrix}\begin{bmatrix}\ddot{q}_1\\ \ddot{q}_2\end{bmatrix} + \begin{bmatrix}c_1 & 0\\ 0 & c_2\end{bmatrix}\begin{bmatrix}\dot{q}_1\\ \dot{q}_2\end{bmatrix} + \begin{bmatrix}k_1 & 0\\ 0 & k_2\end{bmatrix}\begin{bmatrix}q_1\\ q_2\end{bmatrix} = -\begin{bmatrix}\phi_{11} & \phi_{12}\\ \phi_{21} & \phi_{22}\end{bmatrix}\begin{bmatrix}m_s+m_b & m_s\\ m_s & m_s\end{bmatrix}\begin{bmatrix}1\\ 0\end{bmatrix}\ddot{u}_g \tag{1.22}$$

where m_i, c_i, and k_i respectively stand for the i-esim modal mass, modal damping, and modal stiffness; in particular (to first order of ε):

$$m_1 = (m_s + m_b)\cdot(1+2\gamma\varepsilon) \tag{1.23}$$

$$m_2 = (m_s + m_b)\cdot\frac{(1-\gamma)\cdot[1-2(1-\gamma)\varepsilon]}{\gamma} \tag{1.24}$$

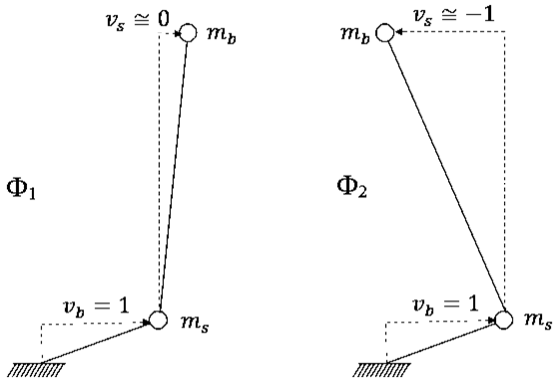

Figure 1.5. Mode shapes of the 2-DOF isolated system: fundamental or "*isolation mode*" (left), and second mode (right)

The response of the system related to each mode is:

$$m_1\ddot{q}_1 + c_1\dot{q}_1 + k_1 q_1 = -\phi_1^T M r \ddot{u}_g \tag{1.25}$$

$$m_2\ddot{q}_2 + c_2\dot{q}_2 + k_2 q_2 = -\phi_2^T M r \ddot{u}_g \tag{1.26}$$

dividing each equation by the relevant modal mass m_i, and noting that $\omega_i = \sqrt{k_i/m_i}$ and $\xi_i = c_i/(2\omega_i m_i)$:

$$\ddot{q}_1 + 2\xi_1\omega_1\dot{q}_1 + \omega_1^2 q_1 = -\Gamma_1\ddot{u}_g \tag{1.27}$$

$$\ddot{q}_2 + 2\xi_2\omega_2\dot{q}_2 + \omega_2^2 q_2 = -\Gamma_2\ddot{u}_g \tag{1.28}$$

where (to first order of ε) first ξ_1 and second ξ_2 modal damping ratio are:

$$\xi_1 = \frac{c_1}{2\omega_1 m_1} = \xi_b\left(1 - \frac{3}{2}\gamma\varepsilon\right) \cong \xi_b \tag{1.29}$$

$$\xi_2 = \frac{c_2}{2\omega_2 m_2} = \frac{\xi_s + \gamma\xi_b\sqrt{\varepsilon}}{\sqrt{1-\gamma}} \cdot \left(1 - \frac{\gamma\varepsilon}{2}\right) \tag{1.30}$$

and related modal participation factors are:

$$\Gamma_1 = \frac{\phi_1^T M r}{\phi_1^T M \phi_1} \cong 1 - \gamma\varepsilon \cong 1 \tag{1.31}$$

$$\Gamma_2 = \frac{\phi_2^T M r}{\phi_2^T M \phi_2} \cong \gamma\varepsilon \ll 1 \tag{1.32}$$

Given a certain seismic input $\ddot{u}_g$, Eq. 1.27 and 1.28 can be solved by means of the following integrals:

$$q_1 = \frac{\Gamma_1}{\omega_1}\int_0^t \ddot{u}_g\,(t-\tau)e^{-(\omega_1\xi_1\tau)}\sin(\omega_1\tau)d\tau \tag{1.33}$$

$$q_2 = -\frac{\Gamma_2}{\omega_2}\int_0^t \ddot{u}_g\,(t-\tau)e^{-(\omega_2\xi_2\tau)}\sin(\omega_2\tau)d\tau \tag{1.34}$$

and hence, since $v(t) = \phi\, q(t)$, the response $v(t)$ of the 2-DOF isolated system is known. The maximum displacements related to each mode shape can be calculated by means of the displacement response spectrum $S_d(\omega, \xi)$:

$$d_{1,max} = S_d(\omega_1, \xi_1) \tag{1.35}$$

$$d_{2,max} = S_d(\omega_2, \xi_2) \tag{1.36}$$

Furthermore, noting that $q_{i,max} = (\Gamma_i\, d_{i,max})$, and using an appropriate combination law (e.g. SRSS), is possible to calculate also peak values of isolation system displacement $v_{b,max}$ and interstorey drift $v_{s,max}$:

$$v_{b,max} = \sqrt{(\phi_{11}q_{1,max})^2 + (\phi_{12}q_{2,max})^2} = \sqrt{(\phi_{11}\Gamma_1\, d_{1,max})^2 + (\phi_{12}\Gamma_2\, d_{2,max})^2} \tag{1.37}$$

$$v_{s,max} = \sqrt{(\phi_{21}q_{1,max})^2 + (\phi_{22}q_{2,max})^2} = \sqrt{(\phi_{21}\Gamma_1\, d_{1,max})^2 + (\phi_{22}\Gamma_2\, d_{2,max})^2} \tag{1.38}$$

Replacing the approximated expressions of ϕ_1 and ϕ_2 (Eq. 1.17 and 1.18), and Γ_1 and Γ_2 (Eq. 1.31 and 1.32), it could be demonstrated that:

$$v_{b,max} \cong (1-\gamma\varepsilon)d_{1,max} = (1-\gamma\varepsilon)\cdot[S_d(\omega_1,\xi_1)] \cong S_d(\omega_b,\xi_b) \tag{1.39}$$

$$v_{s,max} \cong \varepsilon\sqrt{{d_{1,max}}^2 + {d_{2,max}}^2} = \varepsilon\sqrt{[S_d(\omega_1,\xi_1)]^2 + [S_d(\omega_2,\xi_2)]^2} \cong \varepsilon\cdot[S_d(\omega_b,\xi_b)] = \varepsilon\cdot v_{b,max} \tag{1.40}$$

Similarly, considering the acceleration response spectrum $S_a(\omega,\xi)$ and noting that $S_d(\omega,\xi) = S_a(\omega,\xi)/\omega^2$, the base shear coefficient C_s can be approximated as:

$$C_s = max\left|\frac{k_s v_s}{m_s}\right| = \omega_s^2\cdot v_{s,max} \cong \omega_s^2\varepsilon[S_d(\omega_b,\xi_b)] \cong S_a(\omega_b,\xi_b) \tag{1.41}$$

and, multiplying the same by m_s, the maximum shear force at the base of the superstructure $F_{b,max}$ is obtained:

$$F_{b,max} = m_s C_s \cong m_s\cdot[S_a(\omega_b,\xi_b)] \tag{1.42}$$

With all crude assumptions and approximations made so far, the following considerations on the dynamics of 2-DOF base-isolated systems can be drawn:

(a) the fundamental mode (or "*isolation mode*") governs the dynamics of the system ($\Gamma_1 \cong 1-\gamma\varepsilon \cong 1$);

(b) according to components of the "*isolation mode*" ($\phi_1 \cong [1\ 0]^T$) , the superstructure remains practically undeformed while the isolation system accommodates all the seismic displacement;

(c) the dynamic response related to the first mode roughly depends only on the design parameters of the isolation system ($\omega_1 \cong \omega_b$, $\xi_1 \cong \xi_b$);

(d) the second mode shape plays a minor role in the dynamics of the system ($\Gamma_2 \ll 1$);

(e) according to components of the second mode ($\phi_2 \cong [1\ -1]^T$), the superstructure and the isolation system undergo displacements of equal amplitude but opposite direction;

(f) the dynamic response related to the second mode depends on the design parameters of both the isolation system and the superstructure ($\omega_2 = \omega_2(\omega_s, m_s, m_b)$, $\xi_2 = \xi_2(\xi_s, \xi_b, m_s, m_b, k_s, k_b)$);

(g) the peak displacement of the isolation system can be approximated as the spectral displacement corresponding to its period and damping ($v_{b,max} \cong S_d(\omega_b,\xi_b)$);

(h) the maximum interstorey drift is much smaller ($v_{s,max} \cong \varepsilon\cdot v_{b,max}$);

(i) the maximum shear force at the base of the superstructure can be approximated multiplying the mass of the superstructure by the spectral acceleration corresponding to the period and damping of the isolation system ($F_{b,max} \cong m_s\cdot[S_a(\omega_b,\xi_b)]$).

1.3 Energy concepts

Assuming to describe the dynamics of the superstructure by means of the linear theory for a "*shear-type*" frame, the energy balance of a multi-storey base-isolated building (Fig. 1.6), is here developed rearranging the *"relative formulation"* proposed by Uang and Bertero in 1990 [11]. At each time instant of the ground motion, the matrix form of the equations governing the dynamics of the superstructure is [4]:

$$[M_s]\{\ddot{v}_s\} + [C_s]\{\dot{v}_s\} + [K_s]\{v_s\} = -[M_s]\{r\}(\ddot{u}_g + \ddot{v}_b) \tag{1.43}$$

where $[M_s]$, $[C_s]$, and $[K_s]$ are respectively mass, damping, and stiffness matrices of the superstructure; $\{\ddot{v}_s\}$, $\{\dot{v}_s\}$, and $\{v_s\}$ are respectively acceleration, velocity and displacement vectors of the superstructure (relative to the isolation level); $\{r\}$ is a vector of *N* elements equal to 1 (being *N* the number of storey of the superstructure); $\ddot{u}_g$ is the ground acceleration; v_b is the displacement of the isolation system.

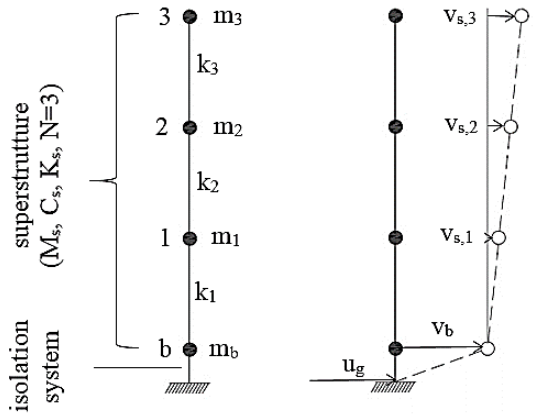

Figure 1.6. Base-isolated "*shear-type*" frame: structural (left) and displacements parameters (right)

The *energy balance of the superstructure* is obtained by integrating Eq. 1.43 over an increment of the superstructure displacement $\{dv_s\}$:

$$\int_0^{v_s^*}\{dv_s\}^T[M_s]\{\ddot{v}_s\} + \int_0^{v_s^*}\{dv_s\}^T[C_s]\{\dot{v}_s\} + \int_0^{v_s^*}\{dv_s\}^T[K_s]\{v_s\} = -\int_0^{v_s^*}\{dv_s\}^T[M_s]\{r\}(\ddot{u}_g + \ddot{v}_b) \tag{1.44}$$

Using the differential relationships:

$$\{dv_s\} = \{\dot{v}_s\}dt \tag{1.45}$$

$$\{d\dot{v}_s\} = \{\ddot{v}_s\}dt \tag{1.46}$$

the terms of Eq. 1.44 can be rewritten as:

$$E'_k = \int_0^{v_s^*}\{dv_s\}^T[M_s]\{\ddot{v}_s\} = \int_0^{t^*}\{\dot{v}_s\}^T[M_s]\{\ddot{v}_s\}dt = \int_0^{\dot{v}_s^*}\{\dot{v}_s\}^T[M_s]\{d\dot{v}_s\} \tag{1.47}$$

$$E_v = \int_0^{v_s^*}\{dv_s\}^T[C_s]\{\dot{v}_s\} = \int_0^{t^*}\{\dot{v}_s\}^T[C_s]\{\dot{v}_s\}dt = \int_0^{v_s^*}\{\dot{v}_s\}^T[C_s]\{dv_s\} \tag{1.48}$$

$$E_e = \int_0^{v_s^*}\{dv_s\}^T[K_s]\{v_s\} \tag{1.49}$$

$$E'_{in} = -\int_0^{v_s^*} \{dv_s\}^T [M_s]\{r\}(\ddot{u}_g + \ddot{v}_b) \tag{1.50}$$

and hence:

$$E'_k + E_v + E_e = E'_{in} \tag{1.51}$$

where E'_k is the kinetic energy of the superstructure (relative to the isolation level); E_v is the viscous energy dissipated by the superstructure; E_e is the elastic energy of the superstructure (work done by internal shear forces of columns); E'_{in} is the seismic energy entering into the superstructure (or "*relative*" input energy).

The "*relative*" input energy E_{in}' physically represents the work done by the equivalent static lateral forces $M_s r(\ddot{u}_g + \ddot{v}_b)$ on the superstructure.

The main limit of the "*relative formulation*" is represented by the fact that other important terms, such as the "*rigid body*" translation of the superstructure (kinetic energy related to the "*isolation mode*"), and the energy absorbed (elastic plus dissipated) by the isolation system do not contribute to the energy balance (Eq. 1.51).

These contributions are instead included into the "*absolute formulation*" of the energy balance [11] for the overall structure (isolation system and superstructure), the treatment of which, however, is much more complex and is not addressed in this study.

1.4 Isolation hardware

In Europe, the manufacturing of anti-seismic devices is regulated by the EN 15129 [12]. According to this Standard, seismic isolators can be divided into two categories (with some subtypes): elastomeric isolators and sliding isolators (Table 1.1).
The *Ultimate Limit State* (ULS) requirements prescribe that the anti-seismic device must be capable to withstand the seismic action without any local or global failure (*No-Failure Requirement*) preserving also a residual strength after the event (*Damage Limitation Requirement*). According to *Service Limit State* (SLS) requirements, the anti-seismic devices must guarantee the design performances and tolerances during all the service life.

category	**subtype**
elastomeric isolators	- Low-Damping Rubber Bearings (LDRB)
	- High-Damping Rubber Bearings (HDRB)
	- Lead-Plug Rubber Bearings (LPRB)
	- Polymer-Plug Rubber Bearings (PPRB)
sliding isolators	- Curved Surface Sliders (CSS)
	- Flat Surface Sliders (FSS)

Table 1.1. Anti-seismic devices classification according to the EN 15129

1.4.1 Elastomeric isolators

The first application of elastomeric isolators (also known as rubber bearings) for base-isolation is dated back to 1969 (retrofitting of the Pestalozzi School in Skopje, Macedonia) [4]. Initially, the bearings were simply composed of large piece of rubber with limited vertical stiffness and load bearing capacity. In the last two decades, elastomeric isolators have been significantly improved by inserting internal steel reinforcements plates that, increasing the vertical stiffness of the bearings, in addition to prevent potential rocking motions during the seismic shaking, reduce also the lateral bulging (Fig. 1.7).

Low-Damping Rubber bearings (LDRB) are composed of natural rubber and internal steel reinforcement plates. These isolators are characterized by a low equivalent damping factor ($\xi=2\div3\%$ at 100% of shear strain), and an approximatively linear force-displacement response. This kind of devices have been widely used in Japan often coupled to supplementary damping devices, such as viscous dampers, steel bars and frictional devices.

High-Damping Rubber Bearings (HDRB) are similar to LDRB but are made of a rubber compound with a higher intrinsic damping. This is obtained by adding to the natural rubber extra-fine carbon block, oil or resin, and other fillers. Nowadays, thanks to the continuous

improvement process, high-damping rubber bearings have damping ratios within the ordinary range $\xi=10\div20\%$ at 100% of shear strain.

Lead-Plug Rubber Bearings (LPRB) consist of traditional LDRB with a lead-plug embedded at the center of the laminated natural rubber. The rubber provides a "linear-spring" reaction, while the lead-plug increases the damping capability resulting in an approximatively bilinear hysteretic loop.

Polymer-Plug Rubber Bearings (PPRB) are similar to LPRB but the central plug is made of a polymeric compound.

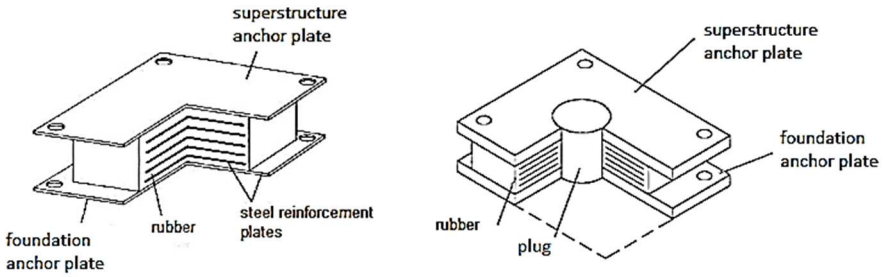

Figure 1.7. LDRB (or HDRB) isolator (left) and LPRB (or PPRB) isolators (right)

1.4.2 Sliding isolators

Flat Surface Sliders (FSS) are free sliding bearings with two or more flat steel sliding surfaces in contact through friction pads of polymeric materials (Fig. 1.8-left). They are often used in combination with other kind of devices (linear spring or elastomeric isolators) to which the re-centring function is entrusted.

Curved Surface Sliders (CSS) are usually comprised of five main parts (Fig. 1.8-right), namely the sliding plate, the pivot, the rotation plate (or basement), and two pads of friction material: the sliding pad, locked to the upper convex surface of the pivot and rubbing onto the concave surface (or primary surface) of the sliding plate, and the rotation pad, bonded to the rotation plate and forming the concave surface (or secondary surface) of a spherical joint. The primary sliding surface accommodates the horizontal movements, while the secondary sliding surface accommodates rotations allowing to keep the two steel plates horizontal and parallel to each other.

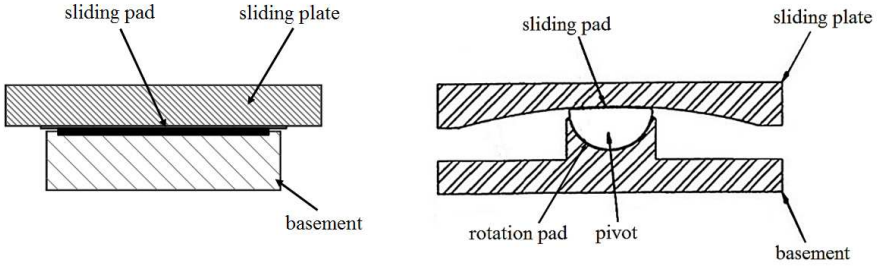

Figure 1.8. Main components of FSS (left) and CSS isolators (right)

1.5 Reference Standards

Despite in past the effectiveness of seismic isolation technique was deeply proven; the first technical standards regulating the design of base-isolated structures are quite recent.
In Italy the OPCM 3274 [13] was endorsed in 2003, while at European level the EN 1998 (Eurocode 8) was completed only in 2005 [7, 14]. The last established design rules for both base-isolated buildings (part 1) and bridges (part 2) which, with small discrepancies, have been then included in the current Italian Building Code (D.M. 14.01.2008) [15].
In the following sections, for sake of brevity, only Eurocode 8 provisions are presented with the exception of those related to the definition of the seismic actions that are entrusted to the national building code of each State Member (see section 1.5.3).

1.5.1 Basic provisions and definitions

Since differences with Italian Building Code [15] are quite limited, for sake of brevity, only EN 1998-1 (Eurocode 8-part1) contents are summarized hereafter [7]. Among basic provisions (§ 10.3-10.5) for the design of base-isolated buildings, there are:

1- the structural elements located above (*superstructure*) and below (*substructure*) the isolation interface should be enough rigid in both horizontal and vertical directions to minimize the effects of differential displacements of the ground motion;
2- in order to minimize the torsional effects, the effective centre of stiffness and the centre of damping of the isolation system should be as close as possible to the projection of the centre of total mass of the structure on the isolation interface;
3- the distribution of gravitational loads should be as uniform as possible in order to minimize potential differences in the response of each isolation device;
4- the reliability of the isolation system is guaranteed by designing devices capable to accommodate the peak seismic displacement amplified by the safety factor $\gamma_x = 1.20$.

Furthermore, a structure is defined *"fully isolated"* if, during the seismic shaking, remains within the elastic range. Otherwise, the superstructure is *"partially isolated"*.
Other preliminary definitions (§ 10.2) are based on the assumption of modeling the response of the isolation system by means of a simplified bilinear law defined by the following parameters (Fig. 1.9): strength at zero displacement (F_0), elastic stiffness (K_E), post-elastic stiffness (K_P), yielding force (F_y), and yielding displacement (d_y).

Design displacement of the isolation system (d_{cd}): maximum horizontal displacement of the isolation system (at its effective stiffness center) in a principal direction occurring during the design seismic action.

Effective stiffness of the isolation system or "*secant stiffness*" (K_{eff}): ratio between the maximum horizontal force (F_{max}) and the design displacement (d_{cd}) in the relevant principal direction.

$$K_{eff} = \frac{F_{max}}{d_{cd}} \tag{1.52}$$

Effective damping of the isolation system (ξ_{eff}): equivalent viscous damping corresponding to the energy dissipated by the isolation system under a cycle (in the relevant principal direction) having amplitude equal to the design displacement (d_{cd}).

$$\xi_{eff} = \frac{1}{2\pi} \frac{E_d}{F_{max}\, d_{cd}} = \frac{1}{2\pi} \frac{4\, F_0 (d_{cd} - d_y)}{F_{max}\, d_{cd}} \tag{1.53}$$

Effective period of the isolated structure (T_{eff}): fundamental period (in the relevant principal direction) of a single degree of freedom system having the mass of the superstructure (M_s) and the effective stiffness of the isolation system (K_{eff}).

$$T_{eff} = 2\pi \sqrt{\frac{M_S}{K_{eff}}} \tag{1.54}$$

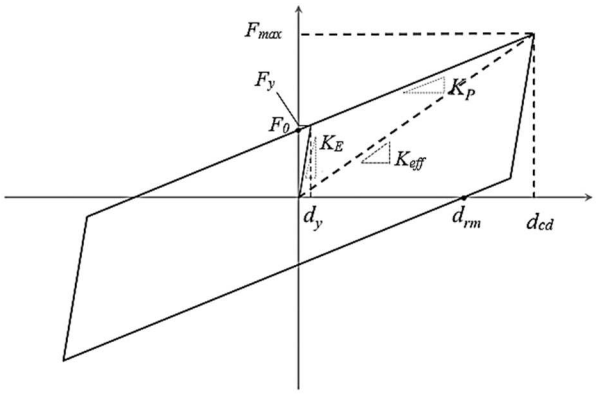

Figure 1.9. Bilinear hysteretic model adopted for the isolation system

1.5.2 Analysis methods

Since differences with Italian Building Code (D.M. 14.01.2008) [15] are quite limited, for reasons of synthesis, only EN 1998-1 (Eurocode 8-part1) analysis methods (§ 10.9) are described hereafter [7].

Non-linear time history analysis: is the reference analysis method since always applicable. The response of the base isolation system (governing the "*isolation mode*") is described by means of a proper hysteretic model, while a linear model is assumed for the superstructure (fully isolation assumption). In particular, the viscous damping of the superstructure should not interfere with the hysteretic damping of the isolation system, and should be the same of the fixed-base superstructure (ξ_{fb}). For higher modes ($T << T_{eff}$), this is usually obtained by

setting $\alpha = (\xi_{fb}T^*)/\pi$ and $\beta = 0$ (e.g. $\alpha = 0.0016$ for $\xi_{fb} = 0.05$, and $T^* = 0.01s$) when calculating the superstructure Rayleigh damping matrix ($C_s = \alpha M_s + \beta K_s$).

Equivalent linear (dynamic) analysis: is a time-history analysis in which both the isolation system and the superstructure are modelled as linear and viscously damped. Damping is introduced by properly calibrating the damping matrix of the base-isolated structure ($C_{b+s} = \alpha M_{b+s} + \beta K_{b+s}$) or, in the modal space, assigning a modal damping (ξ) to each decoupled equation of motion. In particular, the isolation system (governing the "*isolation mode*") is modelled by setting its stiffness $K = K_{eff}$ and its modal damping $\xi = \xi_{eff}$. For higher modes ($T < 0.8T_{eff}$), the modal damping of the isolated structure should be the same of the fixed-base superstructure ($\xi = \xi_{fb}$). The torsional effects due to accidental eccentricities are computed statically and superimposed to results of the dynamic analysis. The behavior of the isolation system can be considered equivalent to linear if all the following conditions are met: (1) K_{eff} is not is not less than 50% of the secant stiffness of the isolation system at a displacement $d = 0.2d_{cd}$; (2) $\xi_{eff} < 0.30$; (3) the force-displacement characteristics of the isolation system do not vary by more than 10% due to the rate of loading or due to the vertical loads; (4) the increase of the restoring force in the isolation system for displacements $0.5d_{cd} < d < 1.0\ d_{cd}$ is not less than 2,5% of the total gravity load above the isolation system.

Iterative equivalent linear (dynamic) analysis: when the effective stiffness or the effective damping of the isolation system depend on the design displacement d_{cd}, an iterative procedure should be applied until the difference between trial and calculated values of d_{cd} does not exceed the 5%.

Simplified equivalent linear (static) analysis: is the classical linear equivalent static analysis based on the assumption that the superstructure behaves as a rigid body above the isolation system (having effective period T_{eff} and damping ξ_{eff}). A synthetic description of the procedure is described hereafter: (1) calculation of the displacement at the stiffness-centre of the isolation system in each horizontal direction ($d_{cd} = \left[M_s \cdot S_a(T_{eff}, \xi_{eff})\right]/K_{eff}$); (2) application of equivalent horizontal forces ($f_i = m_i \cdot S_a(T_{eff}, \xi_{eff})$) along both horizontal directions and at each storey of the superstructure; (3) the torsional effects relevant to each isolator unit may be accounted for applying the amplification factor δ_i in each direction of the seismic actions.

It is worth noting that the torsional movement about the vertical axis may be neglected if the eccentricity between the centre of mass of the superstructure and the centre of stiffness of the isolation system does not exceed 7.5% of the length of the superstructure in the direction transverse to those of relevant seismic action.

In addition to conditions for the equivalent linear (dynamic) analysis, this analysis method can be used if: (1) the distance from the nearest active fault with $M_s \geq 6.5$ is greater than 15 km; (2) the largest planar dimension of the superstructure is not greater than 50m; (3)

$3T_{fb} \leq T_{eff} \geq 3s$ (where T_{fb} is the fundamental period of the fixed-base superstructure); (4) the vertical stiffness of the isolation system $K_v > 150\,K_{eff}$ (negligible vertical displacements); (5) the fundamental period in the vertical direction $T_v = 2\pi\sqrt{M/K_v} \leq 0.1s$.

Multi-modal linear spectral analysis: is the classical modal analysis of the complete base-isolated structure applied separately in all the directions (two horizontal plus vertical). The isolation system is modelled by considering the effective stiffness (K_{eff}), while 50% uncracked section is usually assumed when computing the stiffness of the superstructure elements. In particular, for all modes with $T > 0.8T_{eff}$, the elastic spectrum should be reduced by means of a coefficient η corresponding to the effective damping of the isolation system (ξ_{eff}). For higher modes ($T < 0.8T_{eff}$), the elastic spectrum should be the same of the fixed-base superstructure (e.g. ξ_{fb}=0.05). Torsional effects due to accidental eccentricities are computed statically and superimposed to results of the modal analysis.

Simplified modal linear spectral analysis: is a modal analysis in which it is assumed that the superstructure is a rigid solid translating (only "*isolation mode*") above the isolation system with effective period T_{eff}. This method considers only the two horizontal dynamic translations. Torsional effects due to accidental eccentricities are computed statically and superimposed to results of the modal analysis, and overturning effects are neglected.

1.5.3 Seismic design levels

According to the EC8-1 (§ 3.2.1), the territory of each State Member is subdivided into seismic zones depending on the local hazard. In each seismic zone, the hazard is quantified by means of the reference *peak ground acceleration on outcropping bedrock* a_{gR} [7]. This parameter is established by a Technical Committee for each State Member considering, for each zone, a seismic scenario having *reference return period* $T_{N,CRI}$ (relevant to the no-collapse requirement). The *importance factor* γ_I (coefficient that accounts for the consequences of a structural failure) for the reference return period is equal to 1.0. In case of different return periods, the design ground acceleration on outcropping bedrock (a_g) is $a_g = \gamma_I \cdot a_{gR}$.

The Italian Building Code (§ 2.4.1-2.4.3) introduces some new parameters to define the design seismic action [15]. First, it introduces the *reference period* V_R, which is product of the *nominal life of a construction* V_N and its *coefficient of use* C_U ($V_R = V_N \cdot C_U$). Suggested values are V_N = 10 years for temporary structures, V_N = 50 years for ordinary buildings and structures, and V_N= 100 years for large or strategic constructions.

The coefficient of use is directly linked to the *class of use* of the construction, from Class I (rare presence of people, C_U = 0.7), and Class II (normal presence of people, C_U = 1.0) up to Class IV (important public and strategic buildings, C_U = 2.0).

The seismic action, and relevant performance requirements, are defined according to different design levels (or limit states). Among *serviceability limit states* (SLE) there are:

1. *Operability limit state* (SLO): after the earthquake, the overall structure, including both structural and non-structural elements, does not suffer any damage and is fully operational;
2. *Limit state of damage* (SLD): after the earthquake, the overall structure, including both structural and non-structural elements, suffers limited damages. The stiffness of structural elements, and their strength against vertical and horizontal actions, is not impaired. Plants might be subject to repairable malfunctioning.

Among *ultimate limit states* (SLU) there are:

3. *Limit state for the safeguard of human life (SLV):* after the earthquake, non-structural components suffer significant damages and failures. Structural elements retain a significant stiffness and strength against vertical actions. A satisfactory safety margin against the collapse from horizontal seismic actions is ensured (good overall residual horizontal stiffness);
4. *Limit state for collapse prevention (SLC):* after the earthquake, non-structural components suffer severe damages and failures. Structural elements retain a significant stiffness and strength against vertical actions. A small safety margin against collapse from horizontal actions is ensured (poor overall residual horizontal stiffness).

Adopting the Poisson model to predict the temporal uncertainty of an earthquake, the return period of the event can be calculated as:

$$T_R = -\frac{V_R}{\ln(1-\rho_{VR})} \tag{1.55}$$

where ρ_{VR} is the *exceedance probability* within the reference period V_R of the relevant limit state (Table 1.2).

limit state		**exceed. prob.** ρ_{VR}	**return period** T_R **(years)**	
			V_R **= 50 y.**	V_R **= 200 y.**
serviceability limit state	SLO	81%	30	120
	SLD	63%	50	200
ultimate limit state	SLV	10%	475	1900
	SLC	5%	975	3900

Table 1.2. Return periods T_R and reference periods V_R at different limit states

At both SLE and SLU limit states, the reference *elastic spectrum for the two horizontal components* $S_e(T)$ (Fig. 1.10) is defined for building having fundamental period $T_1 \leq 4.0s$ (reference equivalent viscous damping $\xi = 5\%$ - § 3.2.3.2.1):

$$0 \leq T < T_B \qquad S_e(T) = a_g \cdot S \cdot \eta \cdot F_0 \cdot \left[\frac{T}{T_B} + \frac{1}{\eta \cdot F_0}\left(1 - \frac{T}{T_B}\right)\right] \tag{1.56}$$

$$T_B \leq T < T_C \qquad S_e(T) = a_g \cdot S \cdot \eta \cdot F_0 \tag{1.57}$$

$$T_C \leq T < T_D \qquad S_e(T) = a_g \cdot S \cdot \eta \cdot F_0 \cdot \left(\frac{T_C}{T}\right) \tag{1.58}$$

$$T_D \leq T \qquad S_e(T) = a_g \cdot S \cdot \eta \cdot F_0 \cdot \left(\frac{T_C T_D}{T^2}\right) \tag{1.59}$$

where (§ 3.2.3.2.1): T_B is the period corresponding to the start of the constant acceleration section; T_C is the period corresponding to the start of the constant velocity section; T_D is the period corresponding to the start of the constant displacement section; a_g is the peak ground acceleration at the reference bedrock; $S = S_S \cdot S_T$ is a coefficient that account for soil (S_S) and topographic (S_T) conditions (§ 3.2.2); $\eta = \sqrt{10/(5+\xi)} \geq 0.55$ is a coefficient that account for damping coefficients $\xi \neq 5\%$; $F_0 \geq 2.2$ is a coefficient that quantify the maximum spectral amplification.

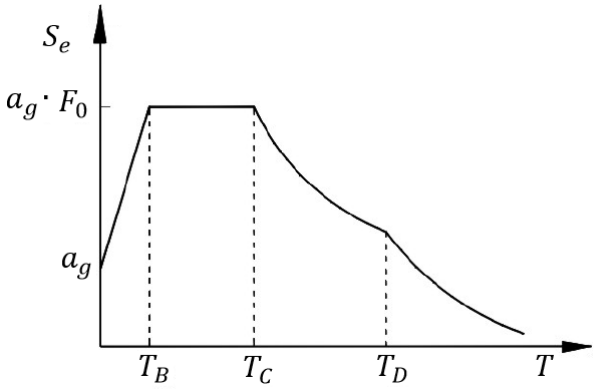

Figure 1.10. Qualitative layout of the reference elastic spectrum

For sake of brevity, the definition of the reference *elastic spectrum for the vertical component* $S_{ve}(T)$ (§ 3.2.3.2.2), since similar to those of horizontal ones, is not presented in this section.

In structural verifications, the seismic action E is combined with other loads according to the following combination rule (§ 3.2):

$$G_1 + G_1 + P + E + \sum_j \psi_{2j}\, Q_{kj} \tag{1.60}$$

where G_1 is the weight of structural elements; G_2 is the permanent weight of non-structural elements; P is pre-tensioning load; Q_{kj} are the variable (live) loads; and ψ_{2j} are combination coefficients (§ 2.5.3).

When structural calculations at SLU limit states are not carried out by means of time-step dynamic analyses, equivalent static seismic actions shall be defined considering the *inelastic response spectrum* that, for base isolated structures (§ 7.10.6.2.1), is obtained substituting η with $(1/q)$ in the *elastic spectrum* (being q = 1.5 the suggested behavior factor). It is worth noting that, according to EC8-1 (§ 10.7) and coherently with the full isolation assumption, the behavior factor should be q = 1.0.
Other important IBC provisions are briefly summarized hereafter: (1) the three components (two horizontal and one vertical) of the seismic action shall be assumed to act simultaneously; (2) if the response of the structure is calculated separately for each seismic component (only for static or dynamic linear analysis), the global response is obtained by means of given combination rules (§ 7.3.5); (3) in case of time-history analyses a set of at least three ground motion records (complying with the reference elastic spectrum) shou1d be used and the structure shall be designed to withstand the most severe among the resultant effects (§ 3.2.3.6, § 7.3.5); (4) alternatively, a set of seven ground motion can be used and the structure shall be designed to withstand the average of the resultant effects (§ 3.2.3.6, § 7.3.5).

1.5.4 Total displacement and self-centring capability

A wide description of Standards provisions and a literature survey about this topic is provided in section 4.1.1. A brief summary is reported hereafter.
According to Eurocode 8 – part 2 (EC8-2) [14], the total displacement capacity (D_i) of each isolator composing the isolation system should be designed according to the following formula (§ 7.6.2):

$$D_i \geq d_{G,i} + \gamma_{IS} \cdot d_{m,i} \tag{1.61}$$

where $d_{G,i}$ is an non seismic offset displacement potentially induced by the permanent actions (e.g. post-tensioning, and creep for concrete members) and 50% of the thermal action, $d_{m,i}$ is the design seismic displacement of the isolator, and γ_{IS} is a reliability factor whose recommended value is 1.2 for buildings and 1.5 for bridges.
The reliability factor (γ_{IS}) amplifies the design seismic displacement ($d_{m,i}$) in order to account for the possible presence of an initial offset displacement due to foreshocks preceding the main design earthquake.
The EC8-2 (§ 7.7.1) establishes also the following criterion to ensure an adequate self-centring capability to the isolation system:

$$\frac{d_{cd}}{d_{rm}} \geq \delta \tag{1.62}$$

where d_{cd} is the maximum design displacement at the centre of stiffness, d_{rm} is the maximum residual displacement for which the isolation system can be in static equilibrium (Fig. 1.9), and δ is coefficient equal to 0.5.

In the same section of code (§ 7.7.1), it is also recommended that systems with a deficient re-centring capacity should be capable to accommodate the accumulation of residual displacements during the service life of the structure; a specific design provision is provided:

$$D_i \geq d_{G,i} + \gamma_{du} \cdot \rho_d \cdot d_{m,i} \tag{1.63}$$

where γ_{du} = 1.2 is a safety factor, and ρ_d is a coefficient accounting for the possible accumulation of residual displacements due to foreshocks foregoing the design earthquake. The coefficient ρ_d is calculated as follow:

$$\rho_d = 1 + 1.35 \frac{1 - \left(d_y / d_{cd}\right)^{0.6}}{1 + 80\left(d_{cd} / d_{rm}\right)^{1.5}} \tag{1.64}$$

where d_y is the yield displacement of the equivalent bilinear system (see Fig. 1.9).

1.6 Chapter references

[1] Naderzadeh, A. (2009) "Historical Aspects of Seismic Base Isolation Applications", Proceedings of the International Symposium on Seismic Response Controlled Buildings for Sustainable Society, Japan Society of Seismic Isolation (JSSI), Tokyo

[2] Giovannardi F., Guisasola A. (2013) "*Base isolation: dalle origini ai giorni nostri*", ProgettandoIng, Nerbini editore, Firenze

[3] Buckle, I.G., Mayes, R.L. (1990) "*Seismic Isolation: History, Application, and Performance – A World View*", Earthquake Spectra

[4] Naeim, F., Kelly, J. M. (1999) "*Design of Seismic Isolated Structures, From Theory to Practice*", John Wiley and Sons, ISBN 0-471-14921-7

[5] Warn, G.P. (2012) "*A Review of Seismic Isolation for Buildings: Historical Development and Research Needs*", Buildings

[6] Martelli, A. (2009) "*I sistemi ed i dispositivi antisismici in Sicilia, in Italia e nel mondo*", Proceedings of the conference "Centenario del Terremoto e del Maremoto di Messina e Reggio Calabria: 1908-2008, un Secolo di Ingegneria Sismica", Messina, 2009

[7] CEN, Eurocode 8 – Part 1 (2004) "*Design of structures for earthquake resistance—Part 1: General rules, seismic actions and rules for buildings*", EN1998-1:2004, European Committee for Standardization, Bruxelles, Belgium

[8] Kelly, J. M. (1990) "*Base Isolation: Linear Theory and Design*", Earthquake Spectra, Vol. 6, No. 2, pp. 223-244

[9] Wen, Y. K. (1976) "*Method for random vibration of hysteretic systems*", Journal of Engineering Mechanics (American Society of Civil Engineers), Vol. 102(2), pp. 249–263

[10] Nagarajaiah, S., Reinhorn, A. M., Constantinou, M. C. (1991) "*Nonlinear dynamic analysis of 3D baseisolated structures*", Journal of Structural Engineering, ASCE, Vo. 117(7), pp. 2035–2054

[11] Uang, C-M, Bertero V. V. (1990) "*Evaluation of seismic energy in structures*", Earthquake Engineering & Structural Dynamics, Wiley, Vol. 19(1), pp. 77-90

[12] CEN, European Committee for Standardization (2009) "*EN 15129: Anti-Seismic Devices*", Bruxelles, Belgium

[13] Presidente del Consiglio dei Ministri (2003), Ordinanza N. 3274 "*Primi elementi in materia di criteri generali per la classificazione sismica del territorio nazionale e normative tecniche per le costruzioni in zona sismica*"

[14] CEN, Eurocode 8 – Part 2 (2005) "*Design of structures for earthquake resistance—Part 2: Bridges*", EN1998-2:2005+A1:2011, European Committee for Standardization, Bruxelles, Belgium

[15] Ministero delle Infrastrutture, D.M. 14.01.2008, "*Norme Tecniche per le Costruzioni*"

CHAPTER 2

The Curved Surface Slider

2.1 Device overview

The Curved Surface Slider (CSS), also known as Friction Pendulum System® (FPS), was first developed (US patent 4644714) by Zayas in the 1987 [1-3]. Among first applications, CSS isolators have been used for seismic protection of bridges and for the retrofitting of historic buildings [4-5].

The principal elements of a CSS device are two concave backing plates (sliding plate and basement) in contact with pads of self-lubricant material (sliding pad and rotation pad) recessed into a pivot element (Fig. 2.1).

The operational principle of CSS is the same of a physical pendulum with oscillation period depending on the radius of curvature only; the relative motion along the curved sliding surfaces lengthens the natural period of the structure. The combined effects of the curvature of the sliding surfaces and of the weight of the superstructure provides a certain re-centering capability while the seismic energy is dissipated by means of frictional forces at the sliding surfaces.

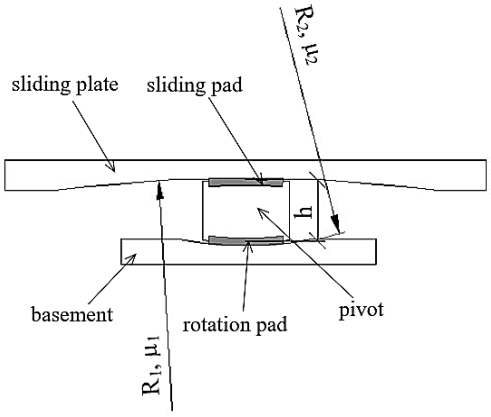

Figure 2.1. Main components and geometrical parameters of a CSS isolator

The pivot starts to move simultaneously along the two surfaces and covers equal angles of rotation ($\theta_1 = \theta_2 = \theta$) with respect to the corresponding centers of curvature; this keeps the two backing plates horizontal and parallel to each other (Fig. 2.2-left). When $R_1 = R_2$, in addition to equal angles of rotation, also displacements along the two surfaces are equal ($d_1 = d_2$).

The force–displacement behavior of the CSS is conventionally described in accordance with the bilinear hysteretic model illustrated in Fig. 2.2-right [6]. In case of simple unidirectional motion (and symmetric with respect to the origin), the resisting lateral force $F(d)$, the undamped natural period of vibration T, the effective period T_{eff}, and the equivalent viscous damping ξ_{eff} can be calculated as:

$$F(d) = F_0 + K_p \cdot d = W \cdot \left(\frac{d}{R_{eff}} + \mu_d \cdot sign(\dot{d}) \right) \tag{2.1}$$

$$T = 2\pi \sqrt{\frac{R_{eff}}{g}} \tag{2.2}$$

$$T_{eff} = 2\pi \sqrt{\frac{M_s}{K_{eff}}} = 2\pi \sqrt{\frac{R_{eff}}{g\left(1+\frac{\mu_d \cdot R_{eff}}{d_{cd}}\right)}} \tag{2.3}$$

$$\xi_{eff} = \frac{1}{2\pi} \frac{E_d}{F_{max}\, d_{cd}} = \frac{1}{2\pi} \cdot \frac{4\,\mu_d\, W\, d_{cd}}{\left(W\mu_d + \frac{W\, d_{cd}}{R_{eff}}\right) \cdot d_{cd}} = \frac{1}{\pi} \cdot \frac{2\,\mu_d}{\left(\mu_d + \frac{d_{cd}}{R_{eff}}\right)} \tag{2.4}$$

where $W = M_s \cdot g$ is the weight of the superstructure (vertical loads induced by seismic rocking motions are neglected), d_{cd} is the amplitude of the cycle, $F_0 = \mu_d \cdot W$ is the characteristic strength, $K_p = W/R_{eff}$ is the post-elastic stiffness, $R_{eff} = R_1 + R_2 - h$ is the effective radius, $K_{eff} = (F_0 + K_p \cdot d_{cd})/d_{cd}$ is the effective stiffness, and $\mu_d = (\mu_1 R_1 + \mu_2 R_2)/(R_1 + R_2)$ is the equivalent dynamic friction coefficient of the curved surfaces [7].

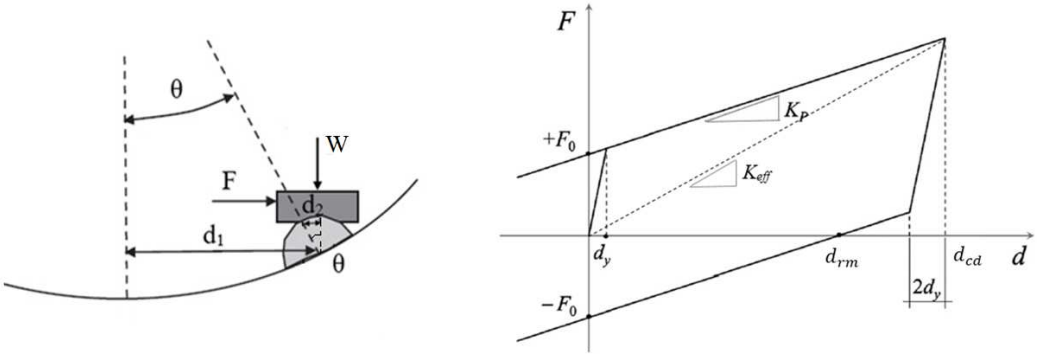

Figure 2.2. Typical kinematics (left) and hysteretic loop (right) of a CSS isolator

For general bidirectional motion, the displacement $d = [d_x \; d_y]$ and forces $F = [F_x \; F_y]$ are given by two-component vectors. The restoring force is always directed towards the origin, while the frictional resisting force is in the opposite direction of the velocity [8]:

$$\begin{bmatrix} F_x \\ F_y \end{bmatrix} = \frac{W}{R_{eff}} \begin{bmatrix} d_x \\ d_y \end{bmatrix} + \mu_d W \frac{1}{\|\dot{d}\|} \begin{bmatrix} \dot{d}_x \\ \dot{d}_y \end{bmatrix} \tag{2.5}$$

Among the main advantages offered by CSS isolators over traditional rubber bearings there are: (i) an high load capacity and the possibility to accommodate large displacements with compact dimensions (which makes them suitable for the retrofitting of existing buildings); (ii) the virtual independence of the oscillation period from the mass of the building (that makes easier to isolate light structures); (iii) the minimization of torsional effects in case of asymmetric buildings. In particular, the first benefit is due to the higher compression strength of plastic materials used for sliding and rotation pads. Indeed, rubber isolators, in order to avoid lacerations and instability problems, ordinarily have a stubby shape and are designed considering a limited capability of shear deformation.

A development of the CSS is represented by the Double Curved Surface Slider (DCSS, Fig. 2.3-left) whose main benefit, compared to CSS bearings of the same planar size, is the possibility to accommodate substantially larger displacements [9]. A central articulated slider enable different instants of sliding activation along the two surfaces (and hence different angles of rotation) resulting in the typical hysteretic loop represented in Fig. 2.3-right.

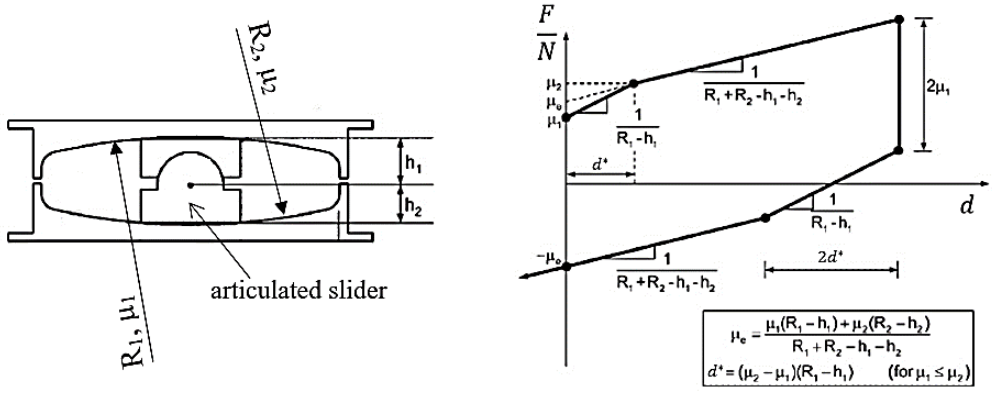

Figure 2.3. Main components (left) and typical hysteretic loop (right) of a DCSS isolator (adapted from [9])

A further development is represented by the Triple Curved Surface Sliders (TCSS) in which the same function of the articulated slider is entrusted to a small internal pendulum (Fig. 2.4-left). The force-displacement behavior of a TCSS was first studied by Fenz and Constantinou (2008) for unidirectional motion [10-11], and then extended for bidirectional trajectories by Morgan *et al.* [12], and Dao *et al.* [13]. The normalized unidirectional hysteretic behavior is represented in Fig. 2.4-right ($L_i = R_i - h_i$ are the effective radii of each curved surfaces).

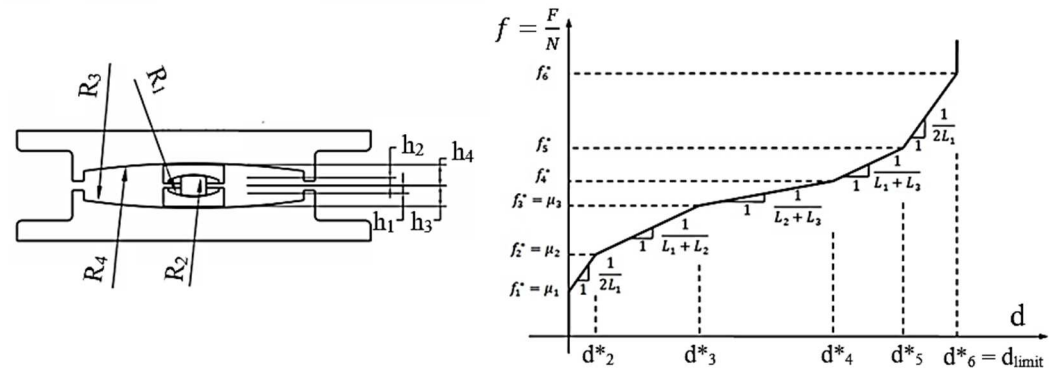

Figure 2.4. Main components (left) and typical hysteretic loop (right) of a TCSS isolator (adapted from [13])

2.2 Sliding material frictional properties

Sliding and rotation pads are ordinarily made of polymeric materials having thickness and radius respectively within the ranges 5-8mm and 50-500mm. The state of the art sliding material is the PTFE but, in the last years, the trend is to implement in CSS different materials able to offer a higher resistance to compression loads, such as PTFE with metal fillers, polyethylene, and polyamide.

The performance of CSS isolator during the seismic excitation mainly depends on the frictional properties of the sliding pads materials. Several experimental studies have shown that the friction coefficient depends on the temperature, pressure, and velocity developed during the sliding motion according to four major effects discussed in the following sections. Among these studies, friction tests were performed at the University Politecnico di Milano on small-scale (SS) specimens of sliding material (SM) by means of a biaxial testing machine [14]. The operational principles of these tests are represented in Fig. 2.5-left: (a) the specimen of SM is recessed into a backing plate that is locked to a roller guide; (b) the upper mating sliding surface is made of stainless steel; (c) a compression load F_v produces the desired contact pressure (up to 60MPa) at the sliding interface; (d) an horizontal force F_H is applied centrally to the sliding material test piece with the possibility to reproduce different displacements waveforms (maximum velocity 200mm/s); (e) a climatic chamber controls the temperature at the sliding surface within the range ±70°C. At each instant t of the motion, the friction coefficient μ of the specimen is calculated as the ratio between the horizontal and the vertical loads:

$$\mu(t) = \frac{F_H(t)}{F_V(t)} \tag{2.6}$$

Fig. 2.5-right shows the typical loop of a friction test: the maximum friction coefficient is the static value measured at the breakaway while lower dynamic values are recorded during the sliding motion.

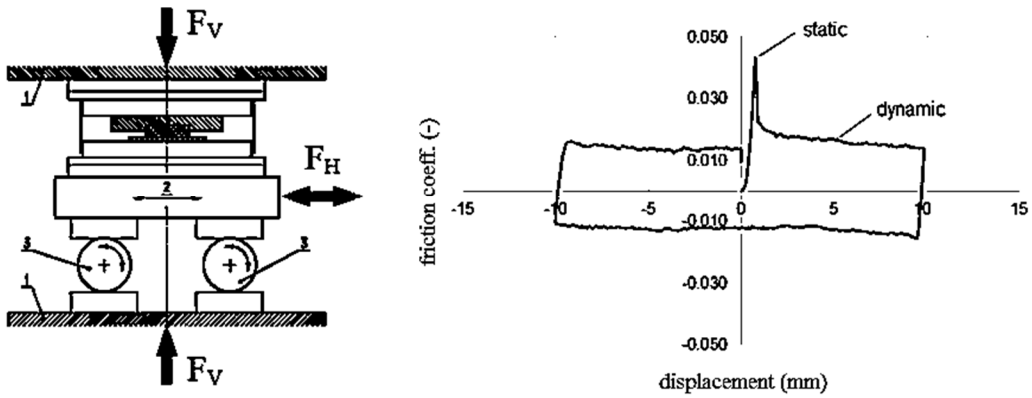

Figure 2.5. Friction tests: operational principle (left) and typical loop (right)

2.2.1 Load effect

The "*load effect*" is the responsible of a reduction of the friction coefficient with the increase of the average contact pressure p at the sliding pad. A first model relating the applied pressure p with the friction coefficient μ was proposed by Browden *et al.* (1964) [15]:

$$\mu(N) = a \cdot p^{-b} \tag{2.7}$$

where a, and b are positive constants to be determined by means of friction tests.
More recent studies dealing with steel–PTFE interfaces confirmed that the sliding friction coefficient reduces while increasing pressure with a rate of reduction practically constant and quite insensitive to sliding velocity [16-17].
Friction tests at different levels of pressure (p = *30, 45, and 60 MPa*) were also performed by the Author on SS specimens of PTFE with metallic fillers. The typical trends of both static and dynamic (v = *200m/s*) friction coefficients with the increasing contact pressure p is represented in Fig. 2.6.

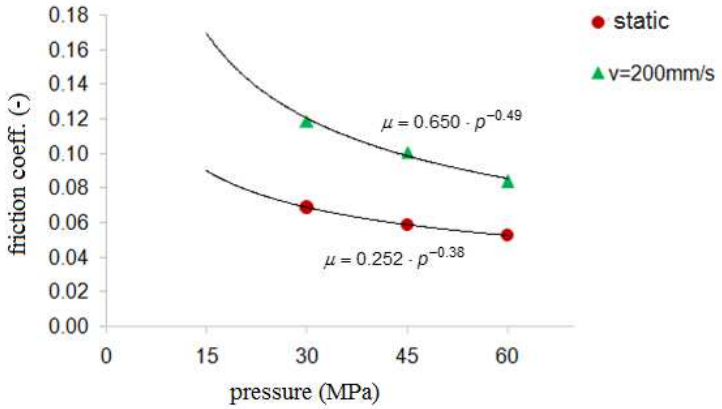

Figure 2.6. Dependence of static and dynamic (v=200mm/s) friction coefficient on the contact pressure

2.2.2 Velocity effect

The "*velocity effect*" takes into account the variation of the friction coefficient with the relative sliding velocity. The most popular model describing the increment of the coefficient of friction μ with increasing sliding velocity v (for a fixed value of pressure) was developed by Mokha *et al*. (1988) [18], and Constantinou *et al.* (1990) [19]:

$$\mu(v) = \mu_{HV} - (\mu_{HV} - \mu_{LV}) \cdot e^{-\alpha_1 |v|} \tag{2.8}$$

where μ_{LV} and μ_{HV} are respectively the friction coefficients at very low (e.g. v < 5mm/s) and very high sliding velocity (e.g. v > 100 mm/s), and α_1 is a parameter regulating the transition between the two phases.

This effect was then observed in more recent experimental studies dealing with PTFE-steel sliding interfaces in specific seismic operational conditions [17, 20].
Friction tests at different sliding velocities (*v = 50, 100, and 200 mm/s*) were also performed by the Author on SS specimens of PTFE with metallic fillers. The typical trend of dynamic friction coefficient with the increasing of the sliding velocity *v* is represented in Fig. 2.7 for two different levels of average contact pressure (p = 30, and 60 MPa).

2.2.3 Breakaway effect

The *"breakaway effect"* manifests as a sudden increase of coefficient of friction at the beginning or at each inversion of the motion, regardless of the applied pressure and the sliding velocity (Figs. 2.5, 2.7). The transition between static and dynamic phase of sliding motion has been studied by several authors [20-22] and relates to two phenomena: (1) a momentary sticking of the interfaces at the start of sliding motion; (2) acceleration impulses at every motion reversal.
A formulation (see section 4.2) capable to account for the transition between the static and dynamic phases has been recently used by Quaglini *et al.* (2014) extending Eq. 2.8 [23]:

$$\mu(v) = \mu_{HV} - (\mu_{HV} - \mu_{LV}) \cdot e^{-\alpha_1|v|} + (\mu_{ST} - \mu_{LV}) \cdot e^{-\alpha_2|v|} \tag{2.9}$$

where μ_{ST} is the static friction coefficient, and α_2 is a parameter regulating the transition from the static to the kinetic friction regime.

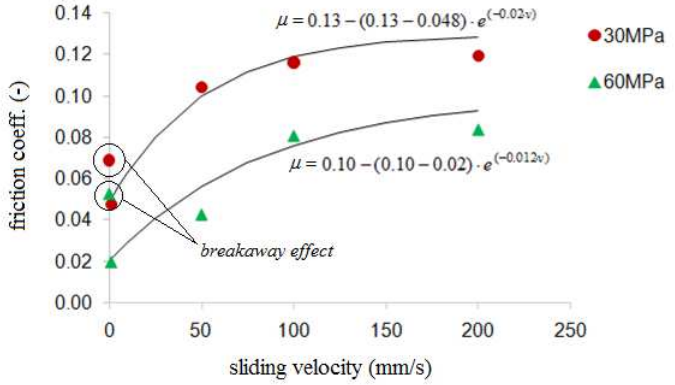

Figure 2.7. Dependence of the dynamic friction coefficient on the sliding velocity

2.2.4 Frictional heating

The "*frictional heating*" causes an increase of the temperature at sliding surfaces that is responsible of a continued reduction of the friction coefficient with the repetition of cycles [24]. This effect was detected by Mokha *et al.* (1991) [16] and Chang *et al.* (1990) [25] for PTFE-steel sliding surfaces but not further investigated. The theoretical analysis of the temperature rise at rubbing friction surfaces is generally based on the work of Carlsaw and

Jaeger (1959) [26]. Constantinou *et al.* (1999) [27] applied this theory to PTFE sliding isolators in order to detect the temperature rise at the sliding interface, achieving a good agreement between experimental and predicted values. In that study, the average temperature rise at sliding surface is related to the instantaneous heat flux $q(t)$ generated by the frictional forces, equal to the power dissipated per unit area:

$$q(t) = \mu \cdot p \cdot v(t) \tag{2.10}$$

where μ and p (supposed constant for simplicity) are respectively the friction coefficient, and the average contact pressure, while $v(t)$ is the instantaneous sliding velocity.
The effect of the frictional heating on the dynamic response (effective damping and stiffness) of a CSS isolator has been deeply investigated by the Author [23] (see section 4.2) by means of a 3D thermo-mechanic FE model implementing the following friction law (Fig. 2.8):

$$\mu(v,T) = \mu(v) \cdot e^{-\beta T} \tag{2.11}$$

where $\mu(v)$ is the velocity-dependent friction coefficient calculated according to Eq. 2.9, β is a thermal decay coefficient, and T is the temperature variable.

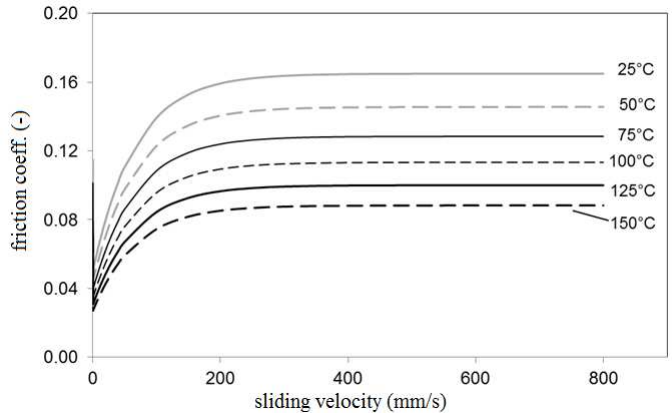

Figure 2.8. Dependence of the coefficient of friction on sliding velocity and temperature

2.3 Open fields of research

In spite of the worldwide large diffusion of CSS isolators in the last decade, a full understanding of their performances, and limits, has not been yet completely reached. The main shaded areas, which are the main topic of chapter 4 of the present thesis, concern the properties of the sliding materials, and the behaviour of the isolator under real earthquakes rather than laboratory tests and are briefly introduced hereafter.

a) The response of CSS isolators during seismic sequences of "*foreshocks - main shock*" or "*main shock – aftershocks*" has not been yet investigated. In particular, the influence of an initial offset, which can be caused by both previous foreshocks and permanent or thermal actions, on the dynamic response (maximum displacement and self-centring capability) of CSS isolators is still not completely clear. Since it may not be possible to re-center the system before the occurrence of close aftershocks, a concern is related to the possibility that closely-spaced ground motions could entail an accrual of displacements, and compromise the deformation capacity of the isolation system (designed on the basis of a single earthquake) possibly leading to its inadequacy at the end of the seismic sequence.

b) Another issue that has been addressed in recent studies is the heat generation occurring at the sliding surface under large friction forces and high velocities, and the effect of the temperature rise on the friction material. Although models predicting the decay of the coefficient of friction with the increase of temperature have been proposed, the effect of this phenomenon on the real performance of the device, such as effective stiffness and damping, it is not yet completely understood. High temperatures may also cause the melting of the polymeric material constituting sliding and rotation pad and the oxidation of steel of backing plates.

c) The "*breakaway effect*" (that is static friction coefficient at the motion begin and at each motion reversal), although already observed in several experimental studies, is not included in the formulations of the main calculation software. Indeed, in recent years, complex friction models aiming at simultaneously reproducing the "*load effect*", the "*velocity effect*", and the "*frictional heating*" have been proposed [28-29] but their common limit is the impossibility to reproduce the "*breakaway effect*". Though not yet deeply investigated, it is fair to assume that this phenomenon can have a significant influence on the peak floor accelerations and deformations (interstory drift) of the superstructure during the seismic event.

2.4 Chapter references

[1] Zayas, V.A. (1987) US PATENT 4644714

[2] Zayas V.A., Low S.S. and Mahin S.A. (1987) "*The FPS earthquake protection system*", Earthquake Engineering Research Center Report, No. 87-01, Berkeley, California

[3] Zayas, V.A., Low, S.S., Mahin, S.A. (1990) "*A simple pendulum technique for achieving seismic isolation*", Earthquake Spectra, Vol. 6(2), pp. 317-333

[4] Zayas, V.A., and Low, S.S. (1999) *''Seismic isolation of bridges using friction pendulum bearings''*, Proceedings of the Structures Congress, Structural Engineering in the 21st Century, New Orleans, Louisiana (US)

[5] Mokha, A.S., Navinchandra, A., Constantinou, M.C., Zayas, V. (1996) *''Seismic isolation retrofit of large historic buildings''*, Journal of Structural Engineering, Vol. 122(3), pp. 298–308

[6] Al-Hussaini, T.M., Zayas, V.A., Constantinou, M.C. (1994) "*Seismic isolation of a multi-story frame structure using spherical sliding isolation systems*", Technical Report No. NCEER-94-0007, National Center for Earthquake Engineering Research

[7] Tsopelas, P., Costantiou, M.C., Kim, Y.S., Okamoto, S. (1996) "*Experimental study of FPS system in bridge seismic isolation*", Earthquake Engineering and Structural Dynamics, John Wiley & Sons, Vol. 25, pp. 65-78

[8] Rabinowicz, E. (1995) "*Friction and wear of materials*", Wiley, New York

[9] Fenz, D.M., Costantiou, M.C. (2006) "*Behaviour of the double concave Friction Pendulum bearing*", Earthquake Engineering and Structural Dynamics, Vol. 35, pp. 1403–1424, DOI: 10.1002/eqe.589

[10] Fenz, D.M., Constantinou, M.C. (2008) "*Spherical sliding isolation bearings with adaptive behavior: Theory*", Earthquake Engineering and Structural Dynamics, Vol. 37(2), pp. 163-183

[11] Fenz, D., Constantinou, M.C. (2009) "*Modelling triple friction pendulum bearings for response-history analysis*", Earthquake Spectra, Vol. 24(4), pp. 1011-1028

[12] Morgan, T.A., Mahin, S.A. (2011) "*The use of innovative base isolation systems to achieve complex seismic performance objectives*", PEER Research Report No. 2011/06

[13] Dao, N.D., Ryan, K.L., Sato, E., Sasaki, T. (2013) "*Predicting the displacement of triple pendulum bearings in a full-scale shaking experiment using a three-dimensional element*", Earthquake Engineering and Structural Dynamics, John Wiley & Sons, Vol. 42, pp. 1677–1695

[14] Quaglini, V., Dubini, P., Poggi, C. (2012) "*Experimental assessment of sliding materials for seismic isolation systems*", Bulletin of Earthquake Engineering, Springer-Verlag, Berlin Heidelberg (D), Vol. 10, pp. 717-740

[15] Bowden, F.P., Tabor, D. (1964) "*The friction and lubrication of solids – part II*" Oxford University Press, London, Great Britain

[16] Mokha, A., Constantinou, M. C., Reinhorn, A. M., and Zayas, V. (1991) "*Experimental study of friction pendulum isolation system*", Journal of Structural Engineering, Vol. 117(4), pp. 1201–1217

[17] Dolce, M., Cardone, D., and Croatto, F. (2005) "*Frictional behavior of steel-PTFE interfaces for seismic isolation*", Bulletin of Earthquake Engineering, Vol. 3(1), pp. 75–99

[18] Mokha, A., Constantinou, M. C., Reinhorn, A. M. (1988) "*Teflon Bearings in Aseismic Base Isolation: Experimental Studies and Mathematical Modeling*", Report NCEER-88-0038, National Center for Earthquake Engineering Research, Buffalo, NY

[19] Constantinou, M. C., Mokha, A., and Reinhorn, A. (1990) "*Teflon bearings in base isolation, Part II: Modeling*", *Journal of Structural Engineering*, ASCE, Vol. 116(2), pp. 455–474

[20] Bondonet, G. and Filiatrault, A. (1997) "*Frictional Response of PTFE Sliding bearings at higher frequencies*", Journal of Bridge Engineering, Vol. 2(4), pp. 139–148

[21] Mokha, A., Constantinou, M. C., and Reinhorn, A. M. (1993) "*Verification of friction model of Teflon bearings under triaxial load*", Journal of Structural Engineering, Vol. 119(1), pp. 240–261

[22] Soong, T. T. and Constantinou, M. C. (1994) "*Passive and Active Structural Vibration Control in Civil Engineering*", Springer, New York

[23] Quaglini, V., Bocciarelli, M., Gandelli E., Dubini, P. (2014) "*Numerical Assessment of Frictional Heating in Sliding Bearings for Seismic Isolation*", Journal of Earthquake Engineering, Vol. 18(8), pp. 1198-1216, DOI: 10.1080/13632469.2014.924890

[24] Sextro, W. (2002) "*Dynamical Contact Problems with Friction*", Springer, Berlin, Heidelberg, pp. 51–54

[25] Chang, J. C., Hwang, J. S., and Lee, G. C. (1990) "*Analytical model for sliding behaviour of Teflonstainless steel interfaces*", Journal of Engineering Mechanics, Vol. 116(12), pp. 2749–2763

[26] Carlsaw, H. S. and Jaeger, J. C. (1959) "*Conduction of Heat in Solids*", 2nd edition, Oxford University Press, London, UK

[27] Constantinou, M. C., Tsopelas, P., Kasalanati, A., and Wolff, E. (1999) "*Property Modification factors for seismic isolation bearings*", Technical Report MCEER-99-0012, Multidisciplinary Center for Earthquake Engineering Research, Buffalo, New York

[28] Kumar, M., Whittaker, A.S., Constantinou, M.C. (2014) "*Characterizing friction in sliding isolation bearings*", Earthquake Engineering and Structural Dynamics, Vol. 44(9), pp. 1409–1425

[29] Lomiento, G., Bonessio, N., Benzoni, G. (2013) "*Friction Model for Sliding Bearings under Seismic Excitation*", Journal of Earthquake Engineering, Vol. 17(8), pp. 1162-1191, DOI: 10.1080/13632469.2013.814611

CHAPTER 3

Seismic performance of hospital buildings

3.1 Problem statement

Strategic buildings, such as hospitals, police stations, communication and first aid centres must be designed to achieve high performance levels under severe earthquakes because of their importance in the immediate emergency response following a catastrophic event.
In particular, hospital full operation after a seismic event is of vital importance for the management of post-earthquake emergency, and this operation capability relies not only on the structural integrity of the building but also of its non-structural components, such as supply lines, plants and architectural elements, as well as of the medical equipment (Fig. 3.1, left). It also to be underlined that the economic value of the technological content of hospitals may overcome the value of the building itself (Fig. 3.1, right) [1].

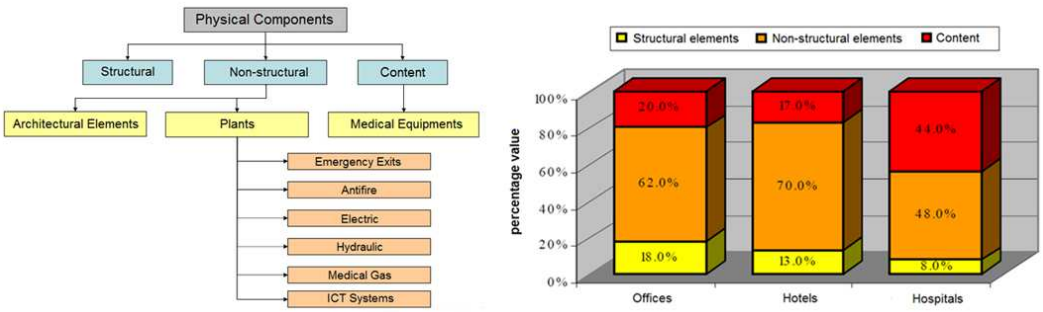

Figure 3.1. Physical components of an hospital complex (left), and their percentage value distribution compared to other kinds of buildings (right) (adapted from [1])

In the last decades, worldwide earthquakes caused extensive damages to several hospital buildings. The 1994 Northridge earthquake, California (US), caused heavy structural damages to the city hospital as well as to the LA County Medical Center, and the St John's Hospital [2]. In Japan, the 2003 Miyagi-Ken Hokubu earthquake, and then the 2004 Niigata event severely stressed the resisting frames of Fukaya and Ojiya city hospitals respectively. Even worse, the 2001 Bhuj earthquake (India) caused the complete structural collapse of

four hospital complexes as, two years later, happened to the Imam Khomeini Hospital during the Bam Earthquake (Iran) [3].

In Italy, the scenario is not reassuring as witnessed by significant damages suffered by local hospitals during past earthquakes [4-5]. A survey conducted in 2009 by the Italian Civil Protection Department over a sample of 200 hospitals located all over the country concluded that about the 75% of Italian hospitals are not adequate to withstand earthquake-induced actions [6].

Irregularities in plan and elevation, poor detailing, and design were the main causes of the partial collapse of the recently built *"San Salvatore"* hospital during the Aquila earthquake occurred in 2009 [7]. Afterwards, the 2012 Emilia Romagna earthquake produced different effects: the hospital of Mirandola suffered failures only to non-structural components and content, while the unreinforced masonry structures of the hospital of Bondeno were severely damaged [8].

The 2016 Central Italy earthquake, whose intense aftershocks are still in progress, had significant effects on hospital buildings. The first shock (24 August 2016) produced considerable damages to both structural and non-structural components of the hospital of Amatrice [9]. Similar effects induced the evacuation of the hospital of Amandola after the strong 30 October aftershock. Due to the same event, structural cracks were also suffered by the intensive care unit of the hospital of Atri, while minor damages were reported by the hospital of Teramo.

Beyond the structural collapse, potential harmful consequences induced by the seismic shaking on a hospital building are (Fig. 3.2): (1) damages to plants and medical equipment; (2) injuries to patients due to overturning or falling of pieces of furniture or architectural elements such as shelves and false ceilings; (3) damages to non-structural walls and partitions.

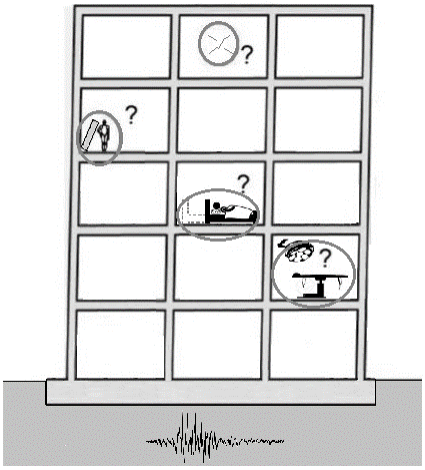

Figure 3.2. Potential damages suffered by hospital buildings during the seismic shaking

3.2 Performance based design

3.2.1 Introduction

Until the late 90's, the traditional structural design was worldwide based on the "*Force-Based Design"* (FBD) approach consisting of a series of provisions that aimed at: (1) avoiding the structural collapse in very rare earthquakes; (2) providing life safety for rare earthquakes; (3) suffering limited and repairable damages in moderate shaking; (4) ensuring the undamaged condition in more frequent and minor earthquakes. Afterwards, in U.S., severe damages and large economic losses suffered by structures during San Fernando (1971), Loma Prieta (1989), and Northridge (1994) earthquakes, increased the awareness that FBD procedures were not always reliable in achieving satisfactory protection levels and appropriate overall seismic performances of buildings.

The *"Performance-Based Design"* (PBD) approach, born in 1997 as a response to these needs, was firstly introduced by the Federal Emergency Management Agency (FEMA), in cooperation with the Applied Technology Council (ATC), and the Building Seismic Safety Council (BSSC), with the "*NEHRP Guidelines for the Seismic Rehabilitation of Buildings"* (FEMA 273) [10-11].

Within the *"Vision 2000"* conceptual framework [12], *Earthquake Design Levels*, and related *Building Performance Levels* (that is admissible levels of damage for both structural and non-structural elements) are defined:

- *Fully Operational*: all services are not interrupted since negligible structural and non-structural damages are reported;
- *Operational*: the structure is safe for immediate occupancy. Essential operations are fully protected, while non-essential ones can be disrupted (quick repairs are required) due to light damages;
- *Life Safe*: moderate structural damages are reported but life safety is guaranteed since the overall stability is not compromised. Possible heavy damages to non-structural components and need to evacuate the building. The repairing is possible, but may be economically impractical;
- *Near Collapse*: severe structural damages are reported but collapse is prevented. Dangers can arise from falling of non-structural elements.

For each seismic level, the *"NEHRP Guidelines"* defines also four linear and nonlinear analysis procedures each to be used to estimate relevant building response parameters, and to evaluate the its overall performance (Fig. 3.3).

More recently, before the FEMA-report356 ("*Prestandard for Seismic Rehabilitation of Buildings*") [13], and then, the ATC-58 project (FEMA-report445) ("*Next-Generation Performance-Based Seismic Design Guidelines*") [14] further developed the PBD approach.

In particular, according to the new provisions, the overall seismic-performance of the building is assessed by means of five structural and four non-structural performance levels with related admissible damages.

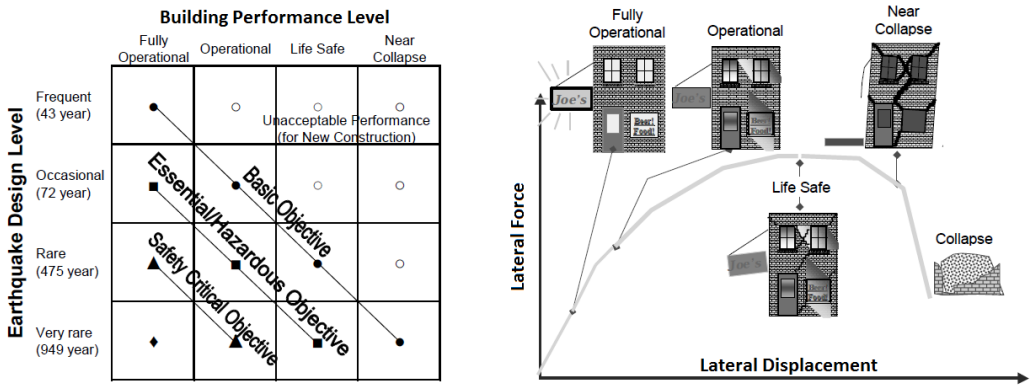

Figure 3.3. *"Vision 2000"* seismic design levels (left) and qualitative representation of damage levels (right) (adapted from [11])

3.2.2 Seismic design levels according to the Italian Building Code

The Italian Building Code (IBC) [15], whose provisions are considered in the present thesis, is based on a PBD approach. Assuming for a hospital building a *"nominal life"* V_N*=100years* and a *"coefficient of use"* C_U*=2.0* (as suggested for strategic public buildings), the *"reference period"* for seismic design levels is $V_R = V_N \cdot C_U = 200 years$ (see section 1.5.3). For each seismic level provided by the IBC, the performance requirements for base-isolated hospitals, with the related verification methods, are summarized in Table 3.1.

seismic level	**return period T_R (years)**	**performance requirements**	**verification method**
SLO	120	- operativity of plants	§ 7.3.7.3
SLD	200	- limited inter-storey drift	§ 7.10.6.1, §7.3.7.2
		- limited damages to non-structural elements	§ 7.3.7.2
SLV	1900	- no hammering with adjacent buildings	intuitive
		- resistance of structural elements	§ 7.10.6.2.1
		- resistance of anchoring systems for plants	§ 7.3.6.3, § 4.1.2.1.1.4
SLC	3900	- isolation system displacement capacity	§ 7.10.6.2.2
		- isolation system load bearing capacity	§ 7.10.6.2.2)
		- resistance of anchoring systems for seismic isolators	§ 7.10.6.2.2, § 4.1.2.1.1.4

Table 3.1. Seismic design levels and relevant performance requirements for hospital buildings according to the Italian Building Code

3.2.3 Performance indices for hospitals

The performance level of a hospital unit in the management of the emergency following a catastrophic event (e.g. earthquake) depends on four components: environmental (external influences), human (preparation of medical staff), organizational (emergency plans), and physical [1]. The last component can be articulated in structural, non-structural and contents (Fig. 3.1-left), and, among them, plants and medical equipment are the most critical in case of earthquake attack.

Indeed numerous surveys carried out in the aftermath of recent earthquakes have shown that the performance of hospitals is rarely impaired by structural damages, whereas functional breakdowns are often the major threats.

In this regard, a synthetic index to assess the overall seismic-safety of hospital units has been recently proposed [16]. The index evaluation is based on data collected by means of questionnaires articulated in three principal sections: the first section is related to structural elements, the second to non-structural elements and facilities, and the last takes into account the organizational aspects. The safety-index (SI) is formulated as follow:

$$SI = VULN \cdot \frac{HAZ}{4} \cdot \frac{EXP}{3} \tag{3.1}$$

where *HAZ* (hazard) depends on the seismic hazard and soil type of the considered site, *EXP* (exposition) is a function of the importance of the building (for hospitals is related to the importance of the offered medical services), *VULN* (vulnerability) is evaluated considering the seismic strength of both structural and non-structural elements as well as the organizational aspects.

Another meaningful measure to quantify the seismic-resilience of hospital systems is the "*hospital treatment capacity"* (HTC index) [17]. The index provides the number of patients with serious injuries that the hospital, in emergency conditions, can treat in one hour. Its formulation takes into account of the influence of organizational, human and physical components:

$$HTC = \alpha \cdot \beta \cdot \frac{\gamma_1 \cdot \gamma_2}{t_m} \tag{3.2}$$

where α and β represent respectively the organizational (emergency plans) and human component coefficients (training and preparation of operators), γ_1 is the number of working operating theatres after the quake (survival of physical components), γ_2 is the Boolean function (equal to 1 if the system survives and to 0 otherwise), and t_m is the mean time for surgical operations (2h from literature review). The first two contributions (α and β coefficients) vary within the range 0.5-1.0 and are usually estimated by means of expert-judgments. The failure of both structural and non-structural components are instead detected by means of complex "*capacity models*" that have been recently developed to assess the

seismic strength of several physical components of hospital buildings (see sections 3.3.1 and 3.3.2).

A more complex methodology capable to estimate the potential impact of an earthquake on a hospital complex has been recently proposed [18]. The method, allowing to estimate the costs of different retrofitting solutions, aims at helping the decision makers in planning interventions for the mitigation of the seismic-risk.

3.3 Fault tree analysis for hospitals

A complete layout of a *"Fault Tree Analysis"* (FTA) for hospital buildings has been proposed in a recent study [17]. It consists of a simple graphical representation (Fig. 3.4) of all potential failure mechanisms of both structural and non-structural components (with possible interactions between the various systems). The FTA can be applied on field after the quake for a quick detection of the main damages, as well as, including specific failure-thresholds for all hospital physical components, for the post-processing of the output results from seismic numerical analyses.

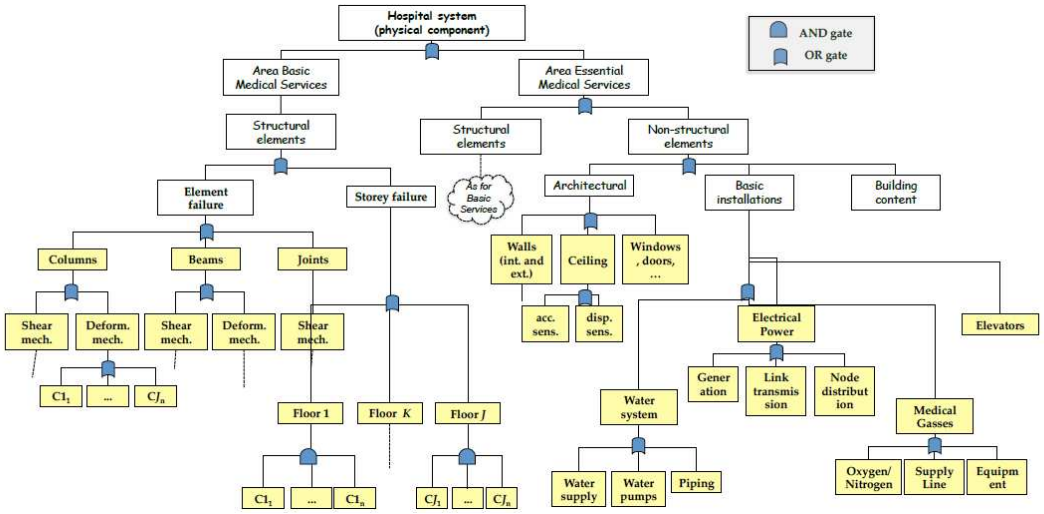

Figure 3.4. Typical layout of a FTA for a hospital complex [1]

3.3.1 Failure thresholds for structural elements

In the present section, failure thresholds for structural elements calculated according to the Italian Building Code (IBC) [15] are presented. The ultimate strength verification of a reinforced-concrete (RC) element subjected to bending moment (typically beams) is conducted as follows (§ 4.1.2.1.2.4):

$$\frac{M_{Ed}}{M_{Rd}} \leq 1 \tag{3.3}$$

where M_{Ed} is the bending moment acting about a principal axis, and M_{Rd} represents the ultimate bending strength of the element cross-section about the same axis.

RC elements subjected to shear forces (typically both beams and columns) are verified as follow (§ 4.1.2.1.3.1):

$$\frac{V_{Ed}}{V_{Rd}} \leq 1 \tag{3.4}$$

where V_{Ed} is the applied shear load, and V_{Rd} is the ultimate shear strength of the cross-section.

During the seismic shaking, some RC elements (typically columns) can be subjected to both compression load and biaxial bending and the relevant verification method is (§ 4.1.2.1.2.4):

$$\begin{cases} \left(\frac{M_{E,yd}}{M_{R,yd}}\right)^{\alpha} + \left(\frac{M_{E,zd}}{M_{R,zd}}\right)^{\alpha} \leq 1 \\ \frac{N_{Ed}}{N_{Rd}} \leq 1 \end{cases} \tag{3.5}$$

where N_{Ed} is the applied compression load, N_{Rd} is the ultimate compression strength of the cross-section, $M_{E,yd}$ and $M_{E,zd}$ are the bending moments acting about the two principal axes of the cross-section, and $M_{R,yd}$ and $M_{R,zd}$ are the related ultimate bending strengths (both depending on N_{Ed}).

The evaluation of the parameter α is not trivial since it depends on several factors such as the geometry of the cross-section, the amount of steel reinforcing bars, and the amplitude of the applied compression load N_{Ed}. However, in the absence of an accurate assessment, the ultimate strength domain of the element cross-section can be approximated in safety favour setting $\alpha = 1$.

3.3.2 Failure thresholds for isolation systems

Failure mechanisms of the isolation systems can have dangerous consequences for the superstructure and, in the worst cases, cause the structural collapse; among them, there are: (1) exceedance of the displacement capacity of the devices; (2) exceedance of the load bearing capacity of the same.

The first phenomenon can be avoided adopting the EC8-1 [19] design provisions reported in sections 1.5.4 and 4.1.1. In order to prevent the second failure mechanism, it should be verified that, during the seismic shaking, the maximum vertical load N_{Ed} applied to the isolation unit does not exceed its load bearing capacity N_{Rd}:

$$\frac{N_{Ed}}{N_{Rd}} \leq 1.0 \tag{3.6}$$

where N_{rd} is calculated according to the method defined in EN1337-7 (§ 6.2.1-6.2.3, 6.3.3) [20].

3.3.3 Failure thresholds for non-structural components

In recent years, few studies aiming at analyzing the seismic response of non-structural components (NSCs) of hospital buildings have been completed.

Bidirectional shake table tests on the typical layout of a hospital room have been carried out at the Structural Engineering and Earthquake Simulation Laboratory (SEESL) at the Buffalo University (New York, US) aiming at evaluating the earthquake effects on medical equipment and other nonstructural components. The research focused primarily on steel-stud

gypsum partition walls, lay-in suspended ceiling system, and fire protection sprinkler piping systems [21].

A number of shake table tests, dealing with medical laboratory components, such as low-temperature refrigerators, heavy incubators, freezers, microscopes, and computer equipment located on desks or shelves, were carried out at the University of California, Berkeley. The main expected goals were the derivation of *"fragility curves"* to be used for earthquake loss estimation, and for the definition of retrofitting intervention strategies [22].

At Hyogo Earthquake Engineering Research Center (Japan), full-scale shake table tests were also carried out on a base-isolated four-story RC hospital structure. The tests were conducted at E-defense Lab. and included both recorded near-fault ground motions and artificial long period records. The introduction of the base–isolation system allowed to achieve significant reductions of peak floor accelerations but was not suitable to ensure the hospital full operations in case of long period motions [23-24].

Similar tests were also conducted at the outdoor UCSD-NEES shake table facility in San Diego (University of California). The experimental campaign aimed at testing the resistance to both fire and earthquake of a wide array of non-structural components, such as elevators, stairs, exterior walls, interior partition walls, piping, heating, ventilation and air conditioning, ceiling, sprinkler system, and building contents [25].

Nevertheless, despite the growing interest on the topic, due to the large variety of NSCs typologies and configurations, the definition of exhaustive failure thresholds (that is admissible damage levels) is still an open issue. Among proposed methodologies, one of the most effective is the *"HAZUS"* approach [26]. It consists in modeling the *"capacity" C* (that is the seismic strength) of a generic NSC as a random variable having lognormal distribution:

$$C = C_m \varepsilon \tag{3.7}$$

where C_m is the median capacity, and ε is a log-normally distributed random variable (with a median value equal to 1 and a logarithmic standard deviation equal to β).

The related *"fragility curve"* represents the probability that the demand of strength D imposed by the ground motion exceeds the capacity C of the element ($P(C < D|D)$). Then, the failure-probability, conditioned on a chosen intensity measure IM parameter (e.g. the storey drift or the peak floor acceleration), is given by the cumulative distribution function of the capacity C:

$$P(C < D|D) = \int_0^{IM} \frac{1}{x\beta\sqrt{2\pi}} e^{-\frac{1}{2}\left(\frac{\log(x/C_m)^2}{\beta^2}\right)} dx = \Phi\left(\frac{\ln(IM/C_m)}{\beta}\right) \tag{3.8}$$

where Φ is the standard Gaussian cumulative distribution function.

According to the *"HAZUS"* approach, four damage thresholds can be observed: (1) *slight damage*; (2) *moderate damage*; (3) *extensive damage*; and (4) *complete damage*.

It is worth noting that the first level corresponds to the functional limit state, while a moderate/extensive damage affects the functionality of the element. The dispersion β of each damage threshold is evaluated by means of the sum of the contributions β_1 and β_2. The first represents the uncertainty in the damage-thresholds identification, while the second stands for the variability of the capacity of the non-structural element.

Although *"velocity-sensitive"* equipment have been addressed in a very recent study [27], the well-established HAZUS methodology categorizes non-structural components into *"drift-sensitive"*, *"acceleration-sensitive"* (that is sensitive to peak floor accelerations - PFA), and *"relative-displacement-sensitive"* elements. The definition of the seismic capacity of elements belonging to the last category (e.g. thermal expansion joints) is trivial; while the typical layout of the fragility curve for both drift-sensitive and acceleration-sensitive equipment is represented in Fig. 3.5. Related reference capacities at each damage level (high-code, *"special building"* category), and dispersion parameters β_1 and β_2 are respectively reported in Table 3.2 and 3.3.

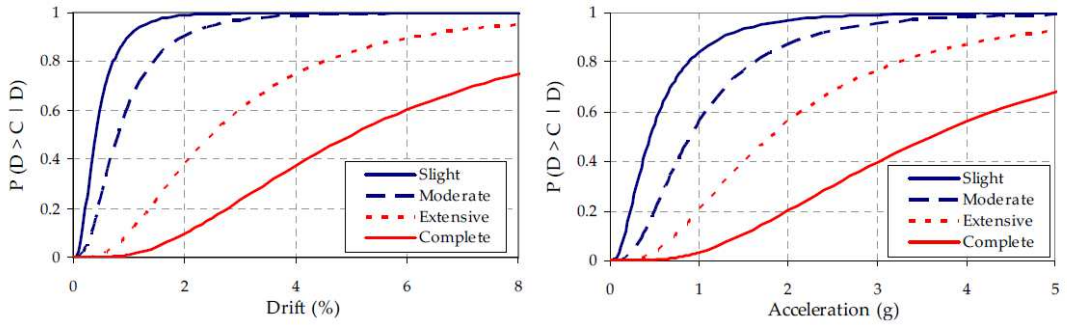

Figure 3.5. Fragility curves for different levels of damage: drift sensitive (left), and acceleration sensitive elements (right) (adapted from [1])

element type	parameter	slight	moderate	extensive	complete
drift-sensitive	drift (%)	0.40	0.80	2.50	5.00
acceleration-sensitive	PFA (g)	0.45	0.90	1.80	3.60

Table 3.2. Reference capacity for both *"drift-sensitive"* and *"acceleration-sensitive"* generic elements at each damage level

element type	β_1 (-)	β_2 (-)	$\beta = \beta_1 + \beta_2$ (-)
drift-sensitive	0.5	0.2	0.7
acceleration-sensitive	0.6	0.2	0.8

Table 3.3. Dispersion parameters β_1 and β_2 for both *"drift-sensitive"* and *"acceleration-sensitive"* generic elements

The model proposed above is general, while an accurate assessment of the dynamic response (natural frequencies and failure thresholds) of a specific non-structural component (NSC)

should be based on shake table tests conducted (for each possible configuration) according to the ICBO-AC156 international guidelines [28]. In this regard, a wide literature survey on available experimental results for specific elements has been recently completed [17]. Typical NSCs of a hospital complex were divided into homogeneous categories providing related *"moderate-extensive damage thresholds"*. A brief summary of that study is proposed hereafter; moreover, the same is extended by adding specific breakdown limits for typical hospital examination rooms and medical equipment.

Architectural components: past experiences have shown that, within this category, curtain walls, false ceilings, glass windows, and doors are among the most vulnerable elements to the earthquakes. Specific failure thresholds for these components are listed Table 3.4.

component	parameter	median capacity C_m	references
curtain walls	drift (%)	0.75	[29]
glass windows and doors	drift (%)	4.60	[30]
false ceilings	PFA (g)	0.90	[31-32]

Table 3.4. Mean capacity limits for architectural components

Power system: this group of NSCs is mainly composed of medium voltage-low voltage transformation stations (MV-LV transformer), diesel emergency generators (EG), uninterruptible power system (UPS), transmission lines, and distribution panels. Specific failure thresholds are listed in Table 3.5.
It should be noted that electricity transmission lines are not considered vulnerable to earthquakes. Moreover, since in case of earthquake attack emergency generators are expected to work properly, also MV-LV transformation stations are not considered among critical components.

component	parameter	median capacity C_m	references
EG diesel conduits	drift (%)	0.90	[33]
UPS battery cabinets	PFA (g)	0.52	[34]
UPS switchboard panels	PFA (g)	1.12	[34]
UPS distribution panels	PFA (g)	1.75	[34]

Table 3.5. Mean capacity limits for power system components

Water system: typically consists of supply and distribution pipelines, emergency buried tanks, and other equipment such as pumps and boilers. Pipelines, even if connected to the main supply system by means of flexible couplings, represent the most critical component

with a specific failure threshold provided in Table 3.6. Other components, if properly anchored (to the floor or walls), should not be vulnerable to quakes.

component	parameter	median capacity C_m	references
pipelines	drift (%)	0.90	[33]

Table 3.6. Mean capacity limits for water system components

Conveying system: is composed of horizontal (corridors) and vertical (elevators and stairs) connection systems. Elevators, due to the large number of assembled components, represent a critical element and the relevant failure threshold is given in Table 3.7.

component	parameter	median capacity C_m	references
elevators	PFA (g)	0.20	[35]

Table 3.7. Mean capacity limits for conveying system components

Medical gas system: is composed by tanks for medical gases (e.g. oxygen, nitrogen), and distribution pipelines. Specific failure thresholds are given in Table 3.8. It is worth noting that tanks are supposed properly anchored to the floor and pipelines connected to the main supply system by means of flexible couplings.

component	parameter	median capacity C_m	references
tanks	PFA (g)	0.50	expert judgement
pipelines	drift (%)	0.90	[33]

Table 3.8. Mean capacity limits for water system components

*Examination rooms: w*ithin a research project of the Italian Research Network ReLUIS, shake table tests were carried out on different configurations of a full-scale examination room aiming at identifying relevant overall limit states [36]. The examination room included different freestanding NSCs such as two cabinets, a desktop computer, and a desk. Three damage states (DS) were identified: (1) at DS1 only quick repairing interventions are required; (2) at DS2 components are partially damaged and more substantial repairing interventions are needed; (3) at DS3 life safety is threatened, and components need to be totally replaced.

Since immediate operations of consultation rooms is vital for the management of the earthquake emergency response, the DS1 failure threshold is considered in the present study (Table 3.9).

component	parameter	median capacity C_m	references
consultation room	PFA (g)	0.45	[36]

Table 3.9. Mean capacity limit for a consultation room (with freestanding components)

Medical equipment: among most important and expensive medical equipment for diagnostic activities there are the computed tomography (CT), the magnetic resonance (MR), the cardio vascular imaging (CVI), and the ultrasound scan (US). A specific failure threshold (Table 3.10) is derived from the installation recommendations of one of the major manufacturing companies. Other provisions concern the anchoring of the equipment to the floor in order to avoid possible overturning, or hammering with other adjacent components.

component	parameter	median capacity C_m	references
medical equipment (CT, MR, CVI, US)	PFA (g)	1.00	manufacturer recommendations

Table 3.10. Mean capacity limits for medical equipment (supposed anchored to the floor)

3.4 Seismic isolation to enhance the hospital performance

During recent earthquakes seismic isolation proved to be an effective solution for the protection of hospitals from potential damages to both structural and non-structural components, including the medical equipment. Moreover, using seismic isolation to enhance damage resistance of hospitals leads, in addition, to significantly smaller repair cost and repair time compared to the ones with a conventional fixed-base structure [37]. Indeed, after the strong 1994 Northridge earthquake, the Southern California Teaching Hospital (Los Angeles), built in 1991 and implementing elastomeric isolators, remained fully-operational. On the contrary, the Olive View Hospital (Los Angeles), built in 1971 with a traditional *"fixed-base"* structure, although not subjected to serious structural damages, was inoperative due to the failure of plants and medical equipment [38].

3.4.1 Some worldwide applications

Since several years, in California (US), elastomeric isolators have been widely used to protect new hospital facilities as well as to retrofit existing ones from potential damages induced by strong earthquakes [39]. On the contrary, in US as in the rest of the world, despite their interesting advantages (see section 2.1), the Curved Surface Sliders (CSSs), also known as Friction Pendulum System® isolators, are still scarcely used for seismic isolation of hospitals. In this regard, a rare example of application is represented by the new hospital of Stanford (CA) whose building completion is expected in few months [40].

In New Zealand, elastomeric isolators coupled with sliding bearings have been recently employed for the seismic-protection of four new hospital buildings [41].

In Turkey, thanks to a new prescription of the Ministry of Health, the number of applications of base-isolation technique to new hospital complexes, as well as to retrofitting interventions, is increasing rapidly [42]. The solution adopted for the seismic-retrofitting of the Marmara University Research and Training Hospital (Istanbul) is challenging; indeed, due to its vertically irregular structures, several elastomeric bearings were disposed on two different isolation levels [43].

Also in Italy, in recent years, seismic isolation technique started to be adopted both for the construction of new hospitals and for the retrofitting of existing ones. Elastomeric isolators have been implemented for the base isolation of the new hospitals of Naples and Udine [44-45], as well as for the redevelopment of a hospital unit in Avellino [46].

3.4.2 Current issues

Among most challenging issues related to the seismic performance of hospital buildings, even if protected by a seismic isolation strategy, there are: (a) the lack of information on the seismic strength of non-structural components (as witnessed by the fact that too often the same is entrusted to a not always reliable *"expert judgment"*); (b) the potential dangerous

effects of the vertical components of seismic excitation that are hardly mitigated; (c) specific problems arise from the morphological model (that is the planer and vertical layout of the structures) adopted for the hospital complex.
The first blackspot could be solved by promoting extensive experimental campaigns (shake table tests) in order to determine specific failure thresholds for most common and important non-structural components (in all their possible different configurations). Even thought not investigated in this thesis, the second and third issues are briefly discussed hereafter.

3.4.2.1 Vertical components of seismic excitation

Since a high vertical stiffness of isolator devices is necessary to support gravitational loads, the effects of the vertical seismic excitation are hardly mitigated. This can amplify the risk of rocking or overturning of non-structural elements and possible damages to *"acceleration-sensitive"* equipment. This aspect has been already highlighted for the seismic isolation of museums containing statues and other artworks whose stability is largely vulnerable to floor vibrations [47]. Experimental and numerical studies, conducted considering structures implementing sliding isolators [48-49], concluded that: (1) vertical components of ground motion have a small influence on the maximum displacement of the isolation system (variations within 10%); (2) more significant variations concern instead the shear forces transmitted to the building by the isolation system (within the range 40-70%).
The Italian Building Code [15] establishes some specific design criteria: (1) in case of ordinary buildings located in low-seismicity areas, vertical components of the seismic excitation can be neglected (§ 3.2); (2) vertical components must be carefully considered in the presence of beams, or other horizontal structural elements, longer than 20m (§ 7.2); (3) in the case of base-isolated structures, the vertical component must be considered when the ratio between the vertical K_V and horizontal K_H stiffnesses of the isolation system is lower than 800 (rare for CSS isolators).
The effects of vertical components could be locally mitigated (in the most critical parts of the building) using proper damping strategies (e.g. vertical tuned mass dampers). However, the definition of a more general solution to this issue, that is common to both fixed-base and base-isolated structures, is very challenging and is beyond the scope of this thesis.

3.4.2.2 Hospital morphological models

Different distribution criteria for the typical functional areas of a hospital unit (e.g. hospital stay, operating theatres) have led to the definition of some common morphological models [50]. In particular, some undesirable effects may occur when applying seismic isolation technique and are discussed hereafter for the main four morphological models (Fig. 3.6).

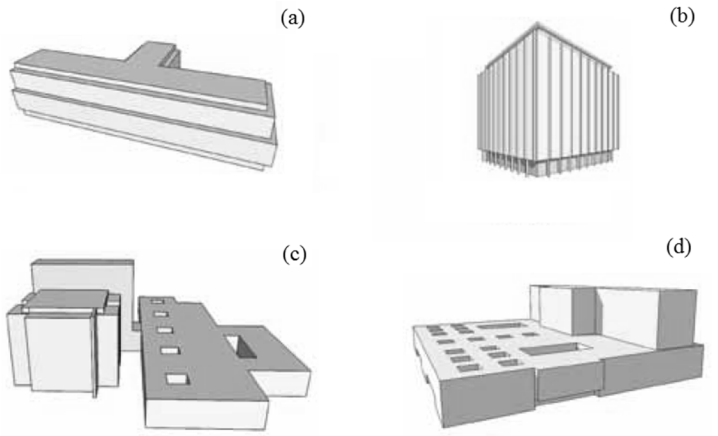

Figure 3.6. Main morphological models for hospital unit: "single block" (a), "tower" (b), "multi-block" (c), and "slab block-tower block" (d) (adapted from [50]).

"*Single Block*": hospital building with a compact shape; generally rectangular, U-shaped, or double-T shaped (Fig. 3.6-a). This model is probably the most suitable for seismic isolation technique since it allows, more easily than the others, to minimize the eccentricity between the centre of gravity of the superstructure and the centre of stiffness of the isolators (minimization of torsional motions).

"*Tower*": hospital building with a compact shape and a significant growth in height (Fig. 3.6-b). During the earthquake, the inertia forces acting on the upper floors generate overturning moments that may cause rubber lacerations for elastomeric isolators and uplifting, with potential loss of contact, for sliding isolators. This problem can be solved by inserting appropriate anti-uplift restraints at the isolation level.

"*Multi block*": hospital building in which each functional area is located in a different block (Fig. 3.6-c). In case of earthquake attack, the seismic isolation at the base of each block can induce relative displacements between the same. Horizontal and vertical conveying systems must therefore be equipped with appropriate flexible joints capable to ensure the continuity of the distribution paths (enabling the motion of stretchers and people with limited mobility). In some cases, additional damping systems may be necessary to avoid the hammering between adjacent blocks. In other cases, the self-centring capability of the isolation system may be fundamental to ensure the full operation in the emergency management.

"*Slab block-tower block*": hospital building composed of a horizontal and a vertical block (Fig. 3.6-d). This model can be affected by the problems of both the morphological type (b) and (c); in addition, during the seismic shaking, the irregular shape in height can induce torsional motions due to eccentricity between the centre of gravity of the superstructure and the centre of stiffness of the isolators. This undesirable effect is evident for elastomeric isolators while CSS isolators are less vulnerable.

3.5 Chapter references

[1] SYNER-G project (2009-2012) "*Systemic Seismic Vulnerability and Risk Analysis for Buildings, Lifeline Networks and Infrastructures Safety Gain*", deliverables D2.8, D3.3 and D3.10, available online: http://www.vce.at/SYNER-G/files/dissemination/deliverables.html

[2] USGS (1996) "*USGS response to an Urban Earthquake - Northridge '94*", United States Geological Survey (USGS), http://pubs.usgs.gov/of/1996/ofr-96-0263/introduc.htm#impacts

[3] Achour, N., Miyajima, M., Kitaura, M., Price, A. (2011) "*Earthquake Induced Structural and Non-structural Damage in Hospitals"*, Earthquake Spectra, Vol. 27(3), pp. 617-634

[4] De Sortis, A., Biondi, S., Di Pasquale, G., Nuti, C., Orsini, G., Sanò, T., Vanzi, I. (1999) "*Damages to hospitals during recent Italian earthquakes*", Proceedings of the Workshop on Seismic Design and Retrofitting of Hospitals in Seismic Areas, Firenze, Italy

[5] De Sortis, A., Di Pasquale, G., Orsini, G., Sanò, T., Biondi, S., Nuti, C., Vanzi, I. (2000) "*Hospitals behavior during the September 1997 earthquake in Umbria e Marche (Italy*)", Proceedings of the 12th World Conference on Earthquake Engineerig (WCEE), Auckland, New Zeland

[6] Commissione Parlamentare di inchiesta sull'efficacia e l'efficienza del Servizio Sanitario Nazionale (2009) "*Relazione finale sull'attività della Commissione*", last session 15th July 2009

[7] EEFIT (2009) "*The L'Aquila, Italy Earthquake of 6 April 2009: A preliminary field report*", London

[8] Masi, A., Santarsiero, G., Gallipoli, M.R., Mucciarelli, M., Manfredi, V., Dusi, A. Stabile, T.A. (2014), "*Performance of the health facilities during the 2012 Emilia (Italy) earthquake and analysis of the Mirandola hospital case study*", Bulletin of Earthquake Engineering, Springer, DOI 10.1007/s10518-013-9518-4, Vol. 12, pp. 2419–2443

[9] Celano, F., Cimmino, M., Coppola, O., Magliulo, G, Salzano, P. (2016), "*Report dei danni registrati a seguito del terremoto del centro Italia del 24 Agosto 2016 (Release 1)"*, Report ReLUIS (Rete dei Laboratori Universitari di Ingegneria Sismica), http://www.reluis.it/images/stories/Centre%20Italy%20earthquake%20damage%20report%20-%20R1.pdf

[10] ATC, Applied Technology Council (1997) "*NEHRP Guidelines for the Seismic Rehabilitation of Buildings*", prepared for the Building Seismic Safety Council (BSSC) and published by the Federal Emergency Management Agency (FEMA), Report No. 273, Washington, DC

[11] ATC, Applied Technology Council (1997) "*NEHRP Commentary on the Guidelines for the Seismic Rehabilitation of Buildings*", prepared for the Building Seismic Safety Council (BSSC) and published by the Federal Emergency Management Agency (FEMA), Report No. 274, Washington, DC

[12] SEAOC, Structural Engineers Association of California (1996) "*Recommended Lateral Force Requirements and Commentary*", Vision 2000, conceptual framework for performance-based seismic design, 6th edition, Sacramento, CA

[13] FEMA, Federal Emergency Management Agency (2000) "*Prestandard and Commentary for the Seismic Rehabilitation of Buildings*", Report No. 356, Washington, D.C.

[14] ATC, Applied Technology Council (2006) "*Next-Generation Performance-Based Seismic Design Guidelines*", prepared for the Federal Emergency Management Agency (FEMA), Report No. 445, Washington, DC

[15] Ministero delle Infrastrutture, D.M. 14.01.2008, "*Norme Tecniche per le Costruzioni*"

[16] Aiello, A., Pecce, M., Di Sarno, L., Perrone, D., Rossi, F. (2012) "*A Safety Index for Hospital Buildings*", Disaster Advances, Vol. 5(4), ISSN 0974262X

[17] Lupoi, G., Franchin, P., Lupoi, A., Pinto, P.E., Calvi, G.M. (2008) "*Probabilistic Seismic Assessment for Hospitals and Complex-Social Systems*", ROSE Research Report No. 2008/02, IUSS Press, Pavia, ISBN 978-88-6198-017-4

[18] Miniati, R., Capone, P., Hosser, D. (2014) "*Decision Support System for Rapid Seismic Risk Mitigation of Hospital Systems. Comparison Between Models and Countries"*, International Journal of Disaster Risk Reduction, Vol. 9, pp. 12-25, DOI: 10.1016/j.ijdrr.2014.03.008

[19] CEN, Eurocode 8 (2004) "*Design of structures for earthquake resistance—Part 1: General rules, seismic actions and rules for buildings*", EN1998-1:2004, European Committee for Standardization, Bruxelles, Belgium

[20] CEN (2004) "*EN 1337 – Structural bearings - Part 7: Spherical and cylindrical PTFE bearings*", European Committee for Standardization, Bruxelles, Belgium

[21] Mosqueda, G., Retamales, R., Filiatrault, A., Reinhorn, A. (2009) "*Testing facility for experimental evaluation of non-structural components under full-scale floor motions. Structural Design of Tall and Special Buildings*", Vol. 18(4), pp.387–404, DOI:10.1002/Tal.441

[22] Konstantinidis, D., Makris, N. (2009) "*Experimental and analytical studies on the response of freestanding laboratory equipment to earthquake shaking*", Earthquake Engineering & Structural Dynamics, Vol. 38(6), pp. 827–848. DOI:10.1002/Eqe.871

[23] Sato, E., Furukawa, S., Kakehi, A., Nakashima, M. (2011) "*Full-scale shaking table test for examination of safety and functionality of base-isolated medical facilities*", Earthquake Engineering & Structural Dynamics, Vol. 40(13), pp. 1435–1453, DOI:10.1002/Eqe.1097

[24] Furukawa, S., Sato, E., Shi, Y., Becker, T., Nakashima, M. (2013) "*Full-scale shaking table test of a base-isolated medical facility subjected to vertical motions*" Earthquake Engineering & Structural Dynamics, Vol. 42(13), pp. 1931–1949, DOI:10.1002/eqe.2305

[25] Chen, M., Pantoli, E., Wang, X., Espino, E., Mintz, S., Conte, J., Hutchinson, T., Marin, C., Meacham, B., Restrepo, J., Walsh, K., Englekirk, R., Faghihi, M., Hoehler, M. (2012) "*Design and construction of a full-scale 5-story base isolated building outfitted with nonstructural components for earthquake testing at the UCSD-NEES facility*", ASCE Structures Congress, Chicago, Illinois, US

[26] FEMA, Federal Emergency Management Agency (1999) "*Earthquake Loss Estimation Methodology Hazus99*", SR2: Techical Manual, Washington, DC

[27] Petrone, C., Di Sarno, L., Magliulo, G., Cosenza, E. (2016) "*Numerical modelling and fragility assessment of typical freestanding building contents"*, Bulletin of Earthquake Engineering, DOI 10.1007/s10518-016-0034-1

[28] ICBO Evaluation Service (2000) "*AC 156 Acceptance Criteria for the Seismic Qualification of Nonstructural Components*", International Conference of Building Officials (ICBO), Whittier, California, USA

[29] Rihal, S.S. (1982) "*Behavior of nonstructural building partitions during earthquakes*", Proceedings of the 7th Symposium on Earthquake Engineering, University of Roorke, India

[30] Behr, R.A., Worrel, C.L. (1998) "*Limit states for architectural glass under simulated seismic loadings*", ATC 29-1, Redwood city, CA

[31] Eidenger, J., Goettle, K. (1998) "*The benefits and costs of seismic retrofits on nonstructural components for hospitals, essential facilities, and schools*", ATC 29-1, Redwood city, CA

[32] Badillo, H., Whittaker, A.S., Reinhorn, A.M. (2003) "*Performance characterization of suspended ceiling systems*", ATC 29-1, Redwood city, CA

[33] Kuwatta, Y., Takada, S. (2003) "*Seismic risk assessment and upgrade strategy of hospital lifeline performance*", Proceedings of Technical Council on Lifeline Earthquake Engineering, ASCE, Long Beach, CA

[34] Swan, S.W., Kassawara (1998) "*The use of earthquake experience data for estimates of seismic fragility of standard industrial equipment*", ATC 29-1, Redwood city, CA

[35] Nutti, C., Santini, S., Vanzi, I. (1999) "*Seismic risk of Italian hospitals*", Proceedings of the workshop on design and retrofitting of hospitals in seismic areas, Florence, Italy

[36] Cosenza, E., Di Sarno, L., Maddaloni, G., Magliulo, G., Petrone, C., Prota, A. (2014) "*Shake table tests for the seismic fragility evaluation of hospital rooms*", Earthquake Engineering & Structural Dynamics, Vol. 44(1), pp. 23-40, DOI: 10.1002/eqe.2456

[37] Moretti, S., Terzic, V., Cimellaro, G., Mahin, S. (2014) "*Utilizing base-isolation systems to increase earthquake resiliency of healthcare and school buildings*", Proceedings of the 4th International Conference on Building Resilience, Manchester, United Kingdom

[38] EERI, Earthquake Engineering Research Institute, (1994) "*Northridge Earthquake January 17, 1994. Preliminary Reconnaissance Report*", Hall, J.F. Editor, California

[39] Kelly, J.M. (1994) "*The implementation of base isolation in United States*", Earthquake Engineering, 10th World Conference, Rotterdam, Netherlands

[40] Structurae - International Database for Civil and Structural Engineering (2016) *"New Stanford Hospital: Friction pendulum isolators as earthquake protection"*, https://structurae.net/products-services/new-stanford-hospital-friction-pendulum-isolators-as-earthquake-protection

[41] Charleson, A.W., Allaf, N.J. (2012) *"Costs of Base-isolation and Earthquake Insurance in New Zealand"*, New Zealand Society for Earthquake Engineering Conference (NZSEE), Canterbury, New Zealand

[42] Erdik, M., Tuzun, C., Ulker, O. (2015) "*Evaluation of seismic isolation applications of health care facilities in Turkey*", Proceedings of the 14th World Conference on Seismic Isolation, Energy Dissipation and Active Vibration Control of Structures, San Diego (CA), USA

[43] Kubin, J., Kubin, D., Özmen, A., Sadan, O.B., Eroğlu, E., Sucuoğlu, H. (2012) "*Seismic Retrofit of an Existing Multi-Block Hospital by Seismic Isolators*", Proceedings of the 15th World Conference on Earthquake Engineering, Lisboa, Portugal

[44] Castellano, M.G., Cosenza, E., Di Sarno, L., Guerriero, L., Lupoi, G. and Infanti, S. (2007) "*Seismic isolation of hospitals: The examples of Udine, Lisbon and Naples hospitals*", Proceedings of the 10th World Conference on Seismic Isolation, Energy Dissipation and Active Vibration Control of Structures, Istanbul, Turkey

[45] Di Sarno, L., Cosenza, E., Pecce, M.R. (2007) "*Application of base isolation to a large hospital in Naples, Italy*", Proceedings of the 10th World Conference on Seismic Isolation, Energy Dissipation and Active Vibration Control of Structures, Istanbul, Turkey

[46] Ferraioli, M., Avossa, A.M. (2012) "*Base Isolation Seismic Retrofit of a Hospital Building in Italy*", Journal of Civil Engineering and Architecture, Vol. 6, No. 3, pp. 308-321

[47] Castiglioni, C.A., Kanyilmaz, A. (2010) "*Seismic Isolation Methods for Ancient Statues on Display*", Proceedings of the 8th International Conference on New Trends in Statics and Dynamics of Buildings, Bratislava, Slovakia

[48] Calvi, G.M., Ceresa, P., Casarotti, C. (2004) "*Effects of axial force variation in the seismic response of bridges isolated with friction pendulum systems"*, Journal of Earthquake Engineering, Vol. 8(1), pp. 187–224

[49] Mosqueda, G., Whittaker, A.S., Fenves, G.L. (2004) "*Characterization and modeling of friction pendulum bearings subjected to multiple components of excitation"*, Journal of Structural Engineering, Vol. 130(3), pp. 433-442

[50] CNETO, Centro Nazionale Edilizia e Tecnica Ospedaliera, (2016) "*Quaderno 4 – Sicurezza strutturale*", download: http://www.cneto.it/

CHAPTER 4

Development of design tools

4.1 Estimating the displacement accrual

4.1.1 Introduction

The accurate estimation of the extreme displacements of the structure under the reference earthquake is a fundamental information for the design of the isolation hardware as well as of all lifelines and non structural elements that cross the isolation plane (e.g. fire protection and weather proofing elements, elevators, etc in a building, or road joints in a bridge), that must be capable to accommodate the relevant displacements.

The European design code, or Eucorode 8 (EC8) [1, 2] recognizes the critical role played by the displacement capability of the isolation system for the safety of the structure, and recommends to verify the maximum total displacement of the isolation units according to:

$$D_i \geq d_{G,i} + \gamma_{IS} \cdot d_{m,i} \tag{4.1}$$

where D_i is the displacement capacity of each isolator i, $d_{G,i}$ is an non seismic offset displacement potentially induced by the permanent actions, the long-term deformations of the superstructure (e.g. post-tensioning, shrinkage and creep for concrete decks) and 50% of the thermal action, $d_{m,i}$ is the design seismic displacement of the isolator, and γ_{IS} is a reliability amplification factor whose recommended value is 1.2 for buildings and 1.5 for bridges. It is worth nothing that Eq. (4.1) implicitly assumes that non seismic and seismic displacements are additive, because $d_{m,i}$ is calculated, by means of either a fundamental mode or multimode spectrum analysis, or a nonlinear response time history analysis, assuming that at the occurrence of the earthquake the isolation unit is its centred configuration. A possible effect of the offset displacement on the seismic displacement is deemed to be covered by the γ_{IS} factor.

It has to be also considered that, further to permanent and thermal actions, the offset displacement of the isolation system can possibly result from an incorrect installation procedure of the isolation units, or can be the residual displacement at the end of a previous

seismic event or ground tremor. There is in fact significant field evidence of seismic sequences characterized by frequent medium-strong intensity ground motions following a strong mainshock after short intervals of time, as recorded also in recent earthquakes [3-8]. Since it may not be possible to re-center the system before the occurrence of close aftershocks, a concern is related to the possibility that ground motion sequences with such characteristics would entail an accrual of displacements, and the deformation capacity of the isolation system designed on the basis of a single earthquake possibly becomes inadequate at the end of the seismic sequence.

According to the prescription of the Eurocode 8, an isolation system is deemed to have sufficient self-centring capability in one horizontal direction when the condition is met:

$$\frac{d_{cd}}{d_{rm}} \geq \delta \tag{4.2}$$

where d_{cd} is the maximum design displacement at the centre of stiffness, d_{rm} is the maximum residual displacement for which the isolation system can be in static equilibrium, i.e. the residual displacement under which the static equilibrium is reached at unloading from d_{cd} under quasi-static conditions, and δ is a numeric coefficient, whose recommended value is 0.5. For isolation systems with bilinear hysteretic behaviour the maximum residual displacement d_{rm} is given by the ratio between the characteristic strength F_0 and the restoring stiffness K_P (Fig. 4.1) and depends only on the fundamental mechanical characteristic of the system, whereas d_{cd} depends also on the details of the seismic ground motion, like the intensity and the frequency content [9-11]. Earthquakes consisting of a single velocity pulse are expected to impose highly asymmetric time histories to the isolated structure thus requiring a strong restoring behaviour to limit the residual displacements. [12-14].

Parametric analyses demonstrated the validity of the Eurocode's re-centring criterion for either bilinear hysteretic isolation systems, where $\delta = 0.5$ [15], and for systems with "flag-shaped" force – displacement characteristic, like systems comprising self-centring elements made of Shape Memory Alloys, where $\delta = 3$ [10]. It is also noted that the Eurocode criterion with $\delta = 0.5$ is in agreement with the re-centring provision given in the European Standard on antiseismic device [16], stating that the isolation system has sufficient re-centring capability when:

$$E_S \geq 0.25 E_H \tag{4.3}$$

where E_S is the reversibly stored energy and E_H is the energy dissipated in hysteretic deformation when the system moves from its origin to the position of maximum displacement [17].

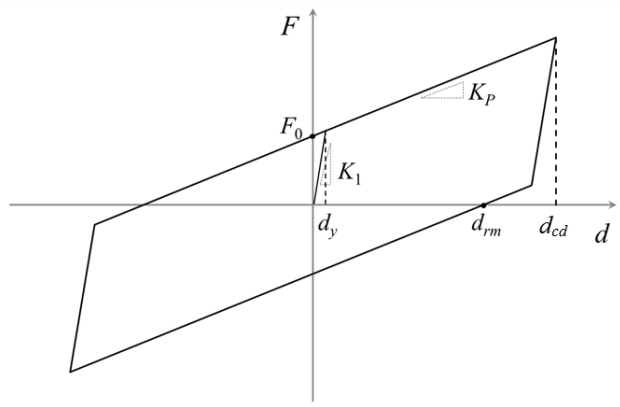

Figure 4.1. Force – displacement characteristic of a bilinear hysteretic isolation system

The Eurocode recommends that systems which do not satisfy the re-centring criterion have sufficient displacement capacity to accommodate, with adequate reliability, the accumulation of residual displacements during the service life of the structure. This requirement is considered satisfied when each isolator meets the condition:

$$D_i \geq d_{G,i} + \gamma_{du} \cdot \rho_d \cdot d_{m,i} \tag{4.4}$$

where $\gamma_{du} = 1.2$ is a numerical coefficient that accounts for the uncertainties in the estimation of design displacements, and ρ_d is a factor that reflects the accumulation of residual displacements under a sequence of earthquake events occurring before the design earthquake, considered to have a collective probability equal to the probability of the design earthquake:

$$\rho_d = 1 + 1.35 \frac{1 - \left(d_y / d_{cd}\right)^{0.6}}{1 + 80\left(d_{cd} / d_{rm}\right)^{1.5}} \tag{4.5}$$

where d_y is the yield displacement of the equivalent bilinear system (see Fig. 4.1). For systems with $d_{cd} / d_{rm} > 0.5$ the effect of the accumulation of residual displacements is insignificant ($\rho_d < 1.05$).

Although Curved Surface Slider (CSS) isolators represent one of the most popular isolation hardware worldwide, their self-centring capability has not yet been investigated in detail.

Some studies have been pubslihed pointing to the importance of the coefficient of friction, which opposes to the restoring force provided by the curvature of the surfaces, as a not negligible factor affecting the re-centering behavior [18, 19], the self-centring capability of the Curved Surface Sliders has not yet been investigated in detail. The force – displacement characteristic of the Curved Surface Slider in principle can be described by a bilinear hysteretic model, but the dependence of the coefficient of friction on a number of factors, like the velocity of sliding, the vertical load and the temperature, which typically vary in the

isolation system during an earthquake, makes questionable to which extent the Eurocode provisions are valid. A parametric investigation covering the production range of an European manufacturer and considering a variety of natural ground motions concluded that sliding isolators with curved surfaces experience negligible residual displacements when d_m / d_{rm} is larger than 2.5 [11]. Independent shake table tests on base isolated structures equipped with either triple friction pendulum isolators [20] or single and double curvature devices [21] and simulating sequences of low-to-moderate and high amplitude seismic ground motions, showed that, depending on the sequence details, the isolation system may either accumulate or recover residual displacements. Based on theoretical considerations, it was eventually concluded [21] that, when pulse-like time-histories are imposed, an initial offset d_o (d_G in EC8) tends to produce a change Δd_{cd} of the maximum seismic displacement in the same direction (Fig. 4.2), and at first approximation proportional to $(d_{cd} / d_{rm})^{-1}$:

$$\Delta d_{cd} \approx \frac{1}{1+\dfrac{d_{cd}}{d_{rm}}} \cdot d_o \tag{4.6}$$

Consequently, when in an unidirectional motion the offset acts in the opposite direction respect to the direction along which the maximum seismic displacement is developed, the final result is a decrease of d_{cd} , as illustrated in Fig. 4.3 [21]. Nevertheless, though a potential effect of the ground motion characteristics was hinted, this subject was not deepened.

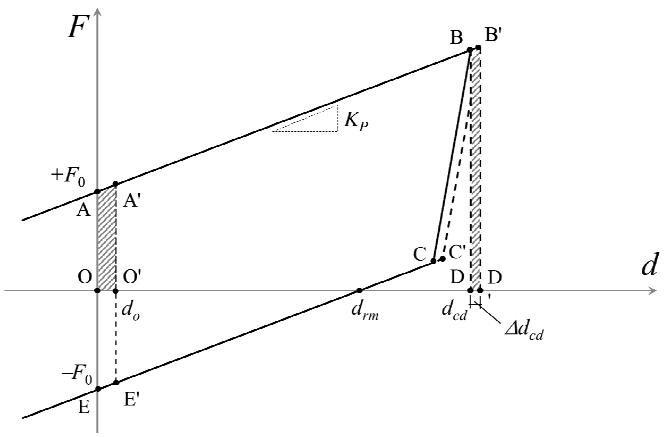

Figure 4.2. Influence of an initial offset d_o on the maximum seismic displacement d_{cd} when $d_o > 0$ and $\Delta d_{cd} > 0$ (shaded area must be equal due to the principle of conservation of energy [21])

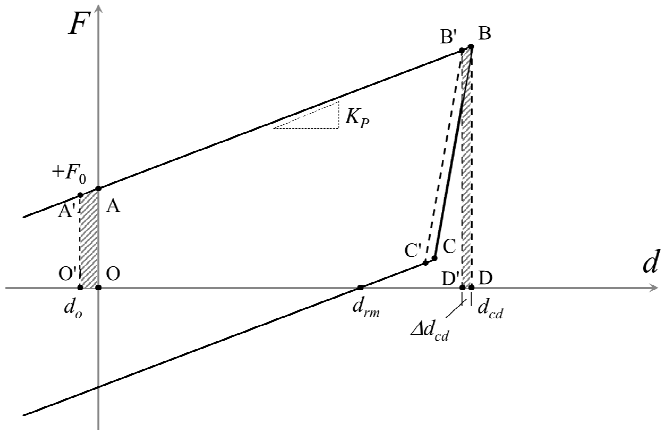

Figure 4.3. Influence of an initial offset d_o on the maximum seismic displacement d_{cd} when $d_o < 0$ and $\Delta d_{cd} < 0$ (shaded area must be equal due to the principle of conservation of energy [21])

The aim the study developed in section 4.1 of the thesis is to give more insight into this argument, investigating the possibility of displacement accrual of the Curved Surface Slider owing to an initial offset displacement. The first part of the study addresses the effect of an imposed non-seismic offset on the displacement of the isolation unit during the earthquake. A parametric study is performed and the properties of the isolation units are varied to cover the production ranges of current manufacturers, while a set of natural ground motions is selected in order to investigate a range of possible seismic scenarios. The second part of the study addresses the response of the isolation system to natural sequences of earthquakes consisting of either foreshock and main shock, or mainshock and aftershock ground motions; in these situations, the residual displacement at the end of the first ground motion of the sequence becomes the offset displacement for the second ground motion. Eventually some analyses considering natural sequences of several ground motions (four to six) are presented and discussed.

4.1.2 Numerical analysis

Nonlinear Response Time History Analyses (NRHA) were carried on Single Degree Of Freedom (SDOF) systems assuming a mass of 100 tons, typical of medium-rise residential buildings [11]. The seismic input consisted of one-directional horizontal ground motion time histories, whereas the vertical component of the seismic excitation was not taken into account. Similarly, the variability of the axial load due to rocking movements of the building was not examined.

The numerical model was implemented in the structural analysis program OpenSees® v.2.5.4 [22], using a nonlinear "friction bearing" element to model the hysteretic behaviour of the isolation system. The velocity dependent friction model was described by the equation [23]:

$$\mu = \mu_{LV} - (\mu_{HV} - \mu_{LV}) \cdot e^{(-\alpha \cdot |v|)} \tag{4.7}$$

where μ_{LV} and μ_{HV} are two parameters that represent the coefficient of friction at very low and very high velocity, respectively, and α is a parameter that describes the rate of transition from μ_{LV} to μ_{HV}. The restoring stiffness of the isolation system was defined as $K_P = W/R$, where W is the vertical load acting though the isolation system, and R is the radius of curvature of the CSS. Finally, an initial stiffness $K_1 = 100\ K_P$ was assumed in order to minimize the elastic deformation of the system.
In the SDOF model, the displacement of the isolation system, d_c, corresponds to the displacement of the isolation unit d_m.

4.1.2.1 Parameters of the Curved Surface Sliders

The values of the radius of curvature R and the coefficient of friction μ of the CSS were chosen in order to cover the typical range of current devices on the European market (Table 4.1). Five values of the radius R were considered, namely 2 200, 3 000, 3 500, 4 000 and 5 000 mm, corresponding to natural periods T from 2 to 4 seconds. The high velocity friction coefficient μ_{HV} ranged between 5% and 12.5%, with a 2.5% step; a ratio $\mu_{HV}/\mu_{LV} = 2.5$ was assumed and the transition rate was set to $\alpha = 0.0055$ s/mm, in accordance with [11]. Although the analysis did not directly consider the effects of normal load and air-temperature variations on the coefficient of friction of the sliding surfaces [24, 25], they are assumed to be indirectly covered by the range of the friction coefficient.

parameter	**tag**	**values**
radius, R	R_1	2 200 mm
	R_2	3 000 mm
	R_3	3 500 mm
	R_4	4 000 mm
	R_5	5 000 mm
coefficient of friction, μ	f_2	$\mu_{LV} = 0.020$; $\mu_{HV} = 0.050$; $\alpha = 0.0055$ s/mm
	f_3	$\mu_{LV} = 0.030$; $\mu_{HV} = 0.075$; $\alpha = 0.0055$ s/mm
	f_4	$\mu_{LV} = 0.040$; $\mu_{HV} = 0.100$; $\alpha = 0.0055$ s/mm
	f_5	$\mu_{LV} = 0.050$; $\mu_{HV} = 0.125$; $\alpha = 0.0055$ s/mm

Table 4.1. CSS parameters examined in the study

4.1.2.2 Seismic inputs classification

To investigate ground motions with different frequency contents, a number of records was obtained from the Pacific Earthquake Engineering Research Center (PEER) database (http://peer.berkeley.edu/nga) and categorized based on the pulse index PI_k (definition given in the Annex) into three groups:

no pulse	$PI_k < 0.40$
weakly pulse	$0.40 \leq PI_k \leq 0.70$
pulse-like	$PI_k > 0.70$

A second classification was based on the period T_{sv} of the maximum undamped spectral velocity; four ranges of T_{sv} were established:

$T_{sv} \leq 2.0$ sec
$2.0 < T_{sv} \leq 3.0$ sec
$3.0 < T_{sv} \leq 4.0$ sec
$T_{sv} > 4.0$ sec

For pulse-like seismic ground motions, T_{sv} coincides with the so-called "pulse period" T_p, corresponding to the dominant peak of the velocity response spectrum at which the largest quantity of seismic energy is available. For no pulse ground motions significant energy content can be available over a range around T_{sv} depending on the smoothness of the spectrum.

4.1.2.3 Single shake with initial non-seismic offset displacement

Selected records: twenty-four ground motion records were selected (Table 4.2) in order to provide at least two time histories for each pulse and period range. Only records with lowest usable frequency (l.u.f.) [26] less than 0.2 Hz were chosen to match the undamped vibration frequency of the CSS isolators with radius R_5 = 5 000 mm. Though not exhaustive, the set of ground motions spans the possible scenarios of pulse character and frequency content of interest for base isolation.
The acceleration time histories were scaled in order to produce displacements of the isolation system of practical interest, but the seismic records do not need to be compatible with any reference response spectrum. Even better, the selected seismic records should generate a great variety of peak displacement values, in order to really investigate the effect of the non-seismic offset on the probability of increase of d_m.

T_{sv} range	Pulse class	Event	PEER file	T_{sv} (s)	PI_k (-)	*l.u.f.* (Hz)	*S.F.* (-)	*PGA* (g)
$T_{sv} \leq 2$ s	no pulse	Chi-Chi, 1999	RSN3860_CHICHI.05_CHY008N	0.37	0.33	0.075	4.7	0.6
		Chi-Chi, 1999	RSN3858_CHICHI.05_CHY004N	0.34	0.38	0.075	10.4	0.6
	weakly pulse	Nahanni, 1985	RSN496_NAHANNI_S2330	0.52	0.56	0.125	1.9	0.6
		Chi-Chi, 1999	RSN3846_CHICHI.03_CHY008W	1.52	0.55	0.063	9.9	0.3
	pulse-like	Morgan Hill 1984	RSN451_MORGAN_CYC285	0.83	0.86	0.125	0.5	0.6
		Coyote Lake, 1979	RSN150_COYOTELK_G06230	1.47	0.84	0.075	1.4	0.6
$2 < T_{sv} \leq 3$ s	no pulse	Chi-Chi, 1999	RSN2938_CHICHI.05_CHY016N	2.34	0.29	0.075	10.7	0.5
		Chi-Chi, 1999	RSN3844_CHICHI.03_CHY004N	2.69	0.34	0.038	7.7	0.5
	weakly pulse	Cape Mendocino, 1992	RSN827_CAPEMEND_FOR000	2.56	0.51	0.070	2.6	0.3
		Chi-Chi, 1999	RSN3844_CHICHI.03_CHY004W	2.90	0.59	0.038	5.6	0.3
	pulse-like	Irpinia, 1980	RSN292_ITALY_A-STU270	2.82	0.82	0.125	0.8	0.3
		Imperial Valley, 1979	RSN171_IMPVALL.H_H-EMO270	2.94	0.85	0.100	1.0	0.3
$3 < T_{sv} \leq 4$ s	no pulse	Alaska, 2002	RSN2102_DENALI_NOAA-90	3.43	0.24	0.026	21.4	0.3
		Irpinia Eq, 1980	RSN297_ITALY_B-BIS270.	3.83	0.39	0.163	7.0	0.5
	weakly pulse	Cape Mendocino, 1992	RSN827_CAPEMEND_FOR090	3.08	0.46	0.070	2.7	0.3
		Chi-Chi, 1999	RSN2695_CHICHI.04_CHY016W	3.82	0.48	0.050	13.3	0.5
	pulse-like	Imperial Valley, 1979	RSN181_IMPVALL.H_H-E06230	3.40	0.89	0.063	0.6	0.25
		Imperial Valley, 1979	RSN182_IMPVALL.H_H-E07230	3.27	0.85	0.075	1.1	0.5
$T_{sv} > 4$ s	no pulse	Chi-Chi, 1999	RSN3851_CHICHI.04_CHY004W	5.07	0.36	0.100	14.0	0.3
		Landers, 1992	RSN834_LANDERS_ARC262	5.05	0.35	0.017	11.0	0.3
	weakly pulse	Alaska, 2002	RSN2115_DENALI_PS11-66	5.76	0.47	0.130	8.3	0.6
		Kocaeli, 1999	RSN1170_KOCAELI_MCD090	5.88	0.59	0.075	8.8	0.6
	pulse-like	Kocaeli, 1999	RSN1148_KOCAELI_ARE090	5.31	0.70	0.088	2.0	0.3
		Imperial Valley, 1979	RSN179_IMPVALL.H_H-E04230	4.08	0.76	0.063	0.8	0.3

Table 4.2. Selected single shake records

Estimation of the offset displacement: according to the design practice, one of the parameters under consideration for choosing the radius of curvature of the Curved Surface Slider is the maximum horizontal displacement expected, in order to limit the vertical displacement of the superstructure, proportional to d_m^2 /2 R. A survey of the portfolios of some leading European manufacturers shows that the displacement capacity is typically adjusted at 4% to 10% of the radius, and in any case no at more than 20% [27].

In the study, the non-seismic offset d_o was assumed as a fraction between 1% and 1.6% of R depending on the low velocity coefficient of friction of the CSS, as specified in Table 4.3, in order to account for the fact that high friction isolators are endowed with low restoring capability even in respect to non-seismic displacements.

μ_{LV} (-)	d_0 / R (%)
0.02	1.0
0.03	1.2
0.04	1.4
0.05	1.6

Table 4.3. Non-seismic offset displacements considered in the study

Nonlinear dynamic analyses were conducted for the 24 seismic ground motion time histories listed in Table 4.2. In order to account for potential direction effects, the offset was imposed in either direction of the longitudinal ground motion. For each examined combination of CSS mechanical parameters in accordance with Table 4.1, five Nonlinear Response Time History Analyses were conducted, considering four offset values (1.0 d_0 , +0.5 d_0, -0.5 d_0 , -1.0 d_0), and additionally the reference condition with no offset. A total number of 2400 analyses was performed.

4.1.2.4 Two shakes sequences

Natural ground motions sequences of two shakes were selected from the Pacific Earthquake Engineering Research Center (PEER). Because of the scarce number of eligible time histories in the database, minimum lowest usable frequencies (l.u.f.) of the record up to 0.25 Hz were accepted, although the frequency of vibration of CSS with curvature R_5 = 5 000 mm is 0.2 Hz. The records are listed in Table 4.4. The acceleration time histories were scaled to a Peak Ground Acceleration (*PGA*) level of 0.5 g for the main shake.

Approximately in a half of the selected sequences the shake with the largest *PGA* was the first one. Nevertheless the sequences were classified as either *"main shock – aftershock"* or *"foreshock – main shock"* type at the end of the nonlinear response analysis depending on whether the absolute peak displacement was produce by the first or the second shake.

A total number of 300 analyses were performed by considering the possible combinations of the CSS parameters in Table 4.1 and the seismic sequences in Table 4.4.

Sequence	Shake	Event	PEER file	T_{sv} (s)	PI_k (-)	*l.u.f.* (Hz)	*S.F.* (-)	*PGA* (g)
1	1	Chalfant Valley, 1986	RSN543_CHALFANT.B_B-BEN360	0.56	0.32	0.250	2.79	0.142
	2	Chalfant Valley, 1986	RSN548_CHALFANT.A_A-BEN360	0.97	0.46	0.125	2.79	0.500
2	1	Chalfant Valley, 1986	RSN543_CHALFANT.B_B-BEN270	0.48	0.20	0.250	2.39	0.141
	2	Chalfant Valley, 1986	RSN548_CHALFANT.A_A-BEN270	1.89	0.42	0.125	2.39	0.500
3	1	Chalfant Valley, 1986	RSN544_CHALFANT.B_B-LAD180	1.15	0.22	0.150	2.01	0.253
	2	Chalfant Valley, 1986	RSN549_CHALFANT.A_A-LAD180	0.78	0.51	0.125	2.01	0.500
4	1	Chalfant Valley, 1986	RSN544_CHALFANT.B_B-LAD270	1.47	0.32	0.150	2.84	0.278
	2	Chalfant Valley, 1986	RSN549_CHALFANT.A_A-LAD270	0.37	0.29	0.125	2.84	0.500
5	1	Chalfant Valley, 1986	RSN545_CHALFANT.B_B-BPL160	1.09	0.47	0.138	3.11	0.273
	2	Chalfant Valley, 1986	RSN550_CHALFANT.A_A-BPL160	1.79	0.69	0.125	3.11	0.500
6	1	Irpinia, 1980	RSN286_ITALY_A-BIS000	2.04	0.35	0.150	5.21	0.500
	2	Irpinia, 1980	RSN297_ITALY_B-BIS000	1.91	0.28	0.163	5.21	0.323
7	1	Irpinia, 1980	RSN286_ITALY_A-BIS270	1.02	0.22	0.150	6.02	0.500
	2	Irpinia, 1980	RSN297_ITALY_B-BIS270	1.70	0.28	0.163	6.02	0.428
8	1	Livermore, 1980	RSN214_LIVERMOR_A-KOD180	1.85	0.55	0.150	1.79	0.268
	2	Livermore, 1980	RSN223_LIVERMOR_B-KOD180	0.77	0.61	0.250	1.79	0.500
9	1	Livermore, 1980	RSN214_LIVERMOR_A-KOD270	0.77	0.30	0.150	6.10	0.390
	2	Livermore, 1980	RSN223_LIVERMOR_B-KOD270	0.78	0.36	0.250	6.10	0.500
10	1	Whittier Narrows, 1987	RSN594_WHITTIER.A_A-NHO180	0.38	0.43	0.100	3.73	0.500
	2	Whittier Narrows, 1987	RSN3686_WHITTIER.B_B-NHO180	0.75	0.33	0.150	3.73	0.235
11	1	Whittier Narrows, 1987	RSN594_WHITTIER.A_A-NHO270	0.96	0.33	0.100	7.81	0.500
	2	Whittier Narrows, 1987	RSN3686_WHITTIER.B_B-NHO270	0.93	0.32	0.150	7.81	0.320
12	1	Whittier Narrows, 1987	RSN692_WHITTIER.A_A-EJS048	0.57	0.83	0.100	1.07	0.500
	2	Whittier Narrows, 1987	RSN3735_WHITTIER.B_B-EJS048	0.20	0.55	0.250	1.07	0.369
13	1	Whittier Narrows, 1987	RSN692_WHITTIER.A_A-EJS318	0.53	0.73	0.100	1.09	0.500
	2	Whittier Narrows, 1987	RSN3735_WHITTIER.B_B-EJS318	0.21	0.57	0.250	1.09	0.343
14	1	Whittier Narrows, 1987	RSN705_WHITTIER.A_A-SOR225	0.37	0.29	0.220	3.57	0.500
	2	Whittier Narrows, 1987	RSN3743_WHITTIER.B_B-SOR225	0.70	0.40	0.125	3.57	0.271
15	1	Whittier Narrows, 1987	RSN705_WHITTIER.A_A-SOR315	0.37	0.39	0.220	2.94	0.500
	2	Whittier Narrows, 1987	RSN3743_WHITTIER.B_B-SOR315	0.89	0.36	0.125	2.94	0.156

Table 4.4. Selected two shakes sequences

4.1.2.5 Multiple shakes sequences

Four ground motion sequences comprising multiple shakes were selected from the PEER database to confirm the general conclusions of the two shake ground motion sequence analysis. Due to the scarcity of multiple shakes seismic sequences in the database, it was therefore necessary to include also records with lowest usable frequency (l.u.f.) greater than 0.2 Hz (Table 4.5). The acceleration time histories of each sequence were scaled of the same Scale Factor (S.F.) as to give a Peak Ground Acceleration (*PGA*) level of 0.5 g for the main shake.

A total number of 80 analyses were performed by considering the possible combinations of the CSS parameters in Table 4.1 and the multiple seismic sequences in Table 4.5.

Sequence	**Shake**	**Event**	**PEER file**	T_{sv} **(s)**	PI_k **(-)**	***l.u.f.* *(Hz)***	***S.F.* (-)**	**PGA (g)**
1	1	Chalfant Valley, 1986	RSN544_CHALFANT.B_B-LAD180	1.15	0.22	0.150	2.01	0.253
	2	Chalfant Valley, 1986	RSN549_CHALFANT.A_A-LAD180	0.78	0.51	0.125	2.01	0.500
	3	Chalfant Valley, 1986	RSN559_CHALFANT.B_C-LAD180	0.53	0.37	0.288	2.01	0.173
	4	Chalfant Valley, 1986	RSN562_CHALFANT.B_D-LAD180	0.45	0.28	0.163	2.01	0.378
2	1	Chalfant Valley, 1986	RSN544_CHALFANT.B_B-LAD270	1.47	0.32	0.150	2.84	0.278
	2	Chalfant Valley, 1986	RSN549_CHALFANT.A_A-LAD270	0.37	0.29	0.125	2.84	0.500
	3	Chalfant Valley, 1986	RSN559_CHALFANT.B_C-LAD270	0.22	0.38	0.288	2.84	0.310
	4	Chalfant Valley, 1986	RSN562_CHALFANT.B_D-LAD270	1.86	0.28	0.163	2.84	0.352
3	1	Chi-Chi, 1999	RSN1215_CHICHI_CHY058-E	2.12	0.35	0.04	10.33	0.500
	2	Chi-Chi, 1999	RSN2182_CHICHI.02_CHY058E	0.29	0.54	0.38	10.33	0.167
	3	Chi-Chi, 1999	RSN2480_CHICHI.03_CHY058E	2.53	0.53	0.05	10.33	0.266
	4	Chi-Chi, 1999	RSN2722_CHICHI.04_CHY058E	2.81	0.47	0.04	10.33	0.454
	5	Chi-Chi, 1999	RSN2962_CHICHI.05_CHY058E	0.56	0.56	0.08	10.33	0.498
	6	Chi-Chi, 1999	RSN3288_CHICHI.06_CHY058E	2.89	0.56	0.05	10.33	0.441
4	1	Mammoth Lakes, 1980	RSN230_MAMMOTH.I_I-CVK180	0.59	0.58	0.250	1.03	0.457
	2	Mammoth Lakes, 1980	RSN233_MAMMOTH.J_J-CVK180	0.34	0.59	0.500	1.03	0.188
	3	Mammoth Lakes, 1980	RSN236_MAMMOTH.AH_A-CVK180	0.52	0.50	0.088	1.03	0.192
	4	Mammoth Lakes, 1980	RSN240_MAMMOTH.AH_B-CVK180	0.31	0.62	0.250	1.03	0.500
	5	Mammoth Lakes, 1980	RSN244_MAMMOTH.K_K-CVK180	0.34	0.45	0.250	1.03	0.102
	6	Mammoth Lakes, 1980	RSN248_MAMMOTH.L_L-CVK180	0.54	0.57	0.150	1.03	0.325

Table 4.5. Selected multiple shakes sequences

4.1.3 Results

4.1.3.1 Single shake with initial non-seismic offset displacement

The response parameters considered for the analysis are defined in Fig. 4.4: $d_{m,o}$ and d_m are the maximum seismic displacements of the isolator either starting from the initial offset displacement d_o, or centred respectively, while $d_{r,o}$ and d_r denote the corresponding residual displacement. As already addressed, d_m is used in the design practice for determining the displacement capacity of the isolation units based on Eq. (4.1) or (4.4).

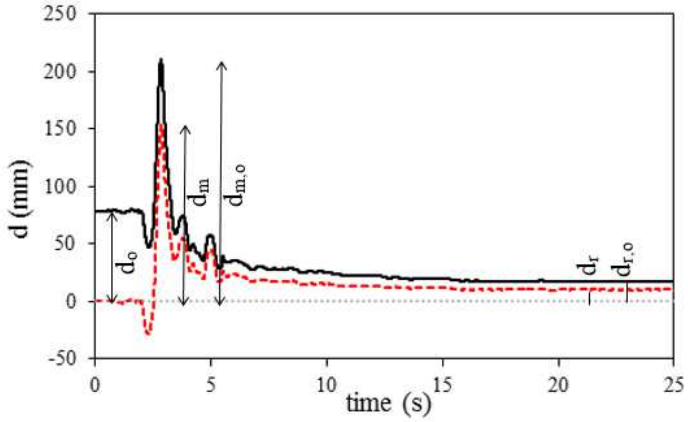

Figure 4.4. Time-histories displacement response of the CSS with initial offset (solid black line) and of the centred CSS (dotted red line)

It is worth noting that reference offset displacement d_0 as defined in Table 4.3 is dependent on the properties of the isolation unit through the radius of curvature and the coefficient of friction, but independent a priori from any assumed seismic input. This way d_o can represent the effect of both the residual displacement of previous ground shakings, and of movements produced by non-seismic actions, as well as of imprecise installation of the isolation bearings, or better a combination of the effects of two or more of the above. The results of the analyses are therefore not limited to any particular assumption on the origin of the offset displacement.

Fig. 4.5-left quantifies the effect of the offset on the maximum displacement, by presenting the change ratio $d_{m,o} / d_m$ as a function of the ratio d_m / d_{rm} between the seismic displacement of the centred isolator and the static residual displacement (see Eq. 4.2).

It is evident that the greater the offset, the higher its influence on the maximum displacement, resulting in either its amplification, $d_{m,o} / d_m > 1$, or a decrease, $d_{m,o} / d_m < 1$. A regression analysis has been performed to determine the curve enveloping the 90th percentile (Fig. 4.5-rigth):

(a) for $d_m / d_{rm} \leq 0.5$, $(d_{m,o} / d_m)_{90th\ percentile} > 1{,}5$ when the offset is $\pm 1.0\ d_o$, and $1.2 < (d_{m,o} / d_m)_{90th\ percentile} < 1.5$ when the offset is $\pm 0.5\ d_o$;

(b) for $0.5 < d_m / d_{rm} \leq 1.0$, $1.2 < (d_{m,o} / d_m)_{90th\ percentile} < 1.5$ when the offset is $\pm 1.0\ d_o$, and $1.1 < (d_{m,o} / d_m)_{90th\ percentile} < 1.2$ when the offset is $\pm 0.5\ d_o$;

(c) for $d_m / d_{rm} > 1.0$, $(d_{m,o} / d_m)_{90th\ percentile} < 1.1$ when the offset is either $\pm 1.0\ d_o$, or $\pm 0.5\ d_o$.

Eventually, when d_m / d_{rm} is greater than 2÷2.5 in the 90th percentile of the examined cases, the maximum seismic displacement does not show a substantial change respect to the design value of the system without offset ($d_{m,o}/d_m$ tends to unity), independently of the offset value and regardless the characteristics of the earthquake and the individual values of R and μ.
This result is in agreement with the conclusion that Curved Surface Sliders demonstrate good re-centring behavior when the ratio d_m / d_{rm} is larger than 2.5 [11], respect to the code prescription $d_m / d_{rm} \geq 0.5$.

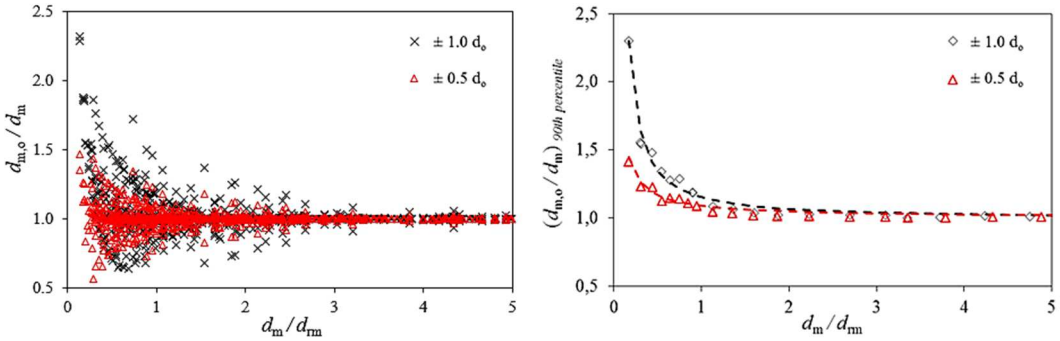

Figure 4.5. Results of analyses with initial non-seismic offset: values of the ratio $d_{m,o}/d_m$ as a function of the ratio d_m/d_{rm} (left) and relevant 90th percentile (right)

To preserve the structural integrity of the base-isolated structures during the seismic shaking the maximum displacement must not exceed the capacity of the isolators. It is therefore useful to compare the seismic displacement $d_{m,0}$ in presence of an offset displacement to the design maximum total displacement D defined in EC8 as the linear superposition of the non-seismic displacement and the seismic displacement of the centred device. In the study D is calculated according to Eq. (4.1) where $d_G = d_0$ is the non-seismic offset, d_m is the maximum displacement of the Nonlinear Response Time History Analysis with no offset, and $\gamma_{IS} = 1.2$ for buildings. It is evident from the plots in Fig. 4.6 that for $d_m / d_{rm} < 2.5$ the application of the formula of EC8 underestimates the displacement demand of the CSS when it is initially affected from an offset displacement on the order of 1% of the radius R.
Deeper information can be obtained by assessing separately the influence of the coefficient of friction (Fig. 4.6-a), the radius of curvature (Fig. 4.6-b), and the pulse character of the ground motion (Fig. 4.6-c). As predictable, devices with high friction (f4 and f5) and large radius (4 500 mm and 5 000 mm) are more sensitive to the offset because characterized by less re-centring capability, but the mechanical parameters of the CSS do not seem to have a

statistically significant influence on $d_{m,o}$ / D. On the contrary, the data show that the pulse character of the ground motion has a not negligible influence on the dependence of the seismic displacement from the initial offset, which is justified by the strong directionality of the ground motion; and an accrual of displacement higher than predicted by Eq. (4.1) is typically related to records with $PI_k > 0.7$. An important consequence is that, in case of base-isolated structures which are likely to be subjected to the occurrence of pulse-like earthquakes, e.g. structures located near active faults [28], the formula given in EC8 should be used with great care, because it could provide unreliable estimation of the displacement accrual for CSS systems with low re-centring capability (d_m / d_{rm} < 2.5 according to this study). The above results are valid under the assumptions of d_0 on the order of 1 to 1.65 of R and of γ_{IS} = 1.2, whereas for γ_{IS} = 1.5 the ratio $d_{m,o}$ / D is always less than unity.

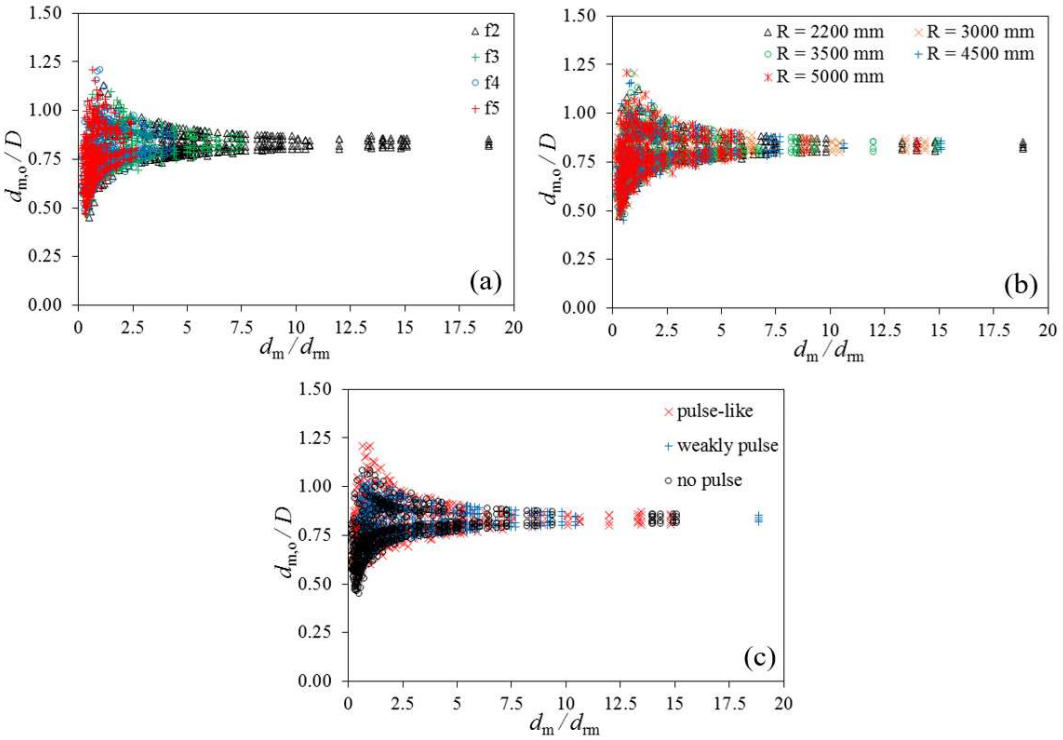

Figure 4.6. Maximum total displacement ($d_{m,0}$) compared to EC8 provision (D): dependence on the friction properties (a), on the radius of curvature (b), and on the pulse level of the quake (c)

A second concern, related to the minimization of damage of base-isolated structures, is the entity of the residual displacement after the earthquake. Fig. 4.7 compares the quantities $d_{r,o}$ and d_r, normalized to the radius of curvature R of the slider. Data points above the bisector of the quadrant correspond to an increase of residual displacement due to the initial offset. The influence of the offset on the residual displacement is evident for CSS isolators with

high friction and large radius. Also the pulse-like character of the earthquake seems to have a marked effect on the accrual or reduction of residual displacement.

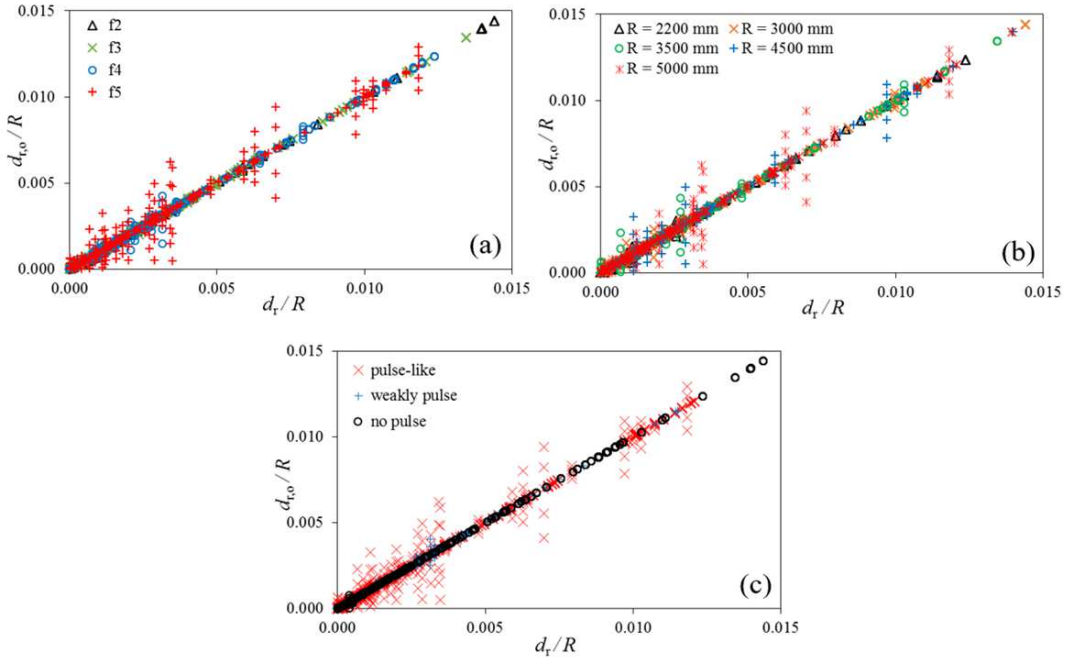

Figure 4.7. Influence of the CSS offset on the residual displacement: dependence on the friction properties (a), on the radius of curvature (b), and on the pulse-level of the quake (c)

In Fig. 4.8 the residual displacement $d_{r,o}$ of the offset system normalized respect to the design displacement d_m of the centred isolator is plotted as a function of the ratio d_m / d_{rm} . The curve enveloping the 90th percentile of the observed data is compared to the formula:

$$d_{r(90th)} = 0.18 \cdot d_m \left(\frac{d_m}{d_{rm}} \right)^{-0.57} \tag{4.8}$$

which was developed and proposed by Cardone *et al.* [11] for estimating at 90% probability the residual displacement of the CSS. A good agreement is visible between the two curves, and small differences can be appreciated only for $d_m / d_{rm} < 1$, whereas they disappear at all for $d_m / d_{rm} > 2.5$. This result points that for systems with good re-centring capability, it is possible to reliably predict the residual displacement based on the design displacement (d_m) estimated directly from the displacement spectrum or from a Time History Nonlinear Response analysis, notwithstanding a possible offset.

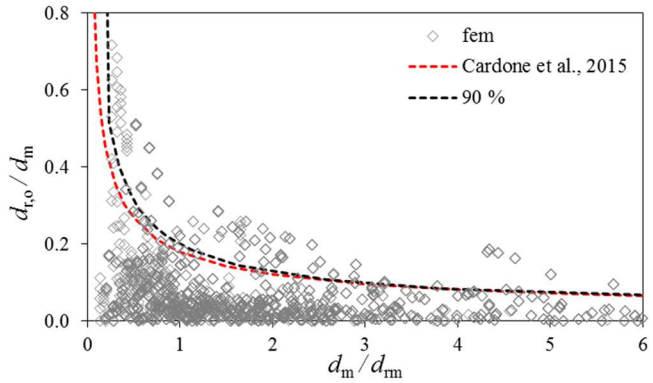

Figure 4.8. Influence of the initial offset on the residual displacement: comparison between the 90th percentile relevant to NRHA data and the prediction of Eq. 4.8 by Cardone *et al.* [11]

4.1.3.2 Two shakes sequences

In the study the ground motion sequences used for the analysis were classified as *"main shock - aftershock"* or *"foreshock - main shock"* sequences depending on whether the absolute maximum displacement was produced by the first or the second shake. In a *"main shock - aftershock"* sequence (Fig. 4.9-a), d_{ms} and $d_{r,ms}$ denote the maximum and the residual displacements produced by the main shock, and $d_{r,as}$ is the residual displacement at the end of the aftershock. In a *"foreshock - main shock"* sequence (Fig. 4.9-b), $d_{r,fs}$ is the residual displacement at the end of the foreshock; d_{ms} is the maximum displacement produced by the main shock and $d_{r,ms}$ is the residual displacement at the end of the main shock and of the sequence. The displacement history produced by the second shake applied to the centred isolator without the offset $d_{r,fs}$ is also calculated (red curve in the figure), and the relevant maximum value denoted as d_{se}.

The results of the analyses are illustrated in Figs. 4.10 to 4.12. Intuitively, the possible increase of the maximum displacement following the offset at the end of the first ground motion is of relevance only for *"foreshock – main shock"* ground motion sequences; on the other hand, the possible increase of the residual displacement at the end of the sequence is of relevance for both kinds of sequences.

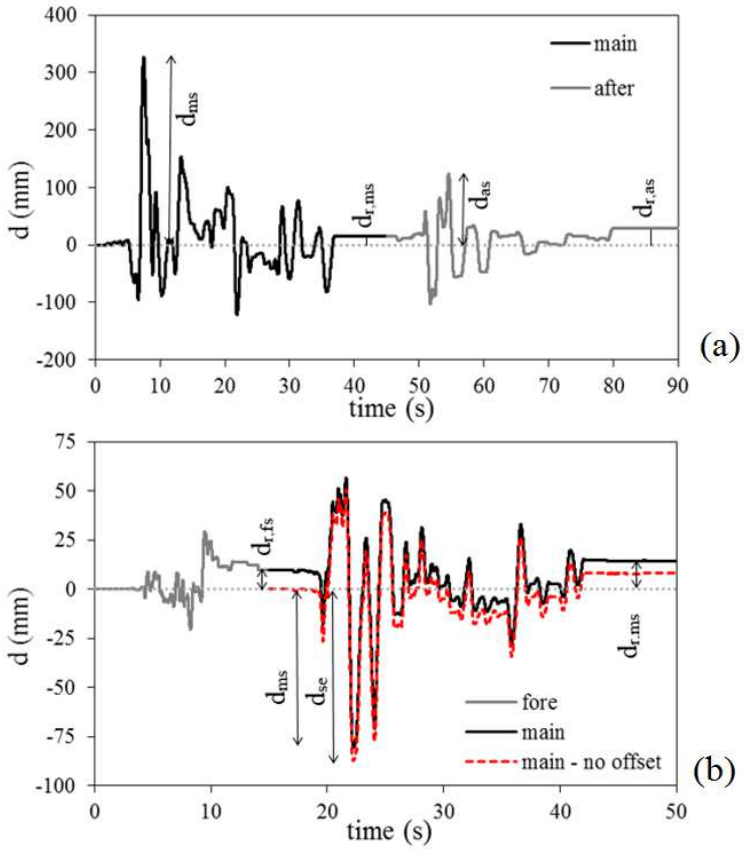

Figure 4.9. Response parameters of *"main shock - aftershock"* (a), and *"foreshock –main shock"* (b) seismic sequences

For *"foreshock – main shock"* seismic sequences, Fig. 4.10 compares the maximum displacement of the sequence with the displacement produced by the main shock's time history on a centred isolation system (d_{ms} / d_{se}) as a function of the ratio d_{se} / d_{rm} which conventionally evaluates the re-centring capability of the centred system. The increase owing to the residual displacement after the foreshock can be as high as the 10% when d_{se} / d_{rm} < 0.5, but it disappears at larger values of d_{se} / d_{rm}. A fair agreement is evident with the formulation of ρ_d given in EC 8 (Eq. 4.5) to reflect the possible accrual of displacement during a sequence of seismic events.

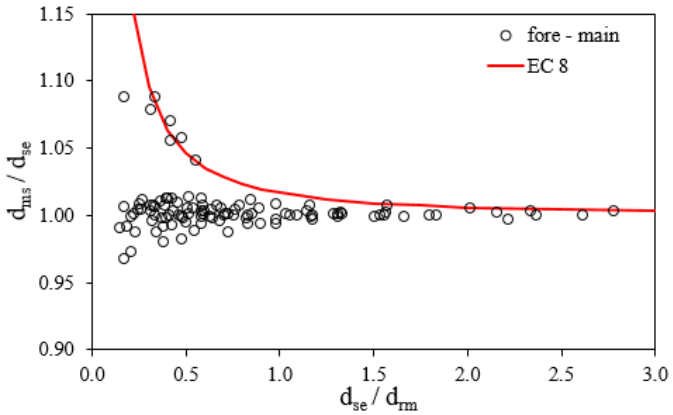

Figure 4.10. Maximum displacement during *"foreshock –main shock"* ground motion sequences respect to the displacement calculated in case of single event, and comparison with EC8 prediction (Eq. 4.5)

In Fig. 4.11 the maximum displacement of the second shake (either d_{ms} or d_{as} as relevant) is compared to the maximum displacement produced by the main event of the sequence on the centred system; all quantities are normalized to the radius of curvature *R* of the CSS. In the picture, data points located above the bisector of the quadrant correspond to an increase of the peak displacement.

In *"main shock - aftershock"* ground motion sequences (Fig. 4.11-left), the displacement demand is generally governed by the main shock, as expected. The seismic displacement of the aftershock ($d_{as} > d_{ms}$) is larger only for weak main shocks inducing small displacements ($d_{ms} < 0.025\ R$) and therefore corresponding to low re-centring capability.

In "*foreshock – main shock*" seismic sequences (Fig. 4.11-right), the displacement demand associated to the main ground motion of the sequence is practically unaffected by the occurrence of the foreshock and the consequent residual displacement.

In both types of ground motion sequences, the increase of displacement, if any, respect to the design value conventionally calculated for the the main event of the sequence on the centred isolation system, is small in comparison to the radius *R*; therefore it can be concluded that a possible displacement accrual has no any practical effect on the capacity of the isolation system because already covered by the reliability factor recommended by the code.

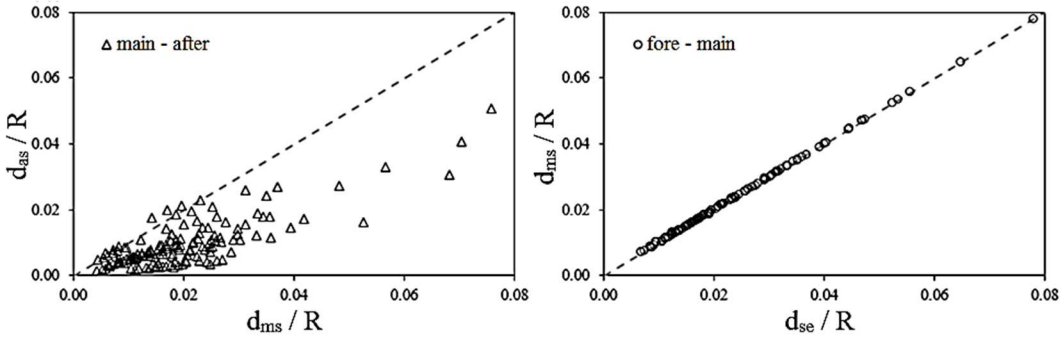

Figure 4.11. Variation of the maximum displacement relevant to the second shake of *"main shock - aftershock"* (left) and *"foreshock –main shock"* (right) ground motion sequences

The effect of the residual displacement at the end of the first shake of the ground motion sequence ($d_{r,ms}$ or $d_{r,fs}$) on the possible accrual of permanent displacement (here quantified as $d_{r,as}$ / d_{ms} or $d_{r,ms}$ / d_{se}) is presented in Fig. 4.12.

It can be noted that for both *"main shock - aftershock*" (Fig. 4.12-left) and *"foreshock – main shock"* ground motion sequences (Fig. 4.12-right) the residual displacement predicted according to Eq. (4.8) envelopes almost the totality of the data points. Despite the small number of natural ground motion sequences analysed, this result suggests that a reliable estimation of the residual displacement at the end of the ground motion sequence can be provided based on the design displacement (d_{ms} or d_{se}) of the centred system, which is in line with the conclusion of the analyses of single event with non-seismic offset illustrated in Fig. 4.6.

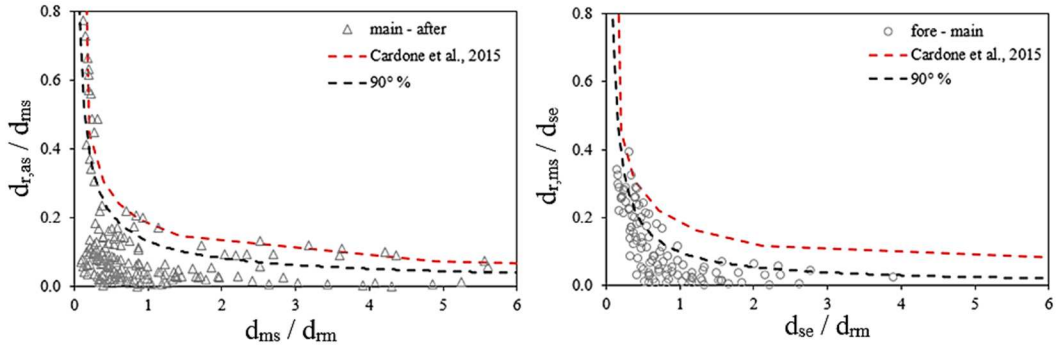

Figure 4.12. Comparison between the residual displacement predicted by Eq. 4.8 [11] and the 90th percentile of NRHA data: *"main shock – aftershock"* (left) and *"foreshock – main shock"* (right) ground motion sequences

4.1.3.3 Multiple shakes sequences

The considered ground motion sequences, composed by four or six consecutive records, were classified as "*f-m-a-a*", "*f-f-f-f-f-m*", or "*m-a-a-a-a-a*" based on the occurrence of the maximum displacement within the sequence, where *"f"* stands for foreshock, *"m"* for main shock, and *"a"* for aftershock (Fig. 4.13). Here d_{ms} denoted the maximum displacement, and $d_{r,f}$ is the residual displacement at the end of the sequence. For the "*f-m-a-a*", "*f-f-f-f-f-m*" sequences, the displacement history produced by the main shock's ground motion on the centred isolation system is also calculated (red curve in Fig. 4.13) and the relevant maximum displacement denoted as d_{se}.

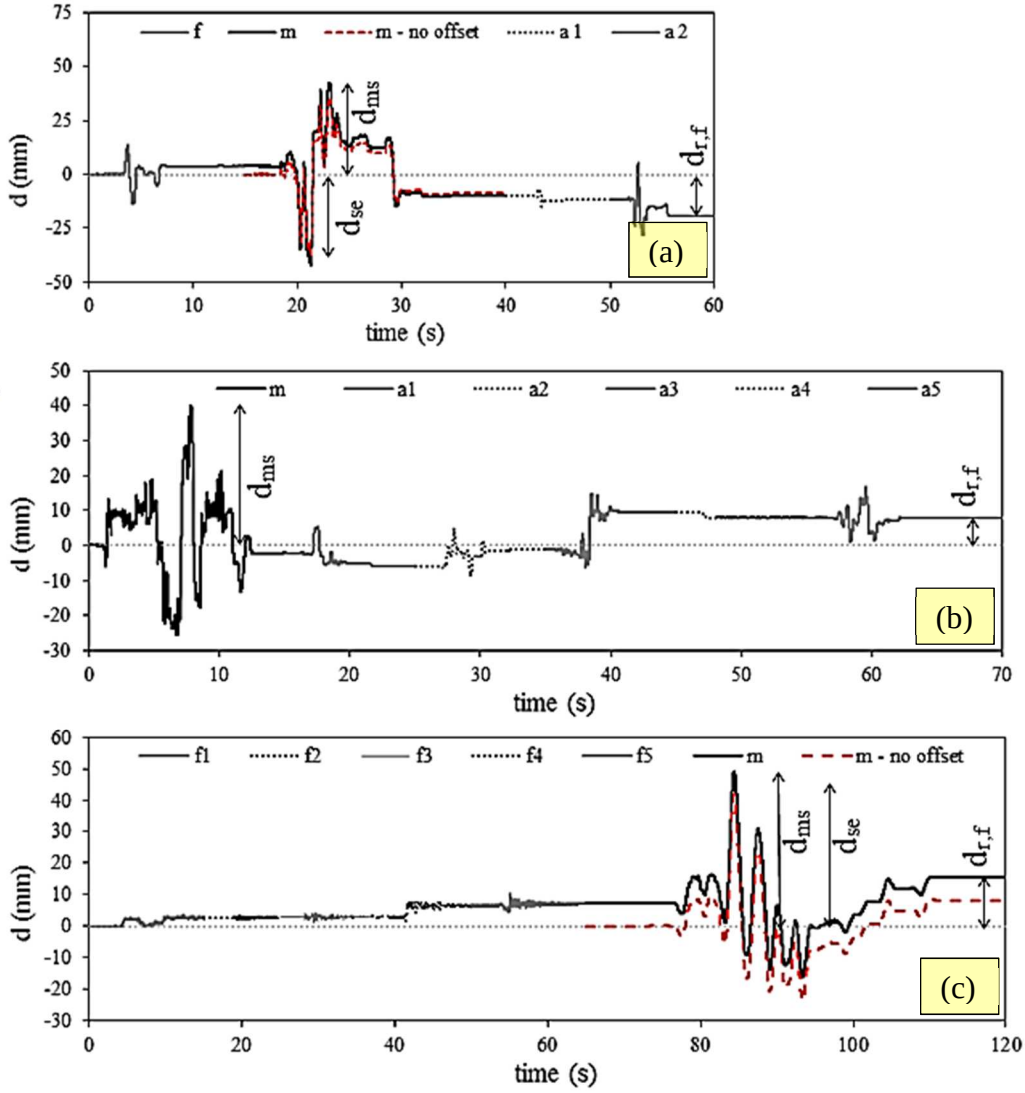

Figure 4.13. Multiple ground motion sequences: "*f-m-a-a*" (a); "*m-a-a-a-a-a*" (b); "*f-f-f-f-f-m*" (c) seismic sequences

The results of NRHA are consistent with the main conclusions drawn on the two shakes ground motion sequences. Fig. 4.14 compares, for "*f-m-a-a*" and "*f-f-f-f-f-m*" seismic sequences, the maximum displacement of the sequence with the displacement produced by the main shock's acceleration time history on the centred CSS (d_{ms} / d_{se}) as a function of the ratio d_{se} / d_{rm} . Most of the analyses are characterized by a reduction of the extreme displacement (d_{ms} / d_{se} < *1*), and only in few cases an increase occurred, but of no practical interest, i.e. less than 2%. No contradiction is observed respect to the formula given in EC 8 (Eq. 4.5).

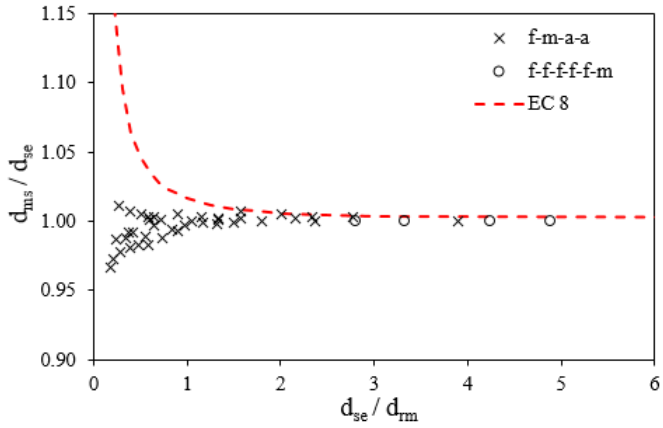

Figure 4.14. Maximum displacement of "*f-m-a-a*" and "*f-f-f-f-f-m*" ground motion sequences respect to the displacement calculated in case of single event, and comparison comparison with EC8 prediction (Eq. 4.5)

Eventually also for the multiple ground motion sequences analysed, the estimation of the residual displacement at the end of the sequence based on the maximum displacement of the main shock in accordance with Eq. (4.8) envelopes the data points (Fig. 4.15).

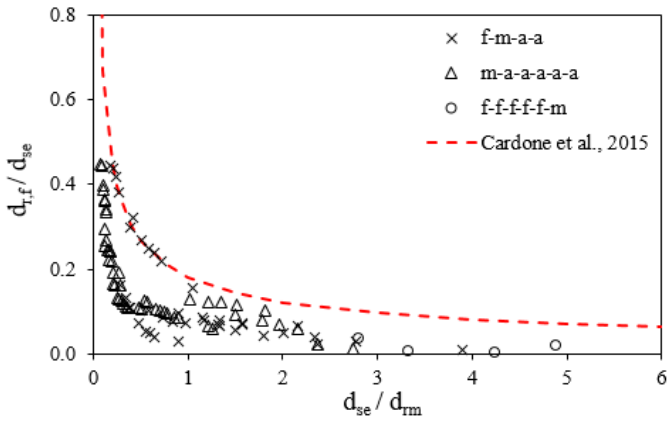

Figure 4.15. Comparison between the residual displacement predicted by Eq. 4.8 [11] and NRHA data for "*f-m-a-a*", "*f-f-f-f-f-m*", and "*m-a-a-a-a-a*" seismic sequences

4.1.4 Conclusions

The study focuses on the possible accrual of displacement of Curved Surface Sliders during ground motions, and aims at evaluating the prediction of the extreme displacements of the isolators based on the design seismic displacement calculated from the displacement spectrum or a Time History Nonlinear Response analysis disregarding any possible offset displacement of the isolation units. In particular, the prescriptions of the current Eurocode 8 [1, 2] for estimating the total displacement are checked against the data generated in Nonlinear Response Time History Analyses.

The main conclusions can be summarized in the next points:

(a) The study confirms that the restoring behavior of Curved Surface Sliders is governed by the parameter d_m / d_{rm} ; CSS demonstrate good re-centring capability and negligible displacement accrual when d_m / d_{rm} > 2.5 respect to the re-centring requirement d_m / d_{rm} > 0.5 prescribed by EC8 for generic bilinear hysteretic isolation systems;

(b) CSS with low re-centring capability can develop accrual of displacement, and an offset displacement may result in an increase of the maximum displacement respect to the design value; in case of base-isolated structures located near active faults, where the probability of occurrence of pulse-like ground motions is higher, the EC8 provision to estimate the total maximum displacement (Eq. 4.1) accounting for non-seismic offsets should be used very carefully as it could provide underconservative values;

(c) During natural ground motion sequences the possible increase, if any, of the maximum displacement respect to the design seismic displacement evaluated on the main shock of the sequence is likely to be small in comparison to the radius *R* of the slider, and has no any practical effect on the capacity of the isolation system because already covered by the reliability factor recommended by the code;

(d) For isolation systems with good re-centring capability, it is possible to reliably predict the residual displacement based on the design displacement (d_m) of the centred CSS estimated directly from the displacement spectrum or from a Time History Nonlinear Response analysis, notwithstanding a possible offset displacement.

Though limited in the number of natural ground motion records and in the level of non seismic offsets considered in the analyses, the study provides valuable information about the restoring behaviour and the possible displacement accrual of the Curved Surface Slider which primarily affects the design of the displacement capacity of the devices. In a future development the investigation will be extended to include a wider range of combinations of offset and earthquakes.

4.2 Estimating the frictional heating

4.2.1 Introduction

After the Curved Surface Slider (CSS) isolator was introduced at the end of the '80s, a number of friction materials like filled PolyTetraFluorEthylene (PTFE) and PTFE-based composite materials, Ultra High Molecular Weight PolyEthylene (UHMWPE) and other thermoplastics have been proposed [25, 29-33]. The friction material is demanded to provide sufficient load bearing capacity, to match a specific value of the coefficient of friction with small variations due to ageing and travel, and provide resistance to deterioration under high velocities and accumulated movements.

During the sliding motions induced by the earthquake, most of the seismic energy dissipated by friction forces at sliding surfaces is converted into heat, producing a temperature rise, usually of short duration and therefore called *"flash temperature"*. High flash temperatures that may occur in presence of large friction forces and high speeds accelerate the wear of the surface materials through the formation of oxides and surface layers, and producing melting of the pad material; further the heating of the pad causes a decrease of the coefficient of friction, therefore modifying the damping response of the isolation system [25, 34].

The modification of the response of sliding isolators due to frictional heating is indeed noted and regulated in the codes: according to the European standard EN 15129 (2009) [16], in three cycles of loading up to the design displacement the maximum lateral force and the energy dissipated per cycle *EDC* must deviate no more than 15% from their design values; ASCE/SEI 7-10 [35] establishes a maximum change of 20% over ten cycles of loading, while the AASHTO Specification (2014) [36] recommends a maximum variation of the effective stiffness and the *EDC* less than 20% and 30% respectively after twenty cycles of loading.

Several studies have addressed the issue in the last years. Constantinou [30] presented an analytical model to calculate the average temperature rise at the FPS surface and at small depths below. For a large FPS bearing designed to carry a gravity load of more than 75 MN in an offshore platform [37] subjected to biaxial motion at velocities up to 0.8 m/s, peak temperatures as high as 400°C were predicted. Drozdov [38] performed a finite element investigation of the steady-state temperature in a spherical bearing under different loading parameters, and underlined the importance of estimating the thermal state inside the friction pendulum system in order to choose suitable friction materials according to their temperature stability. Numerical evaluations of the thermal-mechanical behaviour of curved surface sliders accounting for the dependence of the coefficient of friction on the surface temperature, which was modelled through an exponential expression, were presented in two recent studies [34, 39], both of which concluded that a friction model that ignores the temperature rise may considerably overestimate the damping capacity, and therefore lead to underestimate the peak seismic displacement of the isolator. Only a few experiments have

been reported (e.g. [30, 40]) investigating the relationship between the coefficient of friction and the surface flash temperature in seismic isolators. The main limitation of the experiments is that it is virtually impossible to measure temperature at the sliding surface while the slider is in motion, and measurements performed using a thermocouple below the sliding surface were typically used to indirectly measure temperature rise at the surface through convolution, e.g. [40].

A procedure for the assessment of friction materials for CSSs accounting for their temperature-dependent characteristics has not yet been established. Several methods have been proposed to characterize the coefficient of friction of sliding materials under a range of pressure, velocity and temperature through small scale tests [24, 41], but the ability of such methods to reproduce the actual thermal state at the sliding surface of full scale isolators and provide a reliable estimate of the coefficient of friction during a seismic event is questionable. On the other side, tests at the real scale are expensive and time consuming, and therefore not indicated at the R&D stage for development and selection of new friction materials. To overcome the inherent limits of experimental investigation, theoretical and/or numerical models could be useful to assist the testing and achieve a general understanding of the frictional heating.

A finite element framework for conducting thermal-mechanical analyses of CSS isolators has been very recently presented by the Writer (2014) [34]. Its main characteristics are the use of a three dimensional geometry of the isolator, the implementation of recursive subroutines that adjust the coefficient of friction at the sliding surface upon the current velocity and temperature, and the use of the coupled thermal-mechanical formulation. The method allows to investigate the temperature profile within the isolator, and to account for the variation of the coefficient of friction under the maximum transient temperatures during sliding, and the relevant effect on the properties of the device. The aim of that work [34], described in this section of the thesis, is to demonstrate the usefulness of the numerical procedure as a tool for performing a preliminary evaluation of the isolation response under either the test conditions prescribed by the standards and arbitrary load histories, and providing fundamental information on the variables affecting the frictional heating developed in the CSS.

4.2.2 Finite element framework

A real case of CSS isolator designed for the seismic protection of a large structure is considered in the present study (Fig. 4.16). The sliding pad is made of a PTFE-based composite material with a nominal coefficient of friction $\mu = 0.12$ at ambient temperature and variation limits between 0.05 and 0.13 within the ranges of pressure and velocity considered in the study [25]. The rotation pad is made of a low-friction thermoplastic polymer lubricated with silicon grease. The sliding plate, the rotation plate and the slider are

made of structural steel. The concave surface of the sliding plate and the convex surface of the slider mating the pads are lined with a 2 mm thick stainless steel overlay

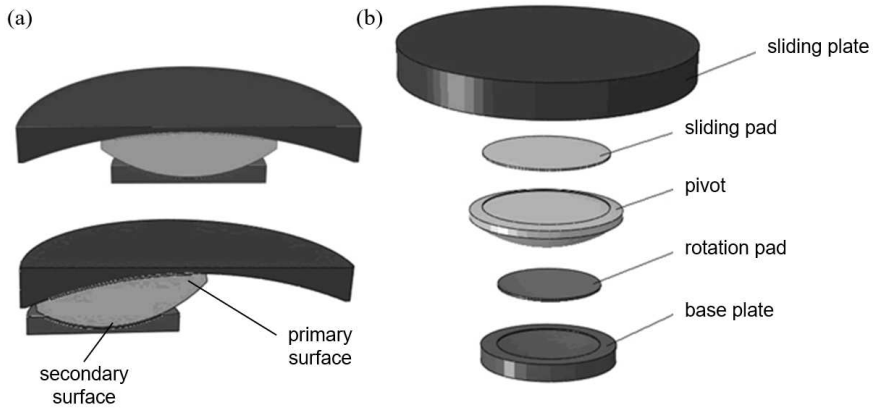

Figure 4.16. CSS isolator unit: kinematics (a) and main components (b)

The CSS unit is designed for a vertical load N_{sd} = 4500 kN and a seismic displacement d_{bd} = 340 mm. The diameter of the sliding pad is 560 mm. The radius of the primary surface is 1650 mm, the radius of the secondary surface is 530 mm and the height of the slider is 186 mm, resulting in an effective radius of the isolator R_e = 1994 mm and a vibration period T_b = 2.13 s.

A three-dimensional model of the CSS unit was created in the commercial code ABAQUS® v. 6.10 (Dassault Systèmes Simulia Corp., Providence, RI) and subdivided in a mesh of three dimensional finite elements [42]. Either linear thermal-mechanical coupled hexaedrical elements and wedge elements, type C3D8T and C3D6T respectively, with four degrees of freedom (the three displacement components along the orthogonal directions *X*, *Y* and *Z*, and the temperature) at each node, were used. Details of the mesh are reported in Table 4.6. Mechanical and thermal properties were assigned to the materials of the CSS in accordance with Table 4.7.

Part	**No. of elements (#)**		**No. of nodes**
	C3D8T	**C3D6T**	**(#)**
sliding plate	7636	2512	11026
sliding pad	5216	-	6815
slider	960	-	1396
rotation pad	3840	-	5045
base plate	340	-	585

Table 4.6. Details of the finite element mesh

Material	Elastic modulus (MPa)	conductivity (mW/(mm K))	specific heat (J/(kg K))
carbon steel	209 000	53.7	$4.9 \cdot 10^5$
stainless steel	196 000	16.0	$5.0 \cdot 10^5$
PTFE composite	800	0.65	$1.1 \cdot 10^6$
rotation pad	2800	0.25	$1.7 \cdot 10^6$

Table 4.7. Material properties

While the CSS is moving, a heat flux is generated due to friction at the primary and, at a less extent, at the secondary sliding surfaces. In the finite element model at each interface a surface heat source spread all over the contour area of the pad is located of instantaneous intensity:

$$q(t) = \mu(t) \cdot p(t) \cdot v(t) \tag{4.9}$$

where $\mu(t)$ is the coefficient of friction of the pad, $p(t)$ is the contact pressure, and $V(t)$ is the sliding velocity. In writing Eq. (4.9) it was assumed that the whole mechanical work carried out from external forces to sustain the motion of the CSS is converted into heat. The heat flux q generated at the contact surface is in turn partitioned into two fluxes, $q_1 = \lambda\, q$ pointing to the stainless steel surface, and $q_2 = (1 - \lambda)\, q$ pointing to the pad, where λ is the heat separation factor that depends on the thermal properties and geometry of the bodies in contact.

The coefficient of friction of the sliding pad was formulated as an explicit function of the surface velocity and temperature:

a) an isotropic velocity–dependent friction model was defined with a smooth transition zone from the low velocity to the high velocity regime regulated by an exponential function (adapted from [23]):

$$\mu(v) = \mu_{HV} - (\mu_{HV} - \mu_{LV}) \cdot e^{-\alpha_1 |v|} + (\mu_{ST} - \mu_{LV}) \cdot e^{-\alpha_2 |v|} \cdot \frac{|sign(v) - sign(d)|}{2} \tag{4.10}$$

where μ_{LV} is the kinetic coefficient of friction at low velocity, μ_{HV} is the kinetic coefficient of friction at high velocity, μ_{ST} is the static coefficient of friction that opposes the initiation of sliding when velocity is zero (e.g at breakaway and at motion reversals), α_1 is a parameter regulating the increase in kinetic friction with velocity, α_2 is a parameter regulating the transition from the static to the kinetic friction regime, v is the velocity variable and d is the displacement variable. The term $|sign(v) - sign(d)|$ is different from zero at the reversal of motion after a stop, like in cyclic displacement histories;

b) the coefficient of friction calculated by Eq. (4.10) was assumed to decay exponentially with increasing temperature:

$$\mu = \mu(v) \cdot e^{-\beta (T - T_0)} \tag{4.11}$$

where $\mu(v)$ is the friction coefficient at a reference temperature T_0, β represents the rate of decay of friction with temperature, and T is the temperature variable.

Mechanical and thermal boundary conditions of the problem were set as follows [34]:

1) the CSS unit is subjected to the application of a constant vertical load, uniformly distributed on the upper surface of the sliding plate;
2) a displacement history in the horizontal direction is imposed to the sliding plate, while the base plate is kept fixed to ground;
3) constraints are introduced to keep the upper surface of the sliding plate parallel to the ground surface of the base plate, but allowing the vertical movement of the sliding plate produced during its horizontal movement by the rotation at the spherical articulation;
4) an uniform temperature T_{ref} is set for every part of the CSS unit at the beginning of the analysis;
5) a heat separation factor $\lambda = 0.99$ is assumed at either sliding surface (i.e. the 99% of the heat flux points to the stainless steel surface); this assumption motivated by the poor thermal conductivity of thermoplastic materials in comparison to steel;
6) the temperature at the top and ground surfaces of the CSS unit is kept constant at T_{ref}, simulating the installation of the unit in a massive structure or test machine where the temperature rise is zero at some distance from the moving surfaces;
7) conductivity heat transmission is allowed at the primary surface;
8) the lateral walls of the CSS unit are adiabatic; this assumption is valid for short time intervals which allow to neglect energy losses by radiation and convection.

The heat transfer problem in the physical model is described by a system of partial differential equations of heat balance with thermal boundaries conditions in terms of either known temperatures or fluxes [43]. Using the finite element approach a numerical solution of the heat balance equation in terms of nodal fluxes and nodal temperatures is calculated by the computer code ABAQUS® [42].

4.2.3 Model validation

The numerical procedure was validated using experimental data. The experiment is reported in [34]: a CSS bearing with same geometry and materials as the one formulated in the FE model was subjected, under a compression load of 4500 kN, to a reversed cyclic displacement history with a period of 2.13 Hz and an amplitude of either 85 mm (Test1) or 170 mm (Test2). The peak velocity was 251 mm/s in Test1 and 502 mm/s in Test 2. Four complete cycles were performed in each test.

The ambient temperature of the laboratory at the beginning of the tests was 23°C. The hysteretic load–displacement curves of the specimen were recorded and used to calculate the effective stiffness and the energy dissipated at each cycle by the isolation unit. Five N-type thermocouples with probe diameter of 0.20 mm were embedded in the sliding plate of the CSS (Fig. 4.17), with their probes in contact with the back of the austenitic steel overlay, and the temperature was continuously recorded throughout the tests.

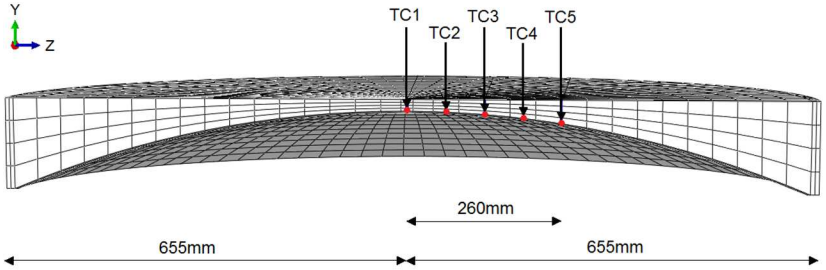

Figure 4.17. Position of the thermocouples (TC1 to TC5) embedded in the sliding plate of the CSS unit. The thermocouples, spaced 65 mm to each other, were aligned perpendicularly (along the Z axis) to the direction of motion of the specimen (along the X axis)

The experimental protocol was reproduced in the finite element analysis, by applying a vertical load of intensity N = 4500 kN to the sliding plate, and a combined unidirectional horizontal movement according to the sinusoidal waveform:

$$\begin{cases} d(t) = \frac{A}{2} \cdot [1 - \cos(2\omega \cdot t)] & for\ 0 \le t \le \frac{T_b}{4} \\ d(t) = A \cdot sen(\omega \cdot t) & for\ \frac{T_b}{4} < t \le nT_b \end{cases} \tag{4.12}$$

where A is the displacement amplitude, T_b is the period, t is the time variable, t_0 = 0 s is the initial time of the analysis, $\omega = 2\pi/T_b$ is the circular frequency , and n is the cycle number. The analysis was divided into two steps, the first corresponding to the movement of the CSS unit from its undeformed configuration (d = 0 mm) at time zero to the maximum displacement A at time $T_b/4$, and the second corresponding to the remaining part of the test. A different waveform was assumed for either steps in order to replicate the actual history of loading performed in the experiments. The thermal and mechanical conditions at the beginning of the second step corresponded to the ones calculated at the end of the first step. Since at the start of motion from the configuration d = 0 mm the term $|sign(v) - sign(d)|$ accounting for the static coefficient of friction was equal to zero, in the first step of the analysis Eq. (4.10) was replaced by the formula:

$$\mu(v) = \mu_{HV} - (\mu_{HV} - \mu_{LV}) \cdot e^{-\alpha_1|v|} + (\mu_{ST} - \mu_{LV}) \cdot e^{-\alpha_2|v|} \tag{4.13}$$

The set of parameters of the friction model assumed for the pad of the primary surface is reported in Table 4.8. The parameters of the velocity–dependent function $\mu(v)$, Eq. (4.10), were calibrated on the experimental force–displacement curve of the CSS unit recorded at the first cycle of Test2, while the temperature decay parameter β of Eq. (4.11) was determined in friction tests performed on small scale samples of the pad material at temperatures between 20°C and 100°C [41]. At the secondary surface a constant value of the coefficient of friction of 0.005 was taken, neglecting the temperature rise due to the small entity of the heat flux.

parameter	value	unit
μ_{LV}	0.050	-
μ_{HV}	0.130	-
μ_{ST}	0.165	-
α_1	0.015	$(mm/s)^{-1}$
α_2	0.020	$(mm/s)^{-1}$
β	0.005	$°C^{-1}$

Table 4.8. Parameters of velocity and temperature–dependent friction model

The thermal boundary conditions set for the analysis are the heat flux distribution at the sliding surfaces and the temperature at the external top and ground surfaces of the CSS unit. At each sliding surface it is assumed that the totality of energy dissipated by friction is converted into heat in accordance with Eq. (4.9), and that 99% of the instantaneous heat flux is directed to the stainless steel surface (λ = 0.99). The numerical integration of the heat balance equation provides the temperature distribution within the bearing. The size of the time increment is self-adjusted by the software between 0.0001 seconds and 0.5 seconds in order to keep the temperature change at the sliding surface less than 5°C per increment. At each calculation step a sub-routine adjusts the coefficient of friction of the primary surface on the nodal surface velocity and temperature according to Eq. (4.10) and (4.11); and feeds it into Eq. (4.9) to update the instantaneous heat flux q. The software calculates also the contact stresses and relative velocities at the surface, which are used to update the heat flux equation (4.9), and the global reaction force of the isolator.

The embedded thermocouples measured the temperature on the back of the stainless steel overlay. Fig. 4.18 illustrates the histories recorded by the thermocouples located at the centre of the bearing (TC1) and at 260 mm from the centre (TC5), perpendicularly to the direction of sliding, where the maximum values were recorded. A continuous increase in temperature occurred with the increasing travel of the isolator, and after 8.5 seconds a thermal steady-state was not yet attained. The temperature histories predicted in the numerical analyses reported are in good agreement with the experimental data, especially at TC5 location (Fig. 4.18).

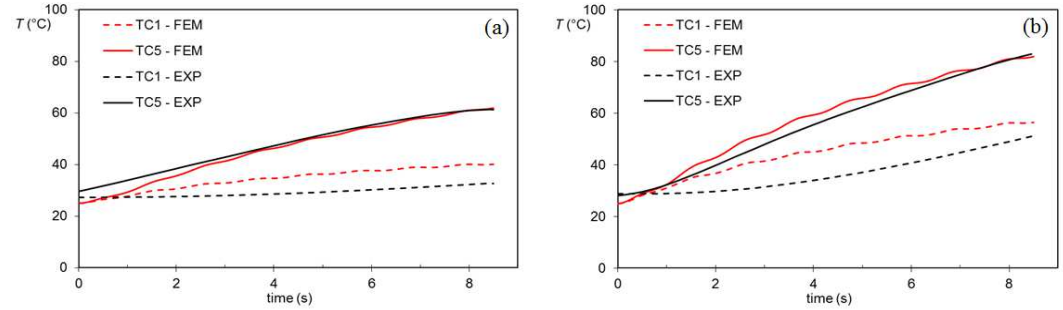

Figure 4.18. Peak temperature on the back of the stainless steel overlay during cycles at displacement amplitude A = 85 mm (a) and A = 170 mm (b): comparison between finite element analyses (FEM) and thermocouple measurement (EXP)

Fig. 4.19 compares the hysteretic force–displacement loops calculated by the finite element model with the experimental curves. The agreement is fair, with just some small discrepancy in the last branch of the cycle (from d = -170 mm to d = 0 mm). The effective stiffness and the Energy Dissipated per Cycle of the CSS specimen present a continuous decrease over time due to the temperature effect on the coefficient of friction (Fig. 4.20). The changes of both properties are matched by the numerical analyses, with a maximum deviation of about 3% for the stiffness and 4% for the *EDC* in Test 2, and of 4.4% for the stiffness and about 7% for the *EDC* in Test 1.

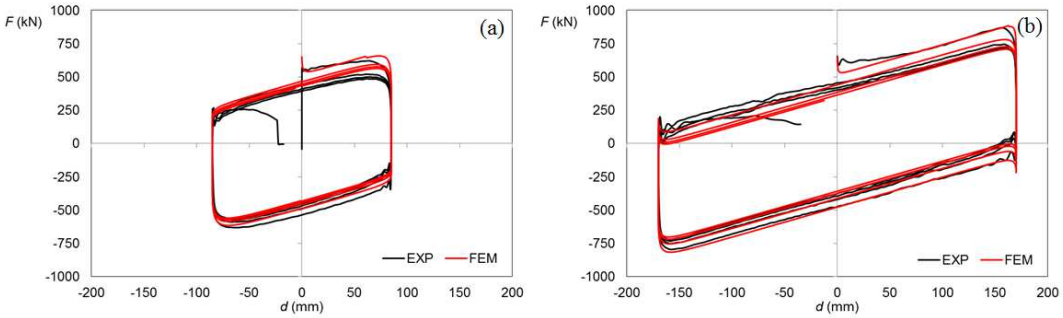

Figure 4.19. Hysteretic load – displacement curves during cycles at displacement amplitude A = 85 mm (a) and A = 170 mm (b): comparison between finite element analyses (FEM) and experimental data (EXP)

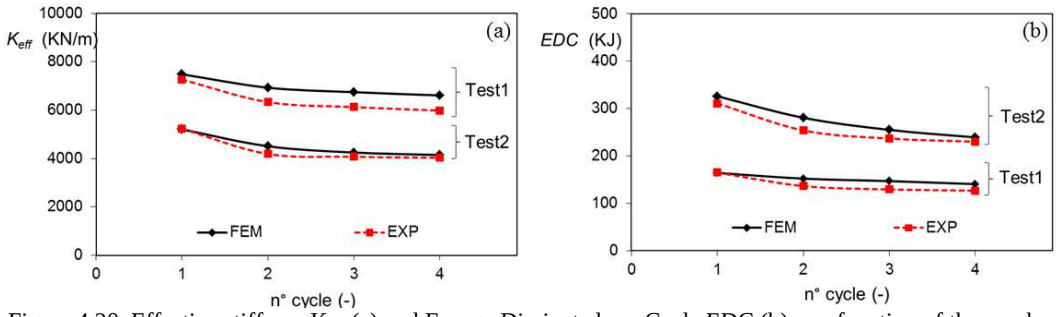

Figure 4.20. Effective stiffness K_{eff} (a) and Energy Dissipated per Cycle EDC (b) as a function of the number of cycles: comparison between experimental values (EXP) and model predictions (FEM)

4.2.4 Seismic performance analysis

The modification of the response of sliding isolators due to frictional heating is regulated in current standards. Analyses were conducted with the finite element formulation replicating the tests conditions of EN 15129 and AASHTO 2014 codes. The validated model of the CSS unit, described in section 4.2.2, was used in the study case.

EN 15129 test conditions and requirements for the seismic performance of sliding isolators are defined in section 8.3 of the standard. During 3 cycles of movement at 0.25, 0.5 and 1.0 times the design displacement d_{bd}, at the natural period of the isolator, the effective stiffness K_{eff} and the Energy Dissipated per Cycle in each of the three cycles shall deviate no more than 15% from their design values. Tests parameters for the study case are listed in Table 4.9.

Test	**Vertical Load (kN)**	**Amplitude (mm)**	**Period (s)**	**Cycles (#)**
D1	4500	85	2.13	3
D2	4500	170	2.13	3
D3	4500	340	2.13	3

Table 4.9. Test parameters according to EN 15129

The AASHTO 2014 code recommends that during 20 cycles of loading at the design displacement d_{bd} the variations of the effective stiffness and the *EDC* must be less than 20% and 30% respectively with respect to the peak values at the first cycle. Tests parameters for the study case are listed in Table 4.10.

Test	**Vertical Load (kN)**	**Amplitude (mm)**	**Period (s)**	**Cycles (#)**
D4	4500	340	2.13	20

Table 4.10. Test parameters according to AASHTO 2014 code

In each analysis the global response of the isolator, represented by the load – displacement curve, and pressure and temperature distributions at the primary sliding surface were computed.

4.2.4.1 *Tests according to EN 15129*

Fig. 4.21 illustrates the load - displacement curves of the CSS unit in numerical tests D1, D2 and D3 and the plots of the average surface temperature of the sliding pad. The resisting force becomes smaller and the surface temperature increases with increasing the number of cycles, and both effects are more evident at higher velocities.

From the hysteretic loops the effective stiffness and the Energy Dissipated per Cycle were calculated (Fig. 4.22). Though both K_{eff} and *EDC* have a continuous decay, the variation from the relevant design value over 3 cycles is lower than 15% (in Fig. 7 the ranges of acceptability are shown as bound by the dotted lines) and the standard requirement is fulfilled.

Fig. 4.23 illustrates the temperature distribution on the sliding pad surface during Tests D1, D2 and D3 (for each cycle, the values calculated in correspondence of position $d = 0$ mm are reported). The temperature increases over the cycles due to frictional heating. The temperature pattern is not uniform, with higher values towards the perimeter and lower values at the centre of the pad. Peak values as high as 106°C in Test D1, 169°C in Test D2 and 221°C in Test D3 respectively, were determined close to the surface edge in two symmetric regions aligned perpendicularly to the direction of sliding. The contact pressure p on the surface of the sliding pad (Fig. 4.24) presents a similar pattern: pressure increases from the centre of the pad towards the perimeter, where larger values are produced due to the effect of the curvature of the sliding surface and the load eccentricity. At the maximum displacement, peak values as high as 60 MPa were produced.

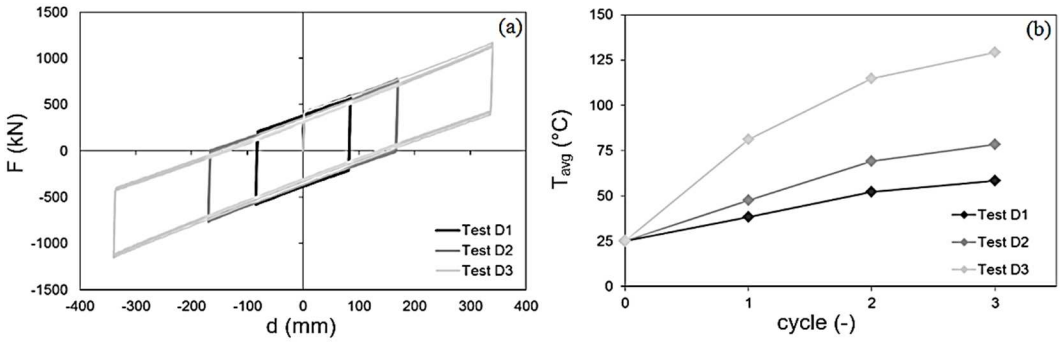

Figure 4.21. Load – displacement diagrams (a), and average temperature histories at the surface of the sliding pad (b) of the CSS unit during tests D1, D2, and D3

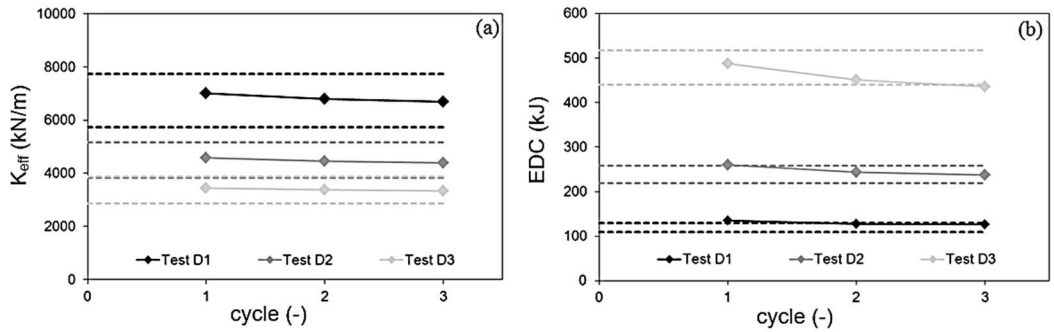

Figure 4.22. Change of Effective Stiffness (K_{eff}) (a), and Energy Dissipated per Cycle (*EDC*) (b) during cycles at different speeds with related range of acceptability (dotted lines) according to EN 15129

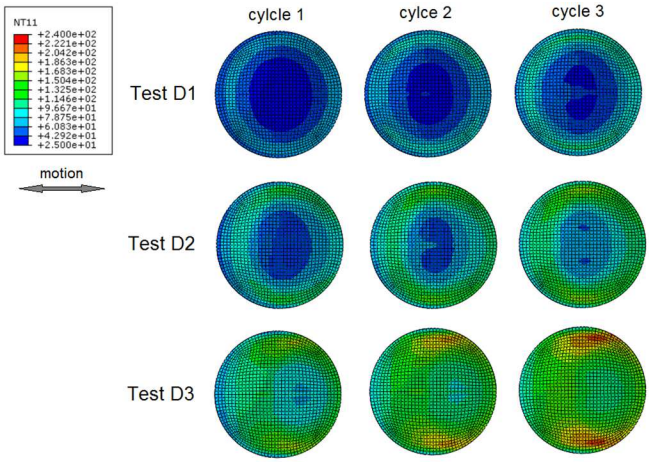

Figure 4.23. Temperature distribution on the surface of the sliding pad during Tests D1, D2 and D3 (values in °C)

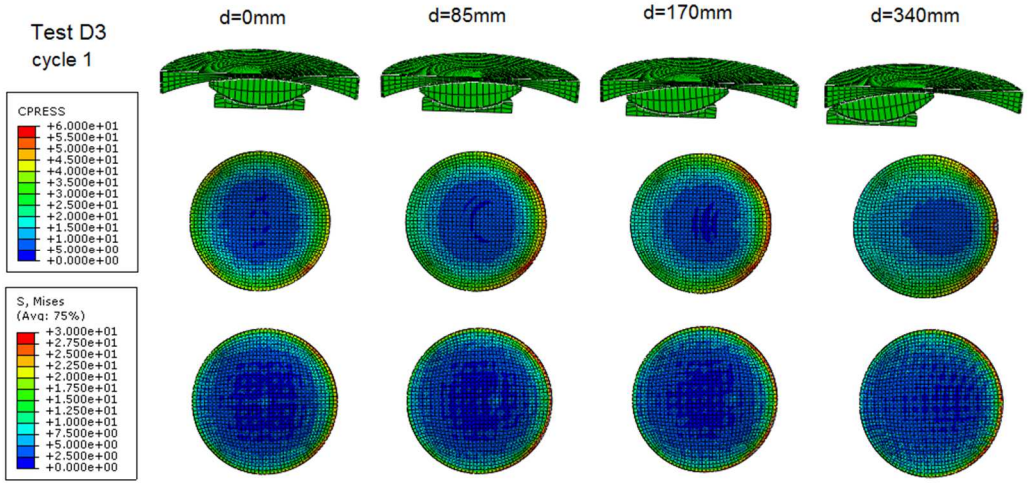

Figure 4.24. Contact pressure (CPRESS) and Von Mises (S. Mises) stress distribution on the surface of the sliding pad during the first cycle of Test D3 (values in MPa)

4.2.4.2 *Tests according to AASHTO*

Fig. 4.25 illustrates the time histories of the average and maximum temperature on the surface of the sliding pad calculated in numerical Test D4. After a fast increase in the first cycles, the rate of temperature increase reduces, and the average surface temperature seems to approach an asymptotic value after 15 cycles. It must be noted that the peak temperature is more than 1.5 times greater than the average one, e.g. 320°C vs 195°C at the twentieth cycle: relying on the calculation of the average surface temperature rise as made in analytical procedures [30] can lead to important underestimation of the actual peak temperature, and of the potential damage of the pad.

Though the huge increase in temperature has an important effect on the response of the isolator (Fig. 4.26), for the CSS unit analysed in the case study the code requirement on the maximum allowable change in stiffness an damping properties are fulfilled.

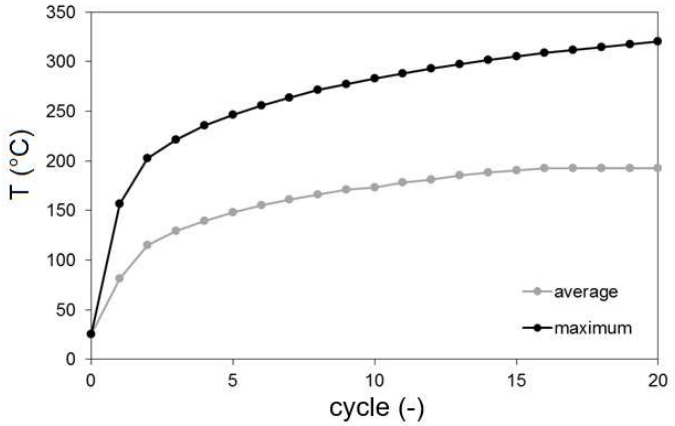

Figure 4.25. Average and maximum temperature histories on the surface of the sliding pad during Test D4

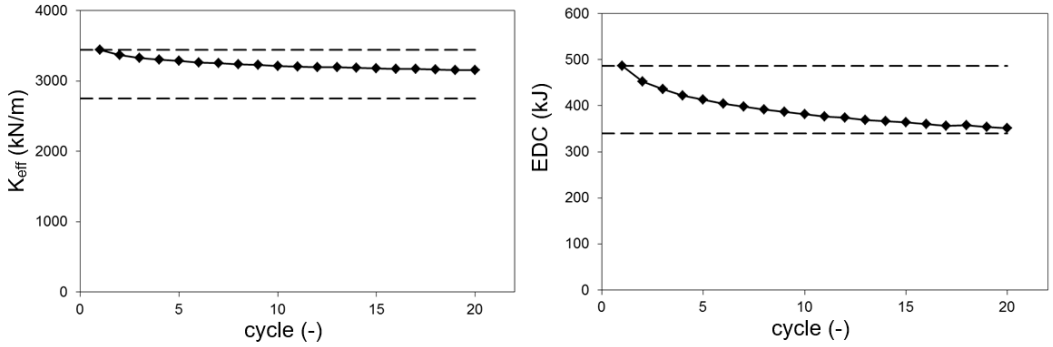

Figure 4.26. Change of the effective stiffness (left) and energy dissipated per cycle (right) during repeated cycles in test D4, and range of acceptability (dotted lines) according to AASHTO 2014

The temperature rise may affect also the strength of the thermoplastic material of the pad, which softens as the temperature approaches its melting point. Fig. 4.27 presents the temperature envelopes through the thickness of the sliding pad calculated at three points, selected in accordance with the temperature distribution shown in Fig. 4.23. The peak surface temperature occurs close to the pad edge, at two symmetric areas aligned perpendicularly to the direction of sliding (point A), where large contact pressure occurs. In the central region of the pad (point B), where the contact pressure is lower, the local temperature is below the average surface temperature. The sliding pad is usually mechanically recessed into the steel slider for approximately half of its thickness (this is 3.5 mm for the CSS unit considered in the present case study) to increase the load bearing capacity and restrain the lateral flow of the material. The large temperature growth occurring in the first three cycles is restricted to a thin layer of material, approximately 1 mm thick,

and the heat developed at the sliding surface takes an (unrealistic) number of cycles to substantially affect the temperature of at the core of the pad. Therefore, a few of cycles even at high seismic velocities is likely not to represent an issue for the mechanical strength of the pad.

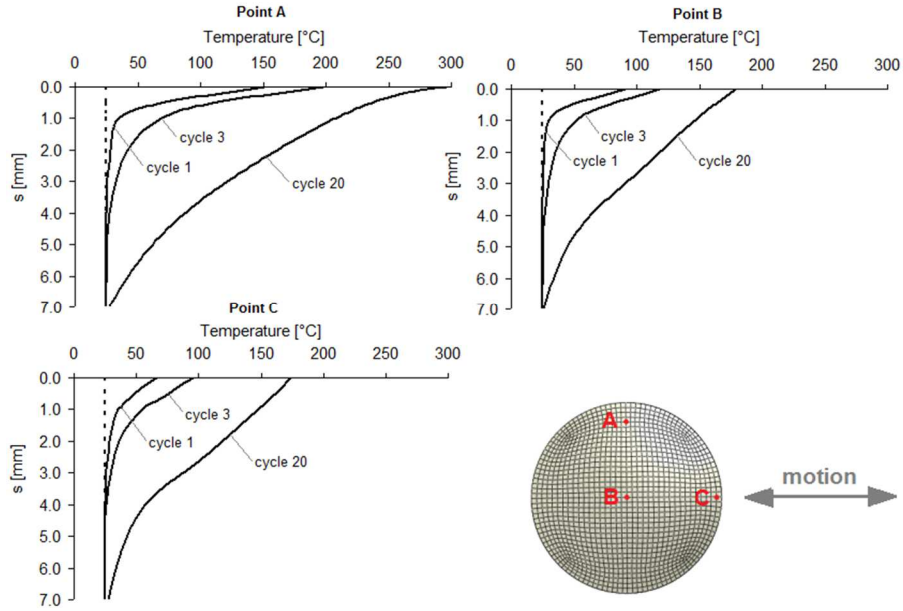

Figure 4.27. Temperature profiles though the thickness of the sliding pad during 20 cycles of motion (Test D4) in correspondence of points marked as A, B, C

4.2.5 Bi-directional motion analysis

The temperature at a point on the pad surface depends on the path of the slider as it is affected by prior heating of the mating stainless steel surface and its decay with time, and on the instantaneous heat flux, which is a function of the temperature at the surface. Response-history analyses on the CSS model (see section 4.2.2) were performed to investigate the influence of the loading path on the thermal – mechanical of the sliding isolation system.
In the numerical procedure, the CSS model was subjected to the application of several unidirectional and multidirectional displacement histories, formulated according to the following expression:

$$\begin{cases} d_x(t) = A_x \cdot \cos(n_x \omega t) \\ d_y(t) = A_y \cdot \cos(n_y \omega t) \end{cases} \tag{4.14}$$

where X and Y denote two horizontal directions, $d_x(t)$ and $d_y(t)$ are the current displacements of bearing in the X (Y) direction, A_x and A_y are the displacement amplitudes in either direction, n_x and n_y are two numerical parameters, t is the time variable, $\omega = 2\pi/T_b$ is the circular frequency, and T_b = 2.13 s is the period.

Analyses were carried out reproducing different displacement orbits in accordance with the parameters established in Table 4.11. The CSS was subjected to a vertical load N = 4500 kN and four complete cycles were simulated in each analysis, for a duration of the motion of 8.52 seconds.

Test	A_x **(mm)**	A_y **(mm)**	n_x **(-)**	n_y **(-)**
Uni-directional	170	0	-	1
Offset	170	0	0	85
Circular	170	170	1	1
Elliptical	170	85	1	1
8-Shaped	170	170	1	2

Table 4.11. Displacement orbit parameters

4.2.5.1 Results

The loading path affects the temperature growth at the sliding surface in two ways. First, the heat flux is proportional to the average sliding speed of the orbit. Second, as the heat source coincides with the pad surface, at any position of the mating stainless steel surface (through which heat flows away from the pad) the heat flux history is periodic and intermittent; orbit paths characterized by longer times between intermittent heating at the same position of the mating surface e allow larger cooling and limit the temperature increase.

The temperature histories reported in Fig. 4.28 point to the importance of the two contributions for the considered loading paths. The average speed of the Circular orbit is greater than the speed of either the Elliptical or the Uni-directional orbit (501.2 mm/s respect to either 386.6 mm/s or 319.2 mm/s), but the temperature rises associated to the orbits are quite similar due to the longer period of intermittent heating of the first path. On the contrary, the 8-Shaped orbit presents the highest sliding speed (752.6 mm/s), and produces the highest temperature rise due to the large importance of the relevant velocity contribution to the heat flux.

In the analyses undertaken in the study the amplitude of the motion in the X direction (170 mm) was smaller than the radius of the pad (280 mm). In most of the practical situations the amplitude of motion is in general larger than the radius of the pad, hence allowing longer time for intermittent heating of the mating steel surface especially in case of multi-directional orbits. This suggests that the results of the analyses presented in this paper cannot be generalized and that an accurate assessment should be done case by case.

Finally, it must be noted the large gap between the average and the peak local temperatures predicted on the pad surface after 8.5 seconds of displacement-controlled movement. A similar finding was already presented and discussed among the results of the numerical Test D4.

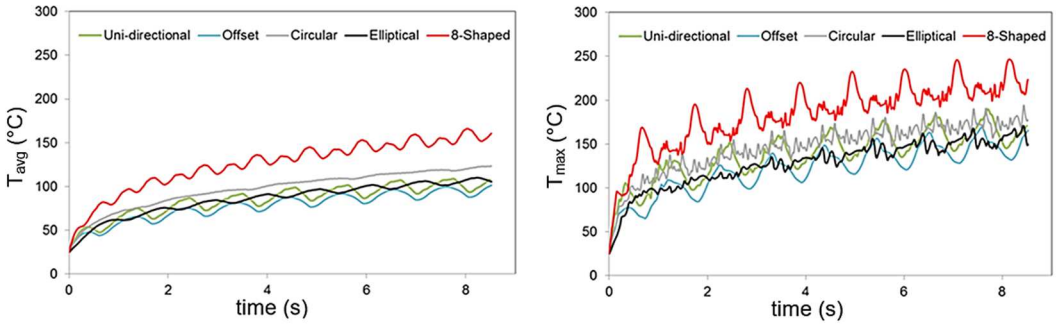

Figure 4.28. Temperature histories on the pad surface for different orbits: average surface temperature (left) and maximum local temperature (rigth)

Fig. 4.29 illustrates the Energy Dissipated per Cycle of the CSS unit for the different loading paths. Both the magnitude of the *EDC* and its variation over repeated cycles are greatly affected by the displacement trajectory, and the decay is important in presence of large temperature rises, e.g. a decrease of 18% is predicted over 8.52 seconds for the 8-Shaped orbit. A practical implication of this result is that the information provided from unidirectional laboratory tests on sliding isolation bearings should be considered carefully when estimating the actual variation of the coefficient of friction in the bearings under earthquake shaking, characterized by a chaotic bidirectional orbit rather than an unidirectional path.

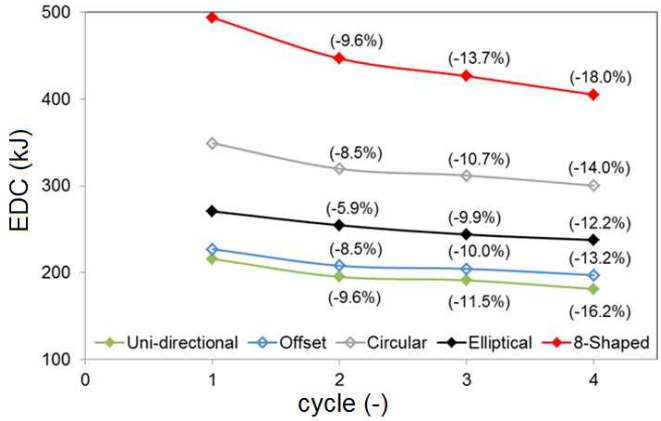

Figure 4.29. Decay of Energy Dissipated per Cycle with repeating cycling for different orbits. Between brackets: relative decrease with respect to the value at the first cycle

4.2.6 Conclusions

A numerical procedure for the assessment of the thermal-mechanical behavior of Curved Surface Sliders was developed by the Writer [34] and has been presented in this section of the thesis.

The basic features of the formulation are (i) the use of a three dimensional model of the isolation unit, and (ii) the implementation of a mathematical expression relating the coefficient of friction to local surface variables like velocity and temperature.

The formulation can be used as a design tool to perform a preliminary evaluation of the seismic hardware reproducing the test conditions prescribed by the standards, providing valuable information for the assessment and selection of friction materials accounting for their temperature-dependent characteristics.

In addition the procedure can support laboratory testing of real scale isolators, e.g. for prediction of the temperature rise history at the sliding surface of the isolator which cannot be directly measured in the experiment. Finally, from the comparison of unidirectional respect to bidirectional displacement history analyses the importance of the loading protocol for a correct assessment of the response of sliding isolators under real earthquake attacks may be argued.

4.3 Estimating the breakaway effect

4.3.1 Introduction

It is well known that the response of the Curved Surface Slider (CSS) devices is governed by the coefficient of friction developed during sliding, and the detailed knowledge and modelling of the friction characteristics of the materials of the sliding surface is fundamental for a correct prediction of the isolation system under an earthquake attack.

Experimental investigations have pointed out the inner complexity of the mechanism of friction especially regarding the dependence on velocity. A sharp distinction exists between the *"dynamic"* or *"kinetic"* coefficient of friction that develops during sustained sliding, and which intensity changes with regularity with speed, and the *"static"* coefficient of friction that opposes to the motion between mating surfaces at zero relative velocity; such static friction develops either at the very first initiation of motion, or breakaway, or at motion reversals, when the instantaneous velocity is null. Usually the transition from the static to the kinetic coefficient of friction is very sharp, and depending on the material, the value at the breakaway can be from 1.5 to more than 4 times higher than the dynamic value [25, 44-50].

The static coefficient of friction is a macroscopic effect of the breaking of the chemical bonds between the mating surfaces. As a consequence of the fact that the number and strength of such bonds increases with the duration of the sticking, the value at the breakaway is generally much larger than at motion reversal. Some experimental works indeed demonstrated that the breakaway friction coefficient for PTFE – stainless steel interfaces disappears after just one cycle of loading [47, 51].

Suitable mathematical formulations have been developed, mainly based on a phenomenological or semi-phenomenological approach, to describe the frictional behavior of the most common sliding materials used in sliding bearings and seismic isolators accounting for pressure, velocity, temperature and wear [39, 52-54].

In current software for structural analysis the hysteretic behavior of the CSS is described by means of either a bidirectional plasticity model [55], where the plastic deformation corresponds to sliding at the surface and the elastic deformation to the deformation of the friction material, or to generalization of the Bouc-Wen smoothed plasticity model [56], whose parameters satisfy an evolutionary differential equation. The bidirectional plasticity model is used in OpenSees® [57], whereas the generalized Bouc-Wen model has been implemented in SAP 2000® [58] and 3-D BASIS® [59-60].

The dependency of the coefficient of friction on velocity is generally implemented by means of the law [53]:

$$\mu = \mu_{HV} - (\mu_{HV} - \mu_{LV}) \cdot exp(-\alpha V) \tag{4.15}$$

where μ_{LV} is the coefficient of friction at low velocity, μ_{HV} is the coefficient of friction at high velocity, and α is a parameter of the exponential function that governs the smooth transition from the low velocity to the high velocity regime [34, 39, 61].
Accounting for this exponential law, the software replicates the friction behavior of the CCS under either slow or high speed loading, but is not capable to reproduce the static friction, due to inherent high nonlinearity associated (Fig. 4.30).
This represents indeed a severe limitation to the reliability of the numerical analysis of base-isolated structures with sliding systems during an earthquake.

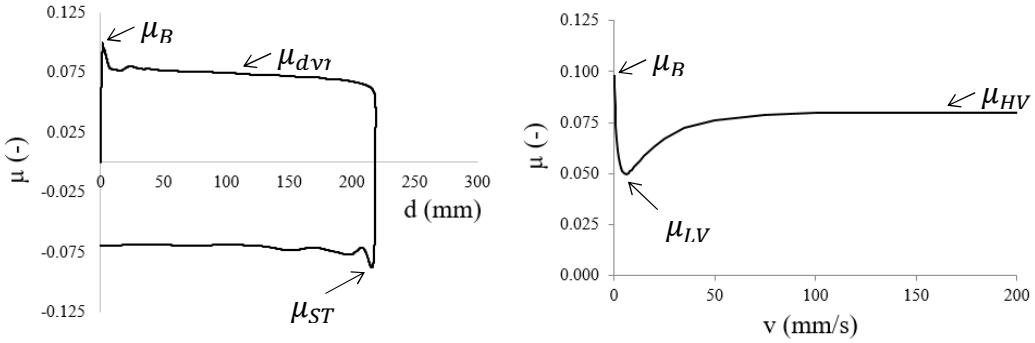

Figure 4.30. Typical layout of friction loops (left) and dependence of the friction coefficient on the sliding velocity (right)

The acceleration threshold over which the ground motion activates the device and sliding along the curved surfaces initiates, is called the *"critical acceleration"* a_{cr}; basically this acceleration produces inertia forces that exceed the friction forces associated to the breakaway friction coefficient (Fig. 4.31).
The critical acceleration, assuming a basic SDOF model (only isolator displacements, superstructure supposed infinitely rigid), can be approximated as:

$$a_{cr} = \mu_B \cdot g \tag{4.16}$$

while for MDOF models (isolators and superstructure displacements) a_{cr} can be calculated with the following formula [27]:

$$a_{cr} = \frac{(N_{BS}+N_{SS})\cdot\mu_B}{M_{BS}+\beta\cdot M_{SS}} \tag{4.17}$$

where μ_B is the static friction coefficient at the motion breakaway (Fig. 4.30), N_{BS} and N_{SS} are respectively the weights (related masses M_{BS} and M_{SS}) of the base slab at the isolation level and of the supported superstructure, $\beta = S_a(T_1)/PGA$ is the ratio between the spectral acceleration $S_a(T_1)$ and the peak ground acceleration PGA (being T_1 the fundamental period of the superstructure in the fixed-base configuration).

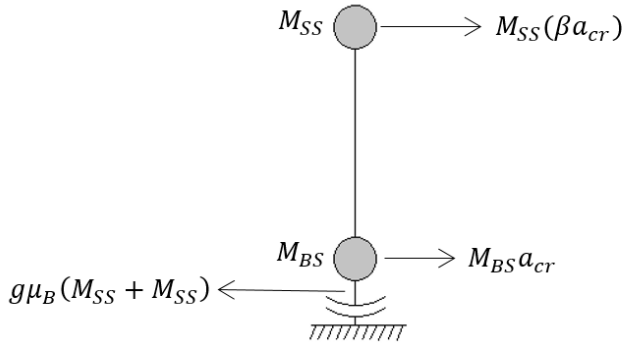

Figure 4.31. Horizontal forces dynamic equilibrium before sliding activation according to Eq. (4.17)

It is worth noting that according to Eq. (4.17) the critical acceleration depends on the structure caracteristics (mass distribution between base slab and superstructure, fundamental period of the superstructure), isolators friction coefficient (μ_B), and the details of the ground motion (β).

Since Eq. (4.15) does not account for the breakaway friction coefficient μ_B, an analysis based on such friction model necessarily assumes that at the motion start the coefficient of friction is μ_{LV}, leading to underestimate the critical acceleration required for the isolator's activation, with substantian deviations in the prediction of the structural response in case the breakaway coefficient of friction is large respect to μ_{LV}. In fact, until the critical acceleration is overcome, the isolators are stuck and the base-isolated structure behaves like a conventional fixed-base structure, and the ground acceleration is fully transmitted to the superstructure.

For a correct assessment of the internal forces and displacements of the superstructure is therefore essential to take into account the actual static friction at breakaway. This is of particular importance in case of buildings endowed with a high technology content that is particular sensitive to accelerations (e.g. medical equipment of hospitals), as well as in case of strategic building for which is fundamental to guarantee the full operativity after a major earthquake for the management of the emergency, preventing the crisis of non structural elements sensitive to accelerations, overturning, or large drifts that can possible hinder access or cause interruption of practicability.

However it is acknowledged that the nonlinearity associated to the transition from the static to the velocity dependent kinetic coefficient of friction represents a big challenge for implementation into numerical procedures, that to date has not yet been completely solved. To the knowledge of the Writer, the static coefficient of friction has been considered only in a few numerical studies, by adapting Eq. (4.15). Quaglini *et al.* (2014) added a further exponential contribution describing a smooth transition from μ_B to μ_{LV}, though with a very high rate, and implemented the final equation into the general purpose software Abaqus [34]. Fagà *et al.* (2015) replaced the parameter μ_{LV} with the static coefficient of friction μ_{ST} evaluated at motion reversal (Fig. 4.30) and performed a parametric study of a multi-storey

building isolated with CSS, concluding that, in case of substantial difference between μ_{LV} and μ_{ST}, ignoring the static friction seems to have a small effect on the maximum displacement, but leads to a not negligible underestimation of the internal forces in the structure [62].
Nevertheless the latter study does not account for the static coefficient of friction at breakaway that is generally larger than at motion reversal.
The influence of the breakaway coefficient of friction on the structural response therefore requires further investigation in order to evaluate whether or not its presence can be neglected.
The aim of the study developed in this section of the thesis is to investigate the importance of the coefficient of friction at breakaway on the structural response in terms of either the global response (maximum base displacement and maximum base shear) and the demand at each story (floor acceleration, inter-story drift). Nonlinear Response Time History Analyses (NRHA) are conducted on a simple case study consisting of a five-storeys building, and reproducing the frictional resistance of the isolators at the breakaway by means of mechanical fuses at the base isolation level. Three different friction behaviors, characterized by ratio of μ_B to μ_{LV} of 0, 2.5 and 5 respectively, are accounted for by adjusting the strength of the fuse element. The results of the analysis confirmed the expected effect of the breakaway friction on all the relevant response parameters of a base isolated structure. Further consideration based on the friction profile of the used sliding materials are drawn.

4.3.2 Materials and Methods

4.3.2.1 Structural model

A regular reinforced concrete moment-resisting-frame building is considered. The structure has five storeys at 3 m, and 2 bays of 5 m length in both longitudinal and lateral direction (Fig. 4.32). Rigid diaphragms simulate the in-plane stiffness of the floor slabs.
Rectangular (300 x 500 mm^2) floor beams are supported by a total of nine square (400 x 400 mm^2) columns. Identical single CSS isolators with an effective radius of curvature of the sliding surface R = 3000 mm are located underneath each column. The total seismic weight of each floor including the base slab, is 1000 kN, resulting in a cumulative weight of the whole building of N_{TOT} = *5000 kN*, and to a vertical load acting on each column of 555 kN. The fundamental period of the superstructure is T_1 = *0.324 sec*, and its equivalent viscous damping is assumed to be 5% of critical damping in all modes.
The structural model is implemented in OpenSees® v.2.5.4 software (Open System for Earthquake Engineering Simulation) [22]. In the analyses, the structure is subjected to unidirectional ground motion time histories acting along one longitudinal axis.

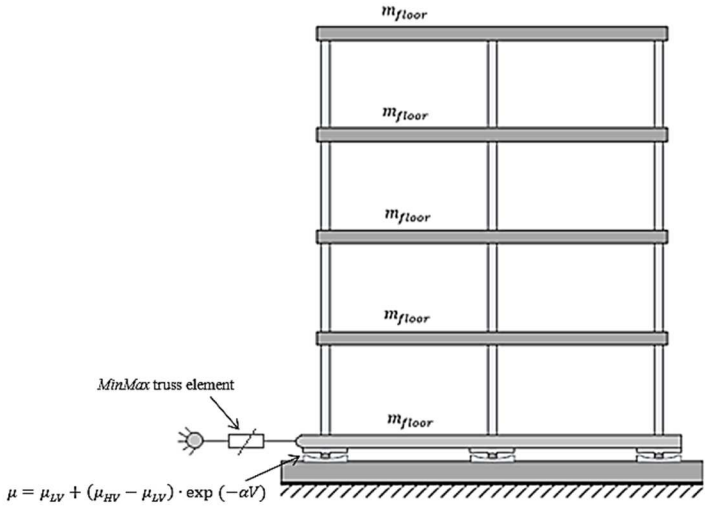

Figure 4.32. Adopted structural model

4.3.2.2 Isolators properties

The isolators are described by means of the *"SingleFPSimple3d"* element available in OpenSees library, where the *"VelDependent"* friction model corresponding to Eq. (4.15) is considered [63].

The detailed model of the isolator allows a complete description of the dynamic behavior, automatically accounting for restoring forces due to sliding on the concave surface, variation of normal load as a consequence of overturning moments, and uplift phenomena.

Rigid contact with friction is used at the sliding interfaces of the isolator. Since the *"VelDependent"* friction model does not account for the breakaway friction coefficient, the effect of a breakaway force below which sliding is prevented is reproduced in the model by introducing a one-directional *"Truss"* element (Fig. 2) aligned to the direction of ground motion shaking and parallel to the *"SingleFPSimple3d"* element, both elements subjected to the dynamic load applied to the structure. The stress-strain behavior of the Truss element in the longitudinal direction is described through the *"MinMax"* material object, i.e. as a linear elastic material with given stiffness. When the strain falls below or above a given threshold value, the material is assumed to have failed, and from that point on, values of 0.0 are returned for the stiffness and axial forces.

For constant values of axial law and coefficient of friction (i.e. at a fixed velocity), the force – displacement characteristic of the curved surface slider in one horizontal direction can be represented by the bilinear relationship illustrated Fig. 4.33 as it is implemented in the *"SingleFPSimple3d"* finite element. The relationship is characterized by the characteristic strength F_0 (the product of the coefficient of friction μ and the axial load N), the post-yield stiffness K_2 (the ratio of the axial load N to the radius of curvature of the bearing), and the

initial stiffness K_1 (which is related to the deformation in shear of the sliding material). The yield displacement d_y is related to the above parameters though the relation:

$$d_y = \frac{F_0}{K_1 - K_2} = \frac{\mu \cdot N}{K_1 - K_2} \tag{4.18}$$

For $0 < d < d_y$ the friction force F_y prevents sliding at the interface: the bearing undergoes pure elastic deformation of the sliding material; at $d = d_y$ the horizontal force equals the frictional resistance and sliding initiates at the interface. According to the assumed bilinear relationship, the equivalent coefficient of friction at breakaway is given by the ratio of the yield force F_y to the axial load:

$$\mu_{B,eq} = \frac{F_y}{N} = F_0 + K_2 \cdot d_y = \left(\mu + \frac{d_y}{R}\right) \tag{4.19}$$

In practice the coefficient of sliding friction depends on the instantaneous values of sliding velocity V. Accounting for the exponential relationship of Eq. (4.15) and observing that in real conditions sliding initiates at low velocity, the value of coefficient of friction to be considered in Eqs. (4.18) and (4.19) is the low-velocity value μ_{LV}. As d_y is usually on the order of 1 mm, whereas the typical radius of curvature of curved surface sliders ranges from 2200 to 6000 mm, from Eq. (4) then $\mu_{B,eq} \cong \mu_{LV}$ follows, which is contradicted by the experimental evidence [48, 51].

In the structural model of Fig. 3, breakaway friction forces before the starting of sliding are introduced by means of the truss finite element with *"MinMax"* material behavior (Fig. 4.34) acting in parallel to the *"SingleFPSimple3d"* element. By setting $d_f = d_y$, the behavior illustrated in Fig. 4.35 then results.

For $0 < d < d_y$ the model response is linear elastic with initial stiffness $K_{1e} = K_1 + K_f$:

$$F = \left(K_1 + K_f\right) \cdot d \tag{4.20}$$

At the first occurrence of $d = d_y$ (at $F = F_B$) the *"MinMax"* material is assumed to fail, and for $d > d_y$ on out the typical post-yielding response of the bilinear model is obtained:

$$F = K_1 \cdot d + K_2 \cdot (d - d_y) \tag{4.21}$$

The *"MinMax"* model is then adjusted in order to provide, at $d = d_y$, a horizontal resisting force of the parallel model in the horizontal direction equal to the frictional resistance force associated to the assumed breakaway coefficient of friction of the sliding material:

$$F_B = \left(K_1 + K_f\right) \cdot d_y = \mu_B \cdot N \tag{4.22}$$

$$K_f = \frac{\mu_B \cdot N}{d_y} - K_1 = \frac{\mu_B}{\mu_{LV}}(K_1 - K_2) - K_1 \tag{4.23}$$

The isolation units had a post-yield stiffness K_2 = 185 kN/m and an initial stiffness K_1 = 18500 kN/m (K_1 = 100 K_2).

In order to cover a range of possible friction profiles of curved surface sliders available on the market, different properties were implemented in the analyses.

The kinetic friction was modelled in accordance with Eq. (4.15) and three materials with different friction characteristic were considered : a low friction material with $\mu_{LV} = 0.01$ and $\mu_{HV} = 0.025$, a medium friction material with $\mu_{LV} = 0.03$ and $\mu_{HV} = 0.075$, and a high friction material with $\mu_{LV} = 0.05$ and $\mu_{HV} = 0.125$; the value $\alpha = 0.0055$ s/mm was assumed for all of them [11]. The low friction material resembles the behavior of lubricated thermoplastic, the medium friction material represents the bahaviour of PTFE , UHMWPE, and the high friction material represents filled plastics.

Further, for each material three different breakaway friction characteristics were modelled by adjusting the stiffness of the fuse element according to Eq. (4.23): (a) No Breakaway ($\mu_B = 0$), (b) Low Breakaway ratio ($\mu_B / \mu_{LV} = 2.5$), and (c) High Breakaway ratio ($\mu_B / \mu_{LV} = 5$). The different combinations of friction parameters considered in the study are summarized in Tab. 4.12.

kinetic friction profile			**breakaway friction ratio**		
			no breakaway	**low breakaway**	**high breakaway**
	μ_{LV}	μ_{HV}	μ_B	μ_B	μ_B
friction 1	0.01	0.025	0	0.025	0.05
friction 3	0.03	0.075	0	0.075	0.15
friction 5	0.05	0.125	0	0.125	0.25

Table 4.12. Parameters of the friction mode

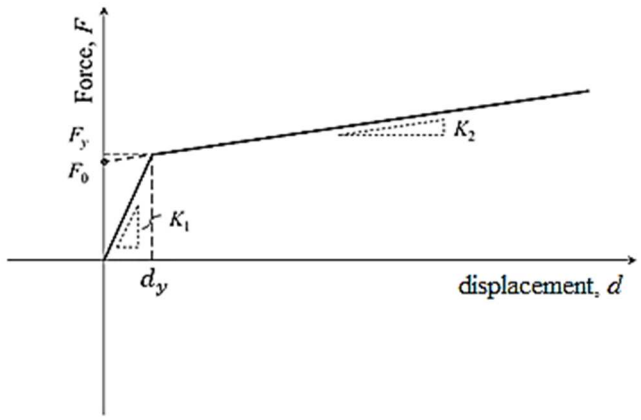

Figure 4.33. Bilinear force–displacement relationship in one horizontal direction of the *SingleFPSimple3d* element

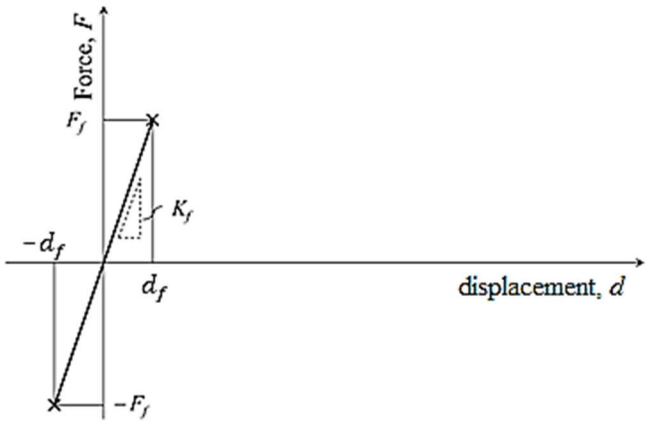

Figure 4.34. Force – displacement relationship of the *Truss* element with MinMax material model

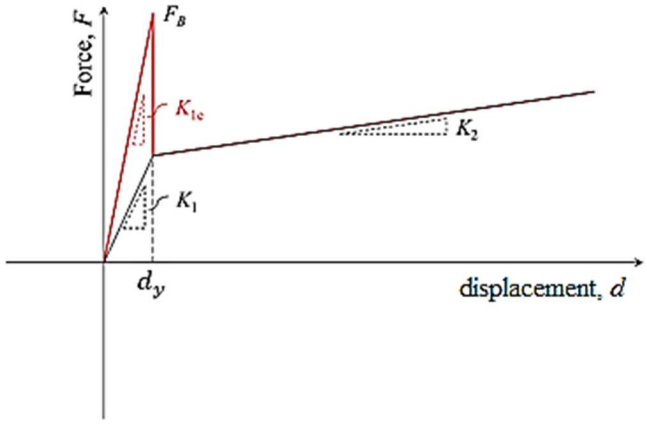

Figure 4.35. Resulting force – displacement relationship (red line) of the curved surface slider with consideration of the breakaway frictional force

4.3.2.3 Ground motions

Nonlinear Response Time History Analyses (NRHA) were carried out to investigate the differences from the breakaway friction. The seismic input consisted of one-directional horizontal ground motion time histories, whereas the vertical component of the seismic excitation was not taken into account.

Seven independent ground motion records consistent with the current Italian Building Code [64] were selected from the European Strong-motion Database [65] using REXEL v3.4 beta software [66]. The selected horizontal acceleration histories are in compliance with the assumed code for the life safety limit state of a strategic structure (functional class IV) located in Naples, Italy (14.2767° longitude, 40.863° latitude) on soil type A (stiff soil or rock) with a nominal life of 100 years (corresponding to a 1898-year return period according to the code).

Only events in the magnitude (Mw) interval [5.3, 7.3] and with an epicentral distance (R) interval [0-80 km] were considered, which reflects the hazard disaggregation for the spectral acceleration $S_a(T)$ for the period of interest in the nonlinear structural behaviour. This selection is representative of regions in Italy with a moderate to high seismic risk. The selected waveforms were scaled to the Peak Ground Acceleration (PGA) level of 0.259 g, which corresponds to the PGA value of the site according to the code assuming a topographic category T1. Scale Factors (SFs) of the acceleration time histories ranged from 0.73 to 1.43. The selected ground motions are listed in Table 4.13 and the scaled 5% damped elastic spectra are illustrated in Fig. 4.36.

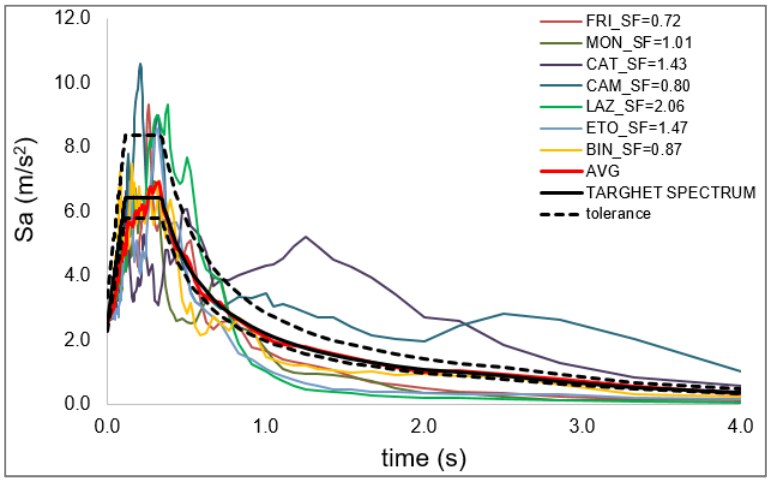

Figure 4.36. Scaled ground motion spectra and target spectrum according to Italian Building Code (SF_{mean} = 1.1981)

Record	Wave ID	Station ID	Date (dd/mm/yy)	Mw	*R* (km)	SF (-)	PGA (m/s^2)
Bingol (BIN)	7142ya	ST539	01/05/2003	6.3	14	0.87	2.55
Friuli (FRI)	55xa	ST20	06/05/1976	6.5	23	0.72	2.55
Montenegro (MON)	200ya	ST68	15/04/1979	6.9	65	1.01	2.55
Etolia (ETO)	428ya	ST169	18/05/1988	5.3	23	1.47	2.55
Lazio Abruzzo (LAZ)	372ya	ST274	07/05/1984	5.9	68	2.06	2.55
Campano Lucano (CAM)	290ya	ST96	23/11/1980	6.9	32	0.80	2.55
Campano Lucano (CAT)	287ya	ST93	23/11/1980	6.9	23	1.43	2.55

Table 4.13. Selected ground motions and details

4.3.3 Results

The structural response is analysed in terms of the following quantities: the critical acceleration at the initiation of sliding of the isolators, the horizontal displacement at the base isolation level, the interstorey drift, the storey floor acceleration, the base shear and the anelastic energy introduced in the structure.

A first outcome of the analyses was that when the high friction material with high breakaway (μ_{LV} = 0.05, μ_{HV} = 0.125, μ_B = 0.25) was considered, three accelerograms, BIN, FRI and ETO, were not able to promote the sliding of the isolators. Under these accelerograms the structure, though supported by sliding isolators, actually demonstrated the response of a fixed base structure. Fig. 4.37 shows the displacement envelopes calculated for BIN ground motion. Under conditions of high friction (friction 5) and high breakaway level (μ_B / μ_{LV} = 5) the isolator displacement envelope d_{iso} = *1.6mm* is lower than the yielding displacement d_y = *7.6 mm* demonstrating that the response of a fixed base structure is achieved.

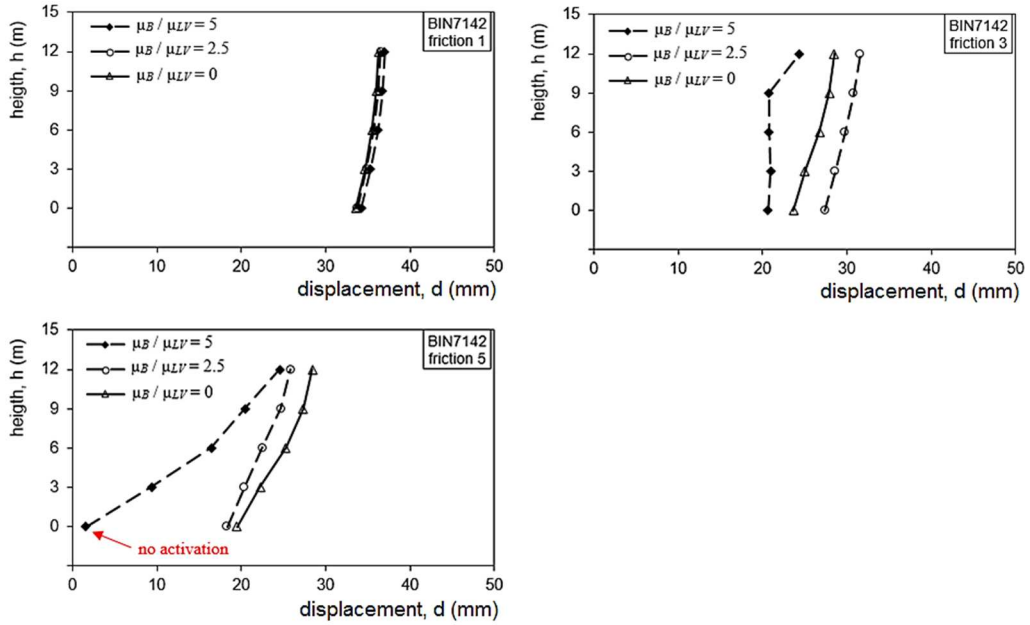

Figure 4.37. Displacement envelopes under BIN seismic input for different friction parameters

Fig. 4.38 illustrates the envelopes of inertial and shear forces at the instant of peak ground acceleration for BIN, FRI and ETO ground motions under which the sliding isolation system was not activated. At each storey level, the shear force is calculated as the algebraic sum of the inertial forces of the storey above. As stated above, activation of the isolation system requires that the shear force at the base level exceeds the resisting force of the isolators:

$$F_B = \mu_B.(N_{BS} + N_{SS}) \tag{4.24}$$

which in the present approach is given according to Eq. (4.21) as the sum of the elastic force of the CSS devices and the elastic force of the truss elements.

Though high inertial forces are developed at each storey, the high vibration modes are not negligible: the storey masses oscillate in phase opposition which limits the resulting shear force at the isolation level below the activation threshold.

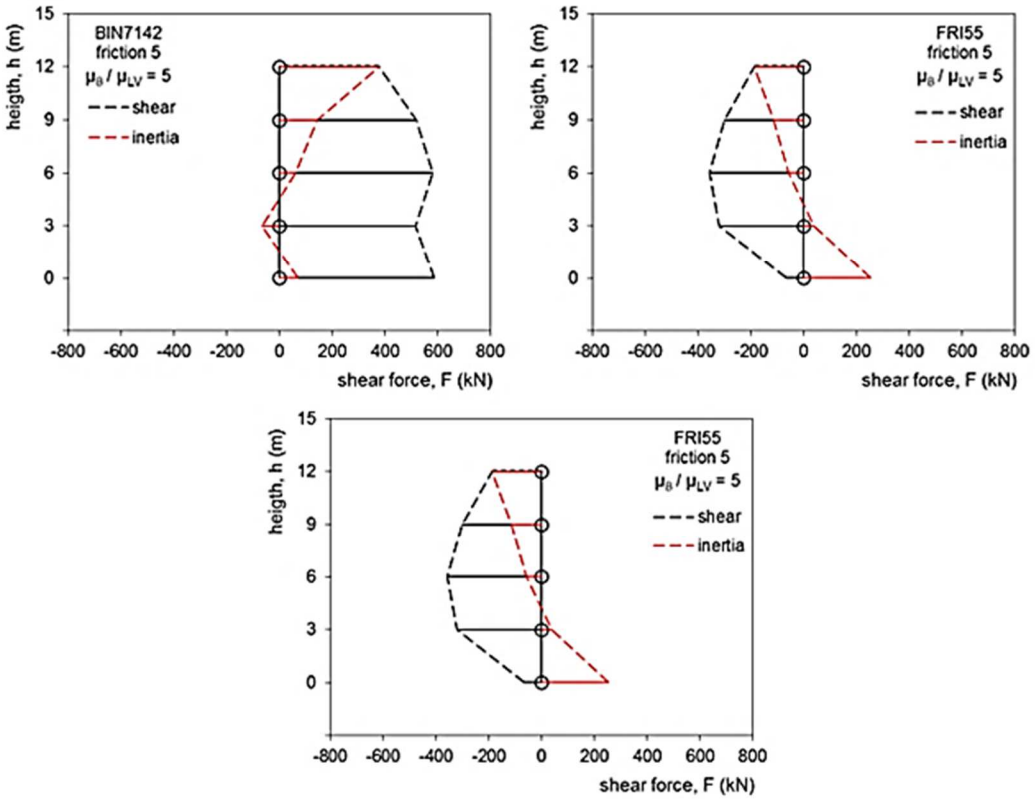

Figure 4.38. Envelopes of inertial and shear forces in the structure isolated with high friction, high breakaway CSS in case of no-activation of sliding surfaces

It is interesting to note that the critical acceleration threshold, calculated according to Eq. (4.17), is not able to catch this behaviour because it accounts only for the fundamental mode. Table 4.14 lists the values of a_{cr} associated to the seven ground motions of Table 4.13 for the isolation system under consideration.

Despite the levels of a_{cr} provided by the formula are quite low, ranging from 0.33 to 0.5 times the actual PGA, FRI, BIN and ETO ground motions did not produce shear forces at the base level sufficiently high to promote the sliding of the isolators, whereas ground motions with higher demand in term of a_{cr} like CAT were able to activate the sliders,

record	$S_a(T_1)$ (g)	β (-)	a_{cr} (g)
FRI	0.57	2.19	0.13
MON	0.66	2.54	0.11
CAT	0.32	1.22	0.21
CAM	0.92	3.55	0.08
LAZ	0.91	3.53	0.08
ETO	0.87	3.35	0.09
BIN	0.70	2.71	0.11

Table 4.14. Critical acceleration calculated for friction f5 and μ_B / μ_{LV} = 5 using Eq. (4.17)

For each friction model, the time-dependent structural responses obtained from the NRHA using the seven accelerograms are averaged to determine the average of the response quantities to be used for the verifications.

Fig. 4.39 illustrates the ratio between the critical acceleration a_{cr} and the peak ground acceleration depending on either the kinetic friction and the breakaway friction. It must be kept in mind that for the material with high friction profile and μ_B / μ_{LV} = 5, the relevant data point reflects the response to only the four accelerograms that activated the isolators.

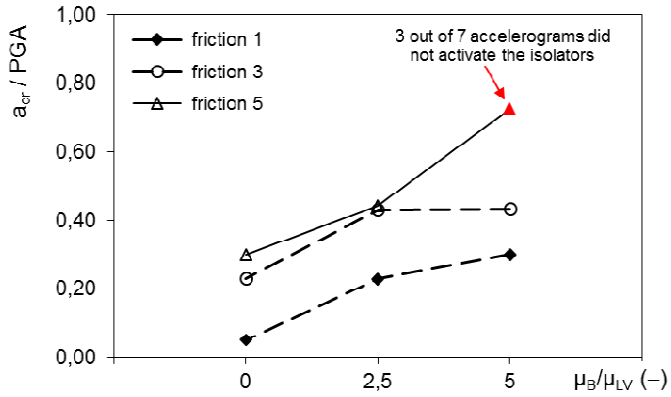

Figure 4.39. Average critical acceleration (normalized to PGA)

Fig. 4.40 illustrates the maximum displacement of the structure at the isolation level. Like for Fig. 4.39, the data point relative to the isolators with high kinetic and high breakaway friction reflect the response to only four accelerograms (for ETO, BIN, and FRI ground motions the isolator response, d_{iso} = 0 mm, was not included in the average).

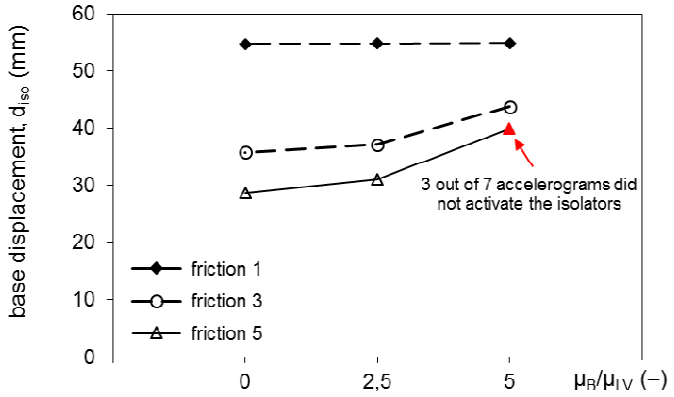

Figure 4.40. Average isolators maximum displacement

Fig. 4.41 illustrates the maximum floor acceleration in the structure normalized to the PGA. The response relevant to accelerograms that did not activate the isolators are now considered in the averaged response.

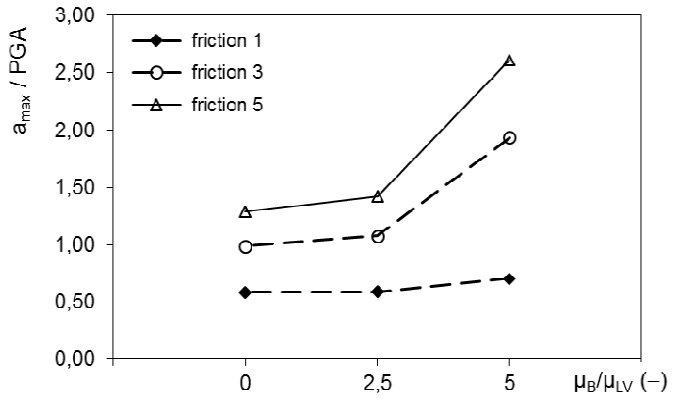

Figure 4.41. Average maximum floor acceleration (normalized to PGA)

Figs. 4.42 and 4.43 illustrate the internal forces and displacements produced in the structure, in terms of the maximum shear force of the isolators (normalized respect to the acting static vertical load) and the maximum inter-story drift (as a fraction of the storey height).

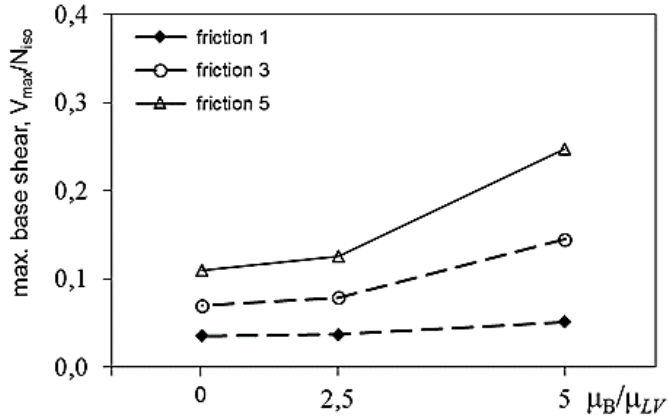

Figure 4.42. Average maximum base shear force of the isolators (normalized to applied static vertical load N_{iso})

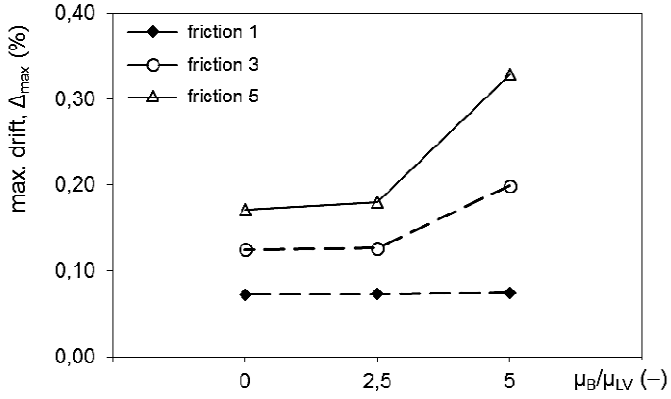

Figure 4.43. Average maximum inter-story drift

The total energy introduced during the ground motion in an isolated structure is partially dissipated by the isolation system (in the present case, by the friction forces developed in the curved surface sliders), and the remaining part must be dissipated by the structure itself by means of viscous damping and, if necessary, plastic deformation. Fig. 4.44 illustrates the energy anelastically dissipated by the structural elements, normalized to the total input energy. Though in the study the beams and columns of the superstructure were modeled as linearly elastic, so the only way to dissipate energy was by means of viscous forces whereas plastic deformation was ruled out, the relevant figure provides an estimate of the dissipation demand for the superstructure depending on the characteristics of the isolation system.

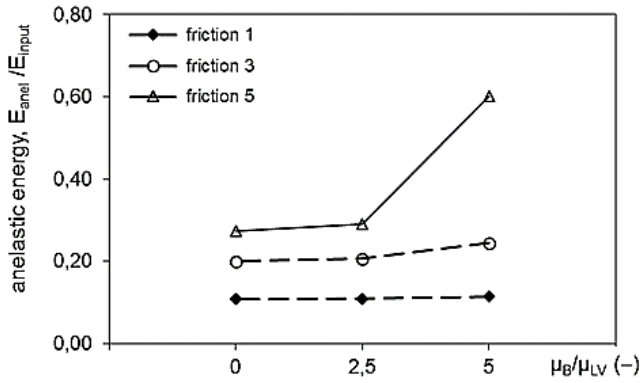

Figure 4.44. Average anelastic energy dissipated by the structural members normalized to the input energy into the structure

4.3.4 Discussion

The study investigates the role of the breakaway friction on the response of CSS isolation system. Three friction profiles covering a large variety of current materials used in curved surface sliders, and two levels of breakaway friction further to the condition $\mu_B = 0$ which is no practical, but represents the "standard" condition under which NRHA are performed using commercial software that do not implement the static coefficient of friction.

The NRHA showed that that for curved surface sliders comprising the material with high friction profile, depending on the characteristics of the ground motion time history the high breakaway friction can possibly prevent the activation of the sliding surfaces (in the analyses this occurred for three out of the seven accelerograms), and the structure though endowed with an isolation system behaves as a fixed base one. The estimation of the critical acceleration based on the elastic spectrum, i.e. considering only the first vibration mode, may be inaccurate because higher vibration modes can result in substantial phase shifts of the inertial forces at the different storeys, and therefore in a reduced base shear force insufficient to overcome a large breakaway friction. However, these effects are sensible to the frequency content of the ground and therefore need to be evaluated case by case.

As a general trend, the critical acceleration necessary to activate the isolators exhibits an increasing trend respect to the breakaway ratio whichever the kinetic friction profile, and its prediction based on the assumption $\mu_B = 0$ reveals to be under conservative.

A second outcome of the NRHA is that for materials with very low friction profile, the influence of the breakaway friction on the structural response of the isolated structure is in general not substantial (Fig. 4.45-a). Only the increase of the base shear force from $\mu_B = 0$ to $\mu_B = 5\mu_{LV}$ is significantly large (+44%), but has a limited practical effect based on the consideration that, being friction low, its contribution to the shear force is expected to be not significant and already covered by safety factors. Therefore in this case the analyses

performed without consideration of the actual breakaway characteristics are expected to provide reliable prediction of the actual behavior.

For materials with medium and high friction profiles, a low breakaway ratio does not introduce significant changes in the response. In case of high breakaway ratio, the response has a sharp increase to levels more than double respect to $\mu_B = 0$ (Figs 4.45-b,c). It is worth noting that in general the variation is much higher for the shear force and the floor acceleration, and smaller for the maximum displacement at the base level, which is in perfect agreement with the conclusions drawn by Fagà *et al.* (2015) [62].

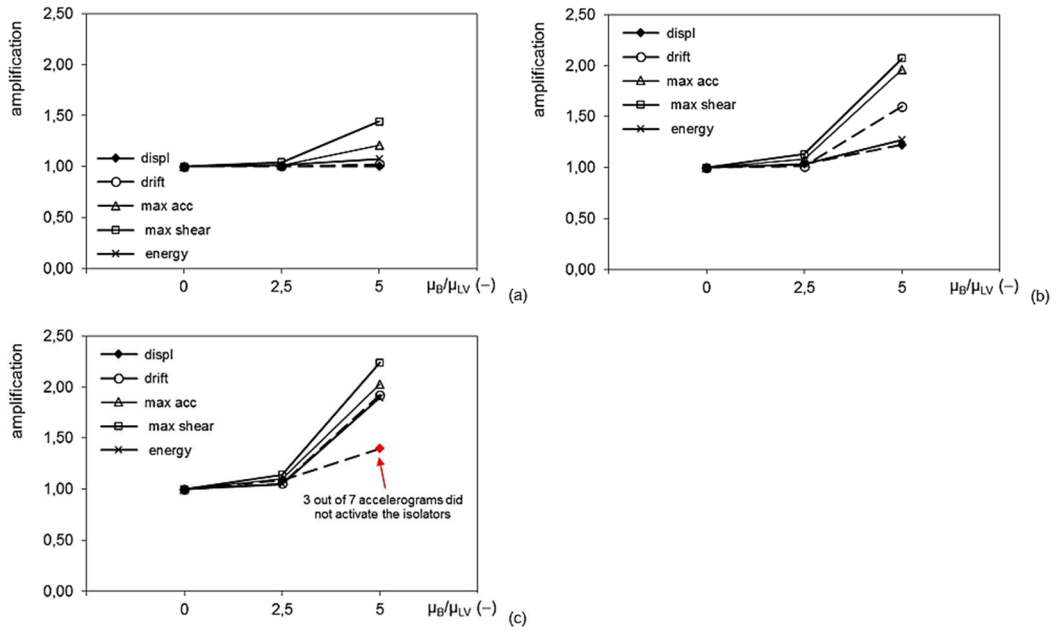

Figure 4.45. Amplification of the structural response with increasing of the breakaway ratio for isolation systems equipped with low friction materials (a), medium friction materials (b) and high friction materials (c)

A particular discussion deserves the influence of the breakaway friction on the base displacement. Whereas for isolators with low friction profile the maximum displacement is not affected by the breakaway friction, in case of either medium or high kinetic friction an increasing trend is disclosed by the NRHA, which is quite counterintuitive. However, as shown in Fig. 4.46 for CAM time history and friction 5 CSS isolator, in case of low breakaway the slider may be activated during the first, weak shocks, and possibly moves in the direction opposite to the direction of maximum displacement; in case of pulse-like ground motions this offset is likely to result in a smaller displacement attained at the instant of peak ground acceleration respect to the isolator that is activated later.

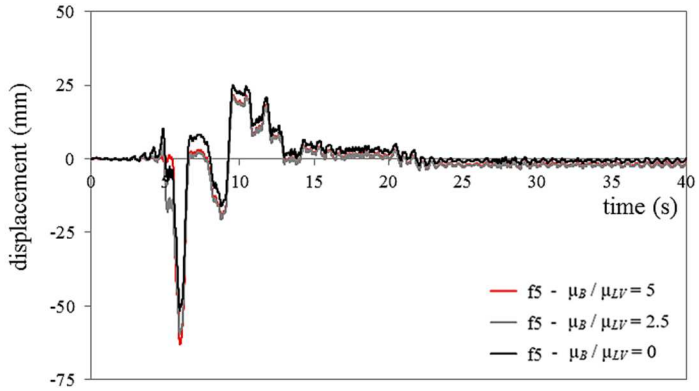

Figure 4.46. Displacement time-histories calculated for CAM seismic input and friction f5 CSS isolators at different breakaway levels

In Fig. 4.46 the three displacement time-histories have similar displacement amplitudes, but since the time history corresponding to $\mu_B = 5\mu_{LV}$ has no offset at the occurrence of the acceleration pulse, the obtained extreme displacement is larger.

This behavior is dependent on the characteristics of the ground motion time histories and cannot be generalized, but must be taken in consideration during the design of the isolation system especially if high friction devices are accounted for.

However, it must be again kept in mind that for isolators with high friction profile the breakaway friction can prevent the activation, and the base isolated structure behaves like a fixed base one. This results in internal forces and displacements substantially larger than those expected assuming that the isolation system is effective.

Some practical consideration can be drawn from the results of the studies regarding the design of isolation systems.

In Europe, the design of curved surface sliders is regulated by the standard EN 15129 [16] that allows the use of either PTFE or UHMWPE (the latter being covered by an European Technical Approval). Both materials are generally used without lubrication, providing a kinetic coefficient of friction at low velocity in the range of 0.03 to 0.05 depending on the contact pressure, and a ratio of breakaway to kinetic friction between 1.5 (UHMWPE) to 2.5 (PTFE). Therefore, according to the study, the response of a simple structure isolated with curved surface sliders employing these materials can be predicted, with sufficient reliability, neglecting the contribution of the breakaway. In case the sliding surfaces are lubricated in order to achieve a very low friction coefficient, the effect of the breakaway should be of no practical effect.

Different is the case of high friction materials with high breakaway ratio, like for example filled thermoplastics. In this case, NRHA performed with current commercial software that does not implement the behavior at breakaway can significantly underestimate the actual response of the structure in terms of both internal stresses and deformation. In this case the Authors believe that the development of custom software is worth the effort.

4.3.5 Conclusions

Current commercial software for structural analysis, whereas are capable to account for the dependence of the kinetic coefficient of friction of Curved Surface Sliders (CSS) on the axial load and the velocity, and at some extent also on temperature, do not implement the static coefficient of friction developed at the breakaway.

The study developed in this section of the thesis investigates, by means of NHRAs, the influence of friction coefficient at motion breakaway on the response of a five-story building equipped with CSS isolators under a set of spectrum-compatible natural ground motions. Results of NHRAs are compared to those obtained from the same analyses neglecting the breakaway friction; the main conclusions are summarized in the next points:

(1) the general effect of the breakaway friction is to increase the level of acceleration threshold that must be overcome to initiate the sliding of the isolators; depending on the characteristics of the ground motion time histories, in case of isolators equipped with high friction materials, an high breakaway friction can prevent the sliding and the structure behaves as it were not isolated;

(2) in case of very low kinetic coefficient of friction, the breakaway friction has a practical limited effect; analyses neglecting μ_B are sufficiently reliable;

(3) in case of medium or high kinetic friction, the influence of the breakaway friction is still not substantial when the breakaway friction is no more than 2.5 times the low velocity kinetic friction; on the contrary it becomes substantial when the breakaway friction is on the order of 5 times the low velocity kinetic level;

(4) the level of breakaway friction has a major effect on the floor acceleration and the base shear at the isolation level, whereas in general the influence on the extreme displacements is smaller.

4.4 Proposed "*BVNC*" friction model

Like some recent formulations available in literature [39, 54], the proposed analytical model (named *"BVNC"*) is capable to reproduce the well acknowledged dependence of the friction coefficient on the instantaneous sliding velocity, and normal load, as well as, its decay due to the "*frictional heating effect*" (see section 2.2). The main novelty is indeed represented by the possibility to catch also the "*breakaway effect*"; that is, the transition from static to kinetic friction each time the system goes from a sticking phase to a sliding phase. The Writer has shown that this phenomenon can have a significant influence on the peak floor accelerations and maximum inter-story drifts experienced by the superstructure during the seismic event (see section 4.3).
The new *"BVNC"* friction model, after being validated by means of comparison with experimental data, has been implemented (see section 4.5) in OpenSees® FEM code [22].

4.4.1 Analytical formulation

The mathematical formulation of the *"BVNC"* model regulates the four main frictional effects (velocity, breakaway, normal load, and frictional heating) by means of the ten constitutive parameters reported in Table 4.15.

parameter	**effect**
α, β	velocity and breakaway
$a_{ST}, n_{ST}, a_{LV}, n_{LV}, a_{HV}, n_{HV}$	normal load
C_{ref}, γ	frictional heating

Table 4.15. Model parameters for each frictional effect

At each time instant t, the normal load $N(t)$ acting on the isolator sliding surface should be known (e.g. from numerical analysis), and the "*normal load effect*" is estimated by means of a potential law [67]:

$$\mu_{ST}(N(t)) = a_{ST} N(t)^{(n_{ST}-1)} \tag{4.25}$$

$$\mu_{LV}(N(t)) = a_{LV} N(t)^{(n_{LV}-1)} \tag{4.26}$$

$$\mu_{HV}(N(t)) = a_{HV} N(t)^{(n_{HV}-1)} \tag{4.27}$$

where μ_{ST} is the static friction coefficient at the motion breakaway, μ_{LV} and μ_{HV} are respectively the friction coefficients at very low and very high sliding velocities, a_{ST}, a_{LV}, a_{HV}, $n_{ST} \leq 1$, $n_{LV} \leq 1$, and $n_{HV} \leq 1$ are constants parameters.
The "*frictional heating*" (or "*cyclic effect*", or even "*thermal effect*") is then taken into account by means of the reduction coefficient $f_C(t)$ proposed by Lomiento *et al.* (2013) [54]:

$$f_C(t) = e^{-\left(\left(\frac{C(t)}{C_{ref}}\right)^{\gamma}\right)} \tag{4.28}$$

where C_{ref} is a parameter that regulates the degradation rate of the friction coefficient, γ controls the shape of the function, and the cyclic variable $C(t)$ is calculated as:

$$C(t) = \int_0^t N(t)v(t)^2 dt \tag{4.29}$$

At each time instant t, the friction coefficients μ_{ST}, μ_{LV}, and μ_{HV} are then reduced by means of $f_C(t)$:

$$\mu_{ST}(N(t), C(t)) = a_{ST}N(t)^{(n_{ST}-1)} \cdot e^{-\left(\left(\frac{C(t)}{C_{ref}}\right)^{\gamma}\right)} \tag{4.30}$$

$$\mu_{HV}(N(t), C(t)) = a_{HV}N(t)^{(n_{HV}-1)} \cdot e^{-\left(\left(\frac{C(t)}{C_{ref}}\right)^{\gamma}\right)} \tag{4.31}$$

$$\mu_{LV}(N(t), C(t)) = a_{LV}N(t)^{(n_{LV}-1)} \cdot e^{-\left(\left(\frac{C(t)}{C_{ref}}\right)^{\gamma}\right)} \tag{4.32}$$

The *"velocity effect"* is lastly taken into account by inserting instantaneous values of Eq. (4.29)-(4.31) in the velocity-dependent friction model proposed by Quaglini *et al.* (2014) [34]:

$$\mu(t) = \mu_{HV} - (\mu_{HV} - \mu_{LV}) \cdot e^{(-\alpha \cdot |v|)} + (\mu_{ST} - \mu_{LV}) \cdot e^{(-\beta \cdot |v|)} \cdot \frac{1}{2}\left[sign\left(\frac{d|v|}{dt}\right) + 1\right] \tag{4.33}$$

where α is a parameter regulating the increase in kinetic friction with velocity, and β is a parameter regulating the transition from the static to the kinetic friction regime. This transition happens when the term $\frac{1}{2}\left[sign\left(\frac{d|v|}{dt}\right) + 1\right]$ is equal to one; that is at the motion breakaway and each time the system starts its motion after a stop, like reverses in cyclic displacement histories.

The operational principles of the proposed friction model are represented in Fig. 4.47.

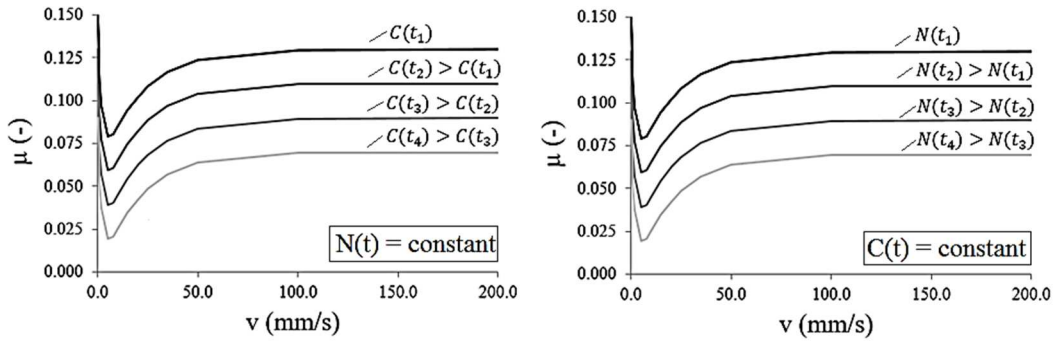

Figure 4.47. Dependence of the friction coefficient on the sliding velocity (breakaway friction at *v=0mm/s* is evident) and its decay for increasing values of the cyclic variable (left) and normal load (right)

4.4.2 Parameters calibration

The model parameters are calibrated by means of experimental unidirectional tests (sinusoidal waveform) conducted on real-scale CSS isolators (Fig. 4.48-left). At each time instant t, the friction force F_μ is calculated from the total measured force F by eliminating the restoring term (Fig. 4.48-rigth):

$$F_\mu(t) = F(t) - \frac{N(t)}{R_{eff}} d(t) \tag{4.34}$$

where N is the vertical load applied on the isolator, d is the displacement, and R_{eff} is the effective radius of the isolator (see section 2.1).

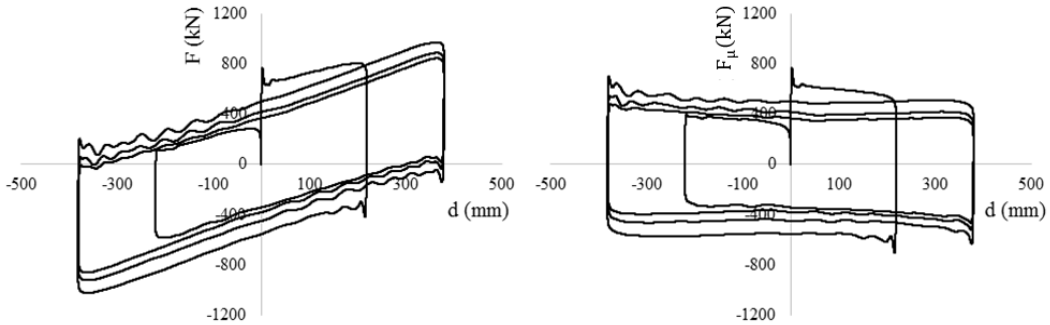

Figure 4.48. Experimental loops of a CSS isolator (left), and relevant frictional cycles (right) obtained using Eq. (4.34)

The instantaneous friction coefficient $\mu(t)$ is then easily calculated:

$$\mu(t) = \frac{F_\mu(t)}{N(t)} \tag{4.35}$$

The parameters of each frictional effect are calibrated separately using the results of experimental tests carried out at different levels of applied vertical load (minimum three levels, that is N_1, N_2, and N_3). Suggested values are the gravitational load (static conditions), and the minimum and maximum vertical loads in seismic conditions (from dynamic analyses).

In order to minimize the influence of the effect of the "*frictional heating*" on the friction coefficient, the "*velocity effect*" and "*load effect*" parameters are firstly calibrated considering only experimental data related to the first half cycle of each test. Since tests with sinusoidal waveform are usually prescribed, the sliding velocity changes at each instant of the motion (Fig. 4.49-right). A MatLab® code [68] has been created to automatically detect, in the most suitable areas of the cycle (Fig. 4.49-left), the static friction coefficient at motion breakaway, one friction coefficient at low-velocity ($v < 25$ *mm/s*), two friction coefficients at medium-high velocities ($v = 50 \div 100$ *mm/s*), and two friction coefficients at high velocity ($v > 200$ *mm/s*).

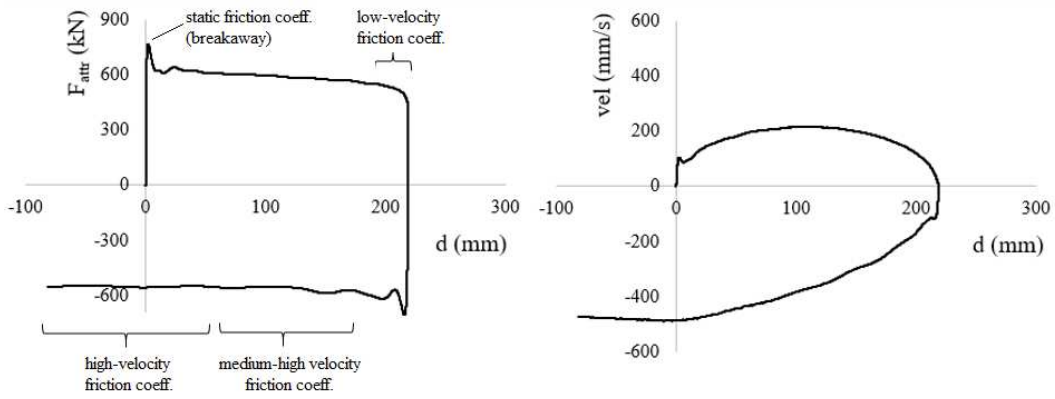

Figure 4.49. First half cycle: frictional force (right), and velocity profile (left)

For each load level N_i, the detected experimental friction coefficients μ are plotted as a function of the sliding velocity v (Fig. 4.50). Obtained couples of values (v, μ) are then fitted using the following equation:

$$\mu(v) = \mu_{HV,Ni} - \left(\mu_{HV,Ni} - \mu_{LV,Ni}\right) \cdot e^{(-\alpha_{Ni} \cdot |v|)} + \left(\mu_{ST,Ni} - \mu_{LV,Ni}\right) \cdot e^{(-\beta_{Ni} \cdot |v|)} \tag{4.36}$$

where $\mu_{ST,Ni}$ is static friction coefficient at the breakaway (v = *0 mm/s*), $\mu_{LV,Ni}$ is the low velocity (v < *25 mm/s*) friction coefficient, and $\mu_{HV,Ni}$ is the high velocity (v > *200 mm/s*) friction coefficient (usually asymptotic value).

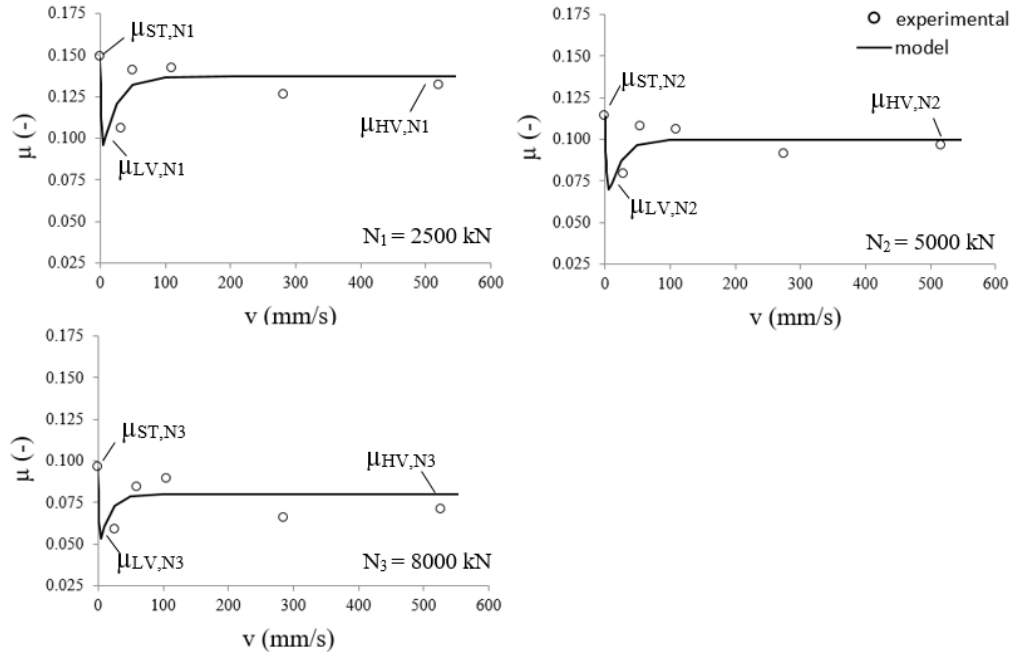

Figure 4.50. Typical trends, at different load levels, of the friction coefficient μ with the increase of the sliding velocity v

Optimal values for the "*velocity effect*" parameters (α_{Ni}, β_{Ni}) are detected by means of a nonlinear least square fitting procedure. The related global parameters (α and β) are then calculated by averaging:

$$\alpha = \frac{\sum_{i=1}^{3} \alpha_{Ni}}{3} \tag{4.37}$$

$$\beta = \frac{\sum_{i=1}^{3} \beta_{Ni}}{3} \tag{4.38}$$

In order to calibrate the "*load effect*" parameters, the friction coefficients $\mu_{ST,Ni}$, $\mu_{LV,Ni}$, and $\mu_{HV,Ni}$ are plotted as a function of the applied vertical load N_i (Fig. 4.51). Obtained couples of values (e.g. N_i, $\mu_{ST,i}$) are then fitted by means of the following equations:

$$\mu_{ST}(N(t)) = a_{ST} N(t)^{(n_{ST}-1)} \tag{4.39}$$

$$\mu_{LV}(N(t)) = a_{LV} N(t)^{(n_{LV}-1)} \tag{4.40}$$

$$\mu_{HV}(N(t)) = a_{HV} N(t)^{(n_{HV}-1)} \tag{4.41}$$

and optimal values for relevant parameters (a_{ST}, n_{ST}, a_{LV}, n_{LV}, a_{HV}, n_{HV}) are again detected by means of a nonlinear least square fitting procedure.

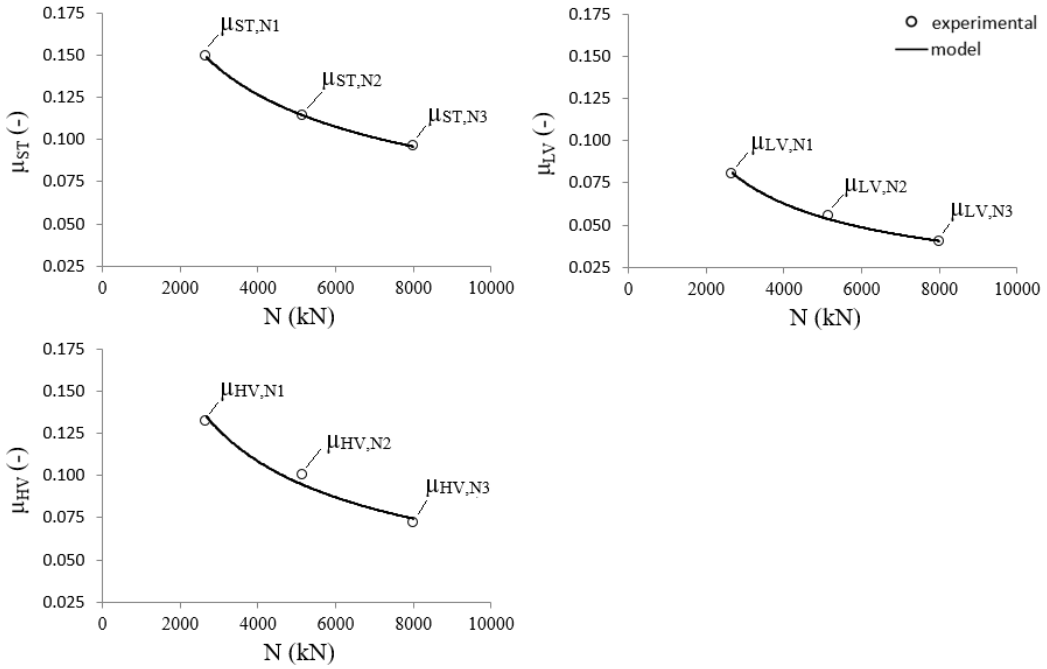

Figure 4.51. Typical decrease of the static μ_{ST}, low-velocity μ_{LV}, and high-velocity μ_{HV} friction coefficients with the increase of the normal load *N* acting on the CSS isolator

The "*frictional heating*" parameters (C_{ref}, γ) are lastly calibrated considering only the test in which the CSS isolator dissipated the largest amount of energy. Every quarter of cycle, the equivalent friction coefficient $\mu_{ED,i}$ and related values C_i of the cyclic variable are calculated:

$$\mu_{ED,i} = \frac{ED_i}{(N \cdot d_i)} \tag{4.42}$$

$$C_i = \int_0^{t_i} N \cdot v(t)^2 dt \tag{4.43}$$

where N is the applied normal load, ED_i, and d_i are respectively the energy dissipated, and the covered path during the i[th] quarter of cycle.

Optimal values of the parameters C_{ref} and γ are again detected by means of a nonlinear least square fitting procedure (Fig. 4.52) and considering the following equation to catch the trend of the couple of values (C_i, $\mu_{ED,i}$):

$$\mu_{ED,i} = \mu_{ED,1} \cdot f_C(C_i) = \mu_{ED,1} \cdot e^{-\left(\left(\frac{C_i}{C_{ref}}\right)^{\gamma}\right)} \tag{4.44}$$

and similarly:

$$f_C(C_i) = \frac{\mu_{ED,i}}{\mu_{ED,1}} \tag{4.45}$$

where $\mu_{ED,1}$ is the equivalent friction coefficient for the first quarter of cycle (when the frictional heating is sill negligible).

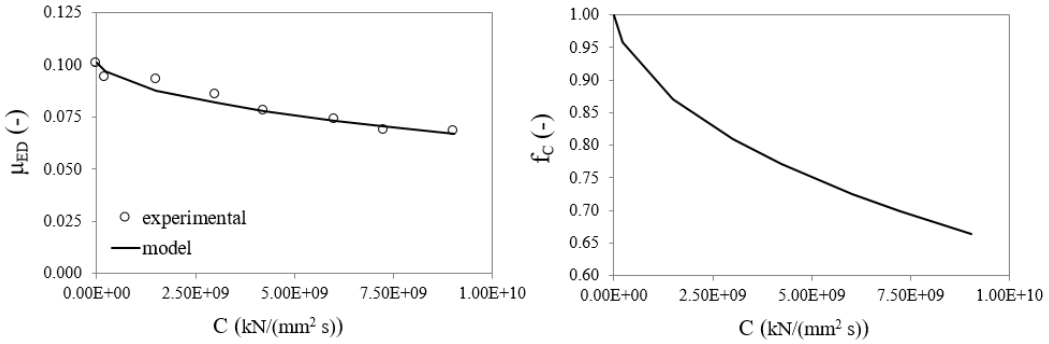

Figure 4.52. Thermal effect: decay of the equivalent friction coefficient μ_{ED} with the increase of the cyclic variable *C* (left), and relevant values of the reduction coefficient f_C (right)

4.4.3 Model validation

The previously described procedure was adopted for the calibration of the model parameters (Table 4.16) of a real CSS isolator tested at the SRMD Lab. of the University of San Diego, California [69]. Three unidirectional tests at different load levels (Table 4.17) are here considered to validate the response of the *"BVNC"* model.

effect	**parameter**	**unit**
velocity and breakaway	$\alpha = 0.035$	s/mm
	$\beta = 0.35$	s/mm
normal load	$a_{ST} = 3.51$	kN^{-1}
	$n_{ST} = 0.60$	-
	$a_{LV} = 11.27$	kN^{-1}
	$n_{LV} = 0.37$	-
	$a_{HV} = 9.65$	kN^{-1}
	$n_{HV} = 0.46$	-
frictional heating	$C_{ref} = 4 \cdot 10^{10}$	(kN mm^2) / s
	$\gamma = 0.60$	-

Table 4.16. Calibrated model parameters

test	**vert. load (kN)**	**ampl. (mm)**	**max vel. (mm/s)**	**freq. (Hz)**	**shape**	**cycles (-)**
1	2500	380	486	0.2035	sine	3
2	5000	380	486	0.2035	sine	3
3	8000	380	486	0.2035	sine	3

Table 4.17. Experimental tests parameters

At each time instant t, experimental values of the applied vertical load $N(t)$, and velocity $v(t)$ are given as input to the model that computes the instantaneous friction coefficient $\mu(t)$ (and hence the instantaneous friction force as $F_\mu(t) = \mu(t) \cdot N(t)$). Fig. 4.53 shows the comparison between experimental loops and those predicted by the model: in general, a fair agreement is reached but a slight discrepancy, probably due to scattered experimental values, can be noted in the slowdown phase at the end of each stroke.

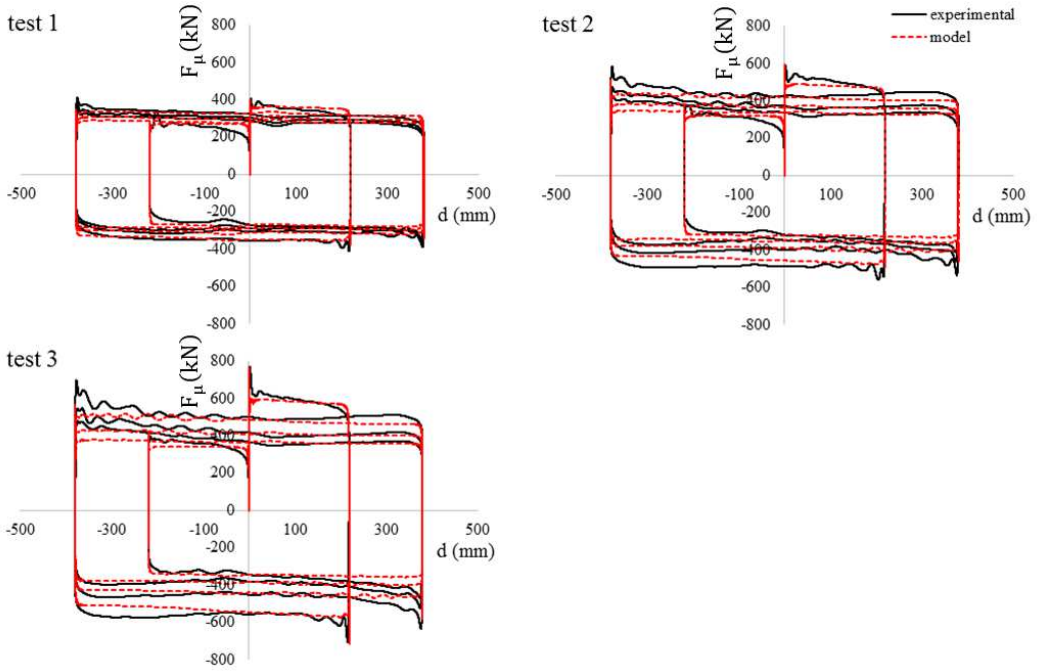

Figure 4.53. Comparison between the experimental friction loops and those predicted by the model

4.4.4 Friction model subcases

Friction model subcases can be obtained from the complete formulation ("*BVNC*") by properly setting the model parameters in order to nullify the contribution of one or more frictional effects. Table 4.18 provides the sets of parameters relevant to subcases of some practical interest; in particular, it is possible to replicate the response of some standard formulations already implemented in OpenSees® such as the "*Coulomb*", the "*VelDependent*", and the "*VelNormalFrcDep*" friction models (see section 4.5).

subcase	**reproduced effect**				**set of parameters**
	B	**V**	**N**	**C**	
VNC		■	■	■	set 1: $\beta \to +\infty$ set 2: $a_{ST} = a_{LV}$, $n_{ST} = n_{LV}$
BVC	■	■		■	$n_{ST} = n_{LV} = n_{HV} = 1$
BVN	■	■	■		$C_{ref} \to +\infty$
BV	■	■			$n_{ST} = n_{LV} = n_{HV} = 1$ $C_{ref} \to +\infty$
VN ("*VelNormalFrcDep*")		■	■		$\beta \to +\infty$ $C_{ref} \to +\infty$
V ("*VelDependent*" $\mu_{HV} = a_{HV}$ $\mu_{LV} = a_{LV}$)		■			$\beta \to +\infty$ $C_{ref} \to +\infty$ $n_{LV} = n_{HV} = 1$ ($n_{ST} = 1$)
"*Coulomb*" ($\mu = cost. = a_{HV}$)					$\alpha \to +\infty$ $\beta \to +\infty$ $C_{ref} \to +\infty$ $n_{HV} = 1$

Table 4.18. Sets of parameters for friction model subcases (shortcuts of reproduced effects: (B) for breakaway, (V) for velocity, (N) for normal load, and (C) for cyclic)

4.5 Proposed FEM formulation

4.5.1 The "CSSBearing_BVNC" element

A new isolator element, named "*CSSBearing_BVNC*", has been implemented in OpenSees® FEM software modifying the original "*SingleFPSimple3d*" formulation [70].

In OpenSees®, the 3D continuum geometry of a CSS isolator is modelled as the 2-node (12 DOF) discrete element shown in Fig. 4.54. The two nodes are virtually connected by springs governing the response of the element in the six basic directions: (1) axial; (2) horizontal shear1; (3) horizontal shear2; (4) torsion; (5) rotation1; (6) rotation2. The shear response of the element is based on a bidirectional plasticity model with isotropic hardening [55]. The force-deformation behaviours in the remaining directions (axial, torsional, and the rotational) can be associated with different elastic "*UniaxialMaterials*" and, since not significantly affecting the overall response of the base-isolated structure [71], are not described in the present section.

The proposed element formulation differs from the original one because is coupled to two friction laws: a Coulomb friction model ($\mu = \mu_B = cost$) defines the plastic domain before the first yielding threshold overcoming (at motion breakaway), and then the hysteretic behaviour is governed by the "*VNC_FrictionModel*" proposed by the Writer (see section 4.4.4). This allows the new element to reproduce the following frictional effects: (1) peak of friction coefficient (μ_B) at motion breakaway; (2) dependence of the friction coefficient on the instantaneous sliding velocity and normal force on the sliding pad; (3) decrease of the friction coefficient due to the frictional heating (cyclic effect).

The main limit of this formulation is the impossibility to catch the transition from the static (μ_{ST}) to the low velocity friction coefficient (μ_{LV}) at motion reversals in unidirectional dynamic analyses.

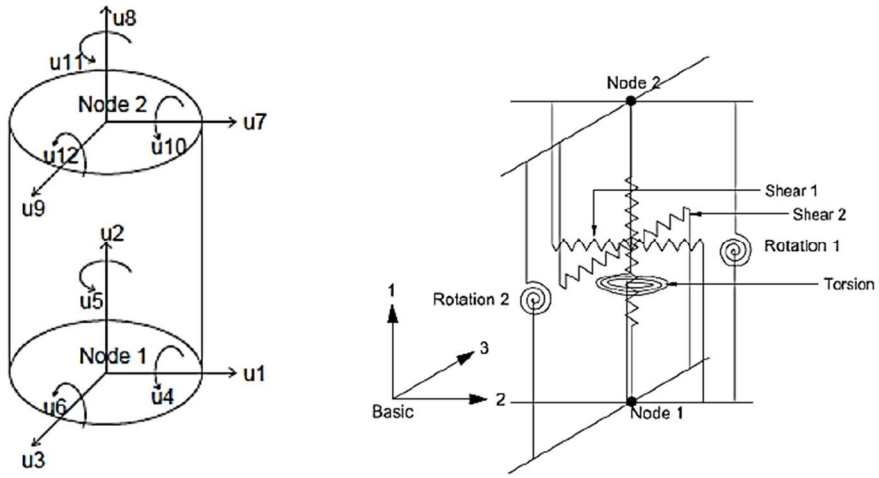

Figure 4.54. CSS isolator element: physical model of a CSS isolator (left) and discrete spring representation (right) (adapted from [70])

In the FE formulation, the two nodes of the element are virtually located in the centres of the lower and upper sliding surfaces of the physical CSS device. The degrees of freedom in the global and local reference systems (Fig. 4.55) are oriented as proposed in literature [72]. Moreover, the element response is formulated in the basic coordinate system (Fig. 4.56) and transformation matrices are used to switch from basic to local and then local to global reference system [71].

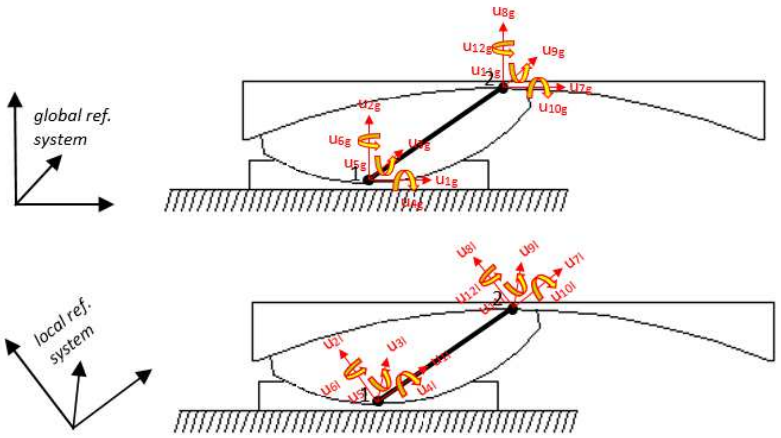

Figure 4.55. Element degrees of freedom in the global (up) and local (down) reference systems

In the basic reference system, the element has six degrees of freedom corresponding to the relative displacements and rotations between the two nodes (Fig. 4.56-right). In particular, assuming that the node 1 is fixed, the displacements at node 2 can be obtained by means of rotations about the centre of curvature of the lower sliding surface (C_1). The resultant kinematics (Fig. 4.56-left) is therefore the same of a physical pendulum having radius equal to R_{eff} (see section 2.1). At each instant of the sliding motion, the basic reference system is oriented in such a way that the axial direction (u_{1b} in Fig. 4.56-rigth) is aligned to the line joining the centre of curvature of the lower (C_1) and upper (C_2) sliding surfaces. In the basic coordinate system, the general form of the element stiffness matrix is [70]:

$$[K_b] = \begin{bmatrix} \text{axial} & 0 & 0 & 0 & 0 & 0 \\ 0 & \text{shear1} & \text{shear12} & 0 & 0 & 0 \\ 0 & \text{shear12} & \text{shear2} & 0 & 0 & 0 \\ 0 & 0 & 0 & \text{tors.} & 0 & 0 \\ 0 & 0 & 0 & 0 & \text{rot. 1} & 0 \\ 0 & 0 & 0 & 0 & 0 & \text{rot. 1} \end{bmatrix} \tag{4.46}$$

with related element force vector:

$$\{q_b\} = \begin{bmatrix} \text{axial} \\ \text{shear1} \\ \text{shear2} \\ \text{tors.} \\ \text{rot. 1} \\ \text{rot. 2} \end{bmatrix} \tag{4.47}$$

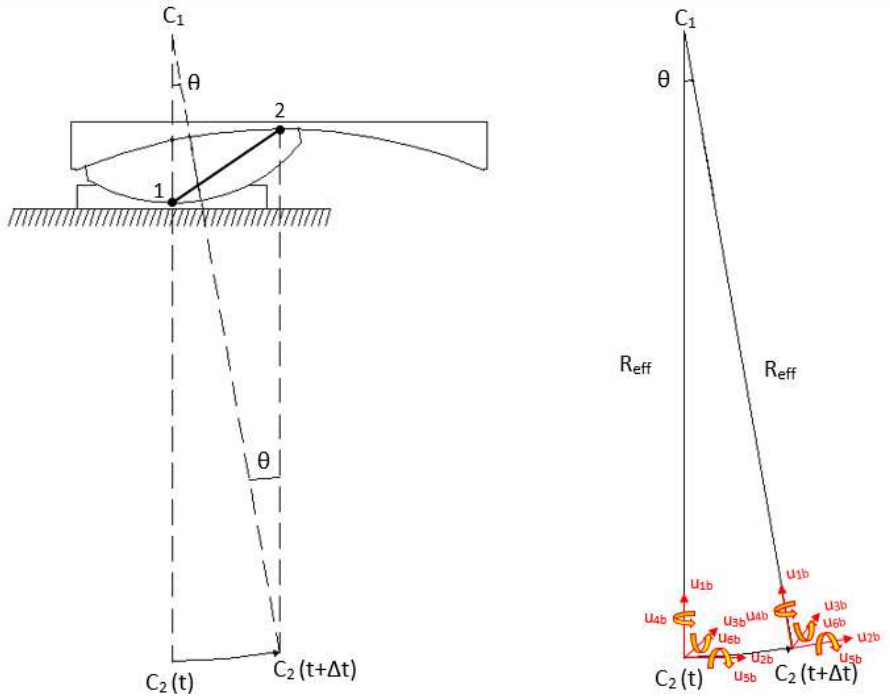

Figure 4.56. Element kinematic (left) and degrees of freedom in the basic reference system (right)

Within this framework, the formulation of the "*CSSBearing_BVNC*" element is described hereafter by means of the two sets of mathematical symbols listed in Tables 4.19 and 4.20. Furthermore, required user input-parameters are reported in Table 4.21.

kinematic variable	size	description
$\{u_g\}$	12 x 1	displacement vector in global coordinates
$\{u_l\}$	12 x 1	displacement vector in local coordinates
$\{u_b\}$	6 x 1	displacement vector in basic coordinates
$\{u_{el,pl}\}$	2 x 1	elastic displacement vector in basic coordinates
$\{u_{b,pl}\}$	2 x 1	plastic displacement vector in basic coordinates
$\{\dot{u}_g\}$	12 x 1	velocity vector in global coordinates
$\{\dot{u}_l\}$	12 x 1	velocity vector in local coordinates
$\{\dot{u}_b\}$	6 x 1	velocity vector in basic coordinates
$[T_{gl}]$	12 x 12	transformation matrix from global to local coordinates
$[T_{lb}]$	6 x 12	transformation matrix from local to basic coordinates

Table 4.19. Element kinematic variables

variable	size	description
$\{q_b\}$	6 x 1	internal force vector
$\{q\}$	2 x 1	internal friction forces vector
q_{yield}	1 x 1	yielding force
$[K_b]$	6 x 6	tangent stiffness matrix
$[K_{b,init}]$	6 x 6	initial tangent stiffness matrix

Table 4.20. Element internal force and stiffness variables (in basic coordinates)

parameter	description
R_{eff}	effective radius of curvature of the isolator
K_{init}	initial (elastic) stiffness of the isolator
$\mu = cost$	Coulomb friction model
$\mu = \mu(\lvert\dot{u}_b\rvert, N, C)$	*"VNC_FrictionModel"*
E	"*UniaxialMaterial*" elastic modulus
Tol	tolerance for convergence criterion
$Max\ Iter$	maximum number of iterations

Table 4.21. User input-parameters

Before proceeding with a detailed description of the *"CSSBearing_BVNC"* element, it is worth providing an insight of the method used by OpenSees® to solve the dynamics of nonlinear MDOF systems. At each time instant t, the code computes the displacement field of the whole system $\{u_g(t)\}$ (in global coordinates) solving the system of equations [70]:

$$[M] \cdot \{\ddot{u}_g(t)\} + [C] \cdot \{\dot{u}_g(t)\} = \{F^{ext}(t)\} + \{F^{int}(u_g(t))\} \tag{4.48}$$

where $\{F^{ext}\}$ and $\{F^{int}\}$ are respectively the external and the internal force fields. The values of internal forces depend on the actual configuration of the system $\{u_g(t)\}$ and on the rheological model associated to each element, this leads to a nonlinear differential problem. At first, the time derivatives are approximated using the Newmark-β method:

$$\{u_g(t+\Delta t)\} = \{u_g(t)\} + \Delta t\{\dot{u}_g(t)\} + \left(\frac{1}{2} - \beta\right)\Delta t^2\{\ddot{u}_g(t)\} + \beta\Delta t^2\{\ddot{u}_g(t+\Delta t)\} \tag{4.49}$$

$$\{\dot{u}_g(t+\Delta t)\} = \{\dot{u}_g(t)\} + (1-\gamma)\Delta t\{\ddot{u}_g(t)\} + \gamma\Delta t\{\ddot{u}_g(t+\Delta t)\} \tag{4.50}$$

The problem is hence reduced to a nonlinear algebraic problem that is solved using the standard Newton's method. The application of the Newton's method produce a sequence of approximations of the solution $\{u_g(t+\Delta t)^i\}$, where:

$$\{u_g(t+\Delta t)^0\} = \{u_g(t)\} \tag{4.51}$$

and:

$$\{u_g(t+\Delta t)^{i+1}\} = \{u_g(t+\Delta t)^{i}\} + \{\Delta u_g(t+\Delta t)^{i+1}\} \tag{4.52}$$

This allows to the update also the velocity and acceleration fields:

$$\{\dot{u}_g(t+\Delta t)^{i+1}\} = \{\dot{u}_g(t+\Delta t)^{i}\} + \frac{\gamma}{\beta\,\Delta t}\{\Delta u_g(t+\Delta t)^{i+1}\} \tag{4.53}$$

$$\{\ddot{u}_g(t+\Delta t)^{i+1}\} = \{\ddot{u}_g(t+\Delta t)^{i}\} + \frac{1}{\beta\,\Delta t^2}\{\Delta u_g(t+\Delta t)^{i+1}\} \tag{4.54}$$

The linearization of the momentum equation using the displacement update $\{\Delta u_g(t+\Delta t)^{i+1}\}$ as unknown leads to following algebraic linear system:

$$[J^i_{t+\Delta t}] \cdot \{\Delta u_g(t+\Delta t)^{i+1}\} = \{R^i_{t+\Delta t}\} \tag{4.55}$$

where $\{R^i_{t+\Delta t}\}$ is the residual vector of the momentum equation:

$$\{R^i_{t+\Delta t}\} = \{F^{ext}(t+\Delta t)\} + \{F^{int}(u_g(t+\Delta t)^i)\} - [M]\cdot\{\ddot{u}_g(t+\Delta t)^i\} - [C]\cdot\{\dot{u}_g(t+\Delta t)^i\} \tag{4.56}$$

and $[J^i_{t+\Delta t}]$ is the "*equivalent Jacobian matrix*" for the whole system:

$$\{J^i_{t+\Delta t}\} = \frac{1}{\beta\,\Delta t^2}\cdot[M] + \frac{\gamma}{\beta\,\Delta t}\cdot[C] + [K^i_{t+\Delta t}] \tag{4.57}$$

The vector $\{F^{int}(u_g(t+\Delta t)^i)\}$ and the matrix $[K^i_{t+\Delta t}]$ are the internal forces and the stiffness matrix of the system associated to the trial displacement configuration $\{u_g(t+\Delta t)^i\}$. In the case of simple elastic systems, there is an algebraic relationship between the forces and the displacements, then the computation of $\{F^{int}(u_g(t+\Delta t)^i)\}$ and $[K^i_{t+\Delta t}]$ is a quite simple operation. For more complex systems, such as elastoplastic isolator elements, there is a nonlinear relationship between forces and displacements and an iterative procedure is again necessary.
For each trial solution of the whole base-isolated system $\{u_g(t)^i\}$, a second nestled solver algorithm performs eleven steps (until convergence is reached) to determine the response of the *"CSSBearing_BVNC"* element. First four steps are preliminary while the iterative procedure involves the steps from 5 to 11.

<u>*Step 1*</u> - the element nodal displacements and velocities in global coordinates are extracted from the trial solution of the whole system and are transformed in local coordinates:

$$\{u_l(t)^i\} = [T_{gl}]\cdot\{u_g(t)^i\} \tag{4.58}$$

$$\{\dot{u}_l(t)^i\} = [T_{gl}]\cdot\{\dot{u}_g(t)^i\} \tag{4.59}$$

and then transformed from local to the basic coordinates:

$$\{u_b(t)^i\} = [T_{lb}]\cdot\{u_l(t)^i\} \tag{4.60}$$

$$\{\dot{u}_b(t)^i\} = [T_{lb}]\cdot\{\dot{u}_l(t)^i\} \tag{4.61}$$

Step 2 - the element radii in the two basic shear directions (Fig. 4.57) are calculated:

$$R_2(t)^i = \sqrt{{R_{eff}}^2 - \left(u_{3,b}(t)^i\right)^2} \tag{4.62}$$

$$R_3(t)^i = \sqrt{{R_{eff}}^2 - \left(u_{2,b}(t)^i\right)^2} \tag{4.63}$$

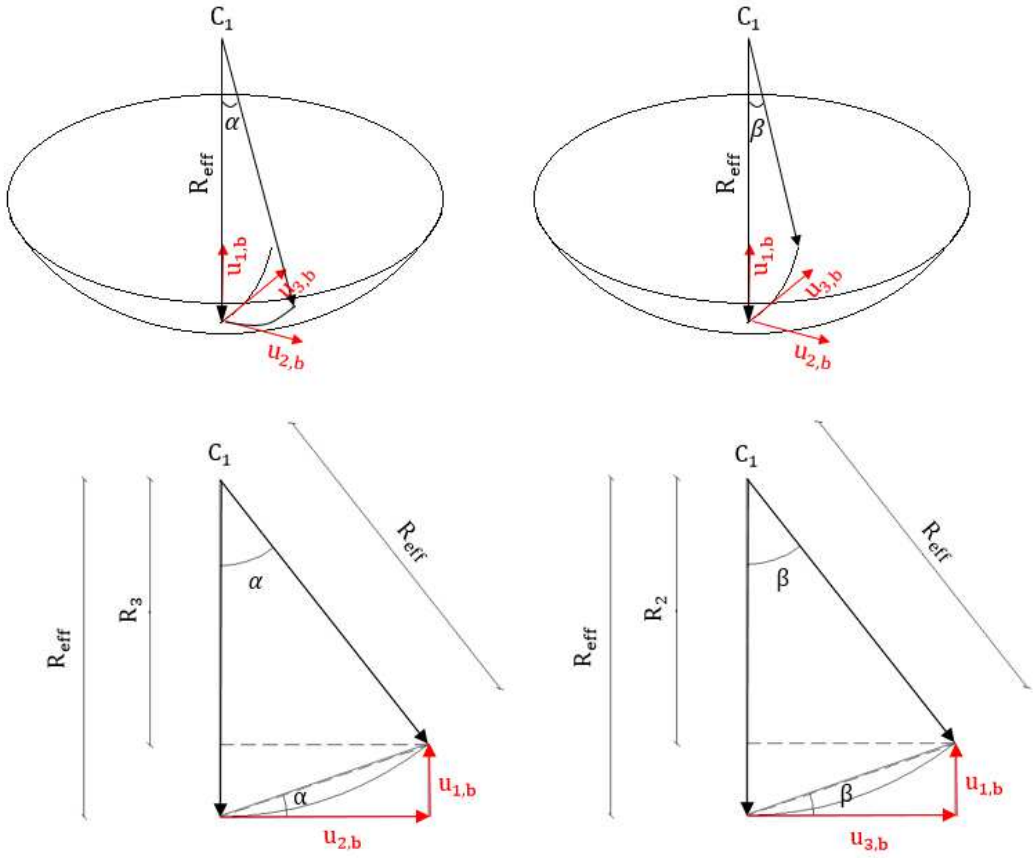

Figure 4.57. Three-dimensional representation of the displacement components (above) and in-plane definition of the element radii in the basic shear directions (below)

Step 3 - noting that for small incremental displacements the directions of vectors u_b and $\dot{u}_b$ are coincident and tangent to the motion trajectory (Fig. 4.57), the absolute sliding velocity in the basic reference system is calculated:

$$\left|\dot{u}_b(t)^i\right| = \sqrt{\left(\dot{u}_{1,b}(t)^i\right)^2 + \left(\dot{u}_{2,b}(t)^i\right)^2 + \left(\dot{u}_{3,b}(t)^i\right)^2} =$$

$$\sqrt{\left(\dot{u}_{2,b}(t)^i \cdot \frac{u_{2,b}(t)^i}{R_2(t)^i} + \dot{u}_{3,b}(t)^i \cdot \frac{u_{3,b}(t)^i}{R_3(t)^i}\right)^2 + \left(\dot{u}_{2,b}(t)^i\right)^2 + \left(\dot{u}_{3,b}(t)^i\right)^2} \tag{4.64}$$

Step 4 – since the response of the element in the basic axial direction is regulated by the elastic "*UniaxialMaterial*", the related internal force component is easily calculated:

$$q_{1,b}(t)^i = (EA/L) \cdot u_{1,b}(t)^i \tag{4.65}$$

where E is the young modulus (user input parameter), while A (equal to 1), and L are respectively the cross section area, and the length of the isolator element.

Step 5 - since the steps 6 to 11 depend on the basic components of the shear force of the isolator element ($q_{2,b}(t)^i$ and $q_{3,b}(t)^i$) that are not known a priori, an iterative procedure (Newton's method) is again introduced (j is the internal cyclic counter variable). At the time instant $t = 0s$, the state variables are initialized as:

$$\begin{cases} j = 1 \\ q_{2,b}(0)^{j,i} = q_{3,b}(0)^{j,i} = 0 \end{cases} \tag{4.66}$$

while for subsequent time steps:

$$\begin{cases} j = 1 \\ q_{2,b}(t)^{j,i} = q_{2,b}(t - \Delta t) \\ q_{3,b}(t)^{j,i} = q_{3,b}(t - \Delta t) \end{cases} \tag{4.67}$$

Step 6 - the trial element normal force in basic coordinates $N(t)^{j,i}$ is then calculated considering also the two contributions of the friction force f (which opposes the sliding motion along the tangent to the displacement trajectory) due to relative displacements (Fig. 4.58) and other two relevant to local rotations at nodes:

$$N(t)^{j,i} = -q_{1,b}(t)^{j,i} + q_{2,b}(t)^{j,i} \cdot \frac{u_{2,b}(t)^i}{R_2(t)^i} + q_{3,b}(t)^{j,i} \cdot \frac{u_{3,b}(t)^i}{R_3(t)^i} - q_{2,b}(t)^{j,i} \cdot u_{6,l}(t)^i + q_{3,b}(t)^{j,i} \cdot u_{5,l}(t)^i \tag{4.68}$$

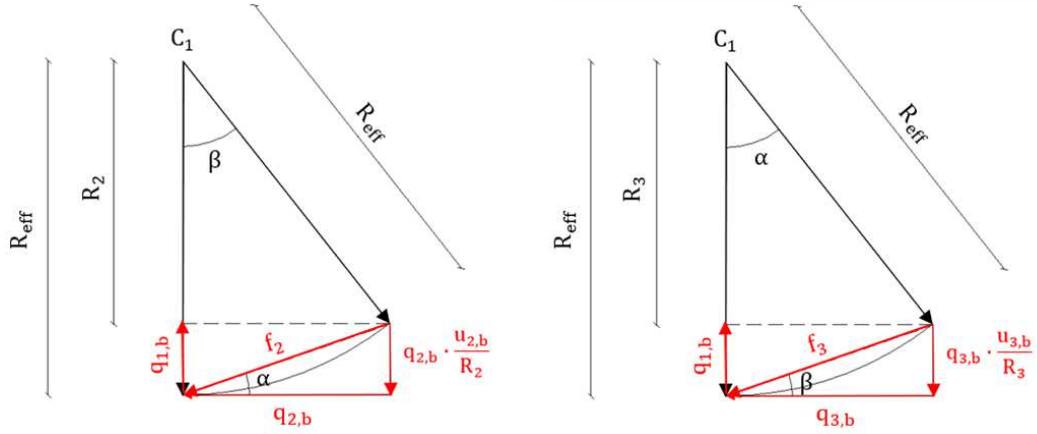

Figure 4.58. First (left) and second (right) contribution of the friction force to the element normal force in the basic system

Step 7 - since the plasticity model with isotropic hardening regulating the element response can be obtained by means of the effects superimposition shown in Fig. 4.59, the code calculates the stiffnesses of elastic and hysteretic components as follows:

$$K2_2(t)^{j,i} = \frac{N(t)^{j,i}}{R_2(t)^i} \tag{4.69}$$

$$K2_3(t)^{j,i} = \frac{N(t)^{j,i}}{R_3(t)^i} \tag{4.70}$$

$$K0_2(t)^{j,i} = K_{init} - K2_2(t)^{j,i} \tag{4.71}$$

$$K0_3(t)^{j,i} = K_{init} - K2_3(t)^{j,i} \tag{4.72}$$

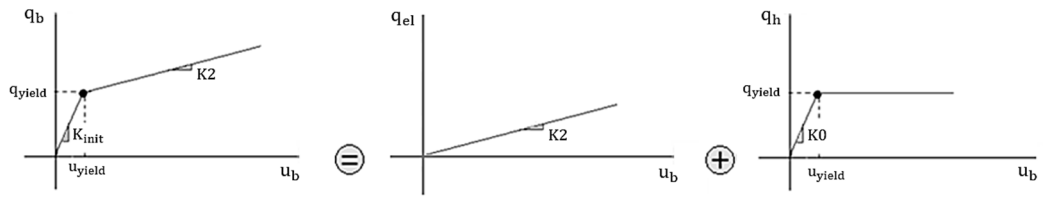

Figure 4.59. Plasticity model with isotropic hardening (left) obtained superimposing the elastic component (centre) with the hysteretic one (right)

Step 8 - the trial hysteretic and elastic components of the shear force are calculated:

$$q_{2,h}(t)^{j,i} = K0_2(t)^{j,i} \cdot u_{2,b,el}(t)^i = K0_2(t)^{j,i} \cdot \left[u_{2,b}(t)^i - u_{2,b,pl}(t-\Delta t)\right] \tag{4.73}$$

$$q_{3,h}(t)^{j,i} = K0_3(t)^{j,i} \cdot u_{2,b,el}(t)^i = K0_3(t)^{j,i} \cdot \left[u_{3,b}(t)^i - u_{3,b,pl}(t-\Delta t)\right] \tag{4.74}$$

$$q_{2,el}(t)^{j,i} = K2_2(t)^{j,i} \cdot u_{2,b}(t)^i \tag{4.75}$$

$$q_{3,el}(t)^{j,i} = K2_3(t)^{j,i} \cdot u_{3,b}(t)^i \tag{4.76}$$

Step 9 (yielding criterion) - the yielding of the element is checked by means of the following bidirectional criterion:

$$Y(t)^{j,i} = \left|q_h(t)^{j,i}\right| - q_{Yield}(t)^{j,i} \tag{4.77}$$

where $q_{Yield}(t)^{j,i}$ is the trial plastic threshold (Fig. 4.60-left) and $\left|q_h(t)^{j,i}\right| = \sqrt{(q_{2,h}(t)^{j,i})^2 + (q_{3,h}(t)^{j,i})^2}$ is the modulus of the resultant hysteretic force.

In general, during initial time steps preceding the actual sliding activation, the element is in the elastic range ($Y(t)^{j,i} \leq 0$) and the plastic threshold is regulated by a Coulomb friction model ($\mu = \mu_B = cost.$):

$$q_{Yield}(t)^{j,i} = \mu_B \cdot N(t)^{j,i} \tag{4.78}$$

where μ_B is the friction coefficient at sliding motion breakaway.

When the first yielding occurs ($Y(t)^{j,i} > 0$), the frictional behaviour is switched to the "*VNC_FrictionModel*" (Fig. 4.60-left) and the yielding force is instantaneously adjusted ($\mu = \mu_{VNC}(t)^i$):

$$q_{Yield}(t)^{j,i} = \mu_{VNC}(t)^{j,i} \cdot N(t)^i \tag{4.79}$$

The plastic domain definition can be therefore summarized as (Fig. 4.60-right):

$$\begin{cases} q_{Yield}(t)^{j,i} = \mu_B \cdot N(t)^{j,i} & t \le t_{breakaway} \\ q_{Yield}(t)^{j,i} = \mu_{VNC}(t)^{j,i} \cdot N(t)^i & t > t_{breakaway} \end{cases} \tag{4.80}$$

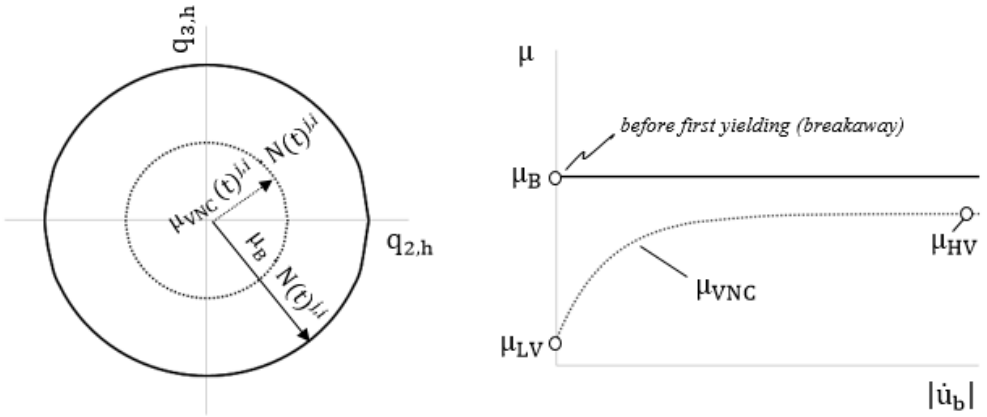

Figure 4.60. Bidirectional plasticity domain (left) and related friction models that regulate the instantaneous trial yielding threshold (right)

Step 10a (elastic step) - if $Y(t)^i \le 0$, the element is in the elastic range and trial shear force components are updated:

$$q_{2,b}(t)^{j,i} = q_{2,h}(t)^{j,i} + q_{2,el}(t)^{j,i} - N(t)^{j,i} \cdot u_{6,l}(t)^i \tag{4.81}$$

$$q_{3,b}(t)^{j,i} = q_{3,h}(t)^{j,i} + q_{3,el}(t)^{j,i} + N(t)^{j,i} \cdot u_{5,l}(t)^i \tag{4.82}$$

and the related components of the element stiffness matrix are set as:

$$K_{2,2,b}(t)^{j,i} = K_{init} \tag{4.83}$$

$$K_{2,3,b}(t)^{j,i} = K_{3,2,b}(t)^{j,i} = 0 \tag{4.84}$$

$$K_{3,3,b}(t)^{j,i} = K_{init} \tag{4.85}$$

Step 10b (plastic step) - if $Y(t)^i > 0$, the element is in the plastic range and the code executes a step known as return mapping method (Fig. 4.61). Trial consistency parameters are first calculated:

$$d\gamma_2(t)^{j,i} = Y(t)^{j,i} / K0_2(t)^{j,i} \tag{4.86}$$

$$d\gamma_3(t)^{j,i} = Y(t)^i / K0_3(t)^{j,i} \tag{4.87}$$

leading to the following trial plastic displacement components:

$$u_{2,b,pl}(t)^{j,i} = u_{2,b,pl}(t-\Delta t) + \Delta u_{2,b,pl}(t)^{j,i} = u_{2,b,pl}(t-\Delta t) + d\gamma_2(t)^{j,i} \cdot \frac{q_{2,h}(t)^{j,i}}{|q_h(t)^{j,i}|} \tag{4.88}$$

$$u_{3,b,pl}(t)^{j,i} = u_{3,b,pl}(t-\Delta t) + \Delta u_{3,b,pl}(t)^{j,i} = u_{3,b,pl}(t-\Delta t) + d\gamma_3(t)^{j,i} \cdot \frac{q_{3,h}(t)^{j,i}}{|q_h(t)^{i}|} \tag{4.89}$$

Finally, the trial components of the basic shear force components are updated:

$$q_{2,b}(t)^{j,i} = q_{Yield}(t)^{j,i} \cdot \frac{q_{2,h}(t)^{j,i}}{|q(t)^{j,i}|} + q_{2,el}(t)^{j,i} - N(t)^{j,i} \cdot u_{6,l}(t)^{i} \tag{4.90}$$

$$q_{3,b}(t)^{j,i} = q_{Yield}(t)^{j,i} \cdot \frac{q_{3}(t)^{j,i}}{|q_h(t)^{j,i}|} + q_{3,el}(t)^{j,i} + N(t)^{j,i} \cdot u_{3,l}(t)^{i} \tag{4.91}$$

and the related components of the element stiffness matrix are set as:

$$K_{2,2,b}(t)^{j,i} = K0_2(t)^{j,i} \cdot \frac{q_{Yield}(t)^{j,i} \cdot (q_{,h3}(t)^{j,i})^2}{|q(t)^{j,i}|^3} + K2_2(t)^{j,i} \tag{4.92}$$

$$K_{2,3,b}(t)^{j,i} = -K0_3(t)^{j,i} \cdot \frac{q_{Yield}(t)^{j,i} \cdot (q_{2,h}(t)^{j,i} \cdot q_3(t)^{j,i})}{|q(t)^{j,i}|^3} \tag{4.93}$$

$$K_{3,2,b}(t)^{j,i} = -K0_2(t)^{j,i} \cdot \frac{q_{Yield}(t)^{j,i} \cdot (q_{3,h}(t)^{j,i} \cdot q_2(t)^{j,i})}{|q(t)^{j,i}|^3} \tag{4.94}$$

$$K_{3,3,b}(t)^{j,i} = K0_3(t)^{j,i} \cdot \frac{q_{Yield}(t)^{j,i} \cdot (q_{2,h}(t)^{j,i})^2}{|q(t)^{j,i}|^3} + K2_3(t)^{j,i} \tag{4.95}$$

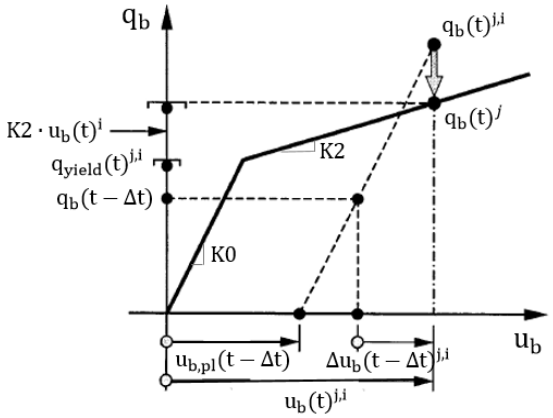

Figure 4.61. Return mapping algorithm: incremental plastic step calculated from the elastic stage of the previous time instant (adapted from [55])

Step 11 (convergence check) - in the last step, the program checks the solution convergence by means of the following criterion:

$$\begin{cases} \sqrt{\left(q_{2,b}(t)^{j,i} - q_{2,b}(t)^{(j-1),i}\right)^2 + \left(q_{3,b}(t)^{j,i} - q_{3,b}(t)^{(j-1),i}\right)^2} \leq Tol \\ j \leq Max\ Iter \end{cases} \tag{4.96}$$

The algorithm is applied iteratively, at each iteration the steps from 6 to 11 are evaluated and the variable j is incremented ($j = j + 1$) until the convergence is reached. If the maximum number of iterations ($Max\ Iter$) is reached the algorithm fails and OpenSees® returns an error. The convergence is verified using a stopping criterion based on control of increments: the convergence is reached when the difference between the element shear forces in two consecutive iterations is less than a given tolerance. This is justified by the fact that the Newton's method is adopted [73]. Once reached the convergence, components of $\{q_b(t)^{j,i}\}$ are used to compute the element stiffness matrix in basic coordinates $[K_b]$. The same is transformed in local components and "*P-Delta*" and "*geometric stiffness*" terms are added. The local stiffness matrix is lastly transformed in global components and assembled to other elements contributions to obtain the system of equations governing the response of the whole base-isolated structure.

4.5.2 Test analyses

The absence of consistency errors in the new element implementation has been verified by means of comparison with the results obtained from analyses carried out in the OpenSees® (v.2.5.0) for frictional models available in the official libraries of the code such as the *"Coulomb"*, and the "*VelDependent*".

A simple SDOF model (Fig. 4.62), composed of a concentrated mass $m = 100tons$ with an applied vertical load $N = m \cdot g = 9.81kN$, and connected to the ground by means of the isolator element, is used to perform the two test analyses. The isolator element has an effective radius $R = 3500mm$ and the initial elastic stiffness is set as $k_{init} = 100 \cdot (N/R_{eff})$. A unidirectional sinusoidal seismic input having amplitude $PGA = 0.40g$ and period $T = 1.0s$ is applied to the ground level.

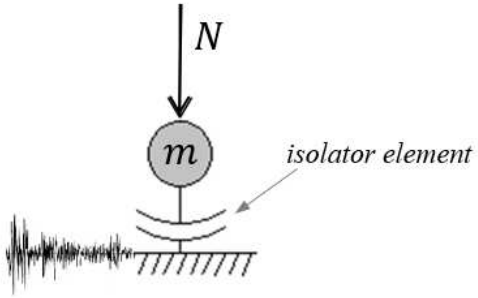

Figure 4.62. SDOF model adopted for the test analyses

Tables 4.22 and 4.23 respectively provide the sets of input parameters assigned to both the standard and the new code in order to reproduce the same *"Coulomb"* and "*VelDependent*" friction models.

standard code	**new code**	
	Coulomb frict. model (before breakaway)	**BVNC frict. Model** (after breakaway)
$\mu = 0.10$	$\mu_B = 0.10$	$\alpha = \beta = C_{ref} = 10^{100}\ (\rightarrow +\infty)$ $n_{HV} = 1$ $a_{HV} = 0.10\ (n.b.\ \mu_{BVNC} = 0.10)$

Table 4.22. Standard (left) and new code (right) input parameters to reproduce the same *"Coulomb"* friction

standard code	**new code**	
	Coulomb frict. model (before breakaway)	**BVNC frict. Model** (after breakaway)
$\mu_{LV} = 0.05$ $\mu_{HV} = 0.15$ $\alpha = 0.005$	$\mu_B = 0.05$	$\beta = C_{ref} = 10^{100}\ (\rightarrow +\infty)$ $\alpha = 0.005$ $a_{LV} = 0.05\ , n_{HV} = 1\ (n.b.\ \mu_{LV} = \mu_B = a_{LV})$ $a_{HV} = 0.15\ , n_{HV} = 1\ (n.b. \mu_{HV} = a_{HV})$

Table 4.23. Standard (left) and new code (right) input parameters to reproduce the same "*VelDependent*" friction

Fig. 4.63 show the comparison between the hysteretic loops (left) and the displacement time-histories (right) obtained with the standard and the new element code for the *"Coulomb"* friction. Moreover, Fig. 4.64 represent the same comparison for the "*VelDependent*" friction model. In both cases, the plots are perfectly overlapped witnessing the absence of consistency errors in the new element code and its capability to reproduce the two simpler frictional models already implemented in the standard OpenSees® v. 2.5.0.

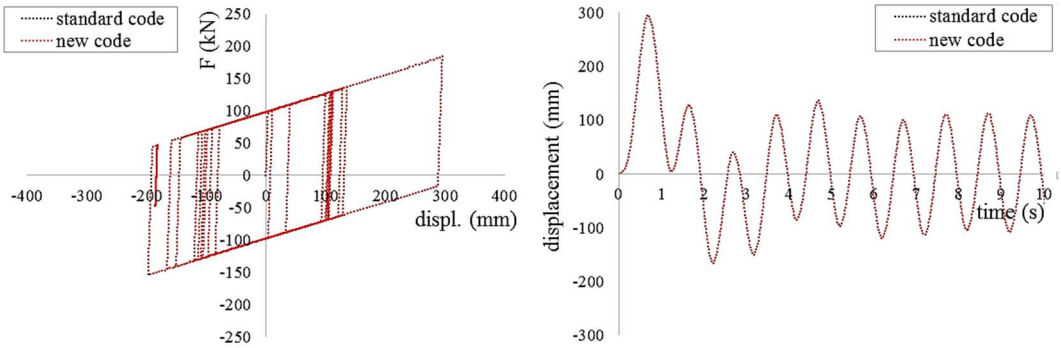

Figure 4.63. *"Coulomb"* friction: comparison between the hysteretic loops (left) and the displacement time-histories (right) obtained with the two codes

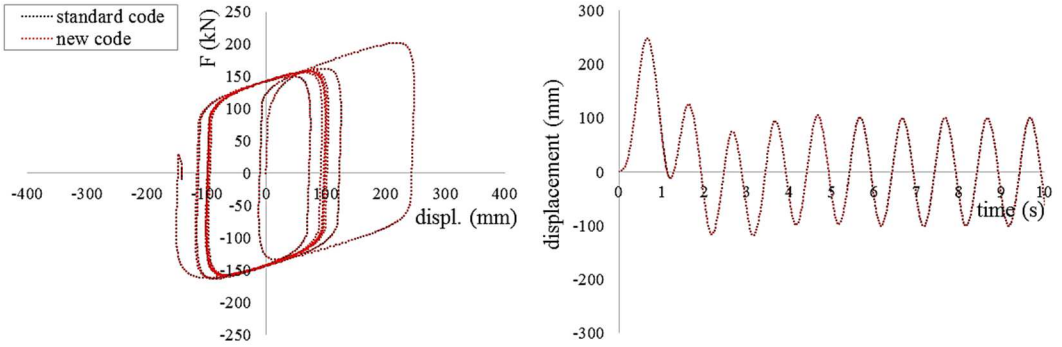

Figure 4.64. "*VelDependent*" friction: comparison between the hysteretic loops (left) and the displacement time-histories (right) obtained with the two codes

In order to appreciate the capability of the new formulation to simulate the breakaway effect, another analysis is carried out in the modified code ("*BV*" friction subcase, see section 4.4.4) with the same previous input parameters with the exception of an increased static friction coefficient at the motion breakaway μ_B (Table 4.24).

Coulomb frict. model (before breakaway)	**BVNC frict. Model** (after breakaway)
$\mu_B = 0.30$	$C_{ref} = 10^{100}\ (\rightarrow +\infty)$ $\alpha = 0.005$ $\beta = 1$ $a_{ST} = 0.30\ , n_{ST} = 1\ (n.b. \mu_{ST} = \mu_B = a_{ST})$ $a_{LV} = 0.05\ , n_{HV} = 1\ (n.b. \mu_{LV} = a_{LV})$ $a_{HV} = 0.15\ , n_{HV} = 1\ (n.b.\ \mu_{HV} = a_{HV})$

Table 4.24. New code input parameters for the "*BV*" friction model

Fig. 4.65-left shows the computed hysteretic loops: it can be clearly noted that the new code is capable to reproduce the peak of shear force in the isolator element due to the static friction coefficient at the motion breakaway μ_B. The delay of the isolator sliding activation causes in addition a slight decrease (-21.0mm) of the maximum displacements (Fig. 4.65-right). It is worth noting that, for more complex multi-story frames, it has been already demonstrated that the breakaway effect can have a significant influence also on the maximum storey drifts and on the peak accelerations at each floor level (see section 4.3).

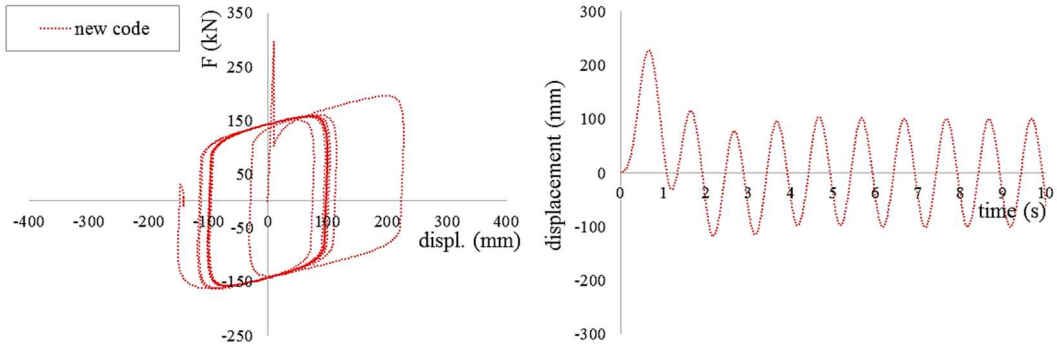

Figure 4.65. "*BV*" friction model: hysteretic loops (left) and the displacement time-histories (right)

In the last analysis, the "*Frictional heating effect*" (available in the new element formulation) is also introduced ("*BVC*" friction subcase, see section 4.4.4) by properly setting the two related input parameters (Table 4.25).

Coulomb frict. model (before breakaway)	**BVNC frict. Model** (after breakaway)
$\mu_B = 0.30$	$\alpha = 0.005$ $\beta = 1$ $C_{ref} = 5 \cdot 10^{15}, \gamma = 1.0$ $a_{LV} = 0.30\,, n_{HV} = 1$ $a_{LV} = 0.05\,, n_{HV} = 1$ $a_{HV} = 0.15\,, n_{HV} = 1$

Table 4.25. New code input parameters for the "*BVC*" friction model

Fig. 4.66-left shows the computed hysteretic loops: a progressive reduction of the dynamic friction coefficient, and hence, of the dissipated energy and of the equivalent viscous damping of the isolator element, with the cumulate heat flow at the sliding surface is quite evident. With respect to the previous case, this causes also a slight increase (+5.0mm) of the peak displacements during the last three-four oscillations of the isolator (Fig. 4.66-right).

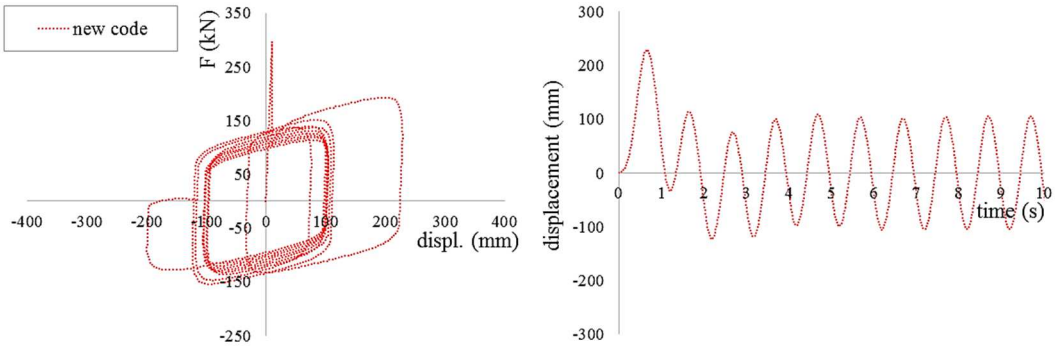

Figure 4.66. "*BVC*" friction model: hysteretic loops (left) and the displacement time-histories (right)

4.5.3 Unit-system for input parameters

As for standard OpenSees® code, the input parameters regulating the dynamic response of the new *"CSSBearing_BVNC"* element are dimensionless [70]. This implies that all input values must be consistent with the unit-system adopted for the fundamental physical quantities. For example, in the analyses carried out in the previous section, the unit-system adopted for fundamental quantities is:

- mass *(kg)*;
- length *(mm)*;
- time *(s)*.

leading to the following units of measure for velocity, acceleration, and force quantities:

- velocity (mm/s);
- acceleration (mm/s^2);
- force $(1kg \cdot 1\,mm/s^2 = 10^{-3}N)$.

and to the units of measure for the "*BVNC*" friction model input parameters reported in Table 4.26.

effect	**parameter**	**unit**
velocity and breakaway	α	s/mm
	β	s/mm
normal load	a_{ST}	$(10^{-3}N)^{-1}$
	n_{ST}	-
	a_{LV}	$(10^{-3}N)^{-1}$
	n_{LV}	-
	a_{HV}	$(10^{-3}N)^{-1}$
	n_{HV}	-
frictional heating	C_{ref}	$((10^{-3}N) \cdot mm^2)) \,/\, s$
	γ	-

Table 4.26. Unit-system for the input parameters of the new *"BVNC"* friction model

4.6 Chapter references

[1] CEN, Eurocode 8 (2004) "*Design of structures for earthquake resistance—Part 1: General rules, seismic actions and rules for buildings*", EN1998-1:2004, European Committee for Standardization, Bruxelles, Belgium

[2] CEN, Eurocode 8 (2005) "*Design of structures for earthquake resistance—Part 2: Bridges*", EN1998-2:2005+A1:2011, European Committee for Standardization, Bruxelles, Belgium

[3] Decanini, L., Gavarini, C., Mollaioli, F. (2000) "*Some remarks on the Umbria-Marche earthquakes of 1997*", European Earthquake Engineering, 2000; 3, pp. 18-48

[4] Huang, Y., Wu, J.P., Zhang, T.Z., Zhang, D.N. (2008) "*Relocation of the M 8.0 Wenchuan earthquake and its aftershock sequence*", Science in China (Series D), Vol. 51(12), pp. 1703–1711, DOI: 10.1007/s11430-008-0135-z

[5] Di Sarno, L., Elnashai, A.S., Manfredi, G. (2011) "*Assessment of RC columns subjected to horizontal and vertical ground motions recorded during the 2009 L'Aquila (Italy) earthquake*", Engineering Structures,Vol. 33(5), pp. 1514-1535, DOI:10.1016/j.engstruct.2011.01.023

[6] Di Sarno, L., Yenidogan, C., Erdik, M. (2013) "*Field evidence and numerical investigation of the Mw = 7.1 October 23 Van, Tabanli and the Mw > 5.7 November Earthquakes of 2011*", Bulletin of Earthquake Engineering, Vol. 11(1), pp. 313-346, DOI: 10.1007/s10518-012-9417-0

[7] Motosaka, M., Mitsuji, K. (2012) "*Building damage during the 2011 off the Pacific coast of Tohoku Earthquake*", Soils and Foundations, Vol. 52(5), pp. 929-944, DOI:10.1016/j.sandf.2012.11.012

[8] Carydis, P., Castiglioni, C., Lekkas, E., Kostaki, I., Lebesis, N., Drei, A. (2012) "*The Emilia Romagna, May 2012 earthquake sequence. The influence of the vertical earthquake component and related geoscientific and engineering aspects*", Ingegneria Sismica – International Journal of Earthquake Engineering, Vol. XXIX, pp. 31-58

[9] Dicleli, M., Buddaram S. (2006) "*Effect of isolator and ground motion characteristics on the performance of seismic-isolated bridges*", Earthquake Engineering and Structural Dynamics,Vol. 35(2), pp. 223-250

[10] Cardone, D. (2012) "*Re-centering capability of flag-shaped seismic isolation systems*", Bulletin of Earthquake Engineering,Vol. 10(4), pp. 1267–1284, DOI 10.1007/s10518-012-9343-1

[11] Cardone, D., Gesualdi, G., Brancato, P. (2015) "*Restoring capability of friction pendulum seismic isolation systems*", Bulletin of Earthquake Engineering, Vol. 13(8), pp 2449-2480, DOI: 10.1007/s10518-014-9719-5

[12] Anderson, J.C., Bertero, V.V. (1987) "*Uncertainties in establishing design earthquakes*", Journal of Structural Engineering, Vol. 113(8), pp. 1709–1724

[13] Alavi, B., Krawinkler, H. (2001) "*Effects of near-fault ground motions on frame structures*", Blume Center Report 138, Stanford, California

[14] Mavroeidis, G.P., Dong, G., Papageorgiou, A.S. (2004) "*Near-fault ground motions, and the response of elastic and inelastic single degree-of-freedom (SDOF) systems*", Earthquake Engineering and Structrual Dynamics, Vol. 33(9), pp. 1023–1049

[15] Katsaras, C.P., Panagiotakos, T.B., Kolias, B. (2008) "*Restoring capability of bilinear hysteretic seismic isolation systems*", Earthquake Engineering and Structural Dynamics, *Vol.*37(4), pp. 557-575, DOI: 10.1002/eqe.772

[16] CEN, European Committee for Standardization (2009) "*EN 15129: Anti-Seismic Devices*", Bruxelles, Belgium

[17] Medeot, R. (2013) "*Re-centring capability of seismic isolation systems: a controversial matter*", Proceedings of the XV ANIDIS National Conference on Earthquake Engineering, Padua, Italy

[18] Medeot, R. (2004) "*Re-centring capability evaluation of seismic isolation systems based on energy concepts*", Proceedings of the 13th World Conference on Earthquake Engineering, paper 3106, Vancouver, Canada

[19] Berton, S., Infanti, S., Castellano, M.G., Hikosaka, H. (2006) "*Self-centring capacity of seismic isolation systems*", Structural Control and Health Monitoring, Vol. 4(6), pp. 895–914, DOI: 10.1002/stc.188

[20] Sarlis, A.A., Constantinou, M.C., Reinhorn, A.M. (2013) "*Shake table testing of Triple Friction Pendulum Isolators under extreme conditions*", Technical Report NCEER-13-0011, National Center for Earthquake Engineering Research

[21] Quaglini, V., Gandelli, E., Dubini, P. (2016) "*Experimental investigation of re-centring capability of curved surface sliders*", Structural Control and Health Monitoring, published online, DOI: 10.1002/stc.1870

[22] McKenna, F., Fenves, G.L., Scott, M.H., Jeremic, B. (2000) "*Open System for Earthquake Engineering Simulation (OpenSees)*", Pacific Earthquake Engineering Research Center (PEER), Berkeley, USA

[23] Constantinou, M.C., Mokha, A., Reinhorn, A.M. (1990) "*Teflon bearings in base isolation. II: modelling*", Journal of Structural Engineering, Vol. 116(2), pp. 455–474, DOI: 10.1061/(ASCE)0733-9445(1990)116:2(455)

[24] Dolce. M., Cardone, D., Croatto, F. (2005) "*Frictional behaviour of steel-PTFE interfaces for seismic isolation*", Bulletin of Earthquake Engineering, Vol. 3(1), 75-99, DOI: 10.1007/s10518-005-0187-9

[25] Quaglini, V., Dubini, P., Poggi, C. (2012) "*Experimental assessment of sliding materials for seismic isolation systems*", Bulletin of Earthquake Engineering, Vol. 10(2), pp. 717–740, DOI: 10.1007/s10518-011-9308-9

[26] Ancheta, T.D., Darragh, R.B., Stewart, J.P., Seyhan, E., Silva, W.J., Chiou, B.S.J., Wooddell, K.E., Graves, R.W., Kottke, A.R., Boore, D.M., Kishida, T., Donahue, J.L. (2013), *PEER NGA-West2 Database*, PEER 2013/03, Pacific Earthquake Engineering Research Center (PEER), Berkeley, USA

[27] Calvi, G.M., Pietra, D., Moratti, M. (2010) "*Criteri per la progettazione di dispositivi di isolamento a pendolo scorrevole*", Progettazione Sismica, Vol. 3(1), pp. 7-30

[28] Baker, J.W. (2007) "*Quantitative Classification of Near-Fault Ground Motions Using Wavelet Analysis*", Bulletin of the Seismological Society of America, Vol. 97(5), pp. 1486–1501, DOI:10.1785/0120060255

[29] Constantinou, M.C., Tsopelas, P., Kim, Y-S., Okamoto, S. (1993) "*NCEER-Taisei Corporation research program on sliding seismic isolation systems for bridges: experimental*

and analytical study of a Friction Pendulum System [FPS]", Report NCEER-93-0020, National Center for Earthquake Engineering Research, Buffalo

[30] Constantinou, M.C., Whittaker, A.S., Kalpakidis, Y., Fenz, D.M., Warn, G.P. (2007) "*Performance of seismic isolation hardware under service and seismic loading*", Report MCEER-07-0012, National Center for Earthquake Engineering Research, Buffalo

[31] Tsai, C.S., Chen, W.-S., Chiang, T-C., Chen, B-J. (2006) "*Component and shaking table tests for full-scale multiple friction pendulum system*" Earthquake Engineering and Structural Dynamics, Vol. 35, pp. 1653-1675

[32] Tsopelas, P., Constantinou, M.C. (1994) "*NCEER-Taisei Corporation Research Program on sliding seismic isolation systems for bridges: experimental and analytical study of a system consisting of sliding bearings and fluid restoring force/damping devices*", Report NCEER-94-0014, National Center for Earthquake Engineering Research, Buffalo

[33] Braun, C. (2009) "*The sliding isolation pendulum – an improved recentring bridge bearing*" Steel Constructions, Vol. 2, pp. 203-206

[34] Quaglini, V., Bocciarelli, M., Gandelli, E., Dubini P. (2014) "*Numerical Assessment of Frictional Heating in Sliding Bearings for Seismic Isolation*", Journal of Earthquake Engineering, Vol. 18(8), pp. 1198-1216, DOI:10.1080/13632469.2014.924890

[35] ASCE/SEI 7-10 (2010) "*Minimum Design Loads for Buildings and Other Structures*", American Society of Civil Engineers ASCE, Reston

[36] AASHTO (2014) "*Guide Specifications for Seismic Isolation Design*", American Association of State Highway and Transportation Officials, Washington DC

[37] Clarke, C.S.J., Buchanan, R., Efthymiou, M. (2005) "*Structural platform solution for seismic arctic environments – Sakhalin II offshore facilities*", Proceedings of Offshore Technology Conference, Houston, Texas, paper OTC-17378-PP

[38] Drozdov, Y.N., Nadein, V.A., Puchkov, V.N., Puchkov, M.V. (2008) "*Heat state of pendulum sliding bearings under seismic effects*" Journal of Friction and Wear, Vol. 29, pp. 265-270

[39] Kumar, M., Whittaker, A.S., Constantinou, M.C. (2015) "*Characterizing friction in sliding isolation bearings*" Earthquake Engineering and Structural Dynamics, Vol. 44, pp. 1409-1425

[40] Wolff, E. (1999) "*Frictional heating in sliding bearings and an experimental study of high friction materials*", MS Dissertation, University at Buffalo, State University of New York, Buffalo

[41] Quaglini, V. and Dubini, P. (2011) "*Assessment of sliding materials for pendulum isolation bearings*" Proceedings of the 7th World Conference on Joints, Bearings and Seismic Systems for Concrete Structures, Las Vegas, Nevada

[42] ABAQUS (2011) "*Standard User's Manual - Version 6.10*", Dassault Systèmes Simulia Corp., Providence

[43] Incropera, F.P., Dewitt, D.P., Bergman, T.L., Lavine, A.S. (2006) "*Fundamentals of heat and mass transfer*", 6th ed., Hoboken, John Wiley and Sons, New Jork

[44] Pooley, C.M., Tabor, D. (1972) "*Friction and Molecular Structure: The Behaviour of Some Thermoplastics*", Proceedings of the Royal Society of London. Series A, Mathematical and Physical Sciences

[45] Constantinou, M.C., Caccese, J., Harris, H.G. (1987) "*Frictional characteristics of Teflon–steel interfaces under dynamic conditions*", Earthquake Engineering & Structural Dynamics, Vol. 15(6), pp. 751–759, DOI: 10.1002/eqe.4290150607

[46] Hwang, J.S., Chang, K.C., Lee, G.C. (1990) "*Quasi-Static and Dynamic Sliding Characteristics of Teflon—Stainless Steel Interfaces*", Journal of Structural Engineering, Vol. 116(10), pp. 2747-2762,

[47] Mokha, A., Constantinou, M.C., Reinhorn A. (1990) "*Teflon Bearings in Base Isolation I: Testing*", Journal of Structural Engineering, Vol. 116:2(438), pp. 438-454, DOI:10.1061/(ASCE)0733-9445

[48] Mokha, A., Constantinou, M.C., Reinhorn A. (1993) "*Verification of Friction Model of Teflon Bearings under Triaxial Load*", Journal of Structural Engineering, Vol. 119(1), pp. 240-261

[49] Bondonet, G., Filiatrault, A. (1997) "*Frictional Response of PTFE Sliding Bearings at High Frequencies*", Journal of Bridge Engineering, Vol. 2(4), pp. 139-148, DOI: http://dx.doi.org/10.1061/(ASCE)1084-0702(1997)

[50] Constantinou, M.C., Whittaker, A.S., Kalpakidis, Y., Fenz, D.M., Warn, G.P. (2007) "*Performance of Seismic Isolation Hardware under Service and Seismic Loading*", Report MCEER-07-0012

[51] Mokha, A., Constantinou, M.C., Reinhorn A. (1988) "*Teflon Bearings in Aseismic Base Isolation: Experimental Studies and Mathematical Modelling*", Technical Report NCEER-880038

[52] Chang, K., Hwang, J., Lee G. (1990) "*Analytical Model for Sliding Behavior of Teflon-Stainless Steel Interfaces*", Journal of Engineering Mechanics, Vol. 116(12), pp. 2749-2763, DOI: http://dx.doi.org/10.1061/(ASCE)0733-9399(1990)116:12(2749)

[53] Constantinou, M.C., Mokha, A., Reinhorn A. (1990) "*Teflon bearings in base isolation II: modeling*", Journal of Structural Engineering, Vol. 116(2), pp. 455-474, DOI: 10.1061/(ASCE)0733-9445(1990)116:2(455)

[54] Lomiento, G., Bonessio, N., Benzoni G. (2013) "*Friction Model for Sliding Bearings under Seismic Excitation*", Journal of Earthquake Engineering, Vol. 17(8), pp. 1162-1191, DOI: http://dx.doi.org/10.1080/13632469.2013.814611, 1162-1191

[55] Simo, J.C., Huges T.J.R. (1998) "*Computational inelasticity*", Springer

[56] Park, Y.J., Wen, Y.K., Ang, A.H.S. (1986). "*Random vibration of hysteretic systems under bi-directional ground motions*", Earthquake Engineering and Structural Dynamics, Vol. 14, pp. 543-557

[57] Mosqueda, G., Whittaker, A.S., Fenves, G.L., Mahin S.A. (2004) "*Experimental and Analytical Studies of the Friction Pendulum System for the Seismic Protection of Simple Bridges*", Report No. UCB/EERC 2004-01

[58] Computers and Structures (1997) "*SAP2000 Analysis Reference*", Vol. 1

[59] Tsopelas, P.C., Roussis, P.C., Constantinou, M.C., Buchanan, R., Reinhorn A.M. (2005) "*3D-BASIS-ME-MB: Computer Program for Nonlinear Dynamic Analysis of Seismically Isolated Structures*", Report MCEER-05-0009

[60] Tsopelas, P.C., Constantinou, M.C., Reinhorn, A.M (1994) "*3D-BASIS-ME: Computer program for nonlinear dynamic analysis of seismically isolated single and multiple structures and liquid storage tanks*" , Report NCEER-94-0010

[61] Huang, W.-H. (2002) "*Bi-directional testing, modeling, and system response of seismically isolated bridges*", P.h.D. Dissertation, Department of Civil and Environmental Engineering, University of California, Berkele

[62] Fagà, E., Ceresa, P., Nascimbene, R., Moratti, M., Pavese. A. (2015) "*Modelling Curved Surface Sliding Bearings with Bilinear Constitutive Law: Effects on the Response of Seismically Isolated Buildings*", Materials and Structures, Vol. 49(6), pp. 2179-2196, DOI: 10. 1617/s11527-015-0642-2

[63] Constantinou, M.C., Tsopelas, P., Kasalanati, A., Wolff E.D. (1999) "*Property modification factors for seismic isolation bearings*", Report MCEER-99-0012

[64] NTC (2008) "*Approvazione delle nuove norme tecniche per le costruzioni*", Gazzetta Ufficiale della Repubblica Italiana n. 29 del 4 febbraio 2008 – Suppl. Ordinario n. 30, (in Italian)

[65] Ambraseys, N., Smit, P., Sigbjornsson, R., Suhadolc, P., Margaris, B. (2002) Internet-Site for European Strong-Motion Data, European Commission, Research-Directorate General, Environment and Climate Programme, http://www.isesd.cv.ic.ac.uk/ESD/

[66] Iervolino, I., Galasso, C., Cosenza E. (2010) "*REXEL: computer aided record selection for code-based seismic structural analysis*", Bulletin of Earthquake Engineering, Vol. 8(2), pp. 339-362, DOI: 10.1007/s10518-009-9146-1

[67] Bowden, F.P., Tabor, D. (1964) "*The friction and lubrication of solids – part II*" Oxford University Press, London, Great Britain

[68] MathWorks, Matlab Documentation, available online: http://it.mathworks.com/help/matlab/index.html?s_tid=gn_loc_drop

[69] Seible, F., Benzoni, G., Filiatrault, A., Post, T., Mellon, D. (2000) "*Performance validation of large seismic response modification devices*" , Proceedings of the 12th World Conference on Earthquake Engineering, Auckland, New Zeland

[70] OpenSeesWiki, online manual, available at: http://opensees.berkeley.edu/wiki/index.php/Main_Page

[71] Kumar, M. (2015) "*Seismic isolation of nuclear power plants using elastomeric bearings*", PhD dissertation

[72] Cook, R.D. (1995) "*Finite element modeling for stress analysis*", John Whiley & sons

[73] Quarteroni, A., Sacco, R., Saleri, F. (2007) "*Numerical mathematics*", Springer

CHAPTER 5

Conceptual design of seismic-retrofitting with CSS isolators

5.1 Introduction

The conceptual design described in the following section is developed per steps and, gradually increasing the complexity of the required calculations (from preliminary equivalent response spectra analyses up to nonlinear dynamic analyses), aims at: (1) defining a robust procedure for the design of seismic retrofitting interventions; (2) identifying the optimal solution with respect to target performances for the protection of both structural and non-structural components; (3) evaluating the effectiveness of the proposed solution (fault tree analysis); (4) obtaining output results more representative of the actual response of structures implementing CSS isolators using refined hysteretic models calibrated by means of experimental data.

5.2 Steps of the conceptual design

Step 1 - *Reference seismic scenario*

This step aims at selecting the seismic input for dynamic analyses at each design level defined according to the reference Building Code. A preliminary analysis of the selected ground motions (assessment of frequency content) is conducted in order to highlights potential issues related to base isolation implementation.

1.1) definition of the reference elastic spectrum (target spectrum) for each seismic design level (or limit state - see section 1.5.3) according to the Italian Building Code [1];

1.2) selection of three or seven accelerograms (recorded ground motions) matching the target spectrum of relevant limit state;

1.3) detect possible critical frequencies for seismic isolation (that is significant frequency contents at high vibration periods - typical of soft foundation soils).

Step 2 – Layout of the fault tree analysis

In this step, the building is decomposed in all its structural and non-structural components (e.g. electric and hydraulic plants) and technological content (e.g. medical equipment for hospitals). All these elements are organized in a fault tree diagram considering specific failure thresholds for each type of element (see section 3.3). This can be summarize in two substeps:

2.1) identification of structural typologies (cross sections of beams and columns) and definition of relevant ultimate strength to bending moments (M_{Rd}), shear (V_{Rd}), and compression loads (N_{Rd}) (see section 3.3.1);

2.2) definition of the capacity models for non-structural components (acceleration and drift sensitive elements) and technological content (see section 3.3.3).

Step 3 – Analyses on the as-built configuration

This step aims at evaluating the seismic performance of the as-built configuration of the building. Nonlinear dynamic analyses are carried out and obtained results are processed by means of the previously defined fault tree analysis to detect possible damages to both structural and non-structural elements. Within this step, the engineer should:

3.1) define the as-built structural model (layout of the resisting frame, materials properties, gravity and seismic loads);

3.2) perform modal analysis to determine mode shapes and natural frequencies;

3.3) carry out nonlinear dynamic analyses applying the previously selected ground motions for each seismic design level. Among requested outputs there should be the internal actions of the most critical structural elements, the peak floor accelerations, and the maximum inter-storey drifts at each level;

3.4) evaluate the obtained results by means of the fault tree analysis in order to detect possible damages to both structural and non-structural components.

Step 4 – Isolation system target performances

The preliminary design of optimal CSS isolators for the seismic retrofitting intervention (step 5) is based on the fulfilment of specific target performances for the protection of both structural and non-structural elements. The definition of these target performances requires to perform two pushover analyses along both horizontal principal directions of the as-built structural model. Inertia forces are applied at each storey level with a gradually increased amplitude. The same are modulated according the components distribution of the fundamental mode shape of the base-isolated configuration ("*isolation mode*" - see section

1.2). Hence, inertia forces can be roughly approximated by a system of horizontal loads having the same acceleration amplitude at each storey level (Fig. 5.1).

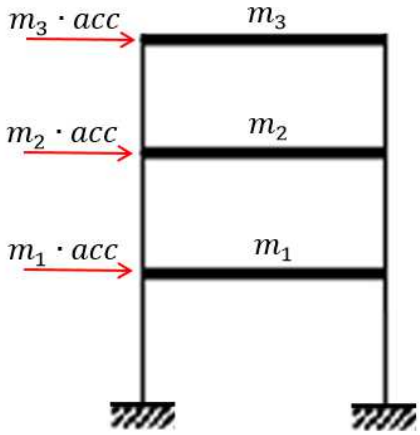

Figure 5.1. Distribution of inertia forces for pushover analyses

4.1) according to EC8-1 provisions, the target performance for the protection of structural components is established assuming that, in the base-isolated configuration, the superstructure remains in the elastic range (*"full-isolation"* assumption - see section 1.5.1). With respect to the "*capacity-curve*" relevant to the pushover analysis in the most flexible direction (Fig. 5.2), the upper limit of the linear-elastic behaviour is identified and then converted in terms of accelerations ($a_{limit,1}$) dividing the base shear force (V_b) for the total mass (m_{tot}) of the building ($a_{limit,1} = V_b/m_{tot}$) [2];

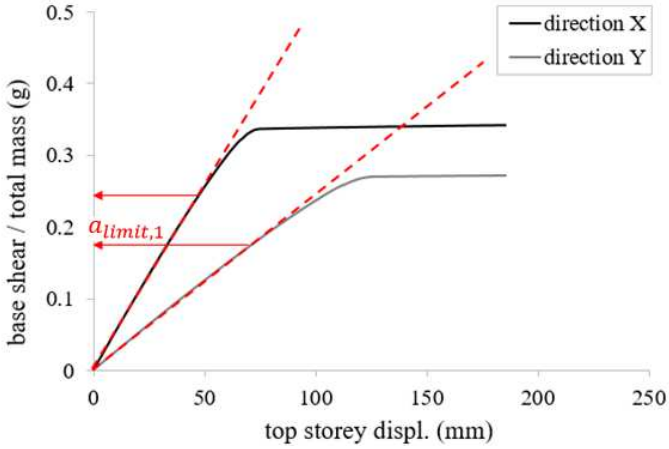

Figure 5.2. Identification of $a_{limit,1}$ based on the "*capacity-curve*" in the most flexible direction

4.2) the two "*capacity-curves*" are then represented in terms of inter-storey drifts (Fig. 5.3) in order to define a target performance for the protection of "*drift-sensitive*"

non-structural components. Considering the most flexible curve and the failure threshold (*max drift*) of the most critical element (see section 3.3.4), a second limit in terms of accelerations ($a_{limit,2} = V_b/m_{tot}$) is established;

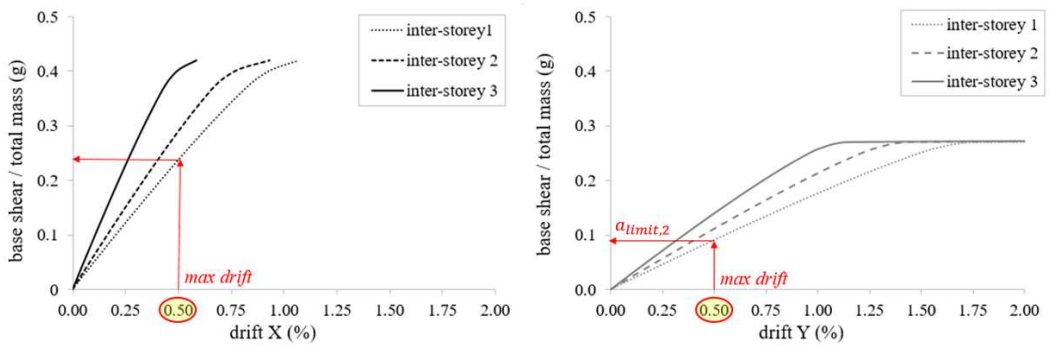

Figure 5.3. Identification of $a_{limit,2}$ based on the "*capacity-curve*" (in terms of inter-storey drift) in the most flexible direction

4.3) a specific target performance for the protection of "*acceleration-sensitive*" non-structural components ($a_{limit,3}$) can be directly identified as the failure threshold of the most critical element (see section 3.3.4);

4.4) a maximum allowable base-displacement D_{limit}, that represents the upper bound for CSS units deformations, is established based on possible physical constraints of the building (e.g. thermal expansion joints, hammering with adjacent structures);

4.5) the self-centring capability of the isolation system represents a minor target performance and can be quantified according to the method described in section 4.1.

Step 5 – Preliminary design of the sliding isolation system

Since final design parameters are established in the last stages of this procedure (consultation with the devices manufacturer and nonlinear analyses), this step aims at defining a first attempt solution for the isolation system layout. A preliminary range of feasible isolator characteristics is identified by means of equivalent acceleration $S_a(T_{eff}, \xi_{eff})$ and displacement $S_d(T_{eff}, \xi_{eff})$ response spectra analyses (adjusting iteratively the reference spectra of the building code) and considering the previously established target performances for the protection of both structural and non-structural elements. Due to the simplicity of the considered design tools, the validity of this procedure is limited to vertically regular buildings with a single isolation system located above the foundations level. Furthermore, it is assumed that the response of CSS isolators during the strong-motion phase of the quake is governed only by the effective radius (R_{eff}) and the high-velocity friction coefficient (μ_{HV}) and is virtually independent from the applied gravitational load W (see section 2.1). Despite these crude assumptions, this step allows focusing the attention on few doable

options of optimized isolators. The design parameters (R_{eff}, μ_{HV}) for CSS isolators are indeed identified applying the previously defined target performances to specific seismic design levels of the Italian Building code [1]:

- at SLD limit state (Fig. 5.4-left), protection of the most critical "*acceleration-sensitive*" and "*drift-sensitive*" non-structural components (that is $S_a(T_{eff}, \xi_{eff}) \cong V_b/m_{tot} \leq min(a_{limit,2}, a_{limit,3})$;
- at SLC limit state (Fig. 5.4-right), protection of the structural elements (that is $S_a(T_{eff}, \xi_{eff}) \cong V_b/m_{tot} \leq a_{limit,1}$) and limitation of the maximum displacement of the isolation system (d_{cd}) within the previously established threshold (that is $S_d(T_{eff}, \xi_{eff}) = d_{cd} \leq D_{limit}$).

It is worth noting that, in order to simplify the design procedure and in safety favour, the protection of the structural elements is required at the SLC limit state (instead of the less severe SLV established by the national code).

Since the spectral acceleration ($S_a(T_{eff}, \xi_{eff})$), the equivalent effective viscous damping (ξ_{eff}), and the spectral displacement ($S_d(T_{eff}, \xi_{eff})$) are mutually dependent on each other, an iterative procedure is needed to calculate, until convergence, the response of the system relevant to the attempt couple of design parameters (R_{eff}, μ_{HV}).

Trial values for the friction coefficient at high sliding velocity μ_{HV} can be selected among average typical values for low ($\mu_{HV} = 0.025$), medium ($\mu_{HV} = 0.075$), and high friction materials ($\mu_{HV} = 0.125$). However, in order to minimize the undesirable effects of the breakaway friction μ_B (see section 4.3), only the first two categories of sliding materials should be preferred. Once a value of μ_{HV} is assumed, acceleration and displacement response spectra are used to identify the minimum values of the effective radius capable to fulfil both SLD ($R_{1,min}$) and SLC ($R_{2,min}$) target performances.

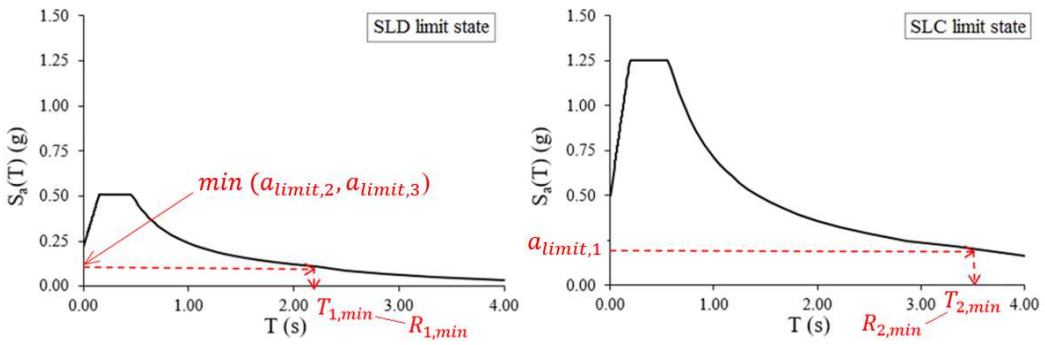

Figure 5.4. Identification of the minimum effective radius R_{eff} required to meet the target performance at both SLD (left) and SLC (right) limit states based on acceleration response spectra

The target performance related to the maximum seismic displacement (Fig. 5.5) is finally assessed ($d_{cd} = S_d(T_{eff}, \xi_{eff}) \leq D_{limit}$ at SLC limit state) and, in case of its fulfilment, the effective radius of CSS isolators is set as:

$$R_{eff} \geq max(R_{1,min}; R_{2,min}) \tag{3.1}$$

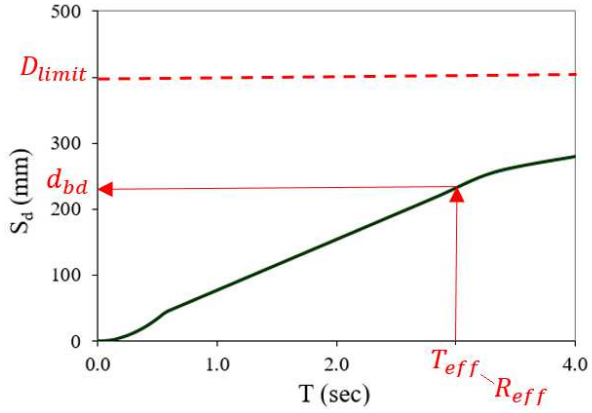

Figure 5.5. Assessment of the target performance related to the maximum seismic displacement based on displacement response spectrum at SLC seismic limit state

If the last target performance is not met, the iterative procedure should be repeated considering another set of design parameters (R_{eff}, μ_{HV}). On the contrary, there could be also multiple sets of compliant design parameters (see section 6.3.2). In this case, the optimal solution is identified considering also the re-centring capability of the isolation system. Assuming a typical ratio between the low and high velocity friction coefficients $\mu_{HV}/\mu_{LV} = 2.5$, the re-centring capability of the isolation system is quantified as $d_{cd}/(\mu_{LV} \cdot R_{eff})$ and, even in presence of initial offset displacements, is judged satisfactory for values higher than 2.5 (see section 4.1).

Step 6 – Technological feasibility and experimental database

In this step, the technological feasibility of the targeted isolators is verified by means of a consultation with the device manufacturer. A significant part of this step is also the acquisition of available experimental data conducted on devices similar (size, load, and frictional properties) to the desired ones.

6.1) calculate the gravitational load W acting on CSS units;

6.2) check for technological feasibility (e.g. availability of sliding materials with the desired frictional properties and load bearing capacity);

6.3) define the diameter of the sliding pad in order to be compliant with desired frictional properties and the compressive strength of the sliding material (note that both μ_{HV} and μ_{LV} depend on the average contact pressure p_{avg}).

If technological feasibility check is satisfied, two scenarios are possible:

6.4) acquisition of the database of available experimental results from tests conducted on CSS isolators with similar design parameters;

6.5) in case of partial or total lack of experimental data, definition of ad hoc tests to be conducted on CSS prototypes.

If technological feasibility check is not satisfied, the engineer should go back to the previous step and identify another set of reasonable design parameters for CSS isolators, or, in worst case, even choice another strategy for the seismic-retrofitting.

Step 7 - Calibration of a refined friction model

In this step, the selected experimental tests (already available or performed on new prototypes) are used to calibrate a refined friction model to be implemented in nonlinear analyses of the isolated structure. In this regard, a new friction model (Fig. 5.4), with a related procedure for the parameters calibration, has been proposed by the writer and has been implemented in OpenSees FEM code [3]. The proposed formulation is capable to reproduce the well acknowledged dependence of the friction coefficient $\mu(t)$ on the instantaneous sliding velocity $v(t)$, and normal load $N(t)$ acting on the isolator. The main novelty of the model is indeed represented by the possibility to simulate also the more challenging "*frictional heating*" and the "*breakaway"* effects (see section 4.4).

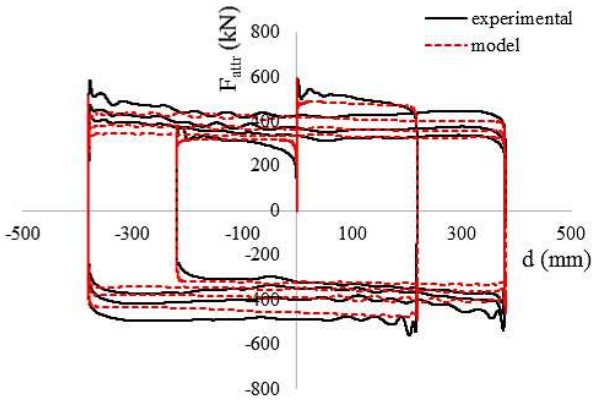

Figure 5.4. Calibration of the refined friction model for nonlinear dynamic analyses

Step 8 – nonlinear dynamic analyses and isolation system design refinement

This step aims at evaluating the seismic performance of the structure implementing CSS isolators. Nonlinear dynamic analyses are carried out using the refined friction model to predict the response of CSS elements. The effectiveness of the proposed solution for the seismic-retrofitting is then assessed processing the output results by means of the fault tree analysis. Finally, the displacement capacity of the CSS units (D) is designed considering the maximum base displacement (d_{cd}) and the possible presence of any initial non-seismic offset (see section 4.1).

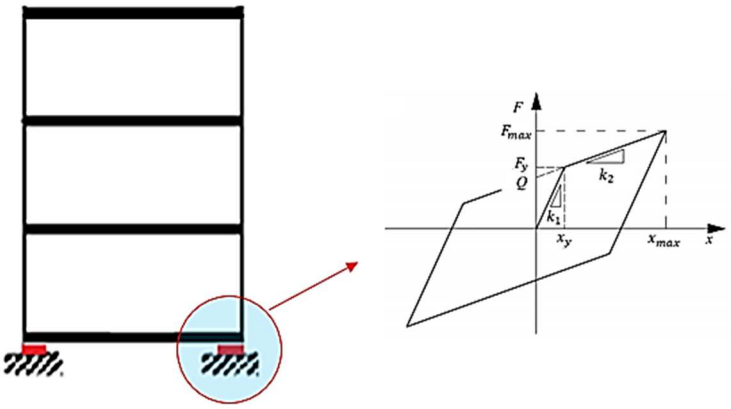

Figure 5.5. Nonlinear dynamic analysis on the base-isolated configuration

5.3 Chapter references

[1] Ministero delle Infrastrutture, D.M. 14.01.2008, "*Norme Tecniche per le Costruzioni*"

[2] Dolce, M., Ponzo, F.C., Di Cesare, A., Arleo, G. (2010) "*Progetto di Edifici con Isolamento Sismico*", 2nd edition, IUSS Press, ISBN: 88-6198-050-1

[3] McKenna, F., Fenves, G.L., Scott, M.H., Jeremic, B. (2000) "*Open System for Earthquake Engineering Simulation (OpenSees)*", Pacific Earthquake Engineering Research Center (PEER), Berkeley, USA

CHAPTER 6

Seismic-retrofitting of a case study hospital

6.1 The Lamezia Terme hospital

6.1.1 Introduction

In this chapter, the conceptual design of sliding isolation system for retrofitting of strategic buildings with high technological content, presented in section 5.2, is illustrated with reference to an existing hospital. The hospital *"Giovanni Paolo II"* of Lamezia Terme (Calabria, Italy), located in a high seismic prone area and capable of providing every medical service typical of large medical complexes, has been chosen as case study. The hospital is already described in a previous study by Lupoi *et al.* (2008): seismic analyses were conducted on the same structure; in addition, a synthetic index to assess the hospital capacity to withstand the post-earthquake emergency was proposed [1, 2]. However, the lack of some information on the structural model (e.g. layout of beam and beam-column joints) assumed in that study and the need to update the analysis in accordance with the requirements of the most recent Italian Building Code [3] made necessary the repetition of the analyses also in the "as built" configuration (fixed base).

The design of the Lamezia Terme hospital dates back to the end of the '60s of the last century. The hospital complex consists of two main buildings, named "*Piastra*" and "*Degenze*", connected by two tower structures ("*Torre Scala*"), and two auxiliary buildings, named "*Riabilitazione*" and "*Uffici*" (Fig. 6.1 and 6.2).

Since the most challenging goal of the present study is to demonstrate the effectiveness of optimized sliding seismic isolation systems for the protection of strategic buildings, seismic analyses are carried out only on the *"Piastra"* building that is equipped with earthquake-sensitive plants, medical equipment, and contains the surgery division of the hospital.

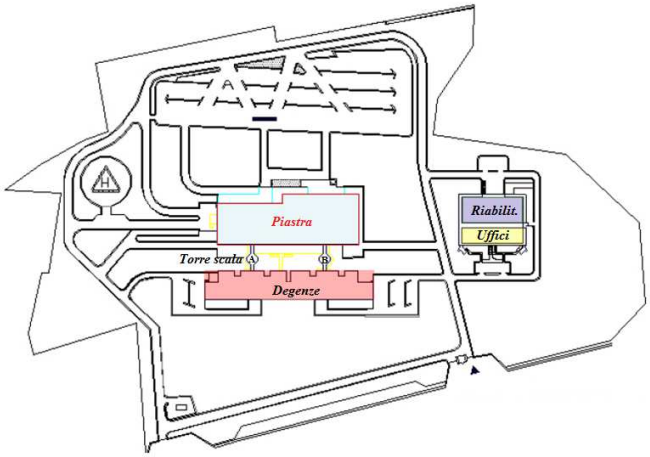

Figure 6.1. General plan of the Lamezia Terme hospital complex (adapted from [2])

Figure 6.2. Side view of the hospital complex

The "*Piastra*" is a quite regular three-storey building with dimensions of about 140m in the longitudinal direction and 50m in the transversal one. The storey heights are 5.1m (basement level), 3.5m (ground floor), and 4.5m (first floor) for a total height of 13.1m. Foundations are located at -5.1m with respect to the ground level. The interior space is partitioned into modules of 7.2m by 9.6m defined by the structural grid (see section 6.1.2); Fig. 6.3 shows the location at the different floors of the medical services, and the technical rooms.

For simplicity, the design of the isolation system for the seismic retrofitting of the "*Piastra*" building is developed skipping some of the steps provided by the procedure outlined in Chapter 5. In particular, instead of performing a detailed fault tree analysis, a survey of the failures occurring to both structural and non-structural elements at each floor level is used to assess the seismic performance of the building. Additionally, the preliminar design of the CSS isolators (nominal period and frictional properties) is based only on the fulfilment of some target performance while the technological feasibility of the identified solution is not verified by means of a consultation with the device manufacturer. The effectiveness of the proposed solution is directly evaluated by means of nonlinear dynamic analyses conducted

in OpenSees® FEM software [4]. The modified formulation of the isolator element (see sections 4.4 and 4.5) is implemented in the software and the relevant model parameters are calibrated by means of friction tests carried out on small scale specimens of the selected sliding material.

Figure 6.3. Spatial distribution of services at each floor level of the "*Piastra*" building

6.1.2 Layout of non-structural components

Based on the information available in literature [1, 2] and derived from an inspection of the building conducted by the Writer, Tables 6.1 and 6.2 provide respectively the floor-distribution of *"drift-sensitive"* and *"acceleration sensitive"* components located in the "*Piastra*" building.

component	capacity (%)	basement	ground floor	first floor
EG diesel conduits	0.90	x		
pipelines *(for water and medical gas systems)*	0.90	x	x	x
curtain walls	0.75	x	x	x
glass windows and doors	4.60	x	x	x

Table 6.1. Floor distribution of "*drift-sensitive*" components

component	capacity (g)	basement	ground floor	first floor
false ceilings	0.90	x	x	x
UPS battery cabinets	0.52	x		
UPS switchboard panels	1.12	x		
UPS distribution panels	1.75	x	x	x
elevators	0.20	x	x	x
medical gas cylinders	0.50	x		
consultation rooms	0.45		x	
medical equipment	1.00		x	x

Table 6.2. Floor distribution of "*acceleration-sensitive*" components

6.1.3 Structural layout

The structural frame of the "*Piastra*" building is comprised of cast-in-place reinforced concrete beams and columns and is subdivided into three blocks (block A, B, and C) by thermal joints (Fig. 6.4).

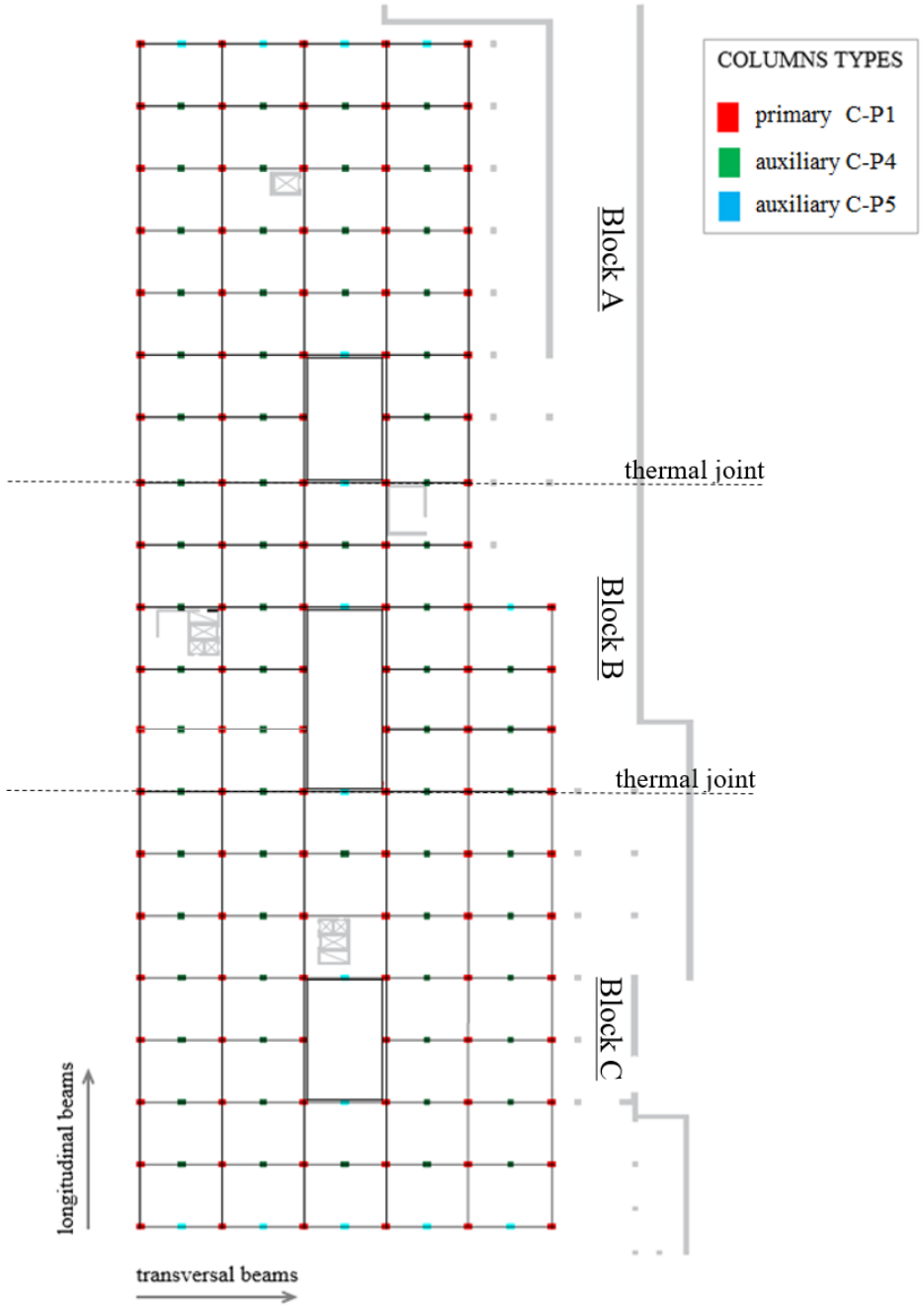

Figure 6.4. Vertical load-carrying system of the "*Piastra*" building

Based on the cross-section designs, columns at the basement level can be categorized into: (1) C-P1 primary columns; (2) C-P4 auxiliary columns; (3) C-P5 auxiliary columns. Whereas auxiliary columns are only at the basement floor, the primary columns runs from the foundations to the roof, with cross-section that reduces passing from the basement level (C-P1) to the ground floor (C-P2), and the first floor (C-P3). The cross-sections of primary and auxiliary columns at the basement floor are reported in Fig. 6.5, while those of primary columns at ground and first floors are shown in Fig. 6.6.

Columns cross-sections are aligned with their main dimension parallel to the transverse side of the building (Fig. 6.4) providing a higher bending stiffness in this direction.

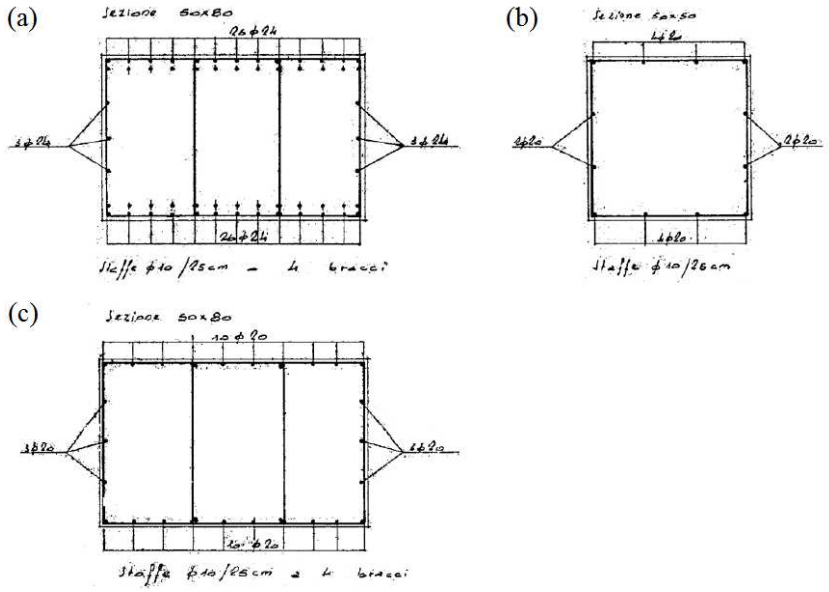

Figure 6.5. Columns cross-sections at the basement floor: (a) primary C-P1, (b) auxiliary C-P4, and (c) auxiliary C-P5 (adapted from original drawings)

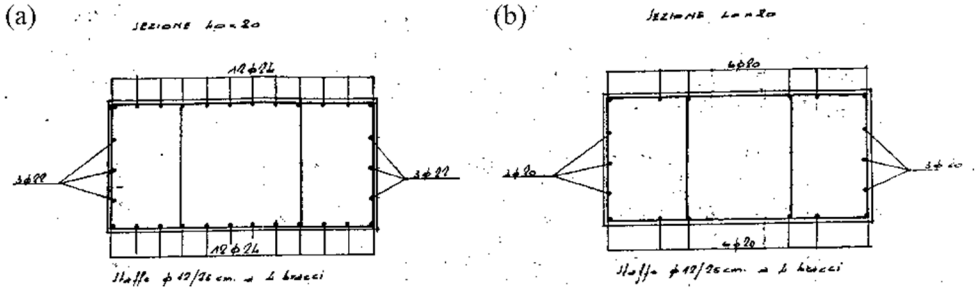

Figure 6.6. Primary columns typologies at the ground and first floors: (a) C-P2 cross section, and (b) C-P3 cross section (adapted from original drawings)

Longitudinal beams have a conventional rectangular cross-section (Fig. 6.7-left), while transversal beams have an "*inverted U*" shaped cross-section (Fig. 6.7-right).

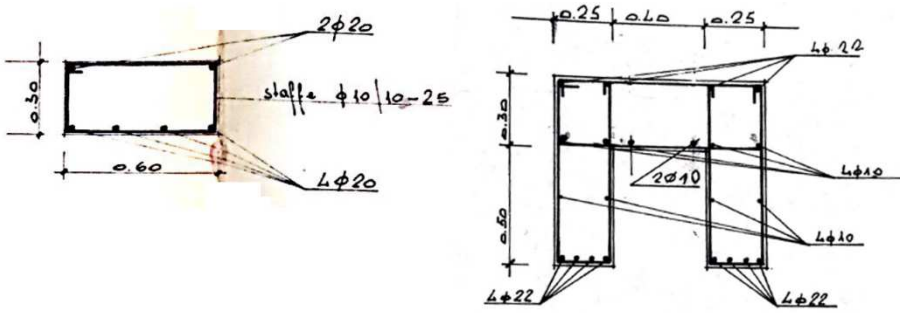

Figure 6.7. Cross-sections of longitudinal (left) and transversal (right) beams in the middle of the span (adapted from original drawings)

The details of columns-longitudinal beams joints (Fig. 6.8) and columns-transversal beams joints (Fig. 6.9) allow hypothesizing different schemes for the resisting frames in the two principal directions.

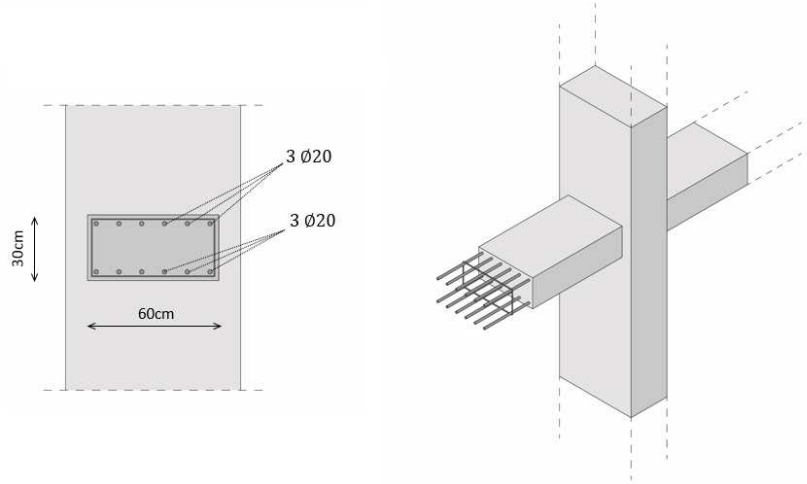

Figure 6.8. Column-longitudinal beam joint: beam cross-section (left) and 3D view (right)

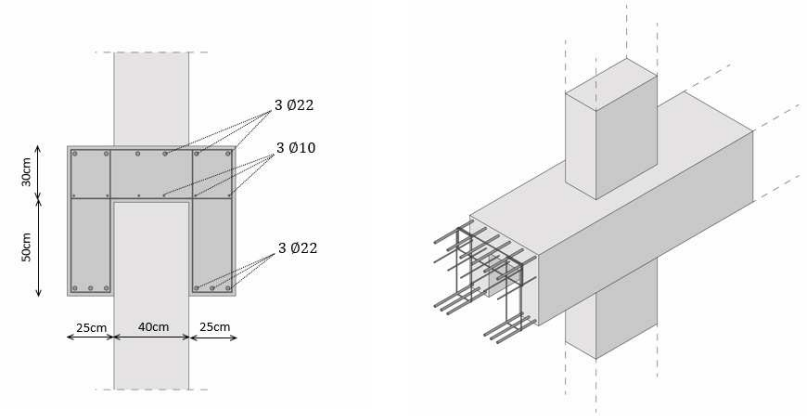

Figure 6.9. Column-transversal beam joint: beam cross-section (left) and 3D view (right)

In the transversal direction, beam-column joints have not an optimal layout for the transmission of bending moments; indeed most of the reinforcing steel bars are located in two vertical flanges of the cross-section and therefore do not contribute to the bending stiffness of the joint. In safety favour, transversal beams are therefore modelled using truss elements (Fig. 6.10). In the longitudinal direction, the beam-column joint is more rigid and suitable for the transmission of bending moments; consequently, a "*moment resisting frame*" scheme is assumed (Fig. 6.11).

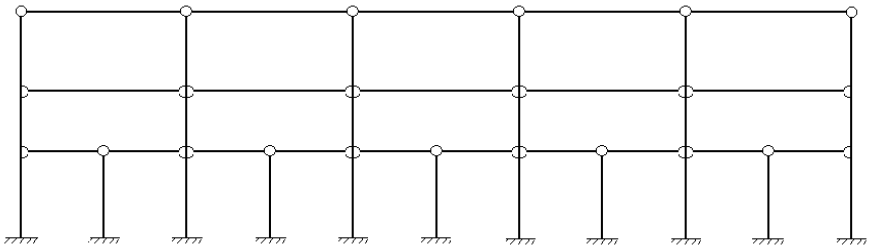

Figure 6.10. Structural scheme of the resisting frame in the transversal direction

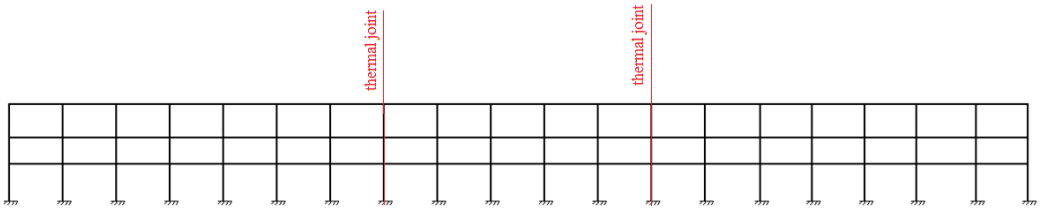

Figure 6.11. Structural scheme of the resisting frame in the longitudinal direction

A structural issue of "*Piastra*" building is represented by the thermal joints. At each joint, the longitudinal beams of one block are simply supported by the columns of the adjacent block (Fig. 6.12). The three structural blocks are therefore not independent from each other, and a quake may cause the collapse of the longitudinal beams due to sliding and loss of support. In seismic analyses, in safety favour, it will be assumed that a displacement greater than the half width of the support ($0.5 \cdot 180mm$) at the joint corresponds to such event. Further, also possible hammering between the adjacent blocks is taken into account considering a clearance of 10mm between the end of the beam and the column.

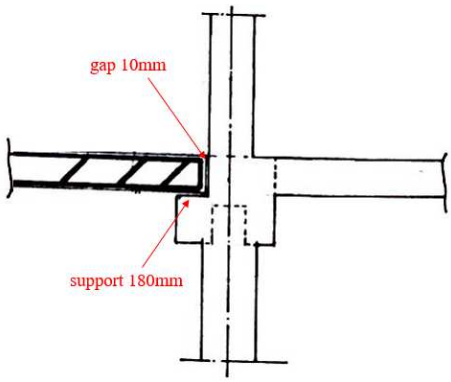

Figure 6.12. Detail of the thermal joints (adapted from original drawings)

6.1.3.1 Material properties

Material properties for the structural analyses are taken from the study conducted by Lupoi *et al.* in 2008 [1].

Based on results of rebound-hammer tests, the concrete strength assumed for beams and columns is $f_{cd} = 41MPa$, while the elasticity modulus of concrete is set to $E = 30000MPa$.

Mechanical properties of steel used for the reinforcing bars is deduced from a survey of the original design documents: the yield strength is assumed to be $f_{yd} = 430MPa$, and the elasticity modulus is set to $E = 210000MPa$.

Based on available information [1], the soil at foundation level is mainly composed of sand and gravel with good mechanical properties ($\varphi = 30 - 35°$).

Although for a reliable definition of material properties a more extensive experimental investigation campaign could be appropriate, an accurate level of knowledge of the characteristics of the structural elements has been assumed in the present study. Therefore, according to the Italian Building Code (§8.5) [3] and the relevant explanatory ministerial note [5], no reduction coefficient has been applied to the mechanical properties of the constitutive materials.

6.1.3.2 Gravity loads

The permanent loads (G_k) considered in structural analyses are deduced from the original calculation report of the hospital building, while live loads (Q_k) are set according to the provisions of the Italian Building code [3] for public buildings (Table 6.3).

floor level	G_k (kN/m^2)	Q_k (kN/m^2)
z = 0.0m	5.28	3.00
z = +3.5m	5.28	3.00
z =+8.0m	4.38	0.50

Table 6.3. Floor distribution of permanent (G_k) and live (Q_k) loads

6.1.4 Reference seismic scenario

For each seismic design level (or limit state) provided by the current Italian Building code [3] (see section 1.5.3), seven independent ground motion records were selected from the European Strong-motion Database [6] using REXEL v3.4 beta software [7]. Only horizontal bidirectional time histories compatible with the elastic spectrum of reference of each limit state were requested to the software. Indeed, although the effect of the vertical component of the earthquake on technological buildings is a complex matter that would deserve further investigations, it has not considered in present study.

The selected records are in compliance with standard provisions for a strategic structure (functional class IV, $c_u = 2.0$) located in Lamezia Terme, Italy (16.18° longitude, 38.58° latitude) on type B soil (very dense sand, gravel, or very stiff clay), topographic category T_1, with a nominal life of $V_N = 100 years$ (corresponding reference period $V_R = c_u \cdot V_N = 200 years$). Table 6.4 summarizes the main features (return period T_R and peak ground acceleration *PGA*) of each limit state (LS) and lists the relevant seismic performance according to the Italian Building code (see section 3.3.1).

LS	T_R (years)	PGA (g)	performance requirements
SLO	120	0.170	operativity of plants
SLD	200	0.217	drift limitation of structural elements
			damage limitation of nonstructural elements
SLV	1900	0.452	no hammering with adjacent buildings
			resistance of structural elements
			resistance of anchoring systems for plants
SLC	3900	0.499	seismic isolators displacement capacity
			seismic isolators load bearing capacity
			resistance of anchoring systems for seismic isolators

Table 6.4. Limit states for seismic performance assessment

Selected records are listed in Tables from 6.5 to 6.8, while Figs. from 6.13 to 6.16 represent the relevant response spectra: at each limit state, the compliance of the mean spectrum to the "*target spectrum matching*" criterion is satisfied (see section 1.5.3).

event	record ID	duration (s)	scale factors	
			dir. X	dir. Y
Ano Liosia	1314	27.4	1.422	1.561
Ano Liosia	1713	30.0	1.531	1.984
Campano Lucano	291	86.0	1.091	0.965
Friuli (aftershock)	147	16.8	1.208	0.718
Montenegro	199	47.1	0.452	0.468
Montenegro (aftershock)	232	28.2	2.973	3.069
South Iceland	6263	25.0	0.271	0.332

Table 6.5. Selected records for seismic analyses at SLO limit state

event	record ID	duration (s)	scale factors	
			dir. X	dir. Y
Ano Liosia	1314	27.4	1.820	1.999
Campano Lucano	291	86.0	1.397	1.236
Friuli (aftershock)	147	16.8	1.540	0.919
Montenegro	199	47.1	0.579	0.599
Montenegro (aftershock)	232	28.2	3.086	3.928
South Iceland	6263	25.0	0.347	0.425
South Iceland	4673	30.0	1.046	0.456

Table 6.6. Selected records for seismic analyses at SLD limit state

event	record ID	duration (s)	scale factors	
			dir. X	dir. Y
Campano Lucano	291	86.0	2.097	2.572
Izmir	548	19,7	15.687	11.543
Montenegro	196	48.2	0.996	1.479
Montenegro	197	48.2	1.540	1.878
Montenegro	199	47.1	1.205	1.247
Montenegro (aftershock)	232	28.2	7.921	8.175
Umbria Marche	594	25.0	0.863	0.977

Table 6.7. Selected records for seismic analyses at SLV limit state

event	record ID	duration (s)	scale factors	
			dir. X	dir. Y
Campano Lucano	291	86.0	3.208	2.838
Campano Lucano	293	84.0	5.054	5.020
Duzce	6501	41.5	3.988	3.167
Montenegro	197	48.2	1.699	2.073
Montenegro	199	47.1	1.330	1.376
Montenegro (aftershock)	230	32.5	4.175	1.865
Montenegro (aftershock)	232	28.2	8.740	9.020

Table 6.8. Selected records for seismic analyses at SLC limit state

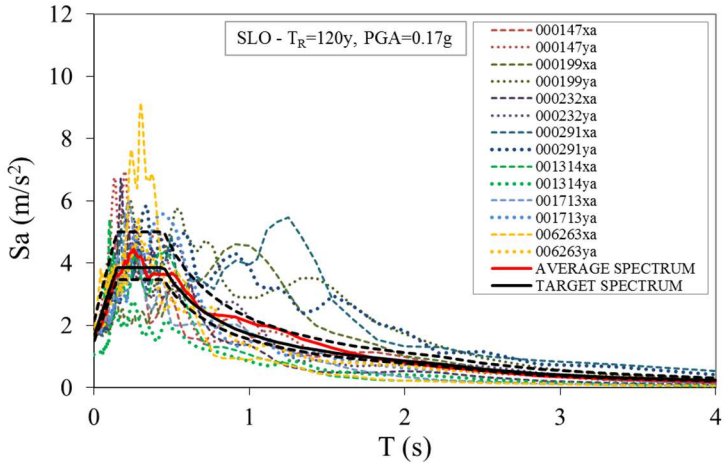

Figure 6.13. SLO limit state: comparison between target spectrum ($\xi_{eq} = 5\%$) and average spectrum of selected records

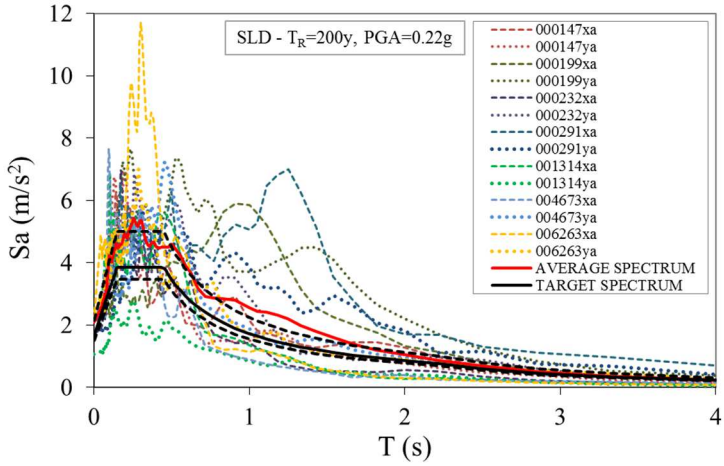

Figure 6.14. SLD limit state: comparison between target spectrum ($\xi_{eq} = 5\%$) and average spectrum of selected records

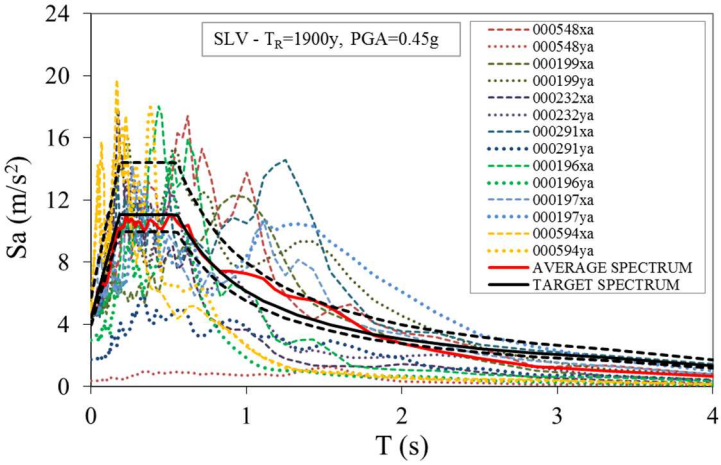

Figure 6.15. SLV limit state: comparison between target spectrum ($\xi_{eq} = 5\%$) and average spectrum of selected records

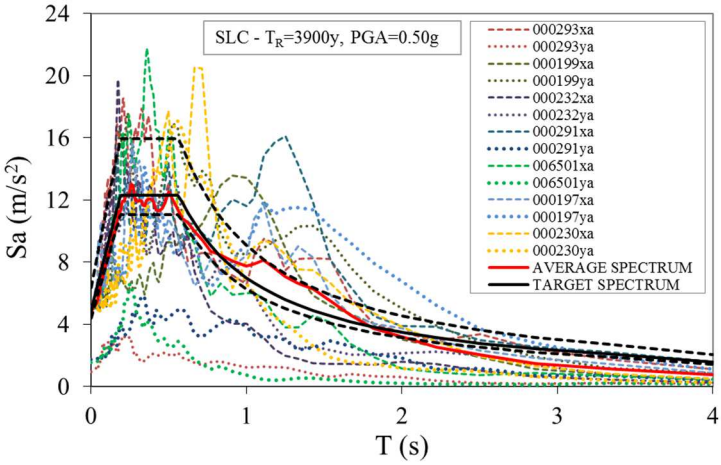

Figure 6.16. SLC limit state: comparison between target spectrum ($\xi_{eq} = 5\%$) and average spectrum of selected records

6.2 Seismic analyses on the "as-built" configuration

6.2.1 FEM model

A 3D model of the "*Piastra*" building (Fig. 6.17) has been developed in OpenSees® v.2.5.0 [4].

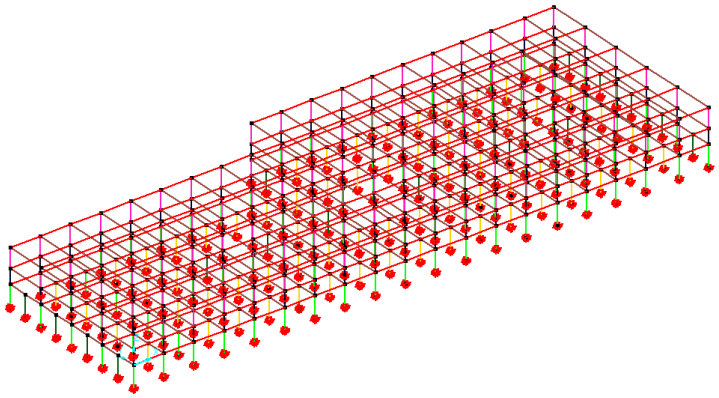

Figure 6.17. 3D view of the FEM model of the "*Piastra*" building

Based on the assumed overall structural behaviour described in section 6.1.3, simple elastic truss elements are used to model transversal beams while nonlinear "*BeamWithHinges*" elements are used for columns (all types) and longitudinal beams. The last are composed of three parts: two plastic hinges at both ends, and a linear-elastic region in the middle [8]. The two plastic hinges are defined by assigning their lengths L_{p1} and L_{p2} and the properties of the "*fiber-section*". Kent-Scott-Park material model, as modified by Karsan-Jirsa ("*Concrete01-ZeroTensileStrength*"), and bilinear material model with kinematic hardening ("*Steel01*") have been employed for concrete and steel, respectively (Fig. 6.18) [8].

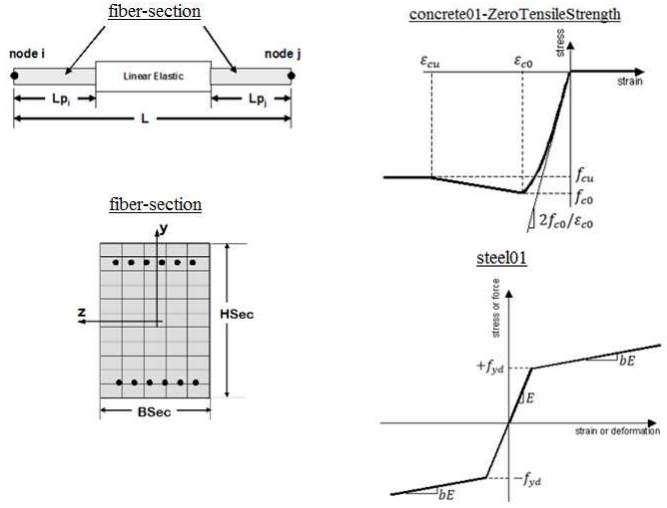

Figure 6.18. "*BeamWithHinges*" elements (left) and constitutive models (right) for concrete and steel in the fiber section (adapted from [8])

In particular, softening of concrete-fibers has been neglected ($f_{c0} = f_{cu} = 41MPa$), while strain-parameters have been set ($\varepsilon_{c0} = -0.002$ and $\varepsilon_{cu} = -0.0035$) as recommended by the Italian Building Code (§ 4.1.2.1.2.2) [3]. In safety favour, also hardening of steel-fibers has been neglected ($b = 0$), while the yield strength and the elasticity modulus have been respectively set to $f_{yd} = 430MPa$ and $E = 210000MPa$ (see section 6.1.3.1).
The length of the plastic hinges has been estimated by means of the simplified formulation proposed by Paulay and Priestly [9]:

$$l_p = 0.08L + 0.022f_{yd}d_b \tag{6.1}$$

where L is the length of the member, and f_{yd} and d_b are respectively the yield strength and the diameter of longitudinal reinforcing bars (adopted units *kN* and *mm*).
Table 6.9 summarizes the resultant lengths of plastic hinges for every column typology, and for longitudinal beams.

element	**plastic hinge length** $l_{p1} = l_{p2}$ **(mm)**
column C-P1	510
column C-P2	382
column C-P3	419
column C-P4	467
column C-P5	467
longitudinal beam	635

Table 6.9. Length of plastic hinges for structural elements

The following boundary conditions have been assigned to the model:

1- the nodes at foundation level are constrained by means of rigid joints and subjected to the application of an "*UniformExcitation*" seismic input [8];

2- translational masses and vertical loads are assigned to every node according to the assumed loads (see section 6.1.3.2);

3- relative displacements between nodes lying on the same floor of each block are prevented by means of "*RigidFloorDiaphragm*" multi-points constraints [8].

To model the non conventional connection between longitudinal beams and columns at the thermal joints, a simplified scheme has been introduced (Fig. 6.19). The columns in correspondence of the joint are doubled (with spatial overlapping) in order to make the frame of each block independent. "*TwoNodeLink*" elements [8] with an elastic - perfectly plastic behaviour in the axial and horizontal shear directions, and a negligible strength in other directions, have been used to model the interaction between the blocks. In order to limit

elastic relative displacements between the nodes at either side of the joint, a very high elastic stiffness was assigned to link elements, while sliding movements starts when the yielding threshold is exceeded:

$$F_y = \mu_{c,c} \cdot R_{v,beam} \tag{6.2}$$

where $\mu_{c,c} = 0.5$ is the concrete on concrete friction coefficient, and $R_{v,beam}$ is the vertical reaction force of longitudinal beams at end supports. Elongation or shortening of link elements is assessed in order to detect potential hammering between blocks (shortening > 10mm), or collapse of longitudinal beams due to loss of support (elongation > 90mm).

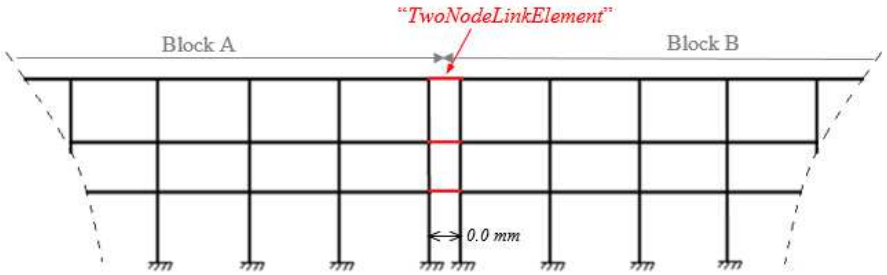

Figure 6.19. Structural model adopted for beam-column connections at the thermal joints

6.2.2 Modal analysis

OpenSees software performs the modal analysis taking into account the mechanical properties that describe the elastic response of each element. Therefore, in the considered model, the link elements behave as stiff connections between the different blocks. In order to analyze the dynamic response of each single block, that characterizes the sliding phases of the thermal joints, a second model, free of link elements, has been developed for the modal analysis. The most important modal shapes and relevant periods calculated for the two models are shown in Fig. 6.20 and Fig. 6.21 respectively.

The modal analyses conducted on the model with link elements provides the following main outcomes:

1- due to the asymmetric configuration of the resisting frames in both principal directions, bending modes in X and Y directions have different vibration periods (respectively T=0.69s and T=1.01s);

2- the natural periods are quite high and typical of a flexible structures;

3- as witnessed by effective modal masses reported in Table 6.10, the dynamic response of the building is dominated by bending modes.

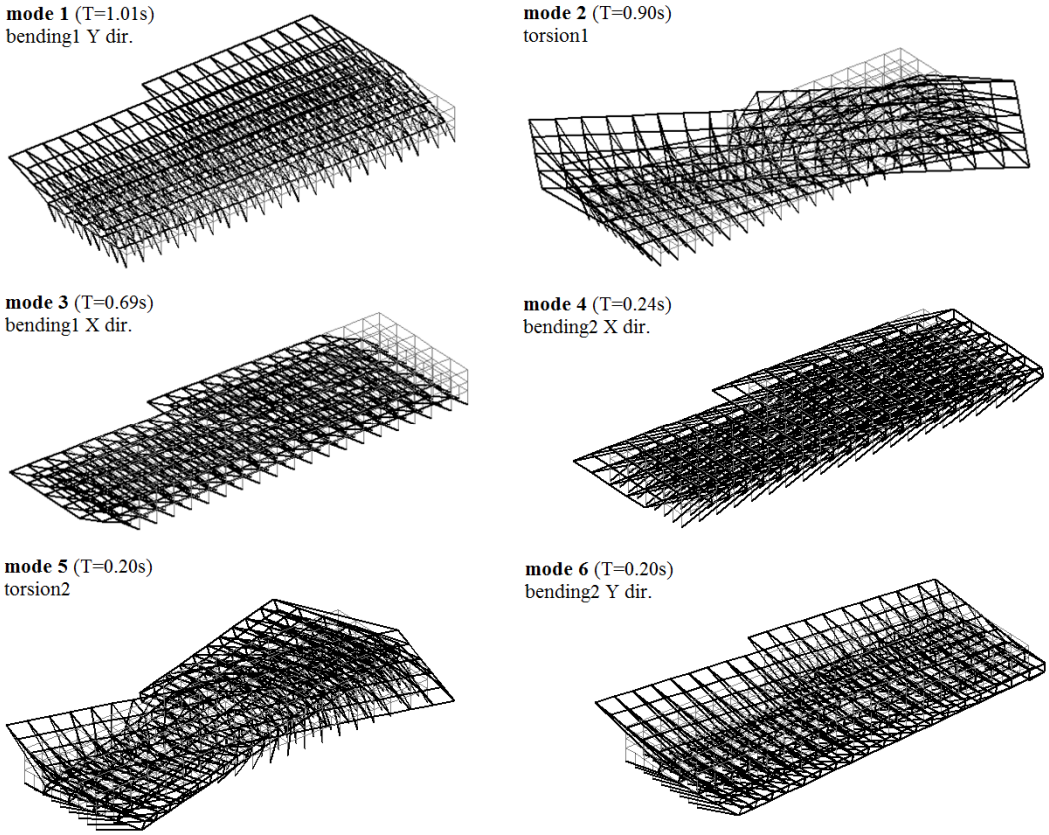

Figure 6.20. Model with link elements: mode shapes and related natural periods

mode n°	**type**	$T\ (s)$	$m_{eff,X}$ (%)	$m_{eff,Y}$ (%)
1	bending1 Y dir.	1.01	≤ 0.1	52.5
2	torsion1	0.90	≤ 0.1	0.3
3	bending1 X dir.	0.69	60.8	≤ 0.1
4	bending2 X dir.	0.24	11.6	≤ 0.1
5	torsion2	0.20	≤ 0.1	2.5
6	bending2 Y dir.	0.20	≤ 0.1	16.9

Table 6.10. Effective modal masses of the model with link elements: percentage values in the longitudinal ($m_{eff,X}$) and transversal ($m_{eff,Y}$) directions

Modal analyses conducted on the model without link elements points out other important information:

1- a practically uniform distribution of masses and stiffnesses among the different blocks of the "*Piastra*" building as witnessed by very similar values of natural periods of bending and torsional modes of the three blocks;

2- effective modal masses suggest again that, also in this configuration, the dynamic response of each block is dominated by bending modes.

mode n°	**type**	**block**	$\boldsymbol{T}$ $(\boldsymbol{s})$	$\mathbf{m}_{\boldsymbol{eff,X}}$ (%)	$\mathbf{m}_{\boldsymbol{eff,Y}}$ (%)	**notes**
1	bending1 Y dir.	B	1.03	≤ 0.1	57.0	of $m_{bl.B}$
2	bending1 Y dir.	C	1.02	≤ 0.1	49.6	of $m_{bl.C}$
3	bending1 Y dir.	A	1.00	≤ 0.1	55.5	of $m_{bl.A}$
4	torsion	A	0.78	≤ 0.1	0.4	of $m_{bl.A}$
5	torsion	C	0.76	≤ 0.1	≤ 0.1	of $m_{bl.C}$
6	torsion	B	0.75	≤ 0.1	≤ 0.1	of $m_{bl.B}$
7	bending1 X dir.	B	0.70	64.4	≤ 0.1	of $m_{bl.B}$
8	bending1 X dir.	C	0.69	57.4	≤ 0.1	of $m_{bl.C}$
9	bending1 X dir.	A	0.69	63.4	≤ 0.1	of $m_{bl.A}$

Table 6.11. Effective modal masses of the model without link elements: percentage values in the longitudinal ($m_{eff,X}$) and transversal ($m_{eff,Y}$) directions

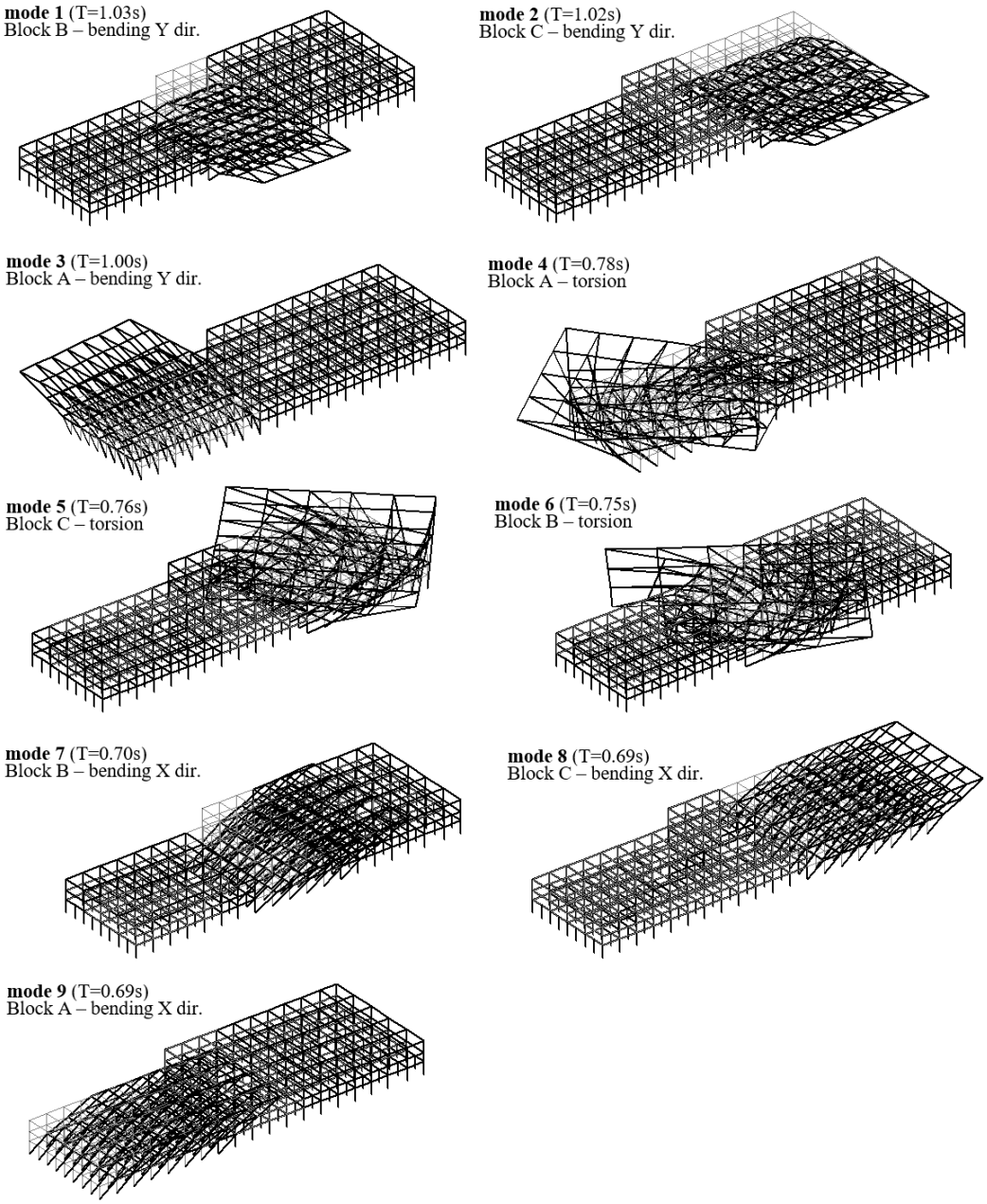

Figure 6.21. Model without link elements: mode shapes with related natural periods

6.2.3 Seismic response assessment

Nonlinear dynamic analyses have been performed for the structural model of the whole "*Piastra*" building under the ground motions time histories defined in section 6.1.4. In accordance with the Italian Building Code (§ 7.3.5), the response of the building at each limit state was assumed as the average of the responses to the seven ground motions selected for that state.

6.2.3.1 Performance of structural elements

Among the main results concerning the seismic response of the resisting frame, it is noted:

1- at both SLO and SLD limit states, the deformation of the link elements is less than 10mm, therefore neither hammering between adjacent blocks nor loss of support of longitudinal beams at the thermal joints occurs;

2- at both SLO and SLD, the maximum axial load in the columns is always significantly below the ultimate strength ($N_{Ed,max}/N_{Rd} \leq 0.15$);

3- at SLO ($PGA = 0.17g$), the columns are severely stressed by biaxial bending moments (Figs. 6.23-6.25);

4- at SLD ($PGA = 0.22g$), some columns have overstepped their ultimate strength and a collapse mechanism is triggered (Fig. 6.26);

5- at SLV ($PGA = 0.45g$), analyses do not reach convergence (for each ground motion time history), meaning again the collapse of the structure.

It is worth noting that, since significant earthquakes with epicentre close to Lamezia Terme never occurred after the hospital construction (1972), the alarming scenario that the analyses have pointed to has never been experienced. Indeed, within an epicentral distance of 100km, according to the European Strong-Motion Database [6], the most intense ground motion was recorded at Bruzzano Zeffirio (RC, 1978) and had a PGA equal to 0.08g.

More in detail, due to the structural scheme adopted for the resistant frame in the transversal direction (hinges in beam-column joints), the structural collapse triggers when yielding at the base of the columns is reached. Indeed, in the longitudinal direction, the onset of plastic hinges at end nodes of beam elements is not sufficient to start a kinematic mechanism. Therefore, for the assessment of the structural integrity it is sufficient to check the resistance of columns to bending moments induced by the seismic action. These checks are conducted according to a simplified approach provided by the Italian Building Code [3] and described in section 3.3.2.

The check is conducted for the whole columns of the building. However, for clarity, hereinafter the results will be illustrated only for a number of columns at each floor that are representative of the behaviour of the whole elements at the same building floor. Fig. 6.22

indicates the monitored columns; while Figs. from 6.23 to 6.25 show the relevant results at both SLO and SLD limit states.

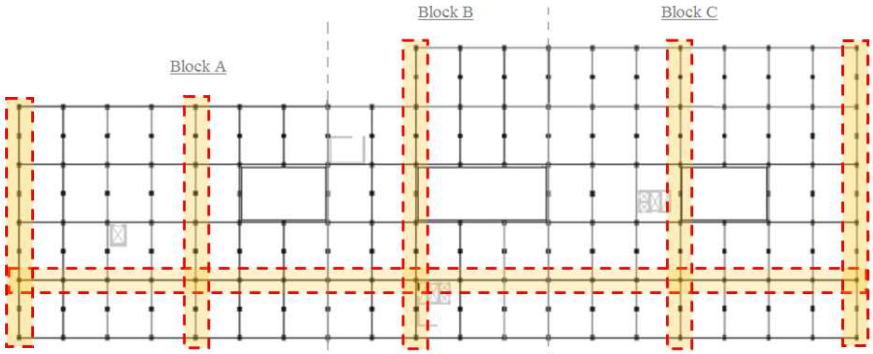

Figure 6.22. Selected column elements for structural integrity check

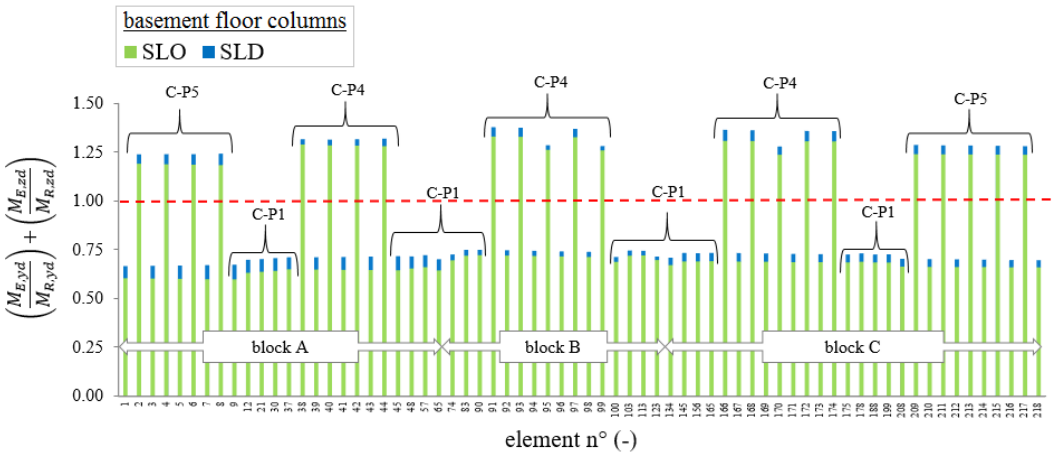

Figure 6.23. Basement floor columns: check of structural integrity at SLO (green bars) and SLD (blue bars) limit states

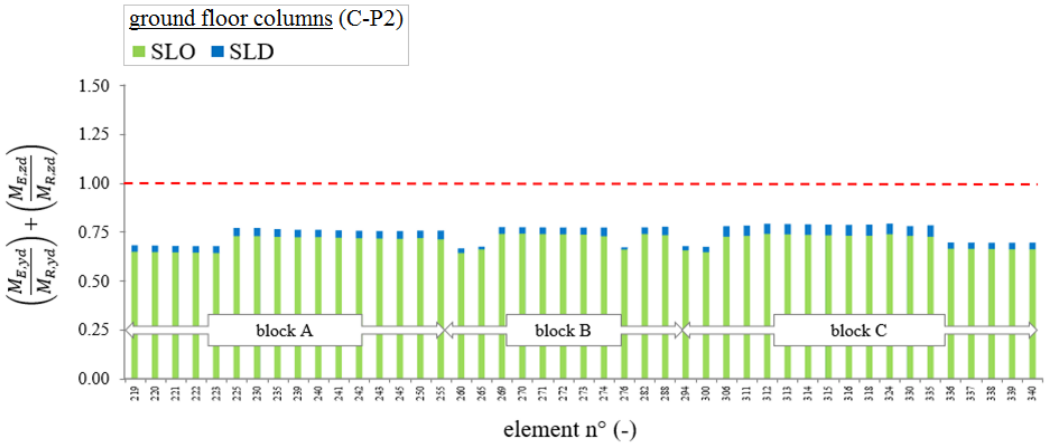

Figure 6.24. Ground floor columns: structural integrity check at SLO (green bars) and SLD (blue bars) limit states

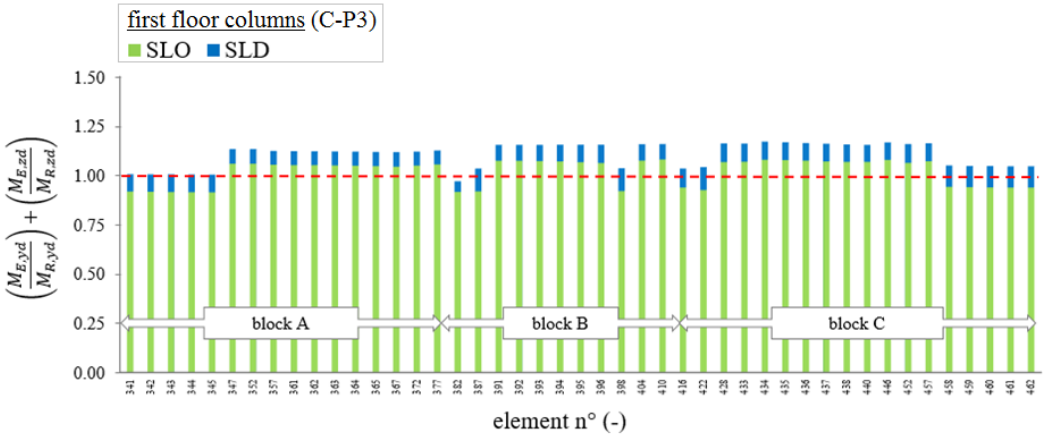

Figure 6.25. First floor columns: structural integrity check at SLO (green bars) and SLD (blue bars) limit states

At both SLO and SLD limit states, all primary columns of the basement floor (C-P1) and the ground floor (C-P2) widely satisfy the structural integrity requirement. At the same floors, the overcoming of the ultimate strength ($max\left[\left(M_{E,yd}/M_{R,yd}\right)+\left(M_{E,zd}/M_{R,zd}\right)\right]>1$) at the base of the auxiliary columns (C-P4 and C-P5) is not sufficient to trigger a collapse mechanism. On the contrary, more severely at SLD limit state, the onset of plastic hinges at the base of primary columns of the first floor level (C-P3) allows free lateral displacements of roof storey causing the structural collapse (Fig. 6.26).

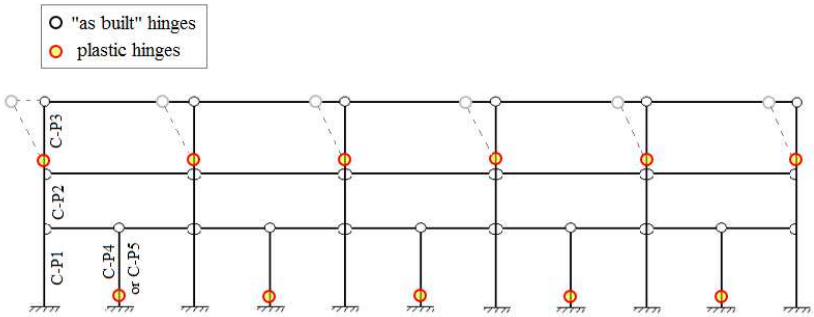

Figure 6.26. Collapse mechanism of the resisting frame in the transversal direction at SLD limit state

It should be noted that, in structural verifications of columns cross-section, values of $\left[\left(M_{E,yd}/M_{R,yd}\right)+\left(M_{E,zd}/M_{R,zd}\right)\right]$ higher than the unity are not physically possible since the columns cross sections have already reached their ultimate strength. This inconsistency is due to the approximation of the ultimate strength domain of the columns cross-sections adopted in simplified analytical checks as described in section 3.3.2. This is evident in Fig. 6.27 where both the actual domain implemented in OpenSees® and the simplified one used in structural checks are shown together with the time-history of bending moments acting at the base of a C-P5 column element close to structural collapse. The points representing the

combination of the moments along the X and Y axes may fall outside the simplified domain, but it is still within the actual one.

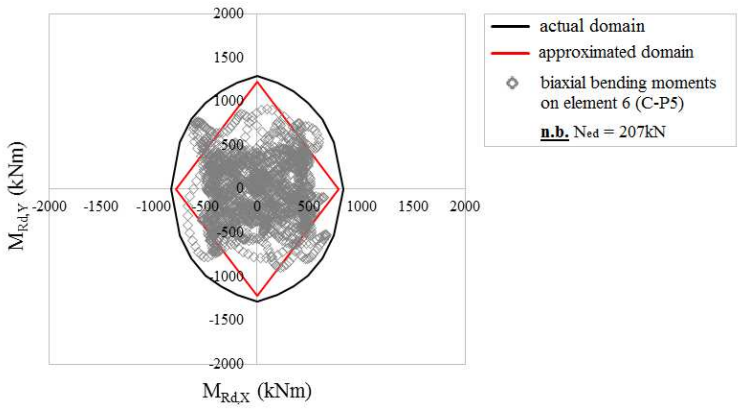

Figure 6.27. Graphic representation of the structural check conducted on a column cross-section subjected to biaxial bending moments

6.2.3.2 Performance of non-structural components

Although at SLO limit state the resisting frame is already severely stressed, it is of primary interest the assessment of the performance of non-structural components during the seismic event. This is useful to define the possible scenario that the first aid operators will have to face in the post-earthquake emergency.

The assessment can be done considering the distribution of "*acceleration-sensitive*" and "*drift-sensitive*" elements given in section 6.1.2. Within the first category, considering the peaks of absolute acceleration at each storey level and the related breakdown thresholds (see section 3.3.4.2), the following damage scenario are envisaged (Fig. 6.28-left):

1- out of order of the elevators at every floor level causing a slowdown in the transport of patients with serious injuries;

2- temporary unavailability of consultation rooms at the first floor level due to possible overturning of not-restrained furnitures and equipment.

Within the second category, other damages and more severe malfunctions can be envisaged analysing the peaks of inter-storey drifts at each level (Fig. 6.28-rigth):

3- damages to curtain walls at ground and first floor;

4- interruption of distribution of water and medical gas due to possible ruptures of pipelines.

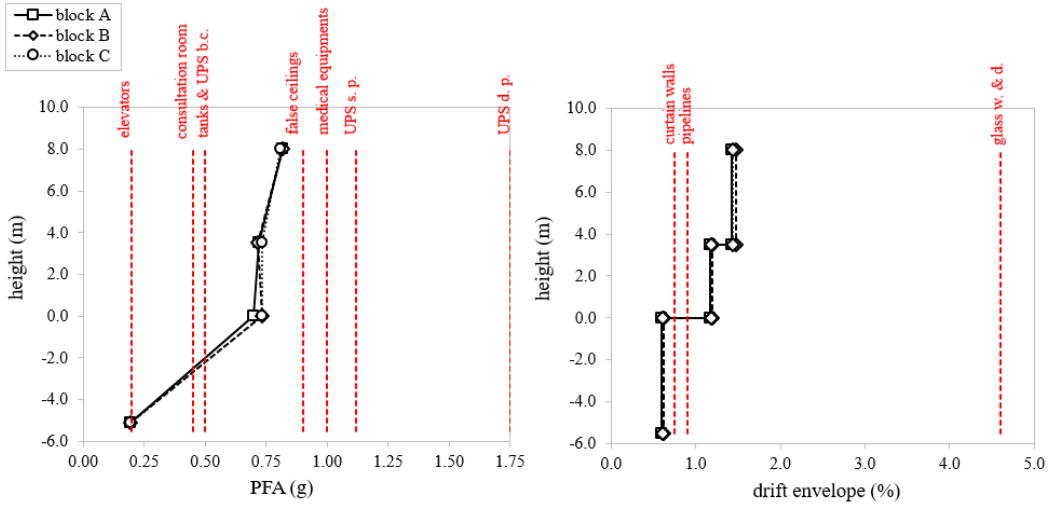

Figure 6.28. Performance checks for "*acceleration-sensitive*" (left) and "*drift-sensitive*" (right) elements at SLO limit state

In general, the hospital complex seems not to be capable to withstand the medical emergency even for low-moderate seismic events such as the ones at SLO limit state. The situation could have been even more alarming if the UPS battery cabinets were not located at the basement floor; in that case, the same could not supply the electricity required for the emergency conditions.

6.3 Design of the sliding isolation system

6.3.1 Layout of the isolation system

Since particular restrictions due to both structural elements and plants of the "*Piastra*" building are not recognized, the isolation system is chosen to be installed between the foundation level and the base of the columns. Based on the typologies of the supported columns (Fig. 6.29), two categories of CSS isolators can be identified: (1) "*primary CSS*" with an applied gravitational load $W = 996kN$; (2) "*auxiliary CSS*" with an applied gravitational load $W = 207kN$.

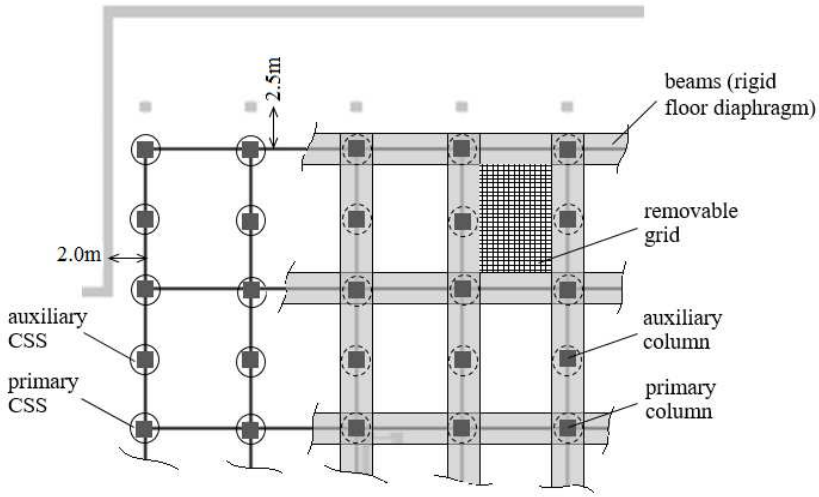

Figure 6.29. Layout of the isolation system

A possible procedure for the installation of the isolators is described in [10]: (1) if needed, enlargement and stiffening of the foundation system (Fig. 6.30-left); (2) realization of a floor diaphragm composed by stiff beams to prevent differential displacements between the CSS units and the bases of the columns (Fig. 6.30-left); (3) installation of hydraulic jacks to support the gravity loads and cutting of the column bases (Fig. 6.30-centre); (4) insertion of isolation devices and removal of hydraulic jacks (Fig. 6.30-right).

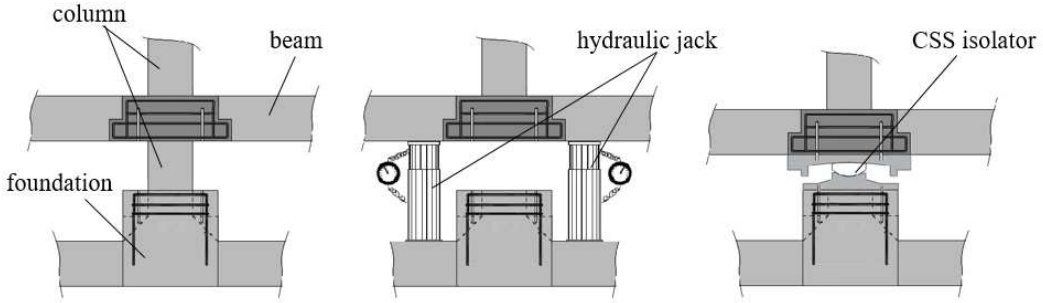

Figure 6.30. Possible installation steps of the isolation system (adapted from [10])

Other secondary provisions are: (5) insertion of a removable grid between the beams (Fig. 6.29) to allow the inspection and maintenance of the isolators (and, if damaged, their replacement after the quake); (6) connection of plants-pipelines by means of flexible joints capable to accommodate the displacements of the isolation system.

6.3.2 Definition of target performance for the isolation system

According to the design procedure described in section 5.2, in order to identify the target performances for the protection of both structural and non-structural components, a pushover analyses along each of the two horizontal principal directions of the "*as-built*" configuration should be carried out. For sake of simplicity, the analysis is performed only along the transversal direction (Y dir.) that, being the most flexible, produces larger deformations of resisting frame (Fig. 6.31). The typical accelerations distribution of the first mode shape of "*base-isolated*" configuration is roughly approximated applying the same acceleration amplitude at each storey level. The inertia forces are then gradually increased ($0.01g$ per step) at each incremental step of the analysis until the structural collapse.

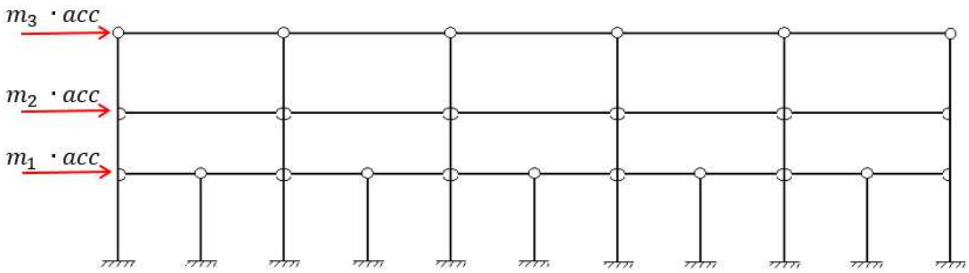

Figure 6.31. Pushover analysis along the Y horizontal direction

According to the "*full-isolation*" assumption of EC8-1 [11] (see section 1.5.1), the target performance for structural components is established considering the upper bound of the linear-elastic range of the "*capacity-curve*" derived from the pushover analysis [10]. Dividing the related shear force at the base of the "*Piastra*" building (V_b) for the total mass of the same (m_{tot}), the previously identified target performance can be expressed in terms of accelerations $a_{limit,1} = V_b/m_{tot} = 0.17g$.

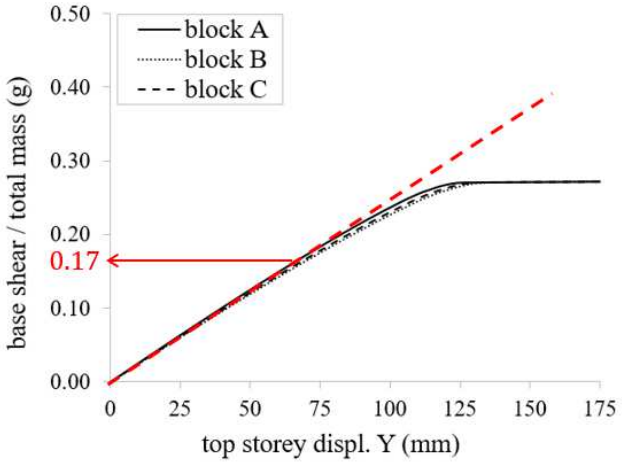

Figure 6.32. Identification of the target performance for structural components based on the "*capacity-curve*" derived from the pushover analysis

Among non-structural components, the target performance for "*drift-sensitive*" elements can be quantified representing the "*capacity-curve*" in terms of inter-storey drifts (Fig. 6.33). Considering the failure threshold ($max\ drift = 0.75\%$) of the most critical element (that is curtain walls according to Table 6.1), the corresponding target performance can be again expressed in terms of accelerations $a_{limit,2} = V_b/m_{tot} = 0.12g$.

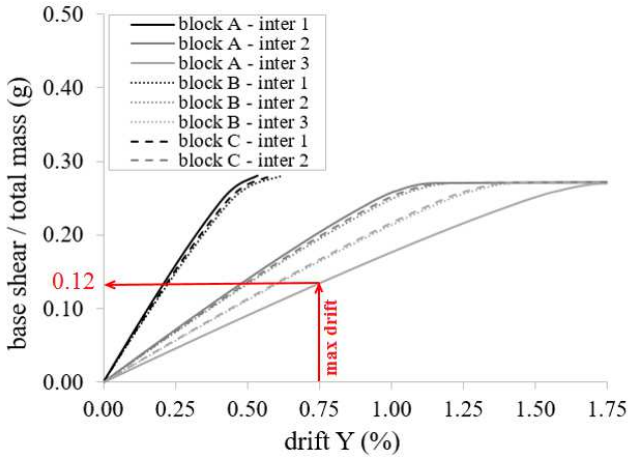

Figure 6.33. Identification of the target performance for "*drift-sensitive*" components based on the "*capacity-curve*" represented in terms of inter-storey drift

A target performance for the protection of "*acceleration-sensitive*" elements is also directly identified as the failure threshold of the most critical component. According to the survey provided in section 6.1.2, in order to prevent the breakdown of the elevators after the quake, the spectral acceleration should be limited within $a_{limit,3} = 0.20g$. In order to prevent the hammering with the adjacent service rooms, ensure the continuity of the connection path,

and allow flexible joints for plants connections having a reasonable size, the maximum admissible displacements is set as $D_{limit} = 0.5m$. In case of multiple solutions compliant with the previous requirements, the best one can be identified considering also the self-centring capability of the isolation system (see next section).

6.3.3 Selection of optimal effective radius and friction coefficients

According to the "*conceptual design*" developed in Chapter 5, equivalent acceleration and displacement response spectra are used, within an iterative procedure, to identify the frictional properties (μ_{HV}) and the effective radius (R_{eff}) of the CSS isolators required to fulfil the following target performances:

1- at SLD limit state, protection of the most critical "*acceleration-sensitive*" and "*drift-sensitive*" non-structural components ($S_a(T_{eff}, \xi_{eq}) \leq min(a_{limit,2}; a_{limit,3}) = 0.12g$);

2- at SLC limit state, protection of the structural elements ($S_a(T_{eff}, \xi_{eq}) \leq a_{limit,1} = 0.17g$) and limitation of the maximum displacement of the isolation system (d_{cd}) within the previously defined threshold ($S_d(T_{eff}, \xi_{eq})) = d_{cd} \leq D_{limit} = 0.5m$).

In order to avoid issues related to the breakaway effect (see section 4.3), only typical values of the high velocity friction coefficient for low ($\mu_{HV} = 0.025$) and medium ($\mu_{HV} = 0.075$) damping sliding materials are considered. For the effective radius R_{eff}, three possible values are assumed: 1.0m, 2.5m, and 4.0m.

Tables 6.12 and 6.13 summarize the isolation system performances calculated respectively under SLD and SLC response spectra.

μ_{HV} (-)	$R_{eff} = 1.0m$	$R_{eff} = 2.5m$	$R_{eff} = 4.0m$
0.025	$S_a = 0.10g, d_{cd} = 65mm$ ($\xi_{eff} = 17.6\%$)	$S_a = 0.06g, d_{cd} = 70mm$ ($\xi_{eff} = 30.0\%$)	$S_a = 0.04g, d_{cd} = 66mm$ ($\xi_{eff} = 38.3\%$)
0.075	$S_a = 0.10g, d_{cd} = 26mm$ ($\xi_{eff} = 47.4\%$)	$S_a = 0.09g, d_{cd} = 25mm$ ($\xi_{eff} = 56.2\%$)	$S_a = 0.09g, d_{cd} = 24mm$ ($\xi_{eff} = 58.9\%$)

Table 6.12. CSS isolator parameters and computed performance using SLD response spectra

μ_{HV} (-)	$R_{eff} = 1.0m$	$R_{eff} = 2.5m$	$R_{eff} = 4.0m$
0.025	$S_a = 0.40g, d_{cd} = 330mm$ ($\xi_{eff} = 4.5\%$)	$S_a = 0.22g, d_{cd} = 447mm$ ($\xi_{eff} = 7.8\%$)	$S_a = 0.17g, d_{cd} = 460mm$ ($\xi_{eff} = 11.4\%$)
0.075	$S_a = 0.28g, d_{cd} = 197mm$ ($\xi_{eff} = 17.6\%$)	$S_a = 0.17g, d_{cd} = 210mm$ ($\xi_{eff} = 30.0\%$)	$S_a = 0.14g, d_{cd} = 216mm$ ($\xi_{eff} = 37.0\%$)

Table 6.13. CSS isolator parameters and computed performance using SLC response spectra

At SLD limit state, all couples of design parameters are suitable to meet the related target performance ($S_a(T_{eff}, \xi_{eff}) \leq 0.12g$).

On the contrary, at SLC limit state, only three sets of design parameters are compliant with the second ($S_a(T_{eff}, \xi_{eff}) \leq 0.17g$) and third ($S_d(T_{eff}, \xi_{eq})) \leq 500mm$) target performances: (1) $\mu_{HV} = 0.025$, $R_{eff} = 4.0m$; (2) $\mu_{HV} = 0.075$, $R_{eff} = 2.5m$; (3) $\mu_{HV} = 0.075$, $R_{eff} = 4.0m$.

Among these sets of compliant parameters, the best solution can be identified considering also the re-centring capability of the isolation system. For CSS isolators, even in presence of an initial offset displacement, this requirement is satisfactory when (see section 4.1.2.1):

$$d_{cd}/(\mu_{LV} \cdot R_{eff}) \geq 2.5 \tag{6.3}$$

where the friction coefficient at low sliding velocity (μ_{LV}) is calculated assuming an average ratio $\mu_{HV}/\mu_{LV} = 2.5$.

The results for the three sets of parameters are: (1) $460mm/(0.01 \cdot 4000mm) = 11.5$; (2) $210mm/(0.03 \cdot 2500mm) = 3.3$; (3) $216mm/(0.03 \cdot 4000mm) = 1.8$.

The re-centring capability requirement at SLC seismic limit state is fulfilled for the first two sets of design parameters. However, the first one is chosen since it offers a better self-centring performance also at SLD seismic limit state. The effective radius of the CSS isolators is therefore set as $R_{eff} = 4.0m$; while, based on results of previous experimental studies [12], PTFE lubricated with silicon grease and under an average contact pressure $p_{avg} = 30MPa$ is identified as a suitable sliding material.

The size (diameter) of the sliding pad of either primary ($\phi_{pad,primary}$) and auxiliary ($\phi_{pad,auxiliary}$) CSS isolators are therefore chosen considering the gravitational loads applied to primary and auxiliary CSS isolators ($W = 996kN$, and $W = 207kN$ respectively):

1- $\phi_{pad,primary} = \sqrt{(4 \cdot 996 \cdot 10^3 N)/(\pi \cdot 30\, N/mm^2)} = 205.7mm \rightarrow 210mm$;

2- $\phi_{pad,auxiliary} = \sqrt{(4 \cdot 207 \cdot 10^3 N)/(\pi \cdot 30\, N/mm^2)} = 93.8mm \rightarrow 95mm$.

6.3.4 Calibration of the "BVNC" friction model

Due to the lack of experimental tests on full-scale (FS) CSS isolators with design parameters comparable to those previously identified ($W = 996kN$, $R_{eff} = 4.0m$, and lubricated PTFE), small-scale (SS) friction tests are carried out to calibrate the "*BVNC*" friction model parameters. The tests are executed at the LPM Lab. of the Politecnico di Milano utilizing the biaxial testing machine shown in Fig. 6.34 [13].

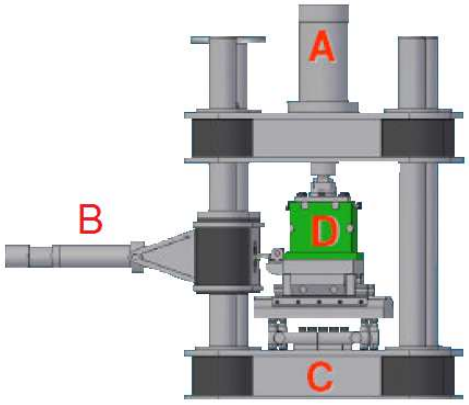

Figure 6.34. Testing equipment: (A) vertical load actuator; (B) horizontal actuator and load cell; (C) vertical load cells; (D) controlled temperature chamber

The tests are conducted on dimpled circular sheets of lubricated PTFE having diameter equal to 75mm, thickness 7mm, and recessed for 4,5mm in a steel backing plate. The mating surface is a sheet of austenitic steel.

In order to calibrate the "*normal load effect*" parameters tests are carried out at the following contact pressures $p_{avg} = 15, 30, 45\ MPa$; while selected sliding velocities for "*velocity effect*" parameters are $v = 1, 10, 25, 50, 100, 200\ mm/s$.

The "*cyclic effect*" (frictional heating) is then assessed by means of a long duration test under an applied small-scale vertical load N_{SS} equal to 132.5 kN ($p_{avg} = 30\ MPa$) and the maximum velocity allowed by the testing machine ($v = 200mm/s$).

In order to ensure an equivalence between the maximum expected dissipated energy per unit area of the pad at small-scale (ED_{SS}) and full-scale (ED_{FS}):

$$ED_{SS} = 4 \cdot (n_{SS} \cdot (4A_{ss}) \cdot \mu_{HV} \cdot N_{ss})/(\pi \cdot \phi_{pad,SS}{}^2) \quad (6.4)$$

$$ED_{FS} = 4 \cdot (n_{FS} \cdot (4d_{bd}) \cdot \mu_{HV} \cdot N_{ed})/(\pi \cdot \phi_{pad,FS}{}^2) \quad (6.5)$$

the number of executed cycles is set as:

$$n_{SS} = \frac{(n_{FS} \cdot \phi_{pad,SS}{}^2)}{\phi_{pad,FS}{}^2} \cdot \frac{(d_{bd} \cdot N_{ed})}{(A_{ss} \cdot N_{ss})} = 133 \rightarrow 135 \quad (6.6)$$

being $n_{FS} = 3$ the number of cycles for (full-scale) required by the EN 15129 [14], $d_{cd} = 460mm$ the expected amplitude at SLC limit state, $A_{SS} = 10mm$ the amplitude of small-scale cycles. Table 6.14 summarizes the testing parameters of all executed tests.

	average contact pressure		
	$\boldsymbol{p_{avg} = 15MPa}$ $\boldsymbol{(N_{SS} = 66.3kN)}$	$\boldsymbol{p_{avg} = 30MPa}$ $\boldsymbol{(N_{SS} = 132.5kN)}$	$\boldsymbol{p_{avg} = 45MPa}$ $\boldsymbol{(N_{SS} = 198.8kN)}$
amplitude (mm)	±10	±10	±10
profile	triangular	triangular	triangular
sliding velocity (mm/s)	1, 10, 25, 50, 100, 200	1, 10, 25, 50, 100, 200	1, 10, 25, 50, 100, 200
n° of cycles (-)	3, 3, 3, 3, 3, 3	3, 3, 3, 3, 3, 135	3, 3, 3, 3, 3, 3

Table 6.14. Testing protocol for SS friction tests

The resulting "*BVNC*" model parameters are listed in Table 6.15 and are expressed in a unit system consistent to the one adopted in numerical analyses in OpenSees® (see section 4.5.3).

effect	**parameter**	**unit**
velocity and breakaway	$\alpha = 0.014$	s/mm
	$\beta = 3.0$	s/mm
normal load	$a_{ST} = 3.271$	10^{-3} N^{-1}
	$n_{ST} = 0.734$	-
	$a_{LV} = 20.539$	10^{-3} N^{-1}
	$n_{LV} = 0.574$	-
	$a_{HV} = 696.14$	10^{-3} N^{-1}
	$n_{HV} = 0.480$	-
frictional heating	$C_{ref} = 9.70^{16}$	(10^{-3}N mm^2) / s
	$\gamma = 0.20$	-

Table 6.15. "*BVNC*" friction model parameters

6.4 Seismic analyses on the base-isolated configuration

6.4.1 FEM model

A 3D model of the "*Piastra*" building (Fig. 6.35), implementing at its base the previously calibrated "*CSSBearing_BVNC*" elements, has been formulated with OpenSees® software. Since the "*RigidFloorDiaphragm*" multi-points constraints is not compatible with isolator elements, very stiff beams are used to rigidly connect the primary columns above the isolation level. The selected ground motions are hence applied to the lower nodes of the CSS units.

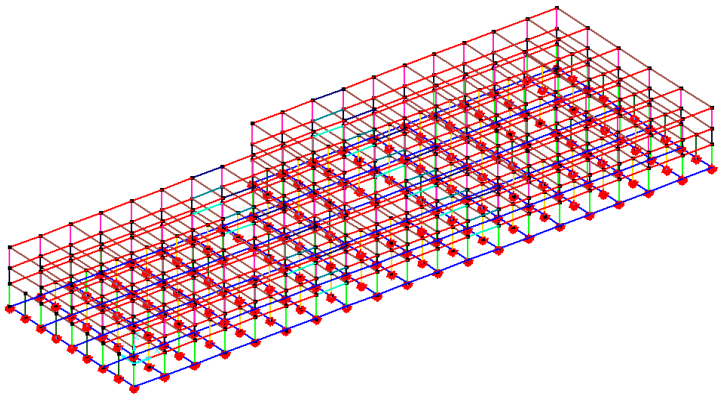

Figure 6.35. 3D view of the FEM model of the "*Piastra*" building implementing "*CSSBearing_BVNC*" isolator elements

6.4.2 Seismic response assessment

As done for the "*as-built*" configuration and in accordance with the Italian Building Code (§ 7.3.5) [3], the response of the building implementing CSS isolators at each seismic limit state was assumed as the average of the responses to the seven ground motions selected for that state.

6.4.2.1 Performance of structural elements

Based on the assumptions described in section 6.2.3.1, structural verifications can be limited to check the resistance of columns to biaxial bending moments induced by the seismic action. These are conducted according to the simplified approach provided by the Italian Building Code [3] and described in section 3.3.2.

Figures from 6.36 to 6.38 show the relevant results for the most severe "*serviceability limit state*" (SLD, PGA=0.22g), and "*ultimate limit state*" (SLC, PGA=0.50g). At both levels, the structural integrity checks are widely fulfilled. In particular, at SLC limit state, the commitment of auxiliary columns at the basement level (most stressed elements) is about the 60% of their ultimate strength; whereas for all other columns it is less than the 30%.

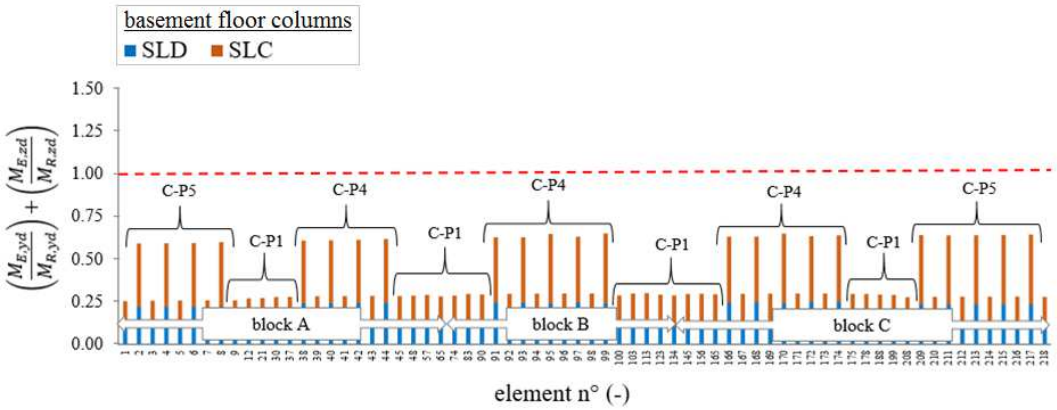

Figure 6.36. Basement floor columns: structural integrity checks at SLD (blue bars) and SLC (brown bars) limit states

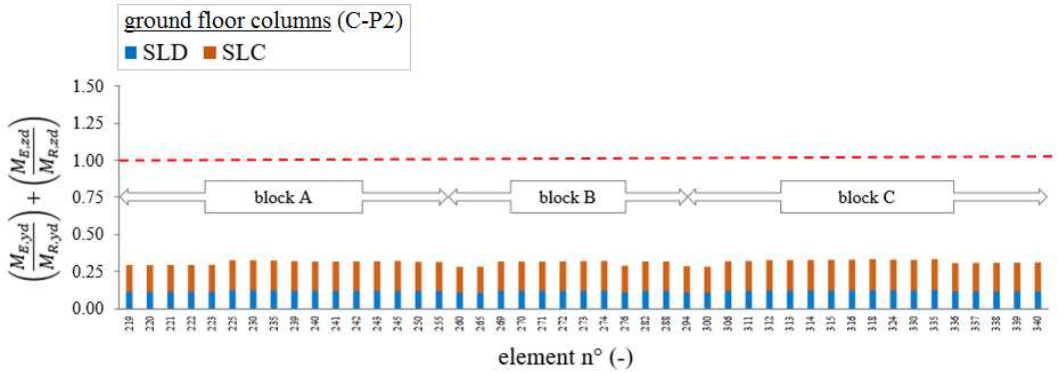

Figure 6.37. Ground floor columns: structural integrity checks at SLD (blue bars) and SLC (brown bars) limit states

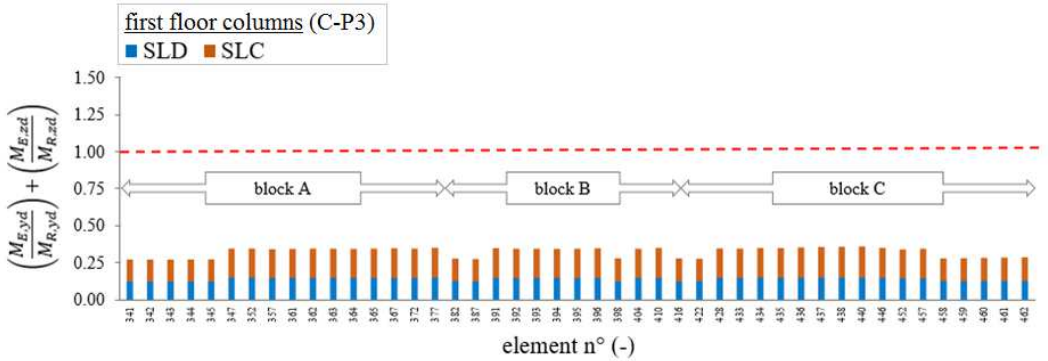

Figure 6.38. First floor columns: structural integrity checks at SLD (blue bars) and SLC (brown bars) limit states

6.4.2.2 Performance of non-structural components

The implementation of optimized CSS isolators for the seismic-retrofitting of the "*Piastra*" building allows to ensure, as required by the Italian Building Code [3] for "*serviceability limit states*", the fully operation of plants and the lack of damages to non-structural components at SLD limit state. This is enlightened by the performance checks on both "*acceleration-sensitive*" (Fig. 6.39-left), and "*drift-sensitive*" elements (Fig. 6.39-rigth): for every element the performance demand is widely below the capacity threshold.
Although not required by the code, performances of non-structural elements are assessed also for the most severe "*ultimate limit state*" (SLC), in order to foresee the possible scenario after a very intense earthquake. The following results are obtained:

1- out of order of the elevators at every floor level causing a slowdown in the transport of patients with serious injuries;

2- slight damages (the capacity exactly matches the performance demand) to curtain walls at the first floor.

It can be therefore concluded that, even in case of a very intense earthquake, the operations of the hospital could be somewhat slowed down but not compromised.

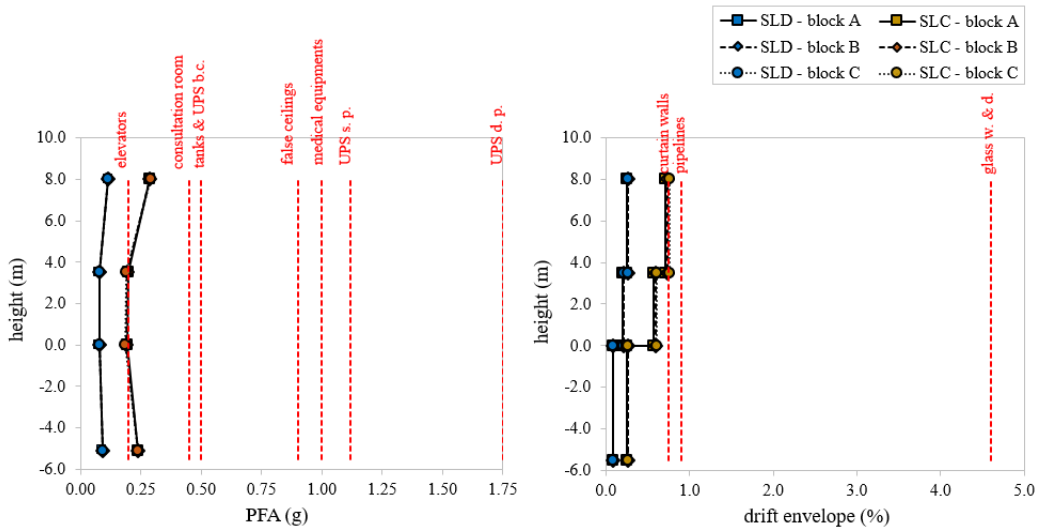

Figure 6.39. Performance checks for "*acceleration-sensitive*" (left) and "*drift-sensitive*" (right) elements at both SLD (blue points) and SLC (brown points) limit states

6.4.2.3 Performance of the isolation system

During the seismic shaking at SLC limit state, the isolation system undergoes very intense and chaotic bidirectional displacements, but in spite of this, a uniform movement of the whole building is provided. Fig. 6.40 shows the horizontal path calculated for Campano Lucano 293 event: relative displacements between each pair of blocks cannot be appreciated,

demonstrating that the assumption of rigid diaphragm behaviour is fulfilled. Relevant bidirectional hysteretic loops predicted for both primary (left) and auxiliary (right) CSS isolators are shown in Fig. 6.41.

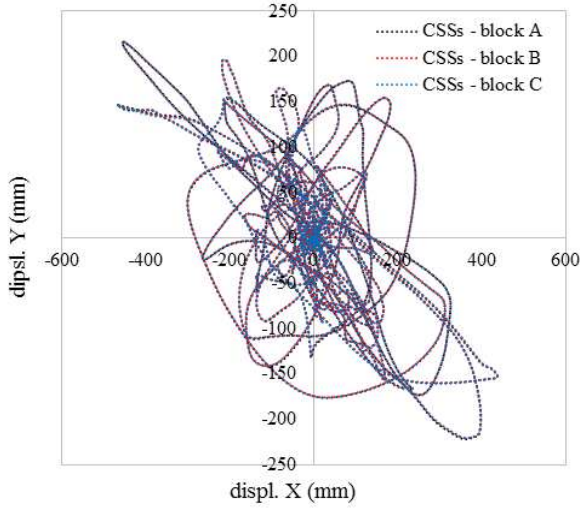

Figure 6.40. Horizontal path of the sliding isolation system calculated for Campano Lucano 293 event at SLC limit state

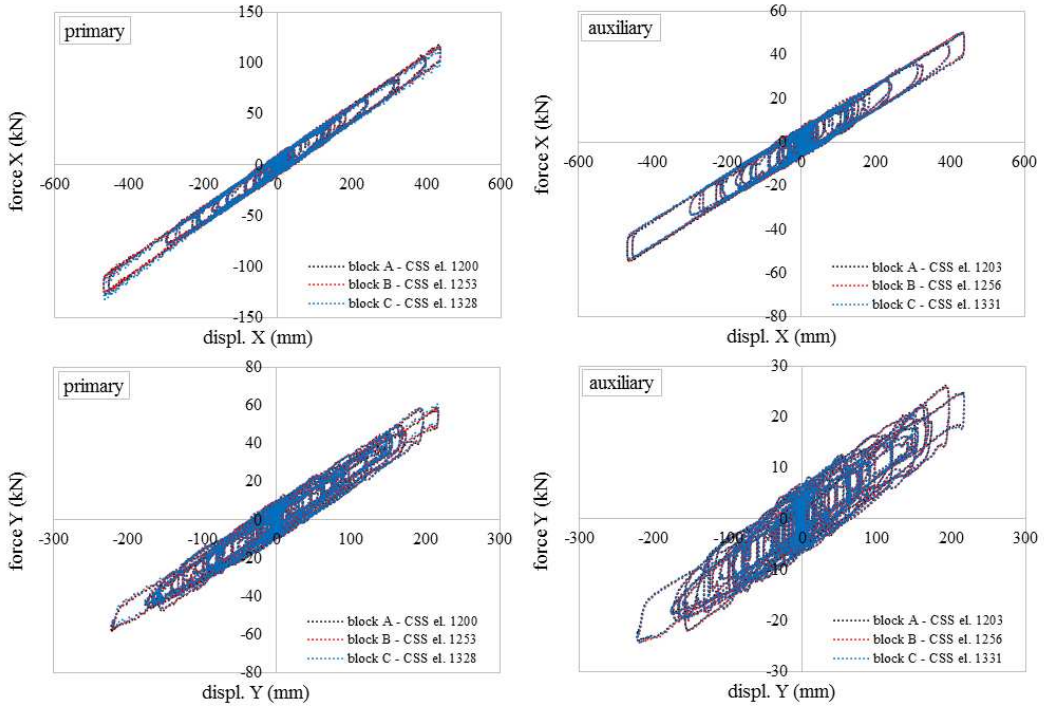

Figure 6.41. Bidirectional hysteretic loops predicted for both primary (left) and auxiliary (right) CSS isolators subjected to Campano Lucano 293 event at SLC limit state

The average performance of the isolation system at SLC limit state in terms of residual displacement, and maximum base displacement, velocity, and base shear is summarized in Table 6.16. The results are satisfactory and in line with the expectations:

1- the residual displacement ($d_{res} = 3.0mm$) is practically insignificant;

2- the maximum shear load at the base of the superstructure is within the specified limit ($V_{b,max}/W = 0.14 \leq 0.17$);

3- the maximum displacement is lower than the value preliminary predicted by the response spectrum analysis ($d_{cd} = 359 < 460mm$) and within admissible threshold ($d_{cd} \leq D_{limit} = 500mm$).

performance	**avg response**
d_{cd} (mm)	359
d_{res} (mm)	3
v_{max} (mm/s)	970
$V_{B,max}/W$ (-)	0.14

Table 6.16. Average performance of the isolation system at SLC limit state

Since $d_{cd}/(\mu_{LV} \cdot R_{eff}) \geq 2.5$, the effect of any initial offset displacements can be neglected (see the results of parametric study reported in section 4.1.3.1), and the displacement capacity (D) required to CSS isolator units is finally calculated as:

$$D \geq \gamma \cdot d_{cd} = 430.8mm \rightarrow 435mm \tag{6.7}$$

being $\gamma = 1.2$ the relevant safety factor according to EC8-2 [15](see section 1.5.4).
Table 6.17 summarizes the optimal design parameters of both primary and auxiliary CSS isolators.

design parameter	**primary CSS**	**auxiliary CSS**
D (mm)	435	435
R_{eff} (mm)	4000	4000
sliding material	lubr. PTFE	lubr. PTFE
$\phi_{sliding-pad}$ (mm)	210	95

Table 6.17. Optimal design parameters for both primary and auxiliary CSS isolators

6.5 Seismic performances comparison

The effectiveness of the optimized CSS isolators for the seismic-retrofitting of the "*Piastra*" building is again assessed comparing the seismic performances of the "as-built" and "isolated" configurations at SLO limit state. In Figs. 6.42 to 6.44 the results of the structural integrity checks in both configurations are compared: at all levels, the reduction of demand on both primary and auxiliary columns ranges between 70% and 80%.

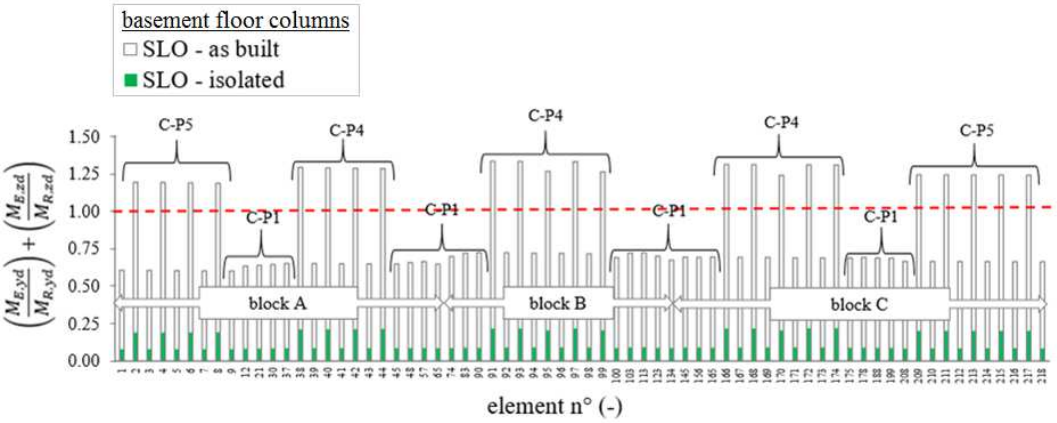

Figure 6.42. Basement floor columns structural integrity checks at SLO limit state: comparison between "*as built*" and "*base-isolated*" configurations

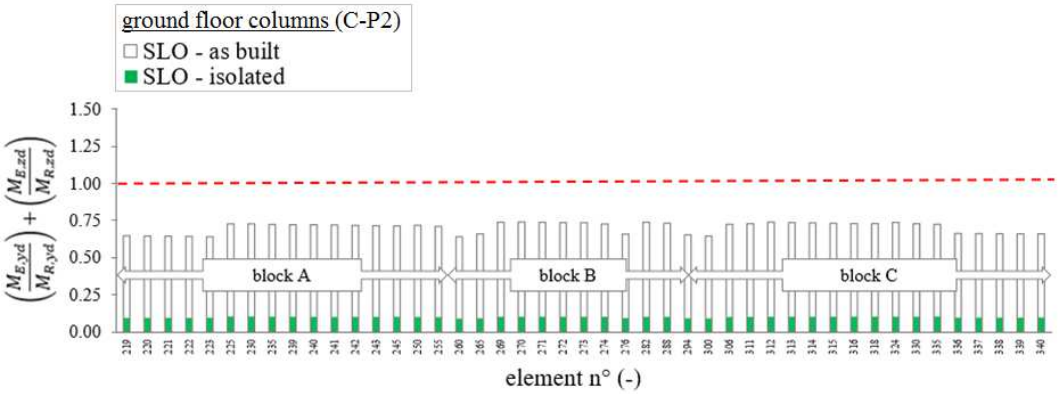

Figure 6.43. Ground floor columns structural integrity checks at SLO limit state: comparison between "*as built*" and "*base-isolated*" configurations

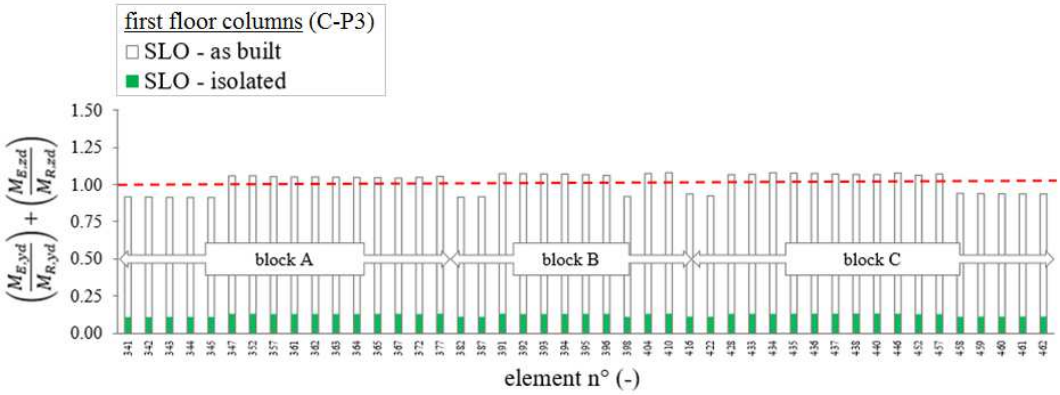

Figure 6.44. First floor level columns structural checks at SLO limit state: comparison between "*as built*" and "*base-isolated*" configurations

These achievements derive from the fact that, while in the "*as built*" configuration the seismic energy induces plastic deformation in the structure, in the "*base-isolated*" building the most of the same energy is dissipated in the isolation devices by the friction forces developed during the sliding of CSS isolators (Fig. 6.45).

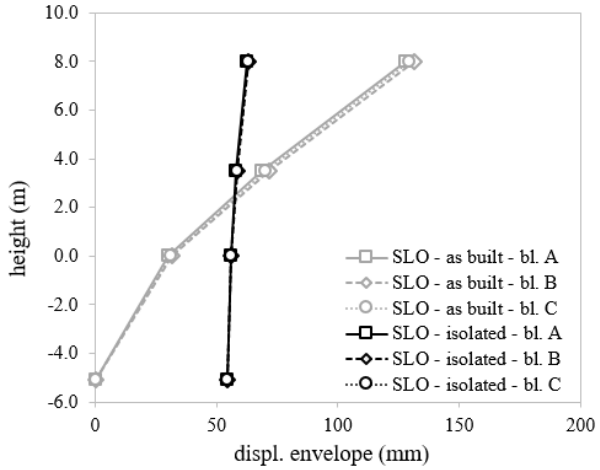

Figure 6.45. Displacements envelopes at SLO limit state: comparison between "*as built*" and "*base-isolated*" configurations

Further comments can be drawn comparing the seismic performances of non-structural components at SLO limit state. The introduction of the CSS isolators allows to reduce the absolute peak floor accelerations (PFA) of about the 60% at the basement floor, and from 75% to 85% at the upper floors (Fig. 6.46-left) leading to a complete protection of "*acceleration-sensitive*" elements. The same positive effect is obtained for "*drift-sensitive*" components thank to a reduction of the inter-storey drifts equal to 80÷85% and quite constant at each level (Fig. 6.46-rigth).

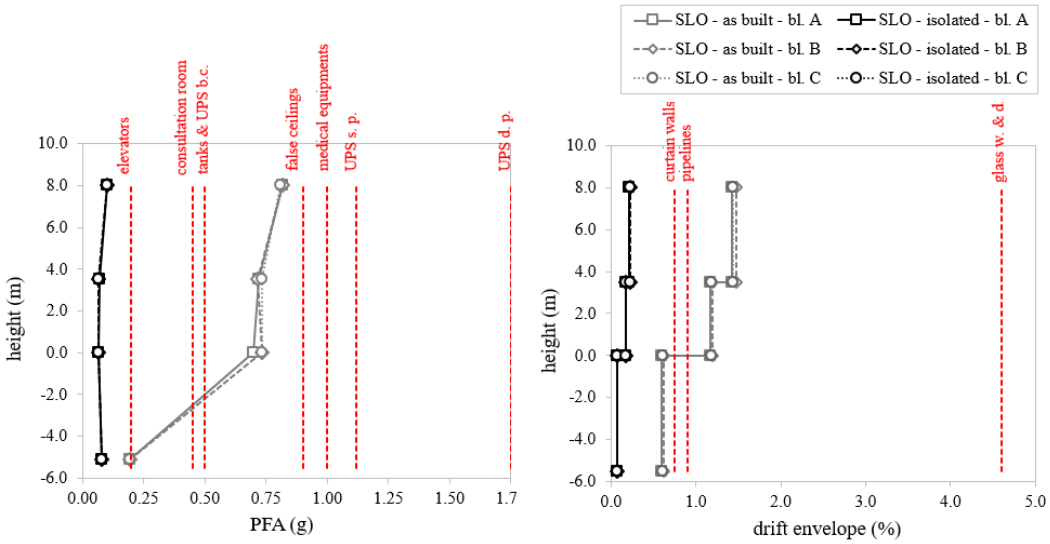

Figure 6.46. Performances of "*acceleration-sensitive*" (left) and "*drift-sensitive*" (right) elements at SLO limit state: comparison between "*as built*" and "*base-isolated*" configurations

Based on all obtained results, Table 6.18 summarizes the expected overall performance of the "*Piastra*" building of both "*as-built*" and "*base-isolated*" configurations at each seismic limit state.

limit state	as-built	base-isolated
SLO	close to collapse, severe damages to plants	undamaged structure, fully operational
SLD	collapsed	undamaged structure, fully operational
SLV	collapsed	undamaged structure, temporarily slowed operations
SLC	collapsed	undamaged structure, temporarily slowed operations

Table 6.18. Expected overall performance of both "*as-built*" and "*base-isolated*" configurations at each limit state

6.6 Chapter references

[1] Lupoi, G., Franchin, P., Lupoi, A., Pinto, P.E., Calvi, G.M. (2008) "*Probabilistic Seismic Assessment for Hospitals and Complex-Social Systems*", ROSE Research Report No. 2008/02, IUSS Press, Pavia, ISBN 978-88-6198-017-4

[2] SYNER-G project (2009-2012) "*Systemic Seismic Vulnerability and Risk Analysis for Buildings, Lifeline Networks and Infrastructures Safety Gain*", deliverables D6.7 "*Application and validation study to a hospital facility (Italy)*", available online: http://www.vce.at/SYNER-G/files/dissemination/deliverables.html

[3] Ministero delle Infrastrutture, D.M. 14.01.2008, "*Norme Tecniche per le Costruzioni*"

[4] McKenna, F., Fenves, G.L. Scott, M.H. (2000) "*Open System for Earthquake Engineering Simulation*", PEER Report

[5] Ministero delle Infrastrutture, circolare 02.02.2009 n. 617, "*Istruzioni per l'applicazione delle «Nuove norme tecniche per le costruzioni» di cui al decreto ministeriale 14 gennaio 2008"*

[6] Ambraseys, N., Smit, P., Sigbjornsson, R., Suhadolc, P., Margaris, B. (2002) "*Internet-Site for European Strong-Motion Data*", European Commission, Research-Directorate General, Environment and Climate Programme, http://www.isesd.cv.ic.ac.uk/ESD/

[7] Iervolino, I., Galasso, C., Cosenza, E. (2010) "*REXEL: computer aided record selection for code-based seismic structural analysis*", Bulletin of Earthquake Engineering, Vol. 8, pp. 339-362, doi: 10.1007/s10518-009-9146-1

[8] OpenSeesWiki, online manual, available at: http://opensees.berkeley.edu/wiki/index.php/Main_Page

[9] Paulay, T., Priestly, M.J.N. (1992) "*Seismic design of reinforced concrete and masonry buildings*", Wiley, New York

[10] Dolce, M., Ponzo, F.C., Di Cesare, A., Arleo, G. (2010) "*Progetto di edifici con isolamento sismico*", 2nd edition, IUSS Press

[11] CEN, Eurocode 8 (2004) "*Design of structures for earthquake resistance—Part 1: General rules, seismic actions and rules for buildings*", EN1998-1:2004, European Committee for Standardization, Bruxelles, Belgium

[12] Dolce, M., Cardone, D., Croatto, F. (2005) "*Frictional Behavior of Steel-PTFE Interfaces for Seismic Isolation*", Bulletin of Earthquake Engineering, Vol. 3(1), pp. 75–99, DOI: 10.1007/s10518-005-0187-9

[13] Quaglini V., Dubini P., Poggi C. (2012) "*Experimental assessment of sliding materials for seismic isolation systems*", Bulletin of Earthquake Engineering, Springer-Verlag, Vol. 10, pp. 717-740, DOI: 10.1007/s10518-011-9308-9

[14] CEN (2009) "*EN 15129 - Antiseismic Devices*", Comité Européen de Normalisation, Brussels

[15] CEN, Eurocode 8 (2005) "*Design of structures for earthquake resistance—Part 2: Bridges*", EN1998-2:2005+A1:2011, European Committee for Standardization, Bruxelles, Belgium

Conclusions

The thesis is focused on the characterization of the dynamic behavior of Curved Surface Sliders (CSS) for base isolation and the development of advanced numerical tools for the design of sliding isolation systems for seismic-retrofitting of hospitals.

Hospitals' full operation after a major seismic event is of primary importance for the management of the post-earthquake emergency. However, recent earthquakes have shown that the traditional approach for the design of earthquake-resistant structures based on the strengthening, though preventing the collapse of the building, may result in severe damages to non-structural elements and electro-medical equipment, eventually compromising the operation of the hospital. On the other side, the "*seismic mitigation*" approach, consisting in providing the building with base isolation and/or supplementary energy dissipation, has shown to be an effective solution for the protection of hospitals and hospital content from earthquake-induced damages, enhancing their resilience and entailing substantial decrease in time and cost of repair compared to a conventional fixed-base structure.

Among the current hardware for seismic isolation, Curved Surface Sliders (known in North America as the Friction Pendulum System) present high load-carrying and displacement capacity combined with compact dimensions, an oscillation period virtually independent on the mass of the superstructure, and minimization of torsional effects in case of asymmetric buildings, which make them the most suitable device for seismic retrofitting of existing buildings, like hospitals. Nevertheless, in spite of the large diffusion worldwide occurred in the last decade, a full characterization and modelling of the behaviour of sliding isolators has not been yet completely achieved, and this is also reflected in the codes and in the design tools available to structural engineers.

Within this framework, the research mainly aimed at deeply characterizing the actual behavior of Curved Surface Sliders during the seismic excitation and at developing numerical tools that can be used by practitioners for the design of sliding isolation systems for seismic-retrofitting of hospitals.

The most important milestones of the thesis are briefly described below.

1) The first achievement arises from the investigation of the *"frictional heating"* at sliding surfaces of CSS isolators under strong earthquakes and the understanding of its effects on the coefficient of friction and on the effective damping and stiffness of the device. A 3D thermo-mechanical model of a CSS isolator has been developed in Abaqus® FEM software to reproduce the heat flow at the sliding surfaces and the associated temperature increase as a function of friction, pressure and velocity, and

validated against the results of experimental tests carried out on full scale isolators. The model is proposed as a design tool to preliminarily investigate and evaluate the response of the seismic hardware under test conditions prescribed by the standards, providing valuable information for the selection of friction materials accounting for their temperature-dependent characteristics. In addition the procedure can support laboratory testing of real scale isolators, e.g. for the prediction of the temperature rise history at the sliding surface of the isolator which cannot be directly measured in the experiment.

2) A second milestone is related to another blackspot of the system: its re-centring capability. Some re-centring criteria are available in the standards, but formulated on empirical approaches and never validated for CSS isolators. In the thesis, the re-centring criterion provided in the European seismic design code is assessed by investigating in a parametric study the seismic response of the isolation system in presence of an initial offset displacement produced by either previous seismic or non-seismic loads. The effect of the initial offset on the peak and residual seismic displacements can be significant for high-friction devices subjected to *"pulse-like"* quakes. On the contrary, CSS isolators exhibit a good re-centring capability and seismic displacements independent from coexisting initial non-seismic displacements when the condition $d_m/d_{rm} \geq 2.5$ is met (where d_m is the design displacement under the reference seismic action, and d_{rm} is a mechanical parameter of the isolator). The above requirement appears to be more reliable for CSS isolators with respect to the criterion $d_m/d_{rm} \geq 0.5$ formulated in Eurocode 8 for generic bilinear isolation systems.

3) Another open issue in the analysis of structures isolated with CSS seismic isolators is the modelling of the increase in friction at the breakaway. Though this phenomenon is well known, a suitable numerical formulation is still missing in commercial software. Two different approaches have been developed to account for the *"breakaway effect"*. The first approach provides the insertion of elasto-fragile trusses at the isolation level of the building with strength adjusted to match the expected frictional resistance of the isolators at the breakaway. Important outcomes have been obtained applying this simple modelling method to a case study relevant to a five-storey building implementing CSS isolators. Indeed, analyses have shown that, in case of CSSs equipped with medium or high friction sliding materials, an high breakaway resistance can amplify both peak floor accelerations and inter-storey drifts up to 150÷200% respect to "no-breakaway" materials.

4) A more refined approach has been achieved through the development of a new friction model (named *"BVNC"*) capable to simultaneously describe the *"breakaway effect"* and the damping decay due to the *"frictional heating"*, as well

as the dependence of the friction coefficient on the instantaneous sliding velocity and normal load. The proposed formulation has been eventually validated against the hysteretic force-displacement loops obtained in experimental tests on full scale CSS isolators carried out at the SRMD Lab. of University of California, San Diego.

5) In order to account for the *"BNVC"* friction model in dynamic analyses, the plastic behaviour regulating the response of the isolator element available in the OpenSees® FEM software has been modified and an "ad hoc" code has been compiled.

6) A novel approach for the *"conceptual design"* of the isolation layout for seismic retrofitting of strategic buildings with high technological contents has been formulated. The procedure is developed step-by-step and, gradually increasing the complexity of the required calculations, aims at: : (a) defining a robust procedure for the design of seismic retrofitting interventions; (b) identifying the optimal solution with respect to target performance for the protection of both structural and non-structural components; (c) evaluating the effectiveness of the proposed solution (fault tree analysis); (d) obtaining output results more representative of the actual response of structures implementing CSS isolators using refined hysteretic models calibrated by means of experimental data.

7) In the last part of the research, the proposed conceptual design has been applied to the design of an optimized sliding isolation system for the seismic-retrofitting of a real hospital. The hospital *"Giovanni Paolo II"* of Lamezia Terme, located in a high seismic prone area in southern Italy, has been chosen as case-study. Nonlinear dynamic analyses have been carried out in OpenSees® on both the *"as-built"* and *"base-isolated"* configurations implementing, in the second case, the *"BVNC"* friction model and the modified isolator element. The proposed solution has been shown to widely improve the overall performance of the hospital complex at each seismic limit state provided by the Italian Building code. In particular, for low-moderate earthquakes at "*serviceability limit states*" (PGA from 0.17 to 0.22g), the implementation of optimized CSS isolators allows a 60÷85% reduction of both seismic-demand on column elements and peak floor accelerations. This improvement, in addition to preventing the structural collapse, allows the complete protection of non-structural components, and hence the full operation of the hospital in the emergency response. For more severe events at "*ultimate limit states*" (PGA from 0.45 to 0.50g), the adopted solution ensures again the structural integrity and limits the damages to plants with minor effects on the hospital's operation.

Significant damages suffered by hospital buildings during the recent earthquake occurred in Central Italy confirmed once again that national facilities are still largely vulnerable to these calamities. Although the Writer hopes that in the near future this study will provide valuable information for the design of optimized seismic-retrofitting interventions, some aspects require further investigations. In particular, some hints for future developments concern:

1) the investigation of potentially dangerous effects of vertical components of seismic excitation (hardly mitigated by base isolation systems) on both structural and non-structural elements of hospital buildings. The study should also aim at identifying effective solutions for the local protection of the most critical functional areas (e.g. surgery division) and the most sensitive non-structural components (e.g. medical equipment);

2) the refinement of the *"conceptual design"* proposed in Chapter 5 in order to include more challenging structures for which it might be necessary an isolation system articulated on multiple levels. In addition, the revised design procedure should also be adapted to provide specific target performances for the protection of *"velocity-sensitive"* non-structural components.

ANNEX

Proposed criterion for *"pulse-like"* quakes detection

A ground motion is conventionally classified as *"pulse-like"* if the velocity time-history contains a pulse that is a large portion of the ground motion. A criterion for the identification of *"pulse-like"* quakes, based on signal processing through wavelet analysis, was proposed by Baker and Shrey [1-2] and used for classification of PEER database ground motion as *"pulse-like"* or *"no-pulse"* [3]. The PEER classification takes into account simultaneously the records of the two orthogonal horizontal acceleration components and provides an overall categorization of the ground motion. On the contrary, in the criterion proposed hereafter, simple unidirectional records are considered and *"pulse-like"* events are detected based on a signal relevant to a single horizontal component. A synthetic pulse index PI_k is defined as the ratio between the time interval $D_{v,T}$, during which most of the seismic energy is introduced in the structure, and the duration of the quake $D_{v,B}$:

$$PI_k = 1 - \frac{D_{v,T}}{D_{v,B}} \tag{A.1}$$

where $D_{v,T}$ and $D_{v,B}$ are the Trifunac [4] and the bracketed [5] durations of the ground motion, respectively. $D_{v,T}$ is the time interval between the instants corresponding to 5% and 95% of the energy integral $I_E = \int_0^\infty v_g^2 dt$ [6]:

$$D_{v,T} = t_{0.95\,I_E} - t_{0.05\,I_E} \tag{A.2}$$

and $D_{v,B}$ is the time interval between the first and the last overcoming of a given threshold (i.e. 1% of the absolute peak velocity) of the strong motion phase.

The pulse index PI_k ranges between 0 and 1: values close to the first limit correspond to oscillatory events; on the contrary, values close to the second limit are relevant to *"pulse-like"* ground motions. Two thresholds have been defined in order to categorize quakes with different pulse contents. The threshold PI_k=0.70, that allows to detect *"pulse-like"* signals ($PI_k \geq 0.70$), has been chosen in order to ensure a good agreement with the classification

obtained through the application of the Baker index. In addition, the threshold PI_k=0.40 has been set to distinguish *"no-pulse"* (PI_k<0.40) and *"weakly-pulse"* ($PI_k \geq$0.40) events. Examples of ground acceleration records classified as *"no-pulse"* (PI_k=0.24), *"weakly-pulse"* (PI_k=0.46), and *"pulse-like"* (PI_k=0.89) are illustrated in Fig. A.1. In the latter case, the presence of a pulse in the displacement time-history is evident.

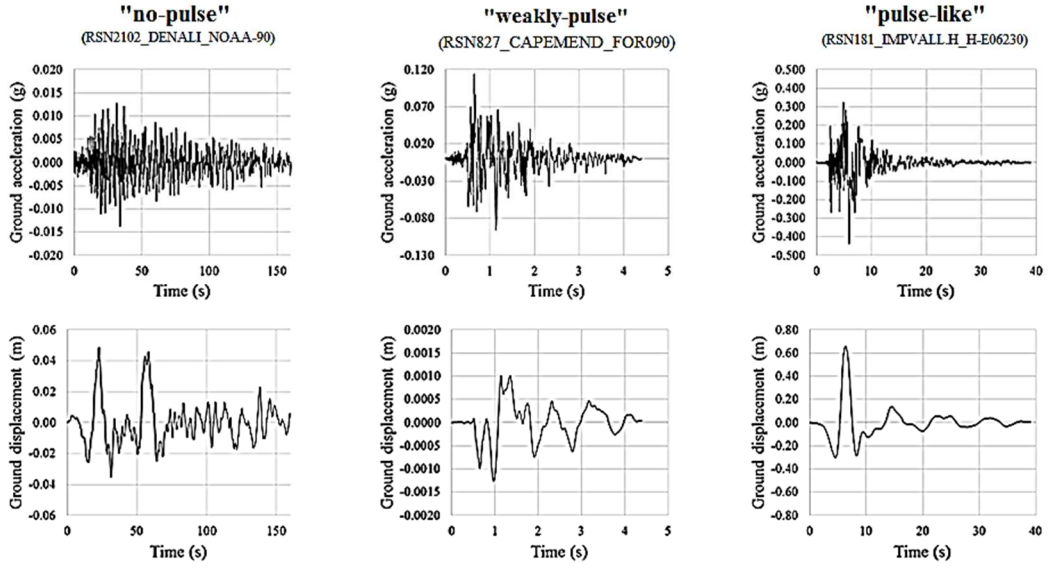

Figure A.1. Ground acceleration (top) and ground displacement (bottom) time-histories relevant to *"no-pulse"* (left), *"weakly-pulse"* (centre) and *"pulse-like"* (right) events

Annex references

[1] Baker, J.W. (2007) "*Quantitative Classification of Near-Fault Ground Motions Using Wavelet Analysis"*, Bulletin of the Seismological Society of America, Vol. 7(5**)**, pp. 1486–1501, DOI:10.1785/0120060255

[2] Shrey, K., Baker, J.W. (2014) "*An efficient algorithm to identify strong-velocity pulses in multicomponent ground motions*", Bulletin of the Seismological Society of America, Vol. 104(5), pp. 2456-2466

[3] Ancheta, T.D., Darragh, R.B., Stewart, J.P., Seyhan, E., Silva, W.J., Chiou, B.S.J., Wooddell, K.E., Graves, R.W., Kottke, A.R., Boore, D.M., Kishida, T., Donahue, J.L. (2013) "*PEER NGA-West2 Database*", PEER 2013/03. Pacific Earthquake Engineering Research Center (PEER), Berkeley, USA

[4] Trifunac, M.D., Brady, A.G. (1975) "*A study of duration of strong earthquake ground motion*", Bulletin of the Seismological Society of America, Vol. 65(3), pp. 581-626

[5] Bolt, B.A. (1969) "*Duration of strong motion*", Proceedings of the 4th World Conference on Earthquake Engineering, Santiago, Chile

[6] Anderson, J.C., Bertero, V.V. (1987) "*Uncertainties in establishing design earthquakes*", Journal of Structural Engineering, Vol. 113 (8), pp. 1709–1724